DIAMOND FOR STEM CELL BIOTECHNOLOGY

Alice Taylor

This thesis is submitted for the degree of Doctor of Philosophy

Department of Electronic and Electrical Engineering
University College London
University of London
2016

DECLARATION

‘ I, Alice Taylor confirm that the work presented in this thesis is my own. Where information has been derived from other sources, I confirm that this has been indicated in the thesis.'

ACKNOWLEDGMENTS

The interview for my PhD took place at the ‘award winning’ curry house the Drummond Villa. I hate this place. Everyone I know hates this place – everyone apart from Professor Richard Jackman. Richards’s ridiculous eating habits and incredible loyalty has no doubt, kept the Drummond Villa in business. Richard isn’t just loyal; he is incredibly generous, extravagant and likes to have fun. It is a combination of these factors that have made my time as a member of the DEG, so far, so positively memorable. Not only is enormous Richard fun, he is also a superb supervisor. Throughout my PhD he has been an invaluable source of advice and guidance. Richard – I owe you a pint.

I would like to thank Dr Robert Edgington for being a great supervisor – you taught me a lot. Also thanks to the long list of DEG members who I’ve had the pleasure of working and hanging out with: Aysha Chaudhary, Joseph Welch, Ana Carolina Parada, Fang Zhao, Mohammad Golsharifi, Suguru Amakubo, Thuong Thuong Nyugen, Alex Pakpour–Tabrizi, Ralph Moors, Abdul Afandi, Will Parfitt, Marie Hicks, Steven Evans and Terry Kang – it wouldn’t have been the same without you guys! A particular shout out goes to Rob, Alex and Joe. By gum – we’ve had fun.

Thank you Dr Patrizia Ferratti for being so enthusiastic throughout out collaborations. Thank you to Barbora Vagaska and Citlali Helenes Gonzalez for performing numerous cell culture assays and putting up with my insistence that nanodiamonds solve everything. I would also like to thank Philippe Bergonzo and Clement Hebert for providing invaluable samples. Steve Hudziak, Steve Etienne, Richard Thorogate, Dale Moulding and Suguo Huo: your technical assistance has been really appreciated! The EU is also acknowledged for funding this research.

Mum, Dad and El – you guys are amazing. Thank you for your love, encouragement and being there for me no matter what. We have such a laugh and I love you all so much. I would also like to thank the rest of my family and my friends – you are a crazy bunch and I’m very lucky to have you. Thank you Blue. You’re the best. Woof. Lastly, I would like to thank Ben Miller, my gorgeous boyfriend. Thanks for your love, support, and scientific advice – I’ve learnt so much from you. Thank you for being my rock, I love you dearly.

ABSTRACT

The recent rise in life expectancy has led an increase in the number of cases of neurological diseases such as Alzheimer's, Parkinson's and macular degeneration. Traditional therapeutic approaches are ineffective as regeneration is limited in the Central Nervous System (CNS). Neural prosthetics and stem cell therapy present exciting solutions for enabling the function of the brain to be restored. Implanted materials for neuronal prosthetics must have outstanding electrical properties whilst being inert and biocompatible. Diamond fulfils there criteria, and is the focus of this thesis.

Results chapter 5 describes a novel approach to pattern diamond to 5 μm resolution, with feature widths of 2 μm. Selective seeding of nanodiamonds (NDs) was performed using a microprinting technique, which was then grown into Nanocrystalline diamond (NCD) films via Chemical Vapour Deposition (CVD) into the desired pattern. The ability to pattern diamond is not only valuable for biomaterial design, but also for photonic and microelectromechanical systems (MEMS) prototyping applications. Chapter 6 describes the quantitative investigation as to whether the inclusion of boron in NCD (BNCD) has any observable effect on biocompatibility. The effect of nanostructuring BNCD on biocompatibility was also investigated. The attachment and proliferation of human Neural Stem Cells (hNSCs) was used to assess biocompatibility. Nanostructuring of BNCD was done using a CNT scaffold resulting in a material with increased capacitance. Combining the capacitive increase, wide electrochemical window and demonstrated biocompatibility, diamond has shown to be an ideal material for interfacing with neurons.

Chapter 7 describes the investigation into whether NDs support hNSC growth. hNSCs were cultured on hydrogen and oxygen functionalised NDs, and it was discovered that O–NDs promote hNSC adhesion whereas H–NDs do not. Contact angle and protein adsorption measurements were employed to investigate and hypothesise why a difference in hNSC adhesion is observed. Chapter 8 demonstrates the capacity of ND for supporting hNSC differentiation. The effect of varying ND functionalisation on differentiation was investigated, with H– and O–NDs inducing the spontaneous differentiation of hNSCs into neurons. Complimenting results obtained in Chapter 7, O–NDs were best at supporting adhesion and promoting neurite outgrowth.

TABLE OF CONTENTS

LIST OF ABBREVIATIONS

AFM	Atomic Force Microscopy
ANOVA	One way Analysis of Variance
AR2G	Amine Reactive 2nd Generation
BBB	Blood Brain Barrier
BDD	Boron–doped Diamond
BDNF	Brain Derived Neurotrophic Factor
BLI	Bio–layer Interfemometry
BNCD	Boron–doped Nanocrystalline Diamond
BSE	Backscattered Electrons
CNS	Central Nervous System
CNT	Carbon Nanotube
CNTF	Ciliary Neurotrophic Factor
CVD	Chemical Vapour Deposition
DCX	Doublecortin
DD	Dot Diameter
DI	Deionised
DIV	Days in Vitro
DND	Detonation Nanodiamond
ECM	Extracellular Matrix
EDC	1-Ethyl-3-[3-dimethylaminopropyl] carbodiimide hydrochloride

EGF	Epidermal Growth Factor
FEG	Field Emission Gun
FGF	Fibroblast Growth Gactor
GFAP	Glial Fibrillary Acidic Protein
hNSC	human Neural Stem Cell
HPHT	High Pressure High Temperature
ICH	Immunocytochemistry
ID	Inner Diameter
IGL	Internal Granular Layer
IPA	Isopropanol Alcohol
LN	Laminin
MAP2	Microtubule Associative Protein 2
MB	Methylene Blue
MEA	Microelectrode Array
MEMS	Microelectromechanical Systems
MWPECVD	Microwave Plasma Enhanced Chemical Vapour Deposition
Nestin	Neuroepithelial Stem Cell Protein
NHS	N-hydroxysulfosuccinimide
NSC	Neural Stem Cell
NCD	Nanocrystalline Diamond
ND	Nanodiamond
NF200	Neurofilament 200
NGF	Nerve Growth Factor
NT–3	Neurotropin–3

NV	Nitrogen–vacency
OD	Outer Diameter
PBS	Phosphate Buffer Solution
PCD	Polycrystalline Diamond
PDF	Platelet–derived Factor
PL	Poly–L–Lysine
ppt	Parts per thousand
RIE	Reactive Ion Etch
RF	Radio Frequency
RMS	Rostral Migratory System
RT	Room Temperature
SCD	Single Srystal Diamond
SCZ	Subcallosal Zone
SGZ	Subgranular Zone
SE	Secondary Electron
SEM	Scanning Electron Microscopy
SEZ	Subependymal Zone
SNT	Simple Neurite Tracer
SPM	Scanning Force Microscopy
SVZ	Subventricular Zone
TCPS	Tissue Culture Polystyrene
t.o.f	Time of flight
UHV	Ultra–high Vacuum
UNCD	Ultra–nanocrystalline Diamond

VACNT	Vertically Aligned Carbon Nanotube
VdW	Van der Waals
XPS	X–ray Photoelectron Spectroscopy

FIGURES AND TABLES

CHAPTER 1 – INTRODUCTION

Since ancient times diamonds have been admired as gemstones. To Greek and Roman civilizations diamonds were seen to be extremely important and powerful. People believed they were the tears of the Gods and bits of broken stars that had fallen to earth. It has only been since the middle of the twentieth century that diamond has been subject to scientific research due to many of its superlative properties. It is a combination of the physical, electrical, chemical and biological properties of diamond that transform it from an object associated with beauty and wealth into a superior material for scientific applications. Successful diamond synthesis was achieved in the 1950s using a high-pressure, high-temperature (HPHT) method. This however resulted in diamond with high impurity content led to the realization that diamond is unsuitable for electronic applications. The discovery of Chemical Vapour Deposition (CVD) in the 1960s led to the growth of diamond of a much higher purity. Diamond grown via this method possessed many superb properties desired for electronic materials.

In recent times there has been a dramatic increase in the average life expectancy of the global population, which has been deemed as one of society's greatest achievements. However, this aging population is faced with increasing occurrence of age–related diseases. Amongst those diseases, Alzheimer's, Parkinson's, Huntington's, macular degeneration and retinis pigmentosa represent a significant proportion, all of which are a consequence of neurodegeneration. Neurodegenerative diseases stem from the incapacity of neurons to regenerate in the human brain. They are debilitating conditions that result in the progressive degeneration of the Central Nervous System (CNS), effecting movement (ataxias) and mental function (dementias). Dementias are the most common type of neurodegenerative disease and are characterised by changes in mood, memory loss and difficulties in communicating. Alzheimer's disease is the most common neurodegenerative disease, accounting for more than two–thirds of all dementia cases. Alzheimer's and related disorders affect over seven million people in Europe and care for those affected costs approximately €130 billion per annum. Traditional therapeutic tissue restoration is ineffective for the treatment of neurodegenerative diseases because of the

limited capacity of the CNS to regenerate neurons. Artificial prosthetic devices are increasingly being used to restore lost function as a result of these neurodegenerative diseases, including cochlear implants, retinal implants and neural prosthetics. These prosthetic devices are subject to intensive research at present as there is currently no cure for dementia.

The main objectives of this thesis were to display the versatility of diamond and to promote the use of diamond as a material with great potential for enabling the treatment of neurological diseases. Currently, diamond is believed to be a difficult material to process because of its extreme physical properties. Herein, a novel, facile method for patterning diamond growth has been described in this thesis, where a bottom–up approach was developed to allow for the patterning of diamond without the use of lithography. This simplistic method facilitates the removal of the negative stigma, which is associated with diamond processing. Nanodiamonds have also been used throughout this thesis as a substrate for investigating their interaction with human Neural Stem Cells (hNSCs). Throughout this thesis reproducible methods for modifying the surface of nanodiamonds have been developed, this variation of termination has shown to be hugely influential in determining hNSC behaviour. Results included in this thesis highlight the use of oxygen functionalised nanodiamonds for increasing hNSC adhesion and manipulating the differentiation into neurons. This also promotes the use of nanodiamond for treating neurodegenerative diseases, where controlling cell fate is crucial. Boron–doped diamond has shown to be a promising material for neural prosthesis due to its outstanding electrical properties, inert chemistry and demonstrated excellent biocompatibility. Herein, the use of diamond has been exploited as a material, which is both easy to process and has demonstrated superb cellular interactions.

Chapter 2 introduces carbon, and specifically diamond as a scientific material. The exceptional properties and history of synthetic diamond production are reviewed, the doping discussed and different forms of diamond are detailed, highlighting nanocrystalline diamond (NCD) films and nanodiamonds (NDs). In particular the formation and purification of NDs is described, alongside surface functionalisation and biological applications. Chapter 3 introduces neural stem cells (NSCs), firstly giving an overview of stem cells, highlighting their

differentiation capacity and role in maintaining healthy organs. NSCs are then discussed, defining neurological function, anatomical location in the adult brain, the main cell types in the brain, and the potential for treatment of a diseased or damaged Central Nervous System (CNS) using stem cell therapy. Chapter 4 details experimental techniques and methods used throughout this thesis.

Chapter 5 is the first results chapter, which describes a novel technique for patterning ND tracks using a micropipette dispensing system. ND–containing inks were printed and then successfully grown via microwave plasma enhanced chemical vapour deposition (MWPCVD) into desired patterns of NCD film. The ability to pattern diamond is useful for many applications, including photonics, microelectromechanical systems (MEMS) prototyping and biomaterial design. Here, a microprinting technique using a computer–driven micropipette has been developed to deposit patterns of ND monolayers from an unreactive water/glycerol ND ink. A lateral patterning resolution of 5 μm and feature widths of ca. 2 μm has been achieved. The concentration and composition of the ND solutions have been optimised using atomic force microscopy (AFM) to realise high–density monolayers of NDs and consistent ND printing. Subsequent NCD patterns grown using CVD show a high level of compliance with the printed ND pattern. This ‘direct-write’, bottom-up and additive process offers a versatile and simple alternative to pattern diamond. The process has the particular advantage that it does not require lithography and destructive processing such as reactive ion etching (RIE); and, pertinently, does not involve reactive chemicals that could alter the surface chemistry of NDs. The technique also allows for the growth of discrete, localised, single crystal nanodiamonds with applications in quantum technology.

Chapter 6 describes the biocompatibility of nanostructured boron doped diamond (BDD) for the attachment and proliferation of human Neural Stem Cells (hNSCs). The biocompatibility of CVD diamond (un–doped) has been investigated numerous times, providing diamond with the ‘biocompatible’ tagline. Here, the inclusion of boron into NCD (BNCD) and its effect on biocompatibility has been quantitatively investigated by observing the interaction of hNSCs on a variety of NCD and BNCD substrates. It was discovered that the inclusion of boron has no observable effect of cell attachment and viability, which was confirmed by

analysis of immunostained images and the quantitative Methyl Blue (MB) assay. The MB assay allows for a specific dye to enter healthy cells, the dye is then eluted and spectrophotometrically measured. The effect of nanostructuring the BNCD films on the survival of hNSCs was investigated. BNCD was nanostructured via growing boron–containing diamond over CNT scaffolds of differing lengths. It was found that the biocompatibility of BNCD was increased upon nanostructuring.

Results in Chapter 7 highlight the potential of ND monolayers as a biomaterial for interfacing with hNSCs. The adhesion of hNSCs on NDs with hydrogen and oxygen functionalisation was investigated for the first time. It was discovered that O–ND monolayers are superb at supporting hNSC attachment, compared to H–NDs where minimal adhesion was observed. The roughness of ND monolayers is comparable to Tissue Culture Polystyrene (TCPS), which is ideal for cell attachment. Contact angle results suggests that O–NDs interact with proteins such as laminin and poly–L–lysine in a unique way, as the surface remains hydrophilic after protein coating, unlike TCPS, glass and H–NDs. Protein adsorption results confirmed this hypothesis as O–NDs readily bound to protein–coated biosensors, whereas H–NDs did not. O–NDs are an exciting material for interfacing with neurological cells and it has been hypothesized that the nano–roughness, hydrophilicity, surface charge and protein adsorption affinity of O–NDs mimics the environment in which hNSCs naturally occur.

Chapter 8, the final results chapter, demonstrates the capacity of ND monolayers as a substrate for supporting hNSC differentiation. Firstly, hNSCs were subject to a neuronal lineage differentiation medium where the cells were successfully induced from hNSCs into neurons on untreated–NDs. The effect of functionalising the NDs on this differentiation was investigated. O–NDs were shown to promote hNSC adhesion, proliferation and differentiation, while the performance of H–NDs was significantly less. These results support conclusions drawn in Chapter 7. hNSCs were then induced into oligodendrocytes on both NDs with and without poly–L–lysine and laminin coating which resulted in a sphere like cluster of cells. This preference for neuronal adhesion was then confirmed via spontaneous differentiation of hNSCs, where inducing factors were removed from the culture medium and cells were left for 25 days *in vitro*. It was discovered that both H–

and O–NDs promoted the differentiation of hNSCs into neurons without exterior manipulation. A statistically significant difference was observed in neurite extension on O–NDs over H–NDs and the glass control, suggesting a substrate suitable for superior neural network formation.

Chapter 9 summarises results attained throughout this thesis, with future work being detailed. The impact of these results and potential applications is discussed.

PUBLICATIONS

Taylor, A. C., Edgington, R., & Jackman, R. B. (2015). Patterning of Nanodiamond Tracks and Nanocrystalline Diamond Films Using a Micropipette for Additive Direct-Write Processing. *ACS Applied Materials & Interfaces*, *7*(12), 6490–6495.

Taylor, A. C., Vagaska, B., Edgington, R., Hebert, C., Ferretti, P., Bergonzo, P., & Jackman, R. B. (2015). Biocompatibility of nanostructured boron doped diamond for the attachment and proliferation of human neural stem cells. *Journal of Neural Engineering*, *12*(6), 066016. Selected for the Journal of Neural Engineering Highlights of 2015 special edition.

Taylor, A. C., Helenes Gonzalez, C., Edgington, R., Ferretti, P., & Jackman, R. B. O vs. H functionalised nanodiamonds on neural stem cell adhesion and protein adsorption. (Manuscript in preparation).

Taylor, A. C., Helenes Gonzalez, C., Edgington, R., Ferretti, P., & Jackman, R. B. Spontaneous differentiation of human neural stem cells on nanodiamond. (Manuscript in preparation).

CONFERENCE PAPERS

POSTER PRESENTATIONS

Patterning of nanodiamond tracks using a versatile microplotting technique
SBDD XVII, Hasselt Diamond Workshop, 2013

Nanodiamond as a platform for human neural stem cell proliferation and differentiation
IMRC XXIII, Cancun, Mexico, 2014

Patterning of nanodiamond tracks using a versatile microplotting technique
SBDD XX, Hasselt Diamond Workshop, 2015

ORAL PRESENTATIONS

Nanodiamond as a platform for neural stem cells proliferation and differentiation
IMRC XXII, Cancun, Mexico, 2013

Nanodiamond as a platform for human neural stem cell proliferation and differentiation
SBDD XVIII, Hasselt Diamond Workshop, 2014

The growth performance of human neural stem cells on boron-doped nanocrystalline diamond coated CNTs
IMRC XXIII, Cancun, Mexico, 2014

Nanodiamond as a platform for human neural stem cell proliferation and differentiation
INASCON, Middelfart, 2014

Biocompatibility of nanostructured diamond for the attachment and proliferation of human neural stem cells
SBDD XX, Hasselt Diamond Workshop, 2015

Biocompatibility of nanostructured diamond for the attachment and proliferation of human stem cells
NCND, Japan, May 2015

CHAPTER 2 – DIAMOND

Diamond has been highly desired for centuries as a gemstone because of its lustre and exceptional brillance. However, diamond is also a highly desirable material for many scienfitic applications due to its extreme and exceptional properties. Diamond is the hardest known material, it is the stiffest and least compressible. It is chemically inert, biocompatible, an excellent thermal conductor, it has a negative electron affinity and it is also transparent from deep UV – far IR.

2.1 BONDING IN CARBON

There is no doubt that carbon is one of the most versatile elements. It is the basis of life on earth and it is the building block upon which all organic chemistry exists. Around 20 million molecules are known, and about 79% of these contain carbon and therefore are organic. The ground state of carbons electronic structure is $1s^2$ $2s^2$ $2p_x^1$ $2p_y^1$ (see Figure 2.1 a). Linus Pauling, a chemist, was first to propose the idea of molecular orbital hybridisaion in 1931, and he used this theory to explain the structure of certain molecules including methane [1]. The two 2s and the two 2p wavefunctions are able to hybridise and there are three types of s and p orbitals which are able to form, these are sp^3 (Figure 2.1 b), sp^2 (Figure 2.1 c), and sp (Figure 2.1 d). Sp^3 orbitals arise from the equal hybridisation of the 2s, $2p_x$, $2p_y$ and the empty $2p_z$ orbital, this results in four sp^3 orbitals which are able form four identical sigma (σ) covalent bonds with a tetrahedral arrangement. The simplest form of this sp^3 hybridisation is methane which is a tetrahedron comprising of four with equivalent C–H bonds with a 109.5° seperation. Sp^2 orbital hybridisation occurs when the 2s, $2p_x$ and $2p_y$ orbitals hybridise to form 3 sp^2 orbitals with one empty $2p_z$ orbital leftover. The sp^2 orbitals form 3 planar σ bonds, and the $2p_z$ orbital which is perpendicular to this plane, and is able to form π bonds with other p orbitals with the same orientation, which results in a double bond. The simplest double bond is that present in ethene (C_2H_4), which is a trigonal planar molecule with 120° seperation between C–H bonds. Sp orbital hybridisation occurs when the 2s and $2p_x$ orbitals hybridise, leaving the $2p_y$ and $2p_z$ orbitals unchanged and able to form two mutually perpindicular π bonds

resulting in a triple bond which is linear. Organic matter in composed of different combinations of these three hybrid orbitals which are sumarised in (Figure 2.1).

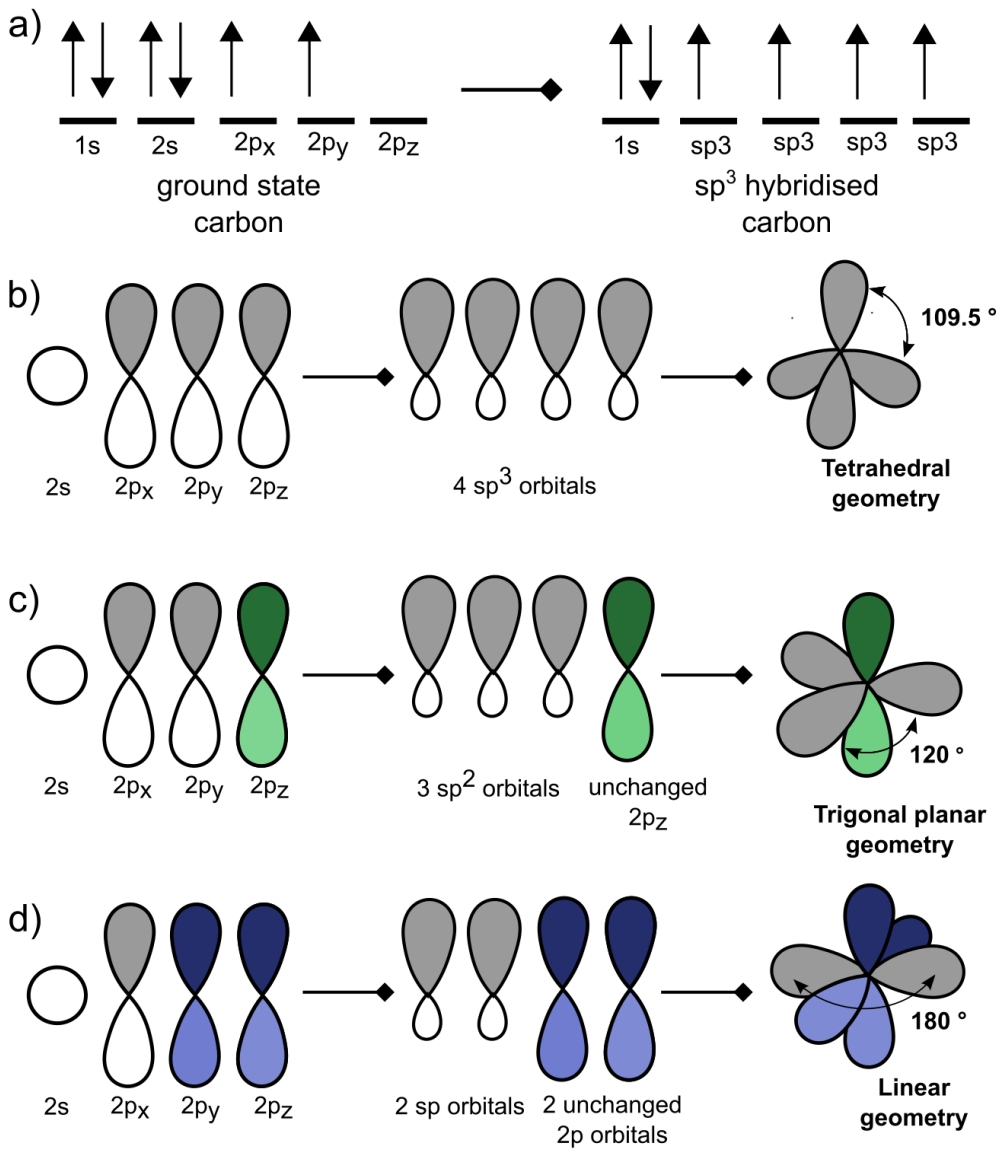

Figure 2.1 (a) the distribution of electrons for the ground state and sp^3 hybridided carbon. (b) shows the molecular orbital hybridisation of s and p orbitals into sp^3 hybrid orbitals, (c) into sp^2 orbitals and (d) sp orbitals.

Carbon is able to form many different allotropes as a consequence of the presence of sp^3, sp^2 and sp orbitals. Diamond and graphite are the most commonly known and commercially exploited, but many other allotropes exist

with some forms only recently being discovered. A non-extensive list of some of these allotropes is presented in (Figure 2.2). The sp^3 hybrid orbital of carbon is responsible for the tetrahedral struture of diamond, and it is this carbon-carbon bond which is accontable for some of diamond's outstanding properties.

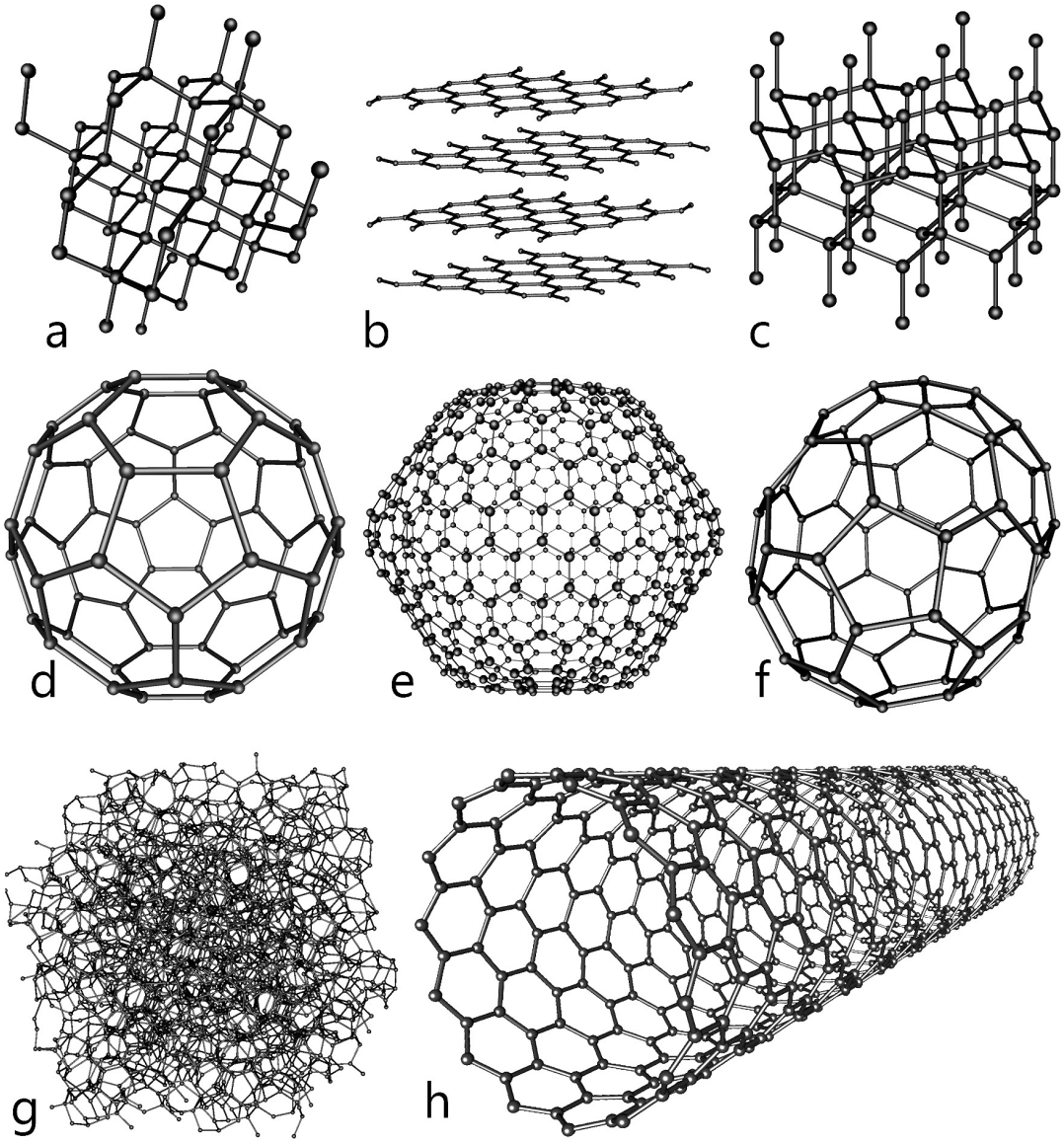

Figure 2.2 A non-exclusive list of some of the possible allotropes of carbon: (a) Diamond, (b) graphite, (c) Londsdaleite, (d) C_{60} (buckminsterfullerene, (e) C_{540} fullerene, (f) C_{70} fullerene, (g) Amorphous carbon, (h) single walled carbon nanotube. (Taken from Wikimedia Commons).

Diamonds crystal structure is face-centre cubic, which consists of 8 carbon atoms per unit cell (Figure 2.3 a). Face-centre cubic systems have lattice atoms on the faces of the cube as well as at the corner lattic points, the location of aditional carbon atoms are at a_0 (¼, ¼, ¼), a_0 (¾, ¾, ¼), a_0 (¾, ¼, ¾) and a_0 (¼, ¾, ¾), where a_0 is the lattice constant (3.566986 Å ± 2.6 x 10^{-6}) [2]. This lattice constant is equal to the length of the cubic side, which at room temperature (300 K) is approximetly equal to 3.567 Å. The C–C bond length (d) is equal to ¼ of the cubic body diagonal, so that d = $\sqrt{(3\ a_0 / 4)}$ = 1.53 Å [3]. The atomic density of diamond is 1.76 x 10^{23} atoms/cm^3 which is the highest of any known material. This explains why diamond is the hardest, stiffest and least compressible of all materials. There are three crystallographic Miller planes within the diamond lattice, these can be used to describe the diamond structure and also the surface of diamond. These are: (100), (110) and (111) (Figure 2.3 b).

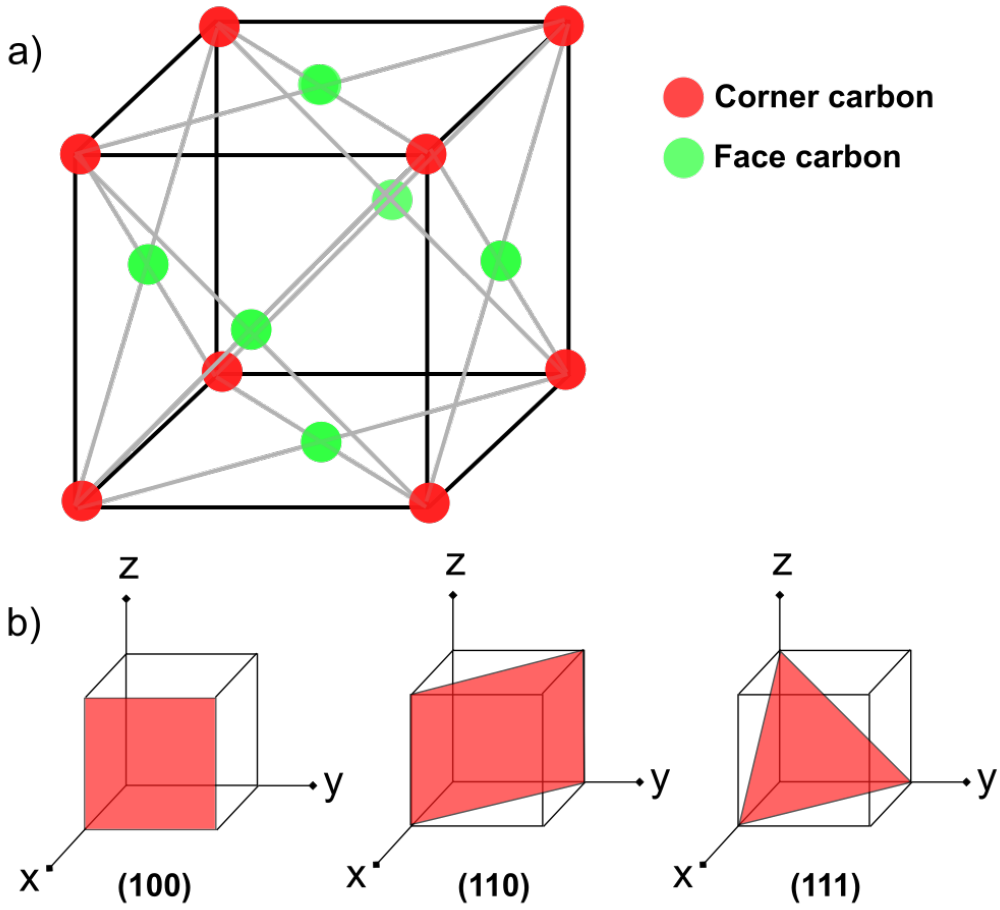

Figure 2.3 (a) Face Centered Cubic (FCC) structure of diamond (b) the (100), (110) and (111) Miller planes.

2.2 THE FORMATION OF DIAMOND

Naturally occuring diamond is formed at very high temperatures (900 – 1400°C) and pressures (4.5 and 6 GPa) [4] between 140 and 200 km below the surface of the earth [5], within the earths mantle. It is believed that most of the abudnant terrestrial diamond was formed between 990 million and 4.2 billion years ago. The quality of naturally occuring diamond is usually obtained visually, and the visual characterestics are determined by defects which are caused by the inclusion of forign atoms including boron, nitrongen and hydrogen, which are described and summaried below [6]:

Type Ia: Nitrogen is the dominant impurity and is present as aggregates or clustered together within the carbon lattice. It has a pale yellow or brown appearance. 98% of diamonds fall into this category.

Type Ib: Nitrogen is present as single substitutional atoms and is uniformly distributed throughout the carbon lattice. These diamonds can appear deep yellow, orange, brown or greenish depending on the concentration and distribution of nitrogen atoms. They account for 0.1 % of diamond.

Type IIa: These diamonds have a miniscule amount of impurities present. They are colourless unless lattice defect are present, which would render them yellow, brown, pink or red. 1-2 % of diamonds are this type.

Type IIb: This type of diamond contains boron as an impurity and appear, blue, grey or near-colourless and make up approximately 0.1 % of diamonds.

The sp^3 carbon bond is stronger than the sp^2 bond (711 kJ/mol compared to 524 kJ/mol) [6]. The sp^2 bond sits 2.88 kJ/mol lower than the sp^3, which makes diamond a metastable allotrope of carbon with respect to graphite, which is thermodynamically the most stable. As a result of this, very high temperatures and pressures are needed to overcome this large kinetic barrier and to form diamond from other carbon phases (Figure 2.4). The transformation of diamond – graphite at atmopheric pressure and temperature is infinitesimally small and so diamond can be classified as stable for all practical purposes. The clevage of sp^3 bonds (711 kJ/mol) require a temperature of over 1600°C at atmospheric pressures.

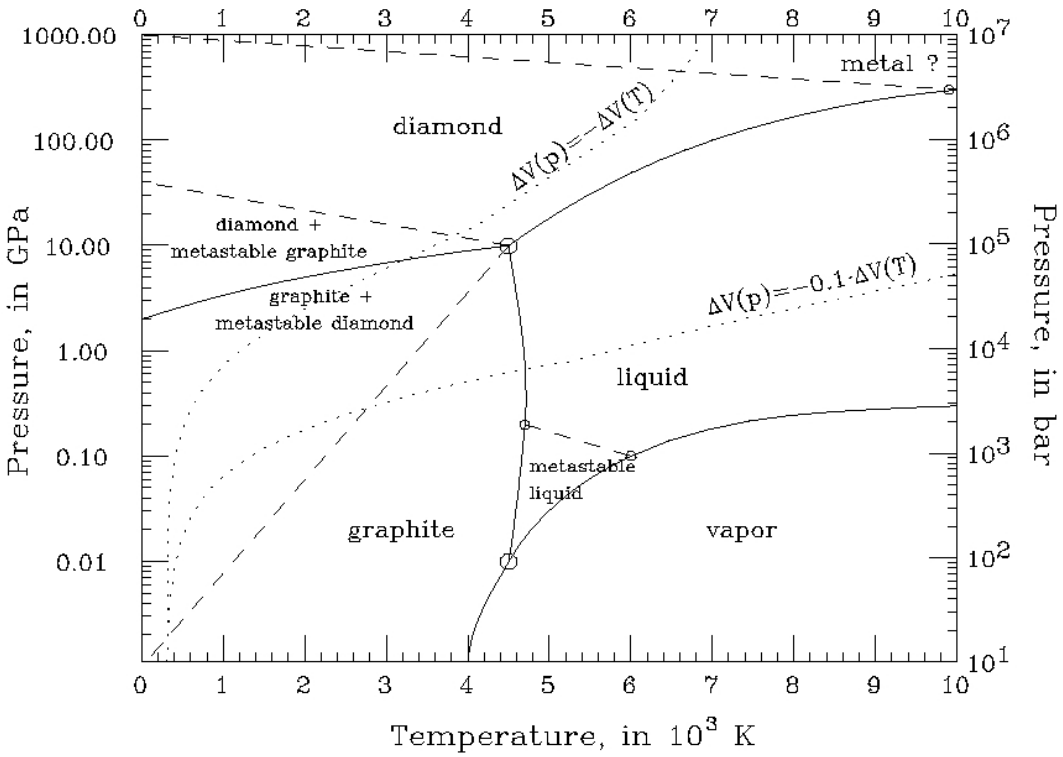

Figure 2.4 Carbon phase diagram, taken from [7].

2.3 DIAMOND GROWTH

Diamond can be synthesised artifically and the earliest reported attempt was recorded in 1879 by James Ballantyne Hannay [8] which, involved heating charcol to above 3500°C. Since the 19th century, many other reports of attempted synthetic diamond growth have been documented, but unquestionable diamond growth was not sucesful until the 1950's. (See 2.3.1 HPHT for more details) This opened up the potential of using diamond for many desirable applications where the limitations of naturally sourced diamond can be overcome. Such limitations include high cost, inhomogeneity and variable impurity cotent. The main classifications of artifical diamond are single crystal diamond (SCD), and polycrystalline diamond (PCD), PCD is formed when small grains of SCD become faceted, this can be further classified into sub catagories which, are detailed in the table below. SCD is where there are no separate domains present within the bulk material, SCD exhibits the greatest of the properties which often make diamond so desirable including it's extreme hardness and imense Young's modulus. Producibility of SCD is difficult, as a homoepitaxial substrate is required in order to grow diamond without the inclusion of grain boundaties, this is usually

in the form of other SCD or single crystal iridium [9]. In general, the smaller the grain size the higher percentage of incoroporated sp^2 carbon and thus a film with properties less like that of SCD.

Degree of crystallinity	Size of grains
Microcrystalline	100 nm – several μm
Nanocyrstalline	5 – 100 nm
Ultrananocrystalline	≤ 5 nm

Table 2.1 Showing the degree of crystallinity asociated with the size of the diamond grain, adapted from [10].

2.3.1 HIGH PRESSURE HIGH TEMPERATURE (HPHT)

HPHT synthesis of diamond is an attempt at mimicing the conditions in which naturally occuring diamond is formed at over 140 km below the surface of the earth. The first sucessful, witnessed and reproducible HPHT diamond synthesis was achieved by F. Bundy and T. Hall of U.S., General Electric (GE) in 1954. Conditions used are reported to be around 100 kbar and 2000°C [11-13]. Another notable early sucessful synthesis was in 1960 by ASEA, a swedish electrical manufacturing company. The first recorded synthetic diamond of naturally occuring gem quality was in 1970 by GE. Development of the catalysed HPHT method was performed by GE and ASEA simultaneously, and still accounts for the majority of synthetic diamond production which is approximetely 75 tonnes per anum [14]. The catalysed HPHT method consists of dissolving carbon in a metal-solvent catalyst, and then transporting it to the growth substrate where it crystallises into diamond when thermodynamic conditions favour the diamond phase. The inclusion of a metal catalyst (e.g. iron, nickel, platinum etc.) reduces

the graphite-diamond transition conditions from 130 kbar and 3000°C to 55 kbar and 1300°C [14]. HPHT diamond contains fewer stacking faults and lattice dislocations than naturally occuring diamond, however a higher concentrations of impurities are obtained, in particular; nitrogen [15]. Therefore HPHT diamond has less potential for electronic and optical application, but is frequently used as cutting and grinding tools and also as the substrate for homoepitaxial SCD growth.

2.3.2 CHEMICAL VAPOUR DEPOSITION (CVD)

CVD diamond is often employed for applications that require high purity diamond, and first reported CVD diamond growth was in 1962 by William Eversole of the Union Carbine Corporation [16]. There are reports which remain unpublished indicating that Eversole had began work on CVD diamond growth before Halls HPHT work was confirmed in 1955 [17]. Eversoles CVD growth of diamond was described using a methy-containing gas precursor, and at less extreme conditions that HPHT synthesis: temperatures between (900 – 1100°C) and lower pressures ranging from (70 – 140 bar) [16]. First CVD attempts produced low quality diamond with a high sp^2 content, and it was work performed by Deryagin and Angus [17] which showed that the encorporation of atomic hydrogen into the gas mix preferentially etched graphitic regions rather than diamond. This allows for higher quality sp^3 diamond carbon to be deposited, as high nucleation rates of diamond on non-diamond is permitted [18]. Growth rates using these paramaters were low, and the process was deemed too slow for any commercial application [14]. Subsequent CVD research by the Russians showed that diamond could be grown on a non-diamond substrate [19,20].

In 1982 researchers from the National Institute for Research in Inorganic Materials (NIRIM), Tsukuba, Japan, developed a CVD diamond growth process which was able to produce high quality films at rates which were great enough to aquire significant commercial interest. The ‘hot filament’ method developed by NIRIM uses relatively low pressures (25 – 40 mbar) and temperatures (700 – 1100°C), and produced high quality diamond on non-diamond substrates at relatively high growth rates (1 μmh^{-1}) [21]. The same group reported using a Microwave Plasma Enhanced CVD (MWPECVD) reactor for producing thin films of diamond the following year [22], and RF glow discharges in 1985 [23].

MWPECVD and RF discharge CVD growth of diamond is facilated by the radicals which are generated using the MW and RF power. It was this continious series of discoveries which stimulated and attracted worldwide interest into CVD diamond as a scientific material, and to this day, extensive research on diamond continues [24]. These two types of CVD reactors were able to produce higher quality diamond films as the filament is eliminated from the growth chamber and thus fewer impurities are incorporated into the bulk of the diamond. Most types of reactor which have been used for CVD diamond growth are summaried in (Table 2.2) below.

CVD method	Rate (µm/h)	Area (cm^2)	Quality (Raman)	Substrate Material	Pros	Cons
Hot-filament	0.3–40	100 – 400	+++	Si, Mo, silica, Al2O3, etc.	Simple, large area	Contamination stability
DC discharge (low P)	<0.1	70	+	Si, Mo, silica, Al2O3, etc.	Simple, area	Quality, rate
DC discharge (medium P)	20–250	<2	+++	Si, Mo, Al2O3,	Rate, quality	Area
DC plasma jet	10–930	2 – 100	+++	Si, Mo, W, Ta, Cu, Ni, Ti, steel	Highest rate, quality	Stability, homogeneity
RF (low P)	<0.1	1–10	-/+	Si, Mo, silica, BN, Ni	Scale-up	Quality, rate, contamination
RF (thermal, 1 bar)	30–500	3–78	+++	Mo	Rate	Stability, homogeneity
Microwave (0.9-2.45 GHz)	1 (low P), 30 (high P)	40	+++	Si, Mo, silica, WC, etc.	Quality, area, stability	Rate
Microwave (ECR 2.45 GHz)	0.1	<40	-/+	Si	Area, low P	Quality, rate, cost, contamination
Flame (combustion)	30–200	1–100	+++	Si, Mo, Al2O3, TiN	Simple, rate	Stability, uniformity

Table 2.2 Taken from [25] comparing various CVD methods for growing diamond. "-" indicates poor quality and "+" excellent quality.

Diamond growth on non–diamond substrates requires a nucelation step in which diamond precursors are seeded onto the surface. This can include carbide interlayers, such as hydrocarbon oils [26] or diamond-like carbon [27]. Diamond particles are most frequently used as the particle and can be nucleated onto the substrate in a number of ways, examples include bias enchanced nucleation which utilises a negative DC bias to the substrate (100–250 V) and results in ions being emplanted onto the surface of the substrate [28]. Another method for nucleation is using an abrasive methods, where diamond particles which are micro– or nano– sized are embeded into the surface of the substrate. Sonication techniques are widely used, where ultrasonic vibrations embed particles into the surface of the substrate [29], and lastly electrostatic seeding which is able to form a monolayer of nanodiamond particles via electrostatic interaction between the colloidal solution and the substrate [30].

2.4 PROPERTIES OF DIAMOND

Diamond as a gemstone is most famous for its brilliant lustre and sparkle, its use as a novel optical and electronic material has only been condiered in the past 25 years or so; since the discoverery of CVD diamond.

The tetrahedral sp^3 carbon bond is responsible for many of diamonds superlative properties. The carbon – carbon directional σ bonds formed are very short and strong which results in a solid that is dense, non-polar, extremely hard (ca. 90 GPa) [31] and chemically inert. The short strong bond also gives rise to diamonds high thermal conductivity: (2200 W m^{-1} K^{-1}) [32], low thermal expansion coefficient at room temperature (1 x 10^{-6} /°C) [31] and the highest phonon energy of any mateiral (E_{opt} = 163 meV) [33]. The high thermal conductivity and low thermal expansion give rise to the high mobilities observed in diamond [34]. Whereas the chemical inertness and un–reactivity of diamond plays a large part in the observed biocompatible nature of diamond as a bio-material.

It posesses a wide optical transparency window, from UV (225 nm) through to the far infrared [35], this combined with the sheer strength and thermal shock resistance make diamond an ideal material for applications within harsh environments. These include synchrotron high power X-ray beam windows [36] and UV windows for missiles [37].

The bonding of four equivalent sp^3 orbitals to four neighbouring sp^3 orbitals creates eight new molecular orbitals, four being bonding and the other four antibonding. The bonding orbitals are all occupied and are lower in energy than the antibonding orbitals, this difference produces a band gap between the states, which, in the case of diamond is wide at ca. 5.5 eV. This wide band gap is responsible for diamonds large breakdown voltage which make it a suitable choice of material for high power devices.

The surface of diamond can be functionalised by various different atomic of molecular groups bonding to the sp^3 dangling bonds [38]. These can range from individual hydrogen atoms to complex arrangements (e.g. hydrocarbon, hydroxyl, amines etc.) and the high strength of some of these bonds gives rise to diamonds wide chemical window (0.75 – 2.35 V), strong polarisability and varying hydrophobicity [39]. This versatility allows for a specific tailoring of molecules present on the surface of diamond, and thus enables diamond to become more biocompatible to both proteins [40,41] and cells [42-44].

The properties of diamond and other semiconductor materials have been sumarised in (Table 2.3) below:

Property		Si	GaAs	SiC (4H)	GaN	Diamond
Band gap (eV)		1.12	1.42	3.26	3.40	5.47
Thermal conductivity ($W\ cm^{-1}\ K^{-1}$)		1.15	0.46	3.6	2	21.9
Carrier mobility ($cm^2\ V^{-1}\ s^{-1}$)	Electron (hall)	1450	8500	981	1245	660 (p–type)
	Electron (t.o.f.)	-	-	-	-	4500 (SCD)
	Hole (hall)	370	400	120	24	1650 (n–type)
	Hole (t.o.f)	-	-	-	-	3800 (SCD)
Dielectric constant		11.9	13.1	9.7	10.4	5.7
Saturation Velocity ($cm\ s^{-1}$)	Electron (calc)	10^7	2×10^7	2.2×10^7	2.5×10^7	1.5×10^7
	Electron	-	1.9×10^7	-	2.5×10^7	2.5×10^7
	Hole	10^7	-	-	-	1.1×10^7
Breakdown field ($MV\ cm^{-1}$)		0.3	0.4	2.7	2.7	10-20

Table 2.3 Adapted from [45] outlining the electrical properties of diamond in comparison to other semiconductor materials. “t.o.f.” indicates time of flight measurements. Note the different mobilities observed for electron and hole mobility from doped diamond and un–doped SCD.

2.5 DOPING DIAMOND

Intrinsic diamond is extremely inulating [46], however conductivity can be induced via the introduction of both p– and n– type dopants, which is desired for numerous electronic applications. Many of diamonds superlative properties stem from the strong sp^3 carbon – carbon bond, however this also means that the incorporation of dopant atoms into the bulk of diamond is very difficult. The metastability of diamond means that vacancies and interstitial atoms do not form upon thermal excitation; and so processes of dopant diffusion that rely upon these defects as carriers are not possible, as opposed to silicon which employs diffusion doping frequently. Viable methods for doping diamond include introducing dopants during growth and injection via ion implantation, however even using these methods the doping of diamond remains limited incorporating larger dopants is difficult due to the short C–C bond length. Substitutional doping in diamond therefore goes hand in hand with large activation energies.

The lowest activaltion energy of any substitutional dopant in diamond is achieved via p–type doping with boron, ($E_a \approx 0.37$ eV) [47]. Very little degradation of the superlative physical properties of intrinsic diamond are observed. Diamond was firstly doped with boron in 1959, it was synthesised by Wentorf [48] using a HPHT method in which boron was added into the metal catalyst, however poor electrical characteristics were obtained due to the large inclusion of impurities. Since then, inlusion of boron in the gas phase using MWPECVD diamond growth has improved mobilities hugely, such reports of mobilities observed for boron doped single crystal diamond are summaried in (Table 2.4) below:

Group (year)	Temperature (K)	Boron concentration (cm^{-3})	Mobilities ($cm^2 V^{-1} s^{-1}$)
Yamanaka *et al.* [49] (1998)	290	2.3×10^{14}	1840
Teraji *et al.* [45] (2006)	290	4×10^{14}	1620
Mortet *et al.* [50] (2008)	290	5×10^{13}	2000
Volpe *et al*. [51] (2009)	292	1×10^{16}	1870

Table 2.4 Mobilities achieved by various research groups using boron as a dopant in single crystal diamond.

Only around 1% of dopant atoms are activated in diamond at room temperature due to the large activation energy (0.37 eV) of the b-acceptor in diamond, increasing the concentration of dopants reduces the activation energy of boron [47]. At boron concentrations ca. 3×10^{20} cm^{-3} the activation energy is ca. 0 eV – few meV, this is due to the metallic impurity band which is formed between adjacent boron acceptors [52]. However, an increase of boron carriers in the diamond lattice reduces the hole mobility, and at 3×10^{20} cm^{-3}, the metallic impurity band is formed [53], and the mobility drops to < 3 cm^2 V^{-1} s^{-1} [47]. This transition of a non-metal to a metal is aslo known as the Mott transition, and has led to much interest in the delta doping of diamond using boron.

Boron precursors include diborane [54], trimethylborane [49], solid boron [47] and boric acid [55]. Boron inclusion can also be done using ion implantation, which has been reviewed extensively by Kalish [56]. Ion implantation enables precise control of dopant concentrations and locations, however the procedure results in crystal damage and thus low mobility values.

A major hinderance of using diamond as an electronic material lies in the search for a feasable n-type dopant, as n-type conductivity has been shown to be much

harder to achieve than p-type [57,58]. Potential substitutional donor dopants are nitrogen and phosphorous from Group V, as the other elements in this group are too large to fit in the diamond lattice. Nitrogen is in the same period as carbon and occurs naturally in diamond, and so it is a obvious candidate as an n-type dopant. However, a high activation energy of 1.7 eV is observed [59], which at room temperature is highly insulating and therefore useless for most electronic applications. Phosphorus has also been used as a donor dopant choice, initial incorporation attempts into the diamond lattice proved difficult as phosphorus has a comparably large atomic radius (0.98 vs. 0.67 Å). MWPECVD growth enabled Koizumi *et al.* to achieve a reduced activation energy of phosphorus to 0.46 eV at room temperature [60]. Theory predicts that activation energies of 0.2 eV [61] and 0.4 eV [62] are obtainable, which ensure phosphorus is the most promising elemental choice for diamond n-type doping. Widespread use of phosphorus as a dopant has not yet been exploited but the table below shows some mobilities achieved.

Group (year)	**Phosphorus concentration**	**Observed activation energy (eV)**	**Mobilities ($cm^2 V^{-1} s^{-1}$)**
Koizumi (1998) [60]	600 ppm	0.46	15
Haenen (2000) [63]	500 ppm	0.46	240
Nesladek (2005) [59]	2.8×10^{16} cm^{-3}	0.56	420

Table 2.5 Mobilities achieved by various research groups using phosphorus as a dopant in single crystal diamond.

2.6 NANODIAMOND

A nanodiamond (ND) is diamond particle with a diameter of less than 100 nm. NDs have been found in ancient sediments which were formed naturally via high pressure high tempereature (HPHT) shockwaves which occur upon meteorites entering the earths atmosphere [64]. The conditions observed at such meterogical formations were first mimicked via controlled detonation explosions in the 1960's by Du Pont de Nemour *et al.* and later by Russians in the 1980's with more success [65]. Particles were termed detonation nanodiamonds (DNDs) and are produced via a detonating carbon containing explosived, most frequenctly TNT–RDX (6:4), in an oxygen deficient environment [66]. The resulting high temperature and pressure create conditions under which a Chapman-Jouguet point is observed. Diamond particles are formed as the shockwave passes through the chamber, the duration of the shockwave is only a few microseconds, but this is long enough for a small amount of sp^3 carbon to form. Initially only 1–2 nm dropets of liquid diamond form, however as the temperature and pressure decreases the droplets coalesce with one another and crystallise. As the temperature and pressure falls below the graphite–diamond phase equlibirum, the formation of graphite is favoured and the NDs become coated in graphite. The soot formed contains ND clusters which are strongly aggregated, and are approximately 5 nm in diameter.

Ultra dispereed NDs are produce by taking the soot produced via the detonation process and subjecting it to a purification procedure. Osawa *et al.* (2005) developed a process to deaggreate the clusters of NDs into a fully dispersed ND colloid [67], the process involves stirr milling using micron sized cermaic beads to de–aggregate the NDs at 4000 rpm. The NDs are then washed using an aggressive acid cleaning treatment (hot HNO_3), which removes graphitic material. It has been since this process development that NDs have become of significant interest within the scientific community. A schematic for de–aggregating NDs is shown in (Figure 2.5 a).

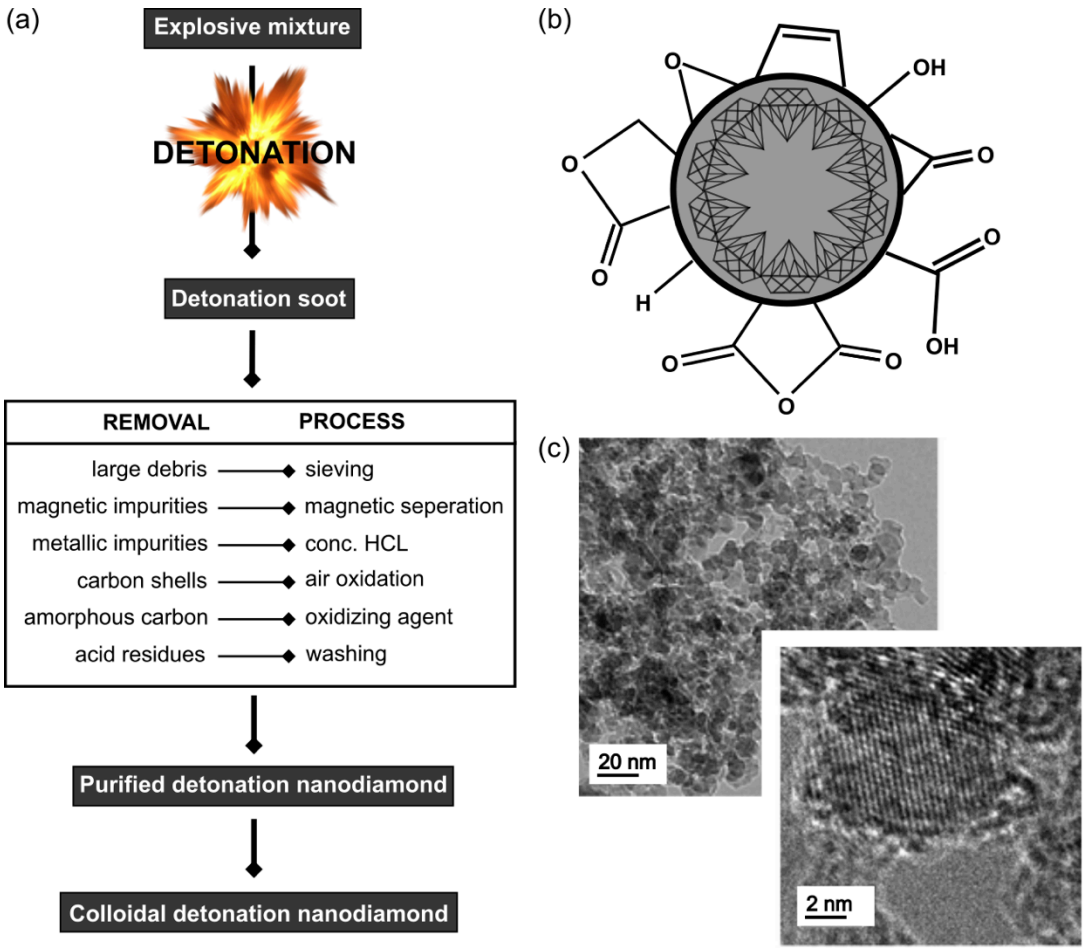

Figure 2.5 (a) A schematic describing the de–aggregation purification process of detonation nanodiamond containing soot. Adapted from [68]. (b) The range of surface groups seen on as received NDs. (c) High-resolution TEM images of DND particles. Note the ordered diamond core, the disordered shell and agglomeration of particles (taken from [69]).

A ND comprises of an sp^3 diamond core which is covered by sp^2 graphitic carbon, they are esentially a diamond covered in graphite [68], the sp^2 delocalised π bonding allows for an extensive variety functional groups to terminate the surface, these include, but and not limited to −COOH (carboxylic), >C=O (carbonyl), −O−C=O (lactone), −C−O−C− (ether) and −OH (hydroxyl) bonds, but are primalry functionalised by −OH (hydroxyl) bonds due to the acid purification step as part of the ND de-aggregation oxidative step [70]. DNDs tend to be nitrogen doped due to the presence of nitrogen which is present in TNT and RDX from within the detonation chamber, NDs are also shown to be highly insulating [71]. NDs have

shown to be highly biocompatible, they have very little if not positive effect on cell adhesion and proliferation [72-74].

Water or ice are usually used as the coolant for the detonation process, therefore the ND surface is able react with avaliable hydroxly radicals. In addition to this, chemicals which are used during the purification process to remove graphitic groups simultaneously oxidise the surface. It is a combination of these two processes which result in a ND surface with a variety of oxygen containing funcitonl groups. Therefore, when refering to 'untreated' NDs, the surface will contain a variety of un–homogeneous oxygen containing functional groups.

2.7 NANOCRYSTALLINE DIAMOND

Single crystal diamond (SCD) growth isn't trivial, there is a shortage in suitable homoepitaxial substrates because of the high demand, and the growth of SCD on heteroepitaxial substrates is still in its infancy. As an alternative to the desired large–scale SCD, nanocrystalline diamond (NCD) is frequently used, which can be grown heteroepitaxially on a very large scale, with the majority of the superlative properties of SCD (Table 2.3) being maintained.

Heteroepitaxal growth of NCD films is achieved by using nucleation sites on the surface, which is ususally in the form of nanodiamonds (NDs) (see section 2.3.2 Chemical Vapour Deposition). A NCD film develops as each ND seed grows until there is a faceted film with continious diamond coverage, once this faceted film is present each facet competes with its neighbours, with the fastest growing facet overtaking and swallowing smaller facets. This results in larger grains at the top of the film compared to the bottom, and the longer the growth the larger the resultant top facets. The surface becomes rougher but at the same time more oriented as the film thickness increases. (Figure 2.6) shows the proposed evolution of NCD film growth, which was first proposed by Van der Drift in 1967.

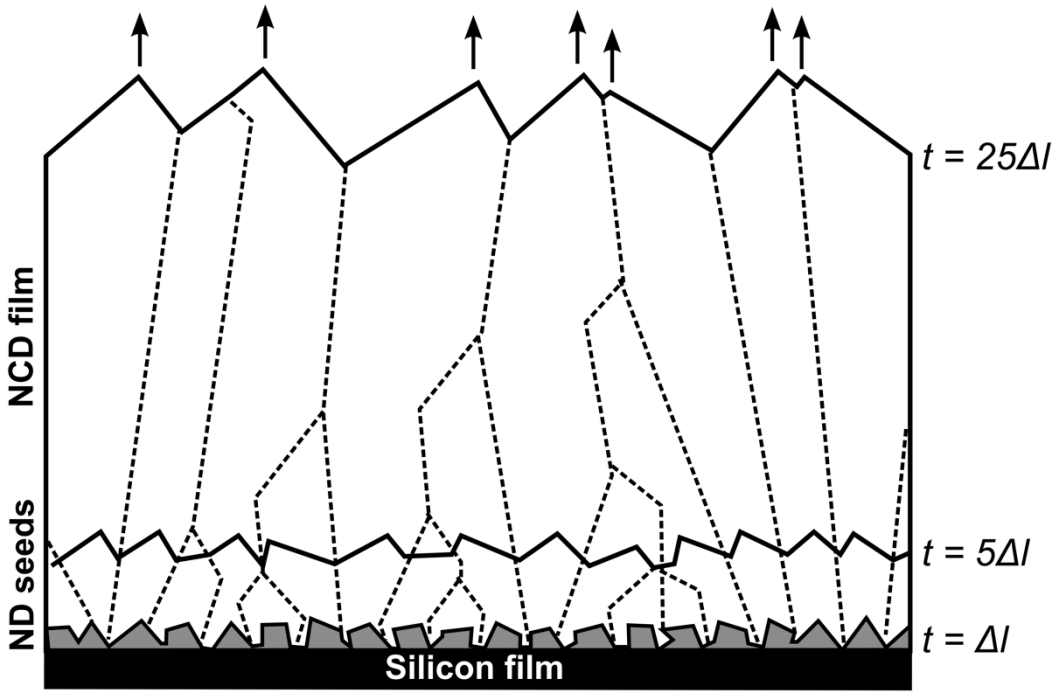

Figure 2.6 A schematic of columnar NCD growth, as predicted by Van Der Drift. The model starts from randomnly oriented nanodiamonds in a two–dimensional space, and adopts the asumption of infinate surface diffusion. The dashed lines show the intercrystal bouncaries, and the size of the crystals are shown at different times, t. Δl is the distance between neighbouring nuclei. Figure adapted from [75].

The difference between the conditions required to grow NCD as oposed to polycrystalline diamond (PCD) lies mainly with the methane concentration, a higher perentage is used for NCD growth, as the additional methane provokes continual re–nucleation during the growth [76]. The smaller grain sizes of NCD (less than 100 nm) allows for thinner, less rough films to be grown, which provides a suitable material for integration into diamond coatings for some micromachining processes. The disadvantege in the increase in grain boundaries is the resultant higher sp^2 content in the diamond film which is larger than 0.1% [77]. This increase in sp^2 carbon increases the scattering of carriers and thus decreases the mobility of the carriers within the film. An extensive review of NCD growth can be seen in [76], a comparison of SCD and NCD films can be seen below (Table 2.6).

Property	SCD	NCD (grown in high methane)	NCD (highest quality)
Growth chemistry	H_2/CH_4	H_2/CH_4	H_2/CH_4
Young's modulus (GPa)	1100	500 – 900	1120
Hardness (GPa)	100	80	–
Macroscopic friction coefficient	0.01 – 0.02	0.02–0.05	0.02–0.05
Surface roughness, R_a, (nm)	Depends on preparation	50–100	5–30 (depends on film thickness)
Grain size (nm)	1 – 10,000	50–100	5–100 (depends on film thickness)
Bonding character	sp^3	Up to 50% sp^2	<0.1 % sp^2

Table 2.6 A comparison of NCD and SCD films adapted from [77].

Despite the reduction in electrical quality, the ease of growth of NCD has transformed diamond from a difficult, expensive material to process into one which is versatile, cheap and easy to fabricate. Despite this degradation in some of the electrical properties, including carrier mobility reductions, crystalline diamond such as NCD has been suitable for biological applications due to the ease in fabrication, versatile conductivty and inert chemisty. All of these properties yield a desired material for neural implant appications due to the biocompatability and function.

2.8 MEDICAL APPLICATIONS OF DIAMOND

2.8.1 NCD FOR MEDICAL DEVICES

NCD coatings have been used to extend implant lifteime for a variety of medical devices including joint prostheses [78], microelectromechanical systems (MEMS) [79] and heart valves [80]. Papo *et al.* tested the wear of an NCD coated temporomandibular joint prothesis in a mandibular simulator which corresponded to two years of use. Raman spectroscopy was used to asses the wear, no film loss and minimal film damage was observed [81]. Film damage was reduced when the coating consisted of a NCD–MCD–NCD stack, instead of just NCD. Diamond is being investigated for its use as a material to fabricate microscale devices for drug delivery and bio–sensing, such devices are know as bio–MEMS. Conventional MEMS devices are fabricated using silicon, however, silicon posseses many physical properties which make it an unsuitable material for *in vivo* applications. These include poor brittle fracture strenght, high tribological and poor mechanical properties. NCD has shown to be more suitable for bio–MEMS applications; tribological studies of NCD have shown a very low frictonal coefficient [82] and a brittle fracture strength 23 times greater than silicon [83]. Lab–on–a–chip devices fabricated using hydrogen–terminated NCD have been developed [84]. It was shown that NCD exhibited the least non–specific binding of DNA compared to silicon, SU8, SiO_2, PDMS and glass. These results demonstate the high sensitivity capacity of such NCD devices.

Diamond is currently being considered for its use as a semi–conducting material in neural prostheses. Hydrogen–terminated SCD has been used to fabricate arrays of solution–gate field–effect transistors, which demonstrated sucessful adhesion and recording of cardiomyocyte cells action potentials [85]. Early investigation into the use of diamond as a coating for implantable microelectrode devices reported that NCD coated retinal implants resulted in minimal flamitory response [86]. More recently, implanted microelectrode devices fabricated using UNCD films have shown long stablility and sucessful biocompatability during *in vivo* retinal prothesis clinical trial [87].

2.8.2 FUNCTIONALISING NANODIAMONDS AND NCD WITH BIOMOLECULES

The dangling sp^2 bonds surrounding NDs and sp^2 carbon in the grain boundaried of NCD have facilitated the covalent bonding a variety of functional groups, including biological molecules, to the surface. NCD has shown to covalently bond to oligonucleotide groups present in DNA [88], the observed bonding was stable. Proteins including catalase and green fluorescent protein have been covalently bound to NCD [89]. Initially, a photochemical process was used to to immobilize amine groups onto hydroen–terminated NCD, then proteins were attached to the surface via peptide bond formation. Such NCD modified electrodes were used for the sensing of hydrogen peroxide. Many other biomolecules including enzymes [90], biotin [91], thionine [92] and various proteins [93,94] have been successfully functionalised onto the ND surface. The simple chemistry required for altering bio–functionalisation, supports the use of NDs for drug delivery.

2.8.3 NANODIAMOND FOR DRUG DELIVERY

The diverse functionalisation NDs can posess has shown to be useful in drug deliverly applications; chemotherapeutic drugs have been successfully immobilized onto the ND surface. NDs have been functionalised with doxorubicin hydrochloride (DOX); DOX induces apoptosis, which is the programmed cell death [95]. Utilising simple organic reagents, DOX was released from the NDs surface and sucessfully induced apoptosis in colon cancer cells. The de–conjugated NDs demonstrated biocompatability and minimal inflammation was observed. NDs were also conjugated with paclitaxel: a drug used to induce apoptosis and inhibit mitosis for the treatment of lung, breast, ovarian and other cancers [96]. ND–paclitaxel particles inhibited tumour growth of lung cancer in mice. ND particles without conjugation did not promote apoptosis. Such research has demonstrated that ND based chemotherapeutic drugs are a promising candidate for the treatment of cancer [97].

2.8.4 NANODIAMOND FOR MEDICAL IMAGING

Fluorescent propterites of nanodiamonds are a consequence of nitrogen–vacency (NV) defects [98], these defects exhibit absorbance at 560 nm and fluorescence at 700 nm [99]. NV NDs have are ueful for medical imaging applications, and they have been used sucessfully for imaging within cells and tissue. NV NDs have been succesfully engulfed, localised and imaged in human kidney cells [100], the NDs were reported to exhibit no photobleaching and also had no cytotoxical effect on the cells. Numerous other studies have shown successful fluorescence imaging of NV NDs which have been englufed by cells, minimal bleaching and low levels of toxicity have been encountered [101-103].

.

2.9 CONCLUSION

In summary, the extreme physical and chemical properties of SCD have been demonstrated. Despite this, the growth of large, defect free SCD wafers has proven difficult due to the lack of homoepitaxial substrates; this has led to the slow uptake of diamond in many engineering applications. Instead, the development of heteroepitaxial growth has enabled large NCD and PCD wafers to be manufactured. The superlative chemical, mechanical and physical properties of SCD are retained in NCD; however, electrical property conservation is poor due to the inclusion of grain boundaries. Therefore, the replacement of SCD with NCD is unlikely to occur for many electrical applications, and large area, defect free growth of SCD is paramount for advances in this field to occur. For many biological applications, the superlative electrical properties of SCD are not of utmost importance. The ease of deposition, extreme physical property retention, inertness and biocompatibility of NCD has promoted its use in many biological applications. Furthermore, the dangling sp^2 bonds on the surface of NDs are able to be functionalised by a diverse array of molecules. The functionalisation of NDs and bio–molecules has shown to be beneficial for many medical applications including cellular imaging and drug delivery.

CHAPTER 3 – NEURAL STEM CELLS

3.1 INTRODUCTION

Neural Stem Cells (NSCs) are able to self renew and differentiation into the main cells in the Central Nervous System (CNS). This chapter contains background information about the function stem cells, NSC function, anatomical location and stem cell therapy.

3.2 STEM CELLS

Organs are composed of cells with specialised functions. Most of the cells are terminally differentiated, and cell function terminates if it undergoes apoptosis: programmed cellular death [104], or if the cell enters senescence which results from biological aging [105]. To maintain function of each particular organ, the lost cells are replaced via a homeostatic system. Homeostatis is the process in which the internal environment of organs is maintained [106]. The homeostatic mechanism involves numerous cell stages with decreasing reproductive capability and thus an increased commitment into their differentation. This mechanism is governed by stem cells, which have the ability to reproduce in prolonging the life of and maintaining the function of organs [107].

Several key and distingusished features define stem cells, these are: i) stem cells are found in all multicellular organisms, ii) there is a much lower population of stem cells, compared to their neighbouring specific tissue cells, iii) stem cells are undifferentiated and are structurally unspecialized, iv) they can self-renew indefinetly, v) stem cells are mostly multipotent, having the capacity to differentiate into multiple yet limited cell types, vi) stem cells have the capability to differentiate and proliferate much after the lifetime of the organ has been exceded, vii) the microenvironment surrounding stem cells critically governs the fate of the cell [108].

Self-replication and offspring production are key parts of stem cell funciton during homeostatis and at times of injury. Stem cell behaviour is both intrinsic and extrinsic, intrinsic regulations originate from the progamming of the cell, and extrinsic behaviour is likely to be generated from external stimuli. Stem cells can

replicate symmetrically; creating two identical cells, and asymmetrically where one stem cell forms and the other which is committed to a differentation pathway [109].

Potency is a term used to describe the gene-activation potential of a cell, stem cells have high potency, as nearly all the genes from within the cell have the potential to be expressed, this is compared to a differentiated cell, which has low potency. During embryonic development, the chromosomes condense and allign for the first round of mitosis. These chromosomes then segregate to opposite poles of the embryo, which forms the nuclei of two new cells. The cells formed are identical, and both still have total potency, and have the capacity to produce all other cell lineages, these are called 'totipotent stem cells' [110]. The zygote and subsequent blastomeres are the only totipotent cell present in mammals. Stem cell potency begins to change once the blastocyst forms; cells have begun to partially differentiate, and are now labeled as 'pluripotent stem cells'. Embryonic stem cells are pluripotent, as they have the potential to differentiate into all cells present in an adult body, and they exist within the blastocyst [111]. Multipotent stem cells have the ability to differentiate into multiple yet limited types of cell, and 'unipotent' cells, unlike stem cells, can only divide to produce more identical cells. Neural stem cells are multipotent as the differentated resultant cell is limited to three posibilities; neurons, astrocytes and oligodendrocytes [112].

3.2.1 STEM CELL DIFFERENTIATION

Stem cell differentiation is the process in which a stem cell forms a more specialised cell, the differentiation leads to a loss of the developmental potential of the cell and is fundamental for development during growth [113]. It occurs during the production of specialised cell, as well as in adults in order to replenish lost cells. Differentiation of each cell occurs many times during the formation of complex of multicellular organisms, as simple zygotes transform into specialised cells.

Differentiation of stem cells continues into adulthood, as cells need to be regenerated after tissue damage and to maintain the cell populations despite normal cell turnover. The differentiation process induces changes in the cells including: shape, size, metabolic activity and responsiveness. Antigen exposure can induce the differentiation of some stem cells [114], the changes in cell type

are mainly due to precise modification in the gene expression of the cell. Post cellular differentiation, the DNA sequence is often unchanged, and therefore different cell types, which have extremely different physical traits, regularly have the same genome.

3.3 Neural Stem Cells

Unlike embryonic stem cells which, originiate in the blastocysts, NSCs are derived from the CNS [115]. Neural stem cells are defined by their ability to differentiate into neurons, astrocytes, oligodendrocytes and microglia [116]. NSCs satisfy the two main criteria for a cell to be classified as a stem cell: they are able to self-renew, and they have multi-lineage differentation pathways.

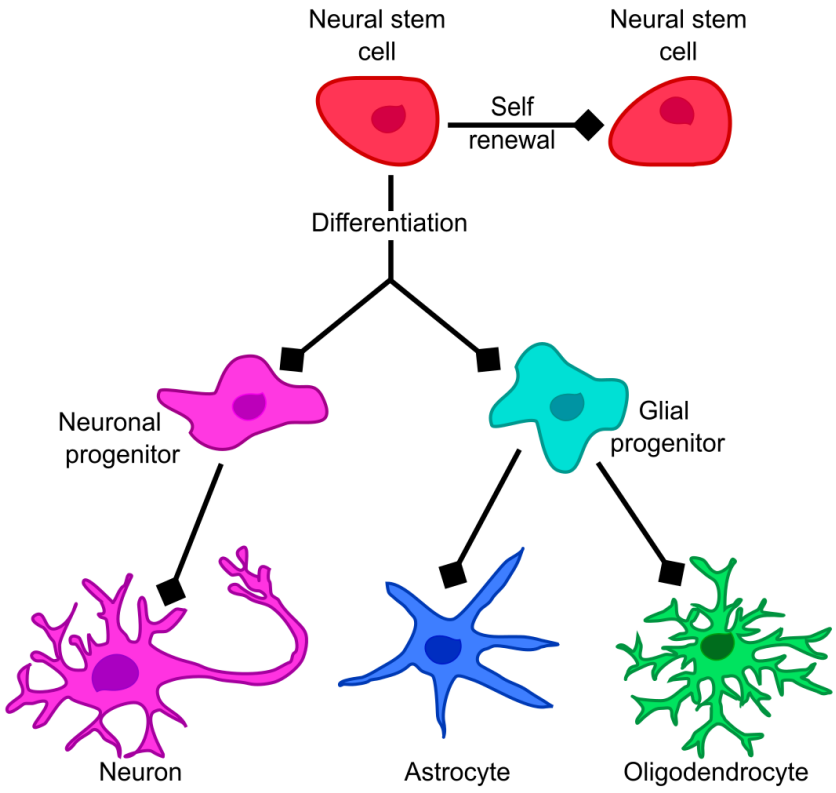

Figure 3.1 The differentation pathway of NSCs highlighting division into a self-renewed NSC and the assymetric differentation into the neuronal progenitor, whose fate is determined and is always a neuron, and the differentiation into the glial progenitor cell, which can both differentiation again into an astrocyte and oligodendrocyte.

NSCs exist at many developmental stages, and NSCs have been isolated from numerous regions in the brain, including the subventricular zone (SVZ), cerebellum, olfactory bulb, hippocampus, cerebral cortex and the spinal chord [117]. Most neural stem cells express Nestin (neuroepithelial stem cell protein), a class VI intermediate filament protein. Upon NSC differentiation, Nestin present is downregulated and is replaced by other intermediate filament proteins, including neurofilaments in neuronal cells, and glial fibrillary acidic protein (GFAP) in astrocytes [118]. NSCs can be investigated in vitro, mediums rich in mitogens such as epidermal growth factor (EGF) and fibroblast growth factor (FGF). The removal of such mitogens leads to the induced differentation of NCSs into neurons, astrocytes and oligodendrocytes [119]. By adding different growth factors, such as ciliary neurotrophic factor (CNTF), platelet-derived factor (PDGF) and thyroid hormone T3, the fate of the NSC can be altered.

3.3.1 ANATOMICAL LOCATION OF NEURAL STEM CELLS IN THE ADULT BRAIN

NSCs have been isolated from five separate locations within the adult brain (Figure 3.2). These are principally surrounding the lateral ventricles [120]. The primary locality of NSCs is in the subventricular zone (SVZ), specifically in the subependymal zone (SEZ). The SEZ is a 3-4 cell deep layer just below the ependyma, located in the lateral venricles, and can be thought of as the adult version of the embryonic forbrain germinal zone [121]. The SEZ has been compared to a beating heart as it is responsible for sending new specalised cells to different areas in the brain, for example glial cells are sent to the cortex and the corpus callosum, and neurons to the olfactory bulbs [122]. Other germinal centres include the subgranular zone (SGZ) which is within the dentate gyrus in the hippocampus [123], the subcallosal zone (SCZ) which is located between the hippocampus and the corpus callosum [124], an area between the white matter of celebellum and the internal granular layer (IGL) and also along the rostral migratory system (RMS) [125]. NSCs have also been successfully been isolated from the postnatal cerebellum [126].

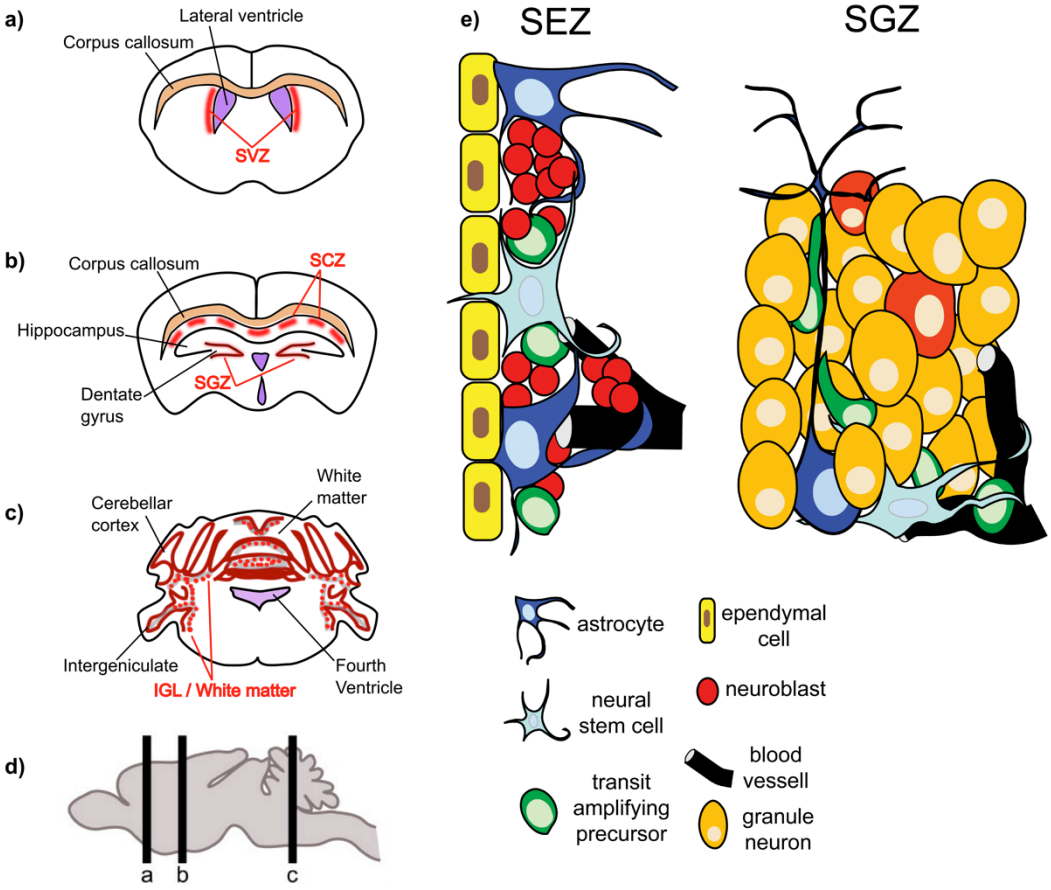

Figure 3.2 (a-d) Anatomical location of neural stem cells (NSC) in the adult mouse brain taken from [127]. Red lines or dots indicate areas containing NSC. (a–c) Coronal slices, (d) sagittal drawing with indication where the coronal slices are located. (a) Subventricular zone (SVZ) in the lateral wall of the lateral ventricles. (b) Subcallosal zone (SCZ) at the border between the corpus callosum and the hippocampus. Subgranular zone (SGZ) within the dentate gyrus. (c) Cerebellum at the border between the internal granular layer (IGL) and the white matter. (e) The adult neural stem cell microenvironment in the subependymal zone (SEZ) and the subgranular zone (SGZ) taken from [128].

3.4 NEURONS AND NEUROGLIA

3.4.1 NEURONS

Neurons are the main cell type in the CNS, they are specialised cells, which are able to process and transmit electrical and chemical signals in order to facilitate brain–body communication. The signalling between neighbouring neurons occurs via synapses, which enable the transfer of electrical and chemical information. The brain is made up of approximately 86 billion neurons [129] and is it responsible for many bodily functions including memory, movement and emotion, to name a few. It is a highly complex system and there are three main types of primary neuron: sensory, motor and interneurons [130]. Sensory neurons are activated by external stimuli including light, sound and touch, and they respond via conveying sensory information to the rest of the CNS [131]. Motor neurons receive signals from the CNS and are responsible for the indirect control of effector organs, principally enabling muscle contraction and glandular outputting. Interneurons are responsible for the creating of neural circuits; they enable the communication between sensory and motor neurons in the CNS [132]. Interneurons interact together allowing complex functions to be performed including decision making and learning. A complex interconnection of these three types of neurons is called a neural network, where elaborate electrical and chemical signals are transmitted and received.

Neurons typically consist of a soma (cell body), multiple dendrites and an axon. A neurite is any projection that extends from the soma; both dendrites and axons [133]. It is a term, which is commonly used during the development of neurons, as it can be difficult to differentiate between dendrites and axons in immature neurons. Dendrites can be distinguished from axons in adult neurons by several features including length, shape and function. Each neuron has multiple dendritic protrusions, which typically extend for hundreds of micrometers whereas there is only one axon per neuron and these are able to extend to lengths over one meter. Dendrites tend to be much more branched than axons, and characteristically axons transmit electrical and chemical signals and dendrites receive them. The simplified structure of a typical neuron is shown in (Figure 3.3).

3.4.2 ASTROCYTES

Astrocytes are star shaped glial cells found in the CNS. They perform many functions including providing the link between neurons and the vasculature via transportation nutrients such as glucose from the bloodstream to the nervous tissue [134,135] glucose is the main energy form used by neurons. They also provide biochemical support to the endothelial cells, which form the blood–brain barrier. Astrocytes maintain and regulate the concentration of extracellular ions in the CNS, this regulation is crucial in ensuring action potentials are able to propagate [136]. Following traumatic injury to the brain, astrocytes produce and release neurotrophic factors which are accountable for scar formation to occur [137]. In addition astrocytes also participate in the immune response of the CNS helping to maintain functioning neural networks.

3.4.3 OLIGODENDROCYTES

Oligodendrocytes are another type of glial cell found within the CNS, they are the last neural cell to be generated [138]. The main function of oligodendrocytes is to provide support to axons whilst simultaneously insulating the processes; they do this by forming a myelin sheath around neuronal extensions in the CNS. The myelin sheath is a predominantly fatty substance (80% lipid, 20% protein), which is electrochemically insulating and is essential in maintaining the function of the CNS. Each oligodendrocyte is able to extend it processes to over 50 axons, and each protected axon requires approximately 1 μm of myelin sheath. Oligodendrocytes also provide nutritional support for neurons, via secreting many neurotrophins including brain derived neurotrophic factor (BNDF), nerve growth factor (NGF) and neurotrophin–3 (NT–3) [139]**.** Neurotrophins are proteins that ensure the development, survival and functions of neurons is retained. They are growth factors that are capable of facilitating the survival, differentiation and development of neurons.

3.4.4 MICROGLIA

Microglia are the CNS equivalent of macrophages: they provide an immune defence against disease and injury. Microglia constitute approximately 10–20 % of glial cells in the CNS [140]. They derive from macrophages, which enter the CNS during development. Microglia are small cells that have numerous branched processes, and they constantly forage for plaques, infections and damaged neurons in the CNS [141].The blood–brain barrier protects the CNS from most infections but it also prevents antibodies from entering. Thus upon pathogenic invasion microglia must work to decrease inflammation and attempt to combat disease by destroying infectious agents [142]. Due to the time sensitivity of infectious diseases, microglia must respond quickly and so are extremely sensitive to changes in the CNS [143]. Following injury, microglia migrate to the affected site [144], where they repair damaged cells.

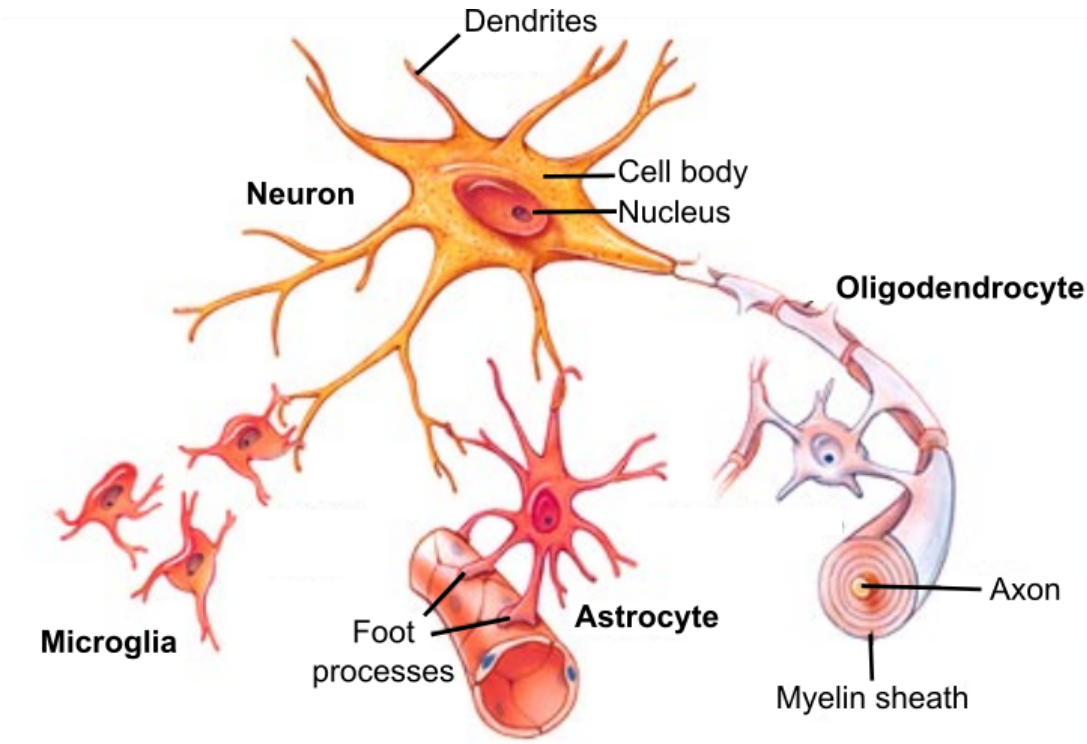

Figure 3.3 Neurons, astrocytes, oligodendrocytes and microglia, displaying how these cells interact within the CNS.

Adapted from (http://www.easynotecards.com).

3.5 STEM CELL THERAPY

Stem cell therapy is a method of treating and preventing diseases via the transplantation of stem cells. The most common type of stem cell therapy is bone marrow transplantation in which multipotent hematopoietic stem cells (HSCs) are transplanted. The HSCs are often derived from bone marrow, umbilical cord or peripheral blood. The transplantation may be autologous or allogeneic [145] (from the patient or donor respectively). HSC transplantation is performed on patients with certain blood and bone barrow cancer; examples include leukaemia and multiple myeloma. Allogeneic transplantation can result in major complications such as graft–versus–host disease, where the donors cells are rejected by the patient [146]. HSC transplantation is also now used to treat certain autoimmune diseases [147]. The first bone marrow transplant was performed in 1958 by the French oncologist Georges Mathé. He treated five Yugoslavians who were nuclear workers, and had marrow damage that was caused by irradiation. Unfortunately, all five of the transplants were rejected, however, Mathé went on to pioneer the use of HSC transplant for the treatment of leukaemia. The first successful HSC transplant was done in 1975; a 16–year–old boy was cured of lymphoma for the first time. Research into transplanting HSCs continued by E. Donnall Thomas, led to the 1990 Nobel Prize in Physiology or Medicine for development of bone marrow transplantation for treating leukaemia.

Current research aims to develop methods of sourcing and transplanting specific stem cells, in order to treat many different neurodegenerative diseases and various conditions including heart disease and diabetes.

3.5.1 NEURAL STEM CELL THERAPY

Neurodegenerative diseases, such as Parkinson's, Huntington's and Alzheimer's disease can be severely debilitating and often incurable. They are a result of the progressive degeneration of cells in the CNS and there is a pressing need for treatments. Neural stem cell therapy provides a hopeful platform for treatment of such neurodegenerative diseases. Most organs in the body are able to repair damaged tissue in a two stepped process. The first is to replace dead cells with newly generated cells and the secondly, these cells must differentiate and organise themselves to restore original structure and function [148]. Therefore, repair is more efficient for tissues that have a high cell turnover and lack of need

for precise patterning. For example, bone fractures and skin wounds heal quickly because cell turnover is high and precision of cell location isn't required. In contrast, the CNS regenerates small populations of endogenous cells and spatial patterning is paramount in order to rewire long–distance connectivity of the brain.

There is evidence that NSCs continue to proliferate and differentiate in the healthy adult brain and that further proliferation and differentiation can be triggered by injury [149,150]. Function of the brain is rarely completely restored after injury due to the limited regeneration capacity and small volume of endogenous neural cells [151]. The potential of neural stem cell replacement therapy after damage to the brain has been researched, with evidence showing that grafts can restore function and integrate into the brain [152,153].

3.6 BIOMATERIALS FOR NEURAL INTERFACES

The ideal neural interface should have a long lifetime and be seamlessly integrated into the CNS. Neuronal cells are very environmentally demanding; their ability to electrically communicate and fire action potentials results in a cell type, which has minimal resilience to exterior stress. The blood brain barrier (BBB) is in place to protect the sensitive neuronal cells, all organisms with a developed CNS poses a BBB [154]. Unlike cells in the rest of our bodies, the BBB prevents the immune response performed by blood, instead; a hypersensitive glial immune system is in place. The glial cells aggressively attack foreign bodies and also play a big role in recovering the brain to normal function after injury [155]. Implanted materials in the brain often result in an immune response because of the aggressive nature of glial cells, in a process called gliosis [156]. Gliosis involves the proliferation of astrocytes, oligodendrocytes and microglia: the main glial cells in the CNS. An extreme form of gliosis is observed after major proliferation and leads to glial scaring. Gliosis can occur on implants, as glial tissue surrounds, isolates and insulates the devices. Unlike neurons, glial cells specifically oligodendrocytes produce myelin, which is highly insulating [157]. The scaring therefore produces an electrically insulating sheath around the implanted device, and the lack of neurites in direct contact with the electrodes renders many implants useless. It is gliosis, which leads to the majority of neural prosthetic failures [158]. Therefore, biomaterials for use at the neural interface must promote minimal oligodendrocyte differentiation in order to prolong the lifetime

and performance of implants. The interaction of neural cells at the surface of such biomaterials is paramount in achieving ideal interfacing, and so it is vastly important that physical and chemical conditions produce materials with maximum biocompatibility. Materials such as silicon [159], ceramics [160], polymers [161,162] metals [163,164] and diamond [165-167] have been used as neural interfaces.

Recent nanotechnological advances have increased potential application in using nanomaterials as neural interfaces. Many nano–materials have been investigated for their role as a neuronal interfacing biomaterials which were originally developed for other applications [168]. Nanostructuring has been used as a tool in boosting the performance of neural stimulating and recording electrodes [169-171]. Not only does nanostructuring increase electrode performance, it has also been shown to preferentially support neuronal growth and attachment without favouring glial cell formation [172-174]. Moreover, nanostructuring of materials has shown to be beneficial for neural interfacing [175].

3.7 CONCLUSION

NSCs are able to self–renew and differentiate into neurons, oligodendrocytes, astrocytes and microglia; the main cells in the CNS. Their anatomical location, differentiation and subsequent specialised cell structure and function have been described, highlighting the importance of the neuron. Neurons transmit and receive electrical and chemical signals and in order to facilitate brain–body communication, they are responsible for many bodily functions including movement, memory and emotion. The potential of using NSCs for stem cell–based therapy and the investigation into suitable biomaterials for neurological prosthesis have been discussed.

CHAPTER 4 – EXPERIMENTAL METHODS

4.1 INTRODUCTION

This chapter provides an overview of experimental methods used throughout this thesis. Background information is presented for techniques where an increased understanding of methodology provides greater insight into results observed.

4.2 SUBSTRATE DEGREASING

All substrates have been degreased prior to use throughout this thesis. The degrease is necessary for producing clean samples as residual dust and dirt are removed from the surface, leaving a contaminant free substrate. Degreased samples provide a platform for better quality processing. An ultrasonic bath is used throughtout the process and samples are dried using an N_2 gun. The order of solvents used for the degrease are shown below:

Solvent	Time	Solvent dissolves
Acetone	5 mins	residule dirt
Isoproponal alcohol (IPA)	5 mins	residule acetone
DI water	5 mins	residule IPA

Table 4.1 The solvents used for substrate degreasing (in order of use).

4.3 MICROPLOTTER

A SonoPlot® GIX Microplotter II is a high precision fluid dispensing method with resolution 5 µm and minimum volume deposition 0.6 pL. The Microplotter uses ultrasonics in order to deposit picolitre volumes of fluid, in a desired pattern, in order to realise high–resolution liquid printing. It consists of a 4x6 mm Lead Zirconate Titonate (PZT) piezoelectric attached to a glass micropipette dispenser; a voltage is applied to the piezoelectric, which in turn induces ultrasonic vibrations, and this is attached to a precise robotic positioning system. The micropipette is filled with a desired 'ink' via capillary action, and the loaded pipette is calibrated. To print the desired ink, an electrical signal, of corresponding frequency and voltage is applied to the piezoelectric, which causes the ink at the tip of the micropipette to be drawn out onto the desired substrate in a desired pattern, which has been drawn on Sonodraw 1.1.3. The deposition of fluid occurs when the frequency of the ultrasonics is in the range of 400 – 700 kHz and it is possible to produce continuous arcs, lines and dots. A photograph of the GIX Microplotter and a diagram of the piezoelectric micropippette set–up is shown below in (Figure 4.1 a + b).

Figure 4.1 (a) A photograph of the GIX Microplotter and (b) the set–up of the micropipette dispensing system, showing nanodiamond ink deposition via ultrasonics.

4.4 Brown-Flaming Micropipette Puller

The brown-flaming micropipette puller consists of a heating filament and pulley system in order to create precise micropipettes. The pulling system is able to transform a glass tube into two micropipettes, both of which are virtually identical. The glass capillary tubes are alligned in V grooves and are secured into place using rubber coated screw clamps. The glass tubes are clamped with the central position being within a rectangular heating filament. A steady and consistent pulling motion allows the pulling movement to be continual and thus micropipette formation is controlled and there is an airjet which provides cooling for the pulled micropipettes. The micropipettes used are very similar to pipettes used for cell physiology patch clamp recordings [176]. Throughtout this thesis Borosilicate glass has been used, spec: outer diameter (OD) 1.5mm, inner diameter (ID) 0.86mm, fire polished. There are 4 variables for each pull; heat, pull, time and velocity.

Figure 4.2 Photograph of a flaming brown micropipette puller, (taken from [177]).

4.4.1 HEAT

The heat setting controlls the current that is supplied to the box filament. The heat needed to melt each glass tube is a function of the glass size, material and the filament. The heat affects the tip size and tip length of the micropipette, and in general a higher heat produces a pipette which is longer and thinner. Throughout this thesis, a constant heat of 500 has been used to pull micropipettes.

4.4.2 PULL

A constant gravatational pull is applied to the glass tubes and most pipettes are pulled without the aditional 'hard pull'. The higher the pull, the thinner the micropipettes, a hard pull is generally only used if sub micron diameter pippetes are required. Throughout this thesis 0 pull was applied througout the pulling of micropipettes.

4.4.3 TIME

The time setting adjusts the length of time in which the cooling airjet is applied to the pulled pipettes. Each unit of time represents 1/2 ms, and througout this thesis a cooling time of 250 units was used, relating to 125 ms.

4.4.4 VELOCITY

The value of velocity determines at which point the heat of the filament is turned off. The velocity is a reflection of the speed in which the carrier bars (clamping the glass tube at either end) are moving. The higher the velocity the faster the speed of the bars when the trip point occurs. Having the velocity higher than the trip point value will produce tips with the same dimensions, the variability is only below this value. The velocity of the system is measure at the point where the glass softens and begins to pull under the constant load. The viscosity of the glass is a function of the glass temperature and pull velocity. The variability of the velocity allows the glass temperature at the trip point to be controlled. Throughout this thesis, velocitys between 20 and 8 have been used to pull tips with an ID ranging between 1 µm and 30 µm respectively.

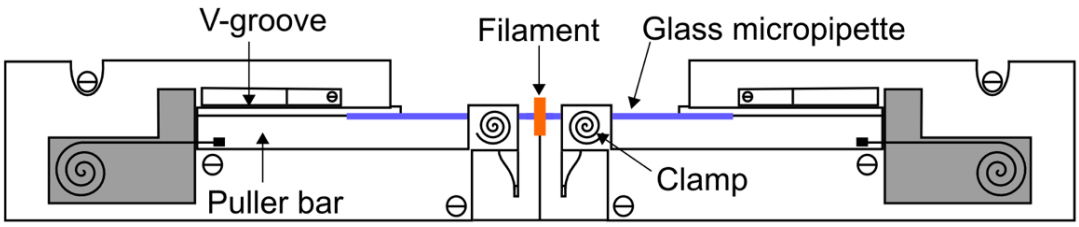

Figure 4.3 Simplified labelled diagram of the Flaming-Brown horizontal micropipette puller (adapted from [177]).

4.5 Solution Sonication

All nanodiamond (ND) solutions have been treated with ultrahigh sonication prior to use. The high powered sonics are able to overcome strong Van der Waals (VdW) forces, and break up aggregates of NDs producing solutions with monodispered NDs present. Various ND containing inks have been used throughout this thesis, and all have been mixed thoroughly using a Sonics vibra-cell for four hours mininmum.

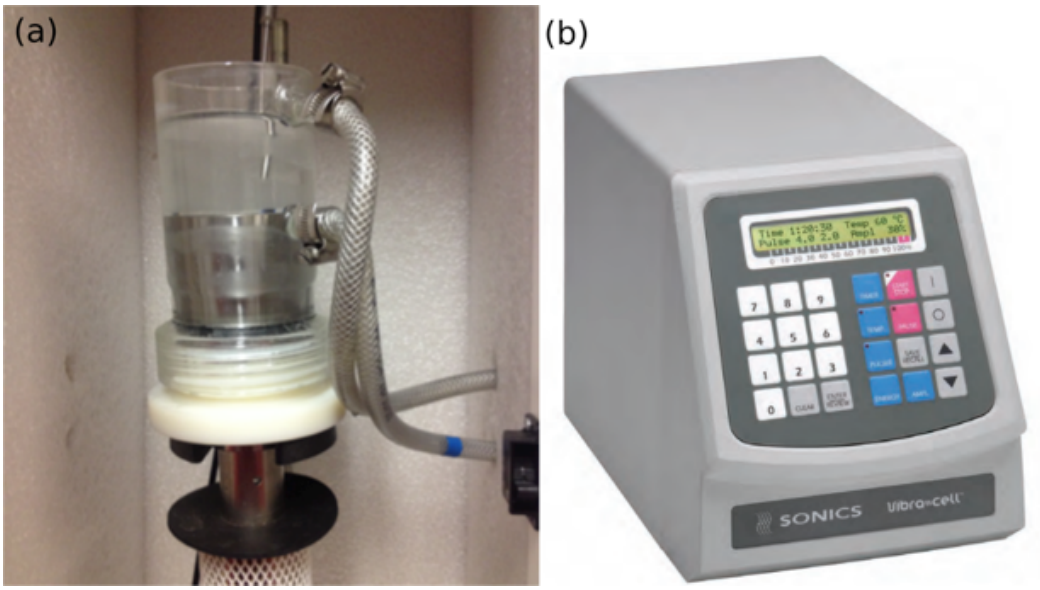

Figure 4.4 Ultra-high power sonication system used to mix nanodiamond containing solutions.

4.6 CVD DIAMOND GROWTH

To produce a diamond film via CVD, it is necessary for the reacting gas to contain carbon molecules. Thermal (hot filament) and plasma (RF, DC, MW) methods can be used to grow a diamond thin films (see section 2.3.2 Chemical Vapour Deposition). (Figure 4.5) shows these two methods.

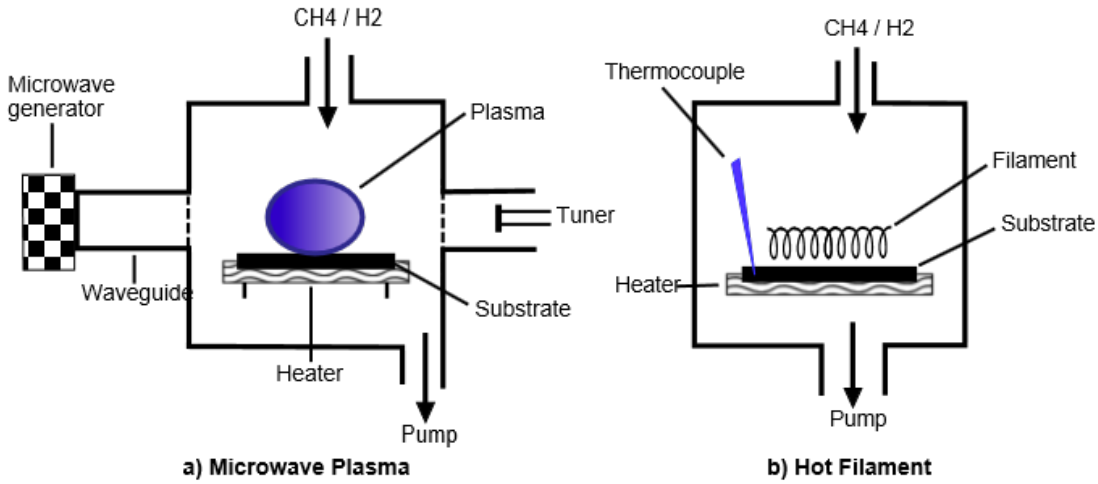

Figure 4.5 The two main types of diamond growth (a) microwave plasma enhanced CVD and (b) Hot filmanet CVD growth.

CVD Diamond growth normally occurs in between 700–1000°C with the precursor carbon containing gas being diluted in excess hydrogen (H_2), typically (CH_4) at 1–2% is used [178]. Hot filament was initially used to grow diamond films, but this method leads to filament contamination, and so currently MWPECVD is used, as the inductively coupled plasma is clean and has the ability to produce high quality diamond with very few contaminants in the bulk of the diamond. A 'standard model' is used to summarise CVD diamond growth and it contains three significant elements: firstly hydrogen atoms stabilize the diamond lattice, by preventing the rearrangement of the carbon structure, and thus hindering the production of graphitic sp^2 carbon. Also the temperature used for CVD diamond growth is below the Debye temperature of diamond, which therefore means the temperature is too low for bulk rearrangement [179]. Secondly, the plasma dissociates H_2 into H atoms, which are highly reactive and react readily with the hydrocarbon source; this facilitates the formation of carbon–containing radicals.

The H atoms formed in the plasma, are able to abstract H atoms that are bonded to carbons on the surface, this creates radical carbon sites on the surface. Occasionally these surface radical sites react with gas phase carbon–containing radicals, resulting in carbon atoms being adsorbed on the surface, furthermore resulting in diamond growth. Thirdly, hydrogen atoms react with sp and sp^2 carbon atoms on the surface, encouraging the formation of sp^3 bonded carbon. This 'standard model' has been summarized by Butler and Woodin [179].

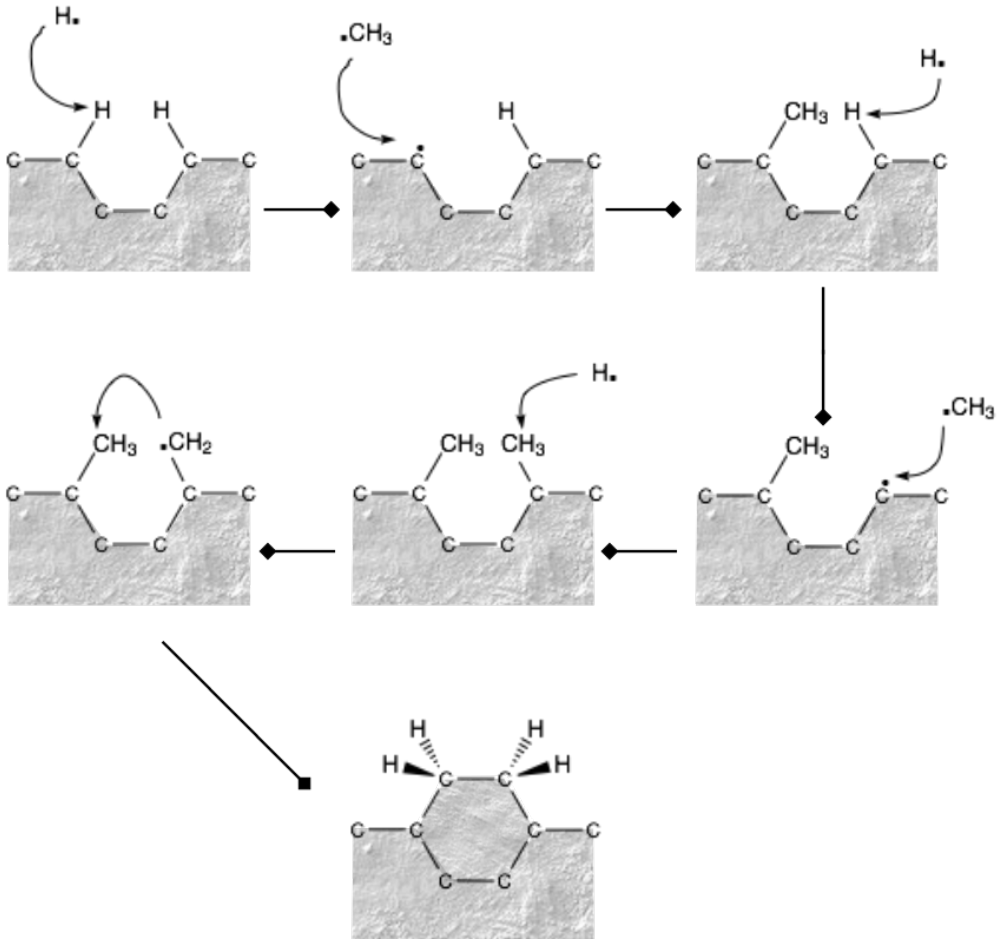

Figure 4.6 Schematic of the reactions occurring at the diamond surface during growth.

4.6.1 MICROWAVE PLASMA ENHANCED CVD (MWPECVD)

MWPECVD has been used throughout this thesis to deposit diamond, using CH_4 and H_2 as the precursor gases. CH_4 is used as the carbon source, and is ionised into methyl radicals ($CH_3\cdot$) in the plasma. H_2 is used to selectively etch non-diamond carbon, and also catalyses the bonding of the $CH_3\cdot$ radicals to the H-terminated surface of the diamond [14]. To produce a diamond film, nucleation of $CH_3\cdot$ must occur on existing diamond particles on the surface of the substrate. Methods used to seed diamond on substrates include mechanical abrasion, electrical biasing, pulsed laser irradiation and ultrasonic seeding [180].

Chemical vapour deposition (CVD) is a chemical process in which thin films are produced after exposing a substrate to volatile procursors. Plasma-enhanced chemical vapour deposition (PECVD) is CVD which is facilated by using a plasma, plasmas are created by supplying energy to a gas which causes charge carriers to form. A plasma is used to aid chemical reactions which occur within between the ionised reacting gasses, and the process occurs in low-pressure vacuum systems. Radiofrequency (RF), DC discharge and microwaves (MW) are the most common methods used for generating a plasma. Typically; RF plasmas operate at 13.56 MHz and MW at 2.45 GHz, with these values for frequency representing the industrial standard [181]. DC plasmas are created by applying a DC electric field across paralel plate electrodes containing reagent gases. DC discharges however can only deposit conducting material as insulating films quickly extingush the discharge. Capactively coupled discharges can be created across parallel plate electrodes using AC electric fields, and inductively coupled discharges can be generated using RF or MW frequency AC magnetic fields, and so the discharge plasma is not extinguished. Inductively coupled plasmas are often more desirable than capacitively coupled plasmas, because the plasma is separated from reaction chamber and so this results in the a higher purity film due to less contaminents. PECVD produces higher quality films at a faster rate than standard CVD processes. Throughout this thesis NCD was grown using MPECVD in a Seki Technotron AX5010 reactor, supplied by a 1.5 kW magnetron (at 2.45 GHz) see (Figure 4.7).

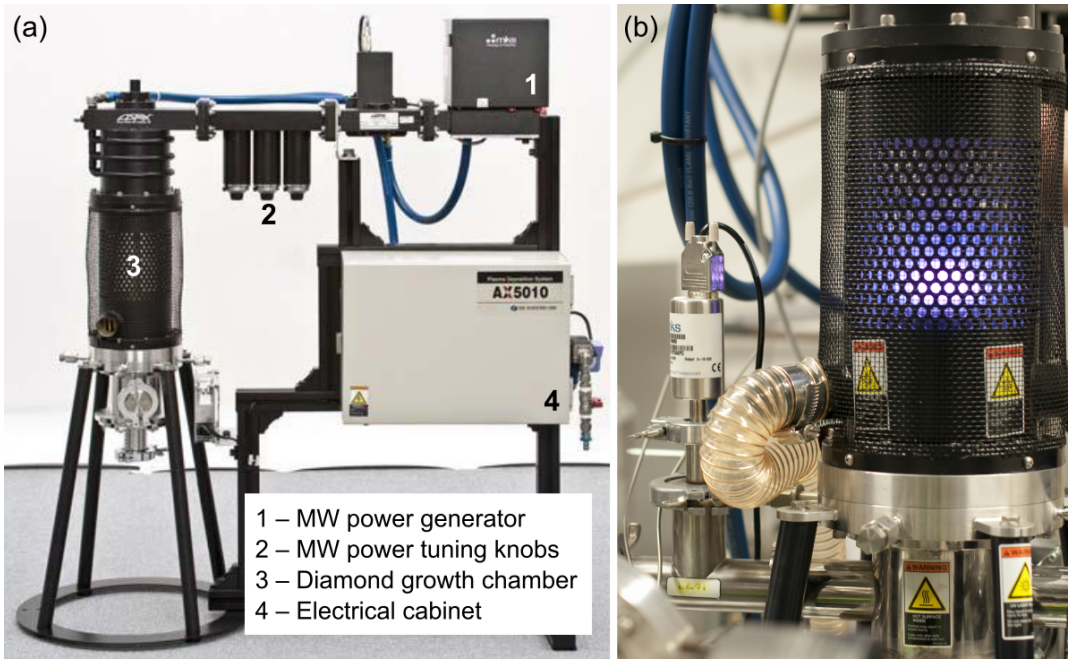

Figure 4.7 (a) Photograph of Seki Technotron AX5010 highlighting the MW power generator and tuner, chamber and electrical cabinet. (b) a photograph of a ignited plasma inside the chamber during diamond growth.

4.7 Atomic Force Microscopy

Atomic Force Microscopy (AFM) is a high-resolution method of scanning probe microscopy (SPM). It was first developed as a method for imaging the surface of non-conductive materials, and was first demonstrated in 1986 by Binnig and Quate [182]. It consists of a sharp tipped cantilever, which is used to scan over the required surface and various forces of deflection can be measured. The radius of the cantilever tip is generally in the order of single nanometres and is often made from silicon or diamond. The deflection of the tip is typically measured using a laser beam that is reflected from the cantilevers surface onto a range of photodiodes. When an AFM cantilever tip is scanned across a surface, piezoelectric positioners expand and contract under applied voltages, and produce an image with sub nanometre resolution [183].

The resolution of the scanning depends upton the number of scan lines, the step size and the tip sharpness. AFM images produced by raster scanning of surface topography are able to reach extremely high magnifications; up to 1,000,000x. The resulting measurments are obtained in three dimensions, the X-Y plane and the Z plane (horizontal and vertical respectively).

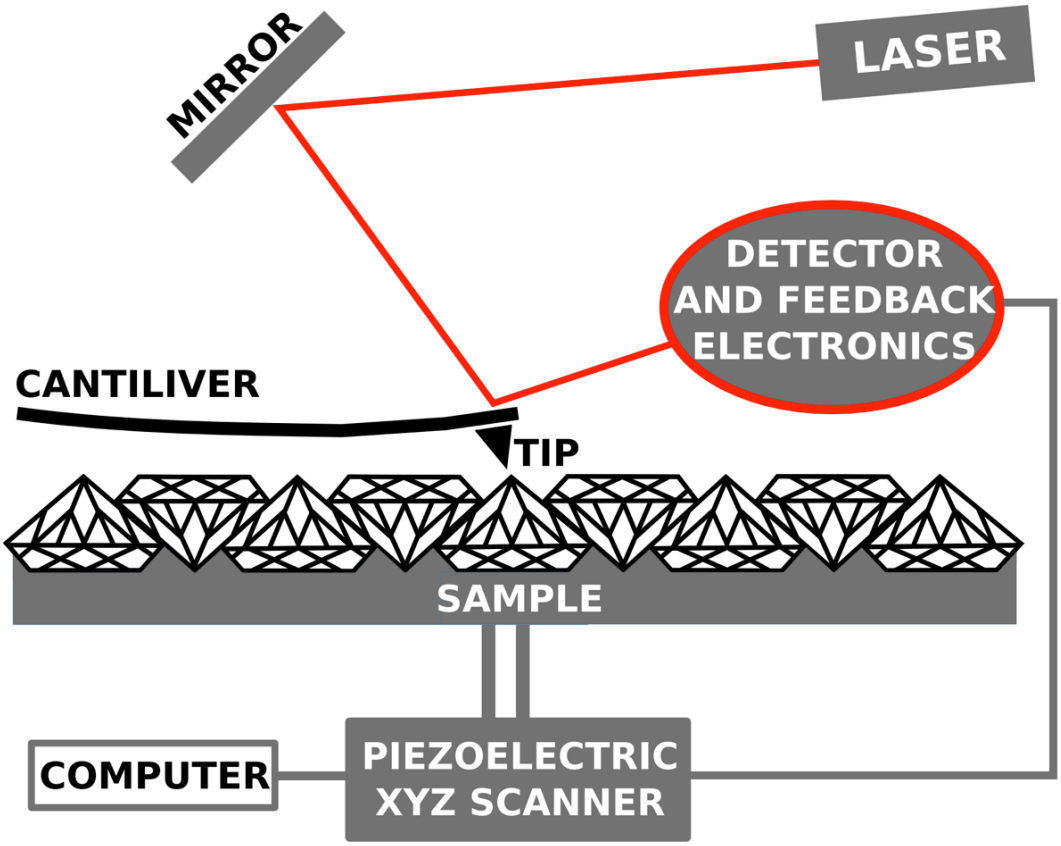

Figure 4.8 Schematic diagram of AFM in contact mode.

At distances of a few angstroms, a very strong repulsive force is observed between the cantilever tip and the sample. The origin of this force is due to the overlap or electronic orbitals which occurs at sub atomic distances. When this repulsive force is dominant, the AFM tip is said to be in contact mode. The attractive regime is resultant from the instantaneous polarization in which an atom induces polarization in neighborouring atoms, this polarization indues an attractive interation.

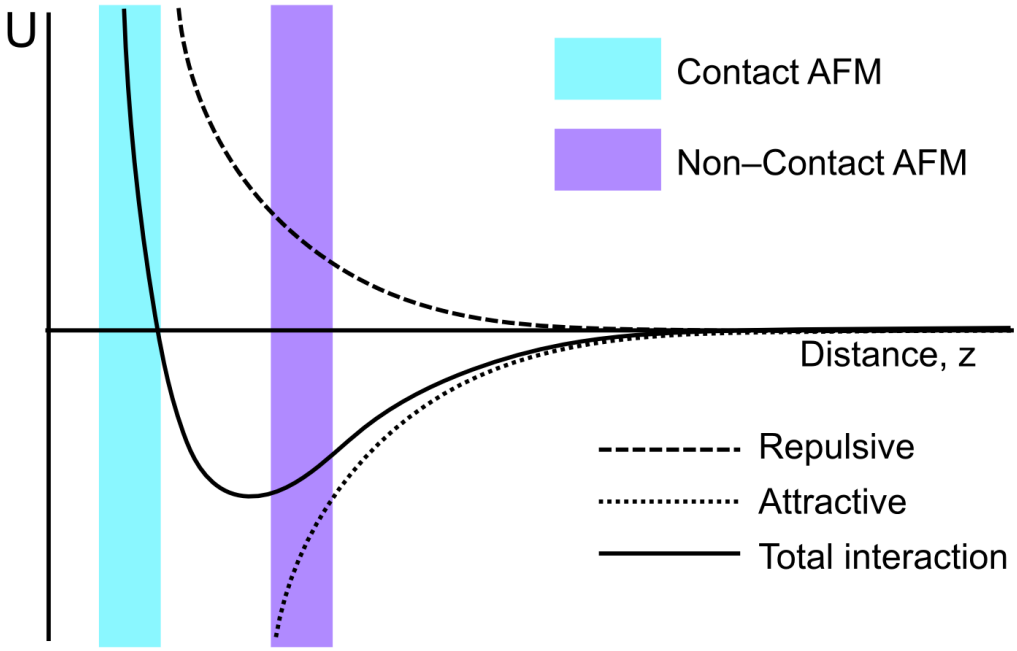

Figure 4.9 Leonard–Jones potential showing attractive and repulsice inter atomic forces, with the corresponding regions of contact and non-contact mode AFM being highlighted (adapted from www.parkafm.com).

The topography of very flat surfaces can be imaged by reading the deflection of the cantilever tip as it rasters across the surface. For rougher surfaces, a method of constant force is used, this mode requires a constant deflection force being observed by the cantilever via varying the tip height. There are two basic modes of AFM 1) Contact mode and 2) Tapping mode. Contact mode is when the tip of the AFM is in constant contact with the surface. Tapping mode is when the cantilever tip is oscillated at its resonant frequency, the surface of the sample is sensed via damping of this resonant oscillation by elecrostatic and Van der Waals forces. Tapping mode is desirable when tip and surface contact is prohibited, examples of this include imaging biological artefacts; DNA, proteins etc. and when imaging hard materials that may break the tip, i.e. diamond. Blunt AFM tips produce images of poor quality and resolution. Throughout this thesis, tapping mode AFM has been used to image Nanocrystalline Diamond (NCD) and nanodiamond (ND) coated materials.

4.8 SCANNING ELECTRON MICROSCOPY

Scanning Electron Microscopy (SEM) is a type of high vacuum microscopy in which a focused high energy primary electron beam rasters the surface of the sample. This electron beam interacts with atoms on the surface and the reflected electrons are detected. The detected signals contain information about the surfaces composition and topography. The most common type of signal is produced by secondary electrons, which occur when atoms at the near-surface of the sample are excited by the primary electron beam, but also backscattered electons (BSE), auger electrons and X-rays are detected. The electron beam is very focused and narrow, and this results in the micrographs having depth which produces images with 3D characterestics. Resolution of SEM is in the order of nanometres, with a magnification of around 500,000x being achieved.

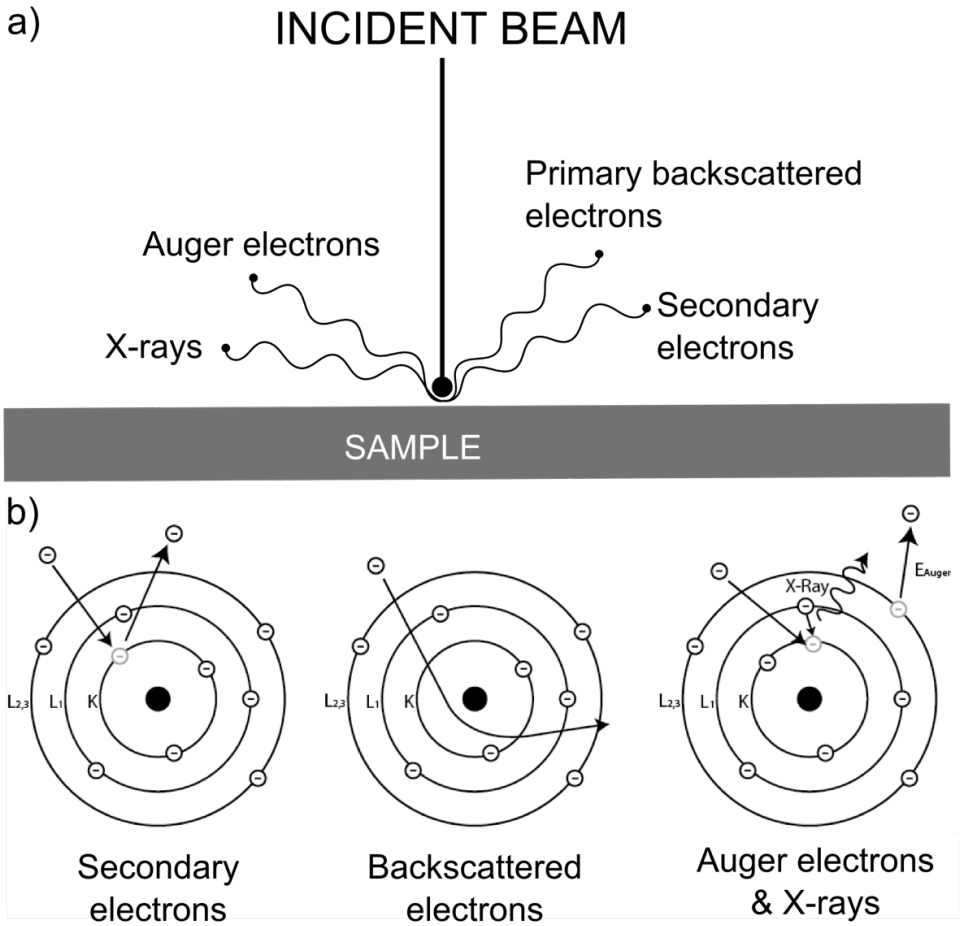

Figure 4.10 (a) simplified illustration of various modes of electron emission that are useful for SEM imaging, such emission occurs upon high–energy electron bombardment of atoms in the sample. (b) Secondary electrons shown being

inelastically scattered, backscattered electrons being elastically scattered and the auger and x-ray produced when are high energy inner shell electrons drop down energy level and produce either an auger electron or X-ray.

The electron beam in a typical SEM is thermionically emitted from the filament cathode from within the electron gun. Tungsten is the most common source of high energy electrons, but lanthanum hexaboride (LaB_6) is also used. Tungsten is the normal choice because it is the metal with the lowest vapour pressure and highest melting point, allowing the highest heating yeilding a high electron emission, it is also a relatively low costing metal. Nonconducting surfaces may be imaged using an environmental SEM, this takes places in a higher pressure chamber, with short working distances used. The vacuum is kept low at the electron gun, and the contrasting higher pressure on the surface of the sample neutralises charge and allows for the secondary electron signal to be amplified. For environmental SEM field emission guns (FEG) are typically used as this electrons produced have a small spot size and are of high brighness at the low acceleration potential. The low acceleration voltage is in the range of 0.5–5 kV, and is adjusted accordingly to ensure that the sum of the primary electron current equals the sum of the SE and BSE currents. After the electron beam is generated, is it accelerated through an anode which focuses the beam, it then passed through a series of magnetic condenser lenses which reduce the diameter of the beam. The beam then passes through a scanning coil which is responsible for the rastering of the beam across the sample. A final lens focuses the beam onto the surface with a resulting size of approximetly 0.5 nm.

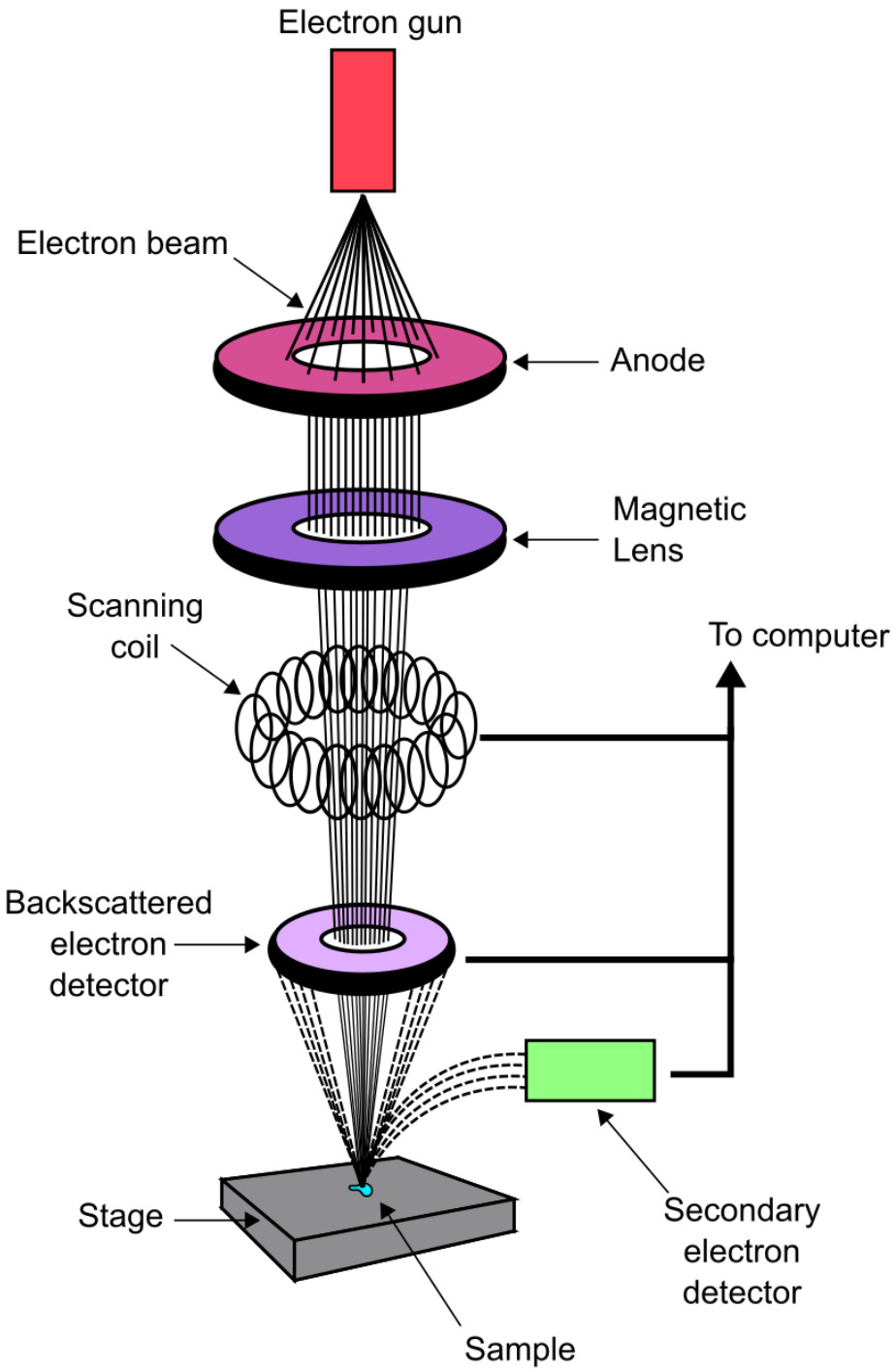

Figure 4.11 Schematic of typical SEM (adapted from www.purdue.edu).

Secondary electrons are low energy electrons (less than 50 eV) that are released from the k-shell (1s orbital) of the atoms that occur from inelastic scattering of the incoming electron beam. The ejected electrons are released from the top few nanometres of the surface due to their low energy, and they are detected using

an Everhart–Thornley detector [184]; a scintillator–photomultipying system. The secondary electrons are first attracted towards an electrical bias of about +400 V, and they accelerated again towards another posotive scintillator bias of about +2,000 V. These highly energised electrons emit a flash of light when collided with the scintillator which is conducted towards a photomuliplier. The photomulipler converts the flashes into a digital pixel, and the process uses a raster scan motion to produce digital images.

Backscattered electrons (BSE) are high energy elecrtons that are reflected from the incident beam, and they occur from elastic scattering interactions with surface atoms. The Everhart-Thornley detector is wrongly located to detect BSEs as they travel at differing angles to the secondary electrons, (Figure 4.10). Heavy elements emit BSEs more than lighter elements, so the detection of BSEs can lead to images showing these constrasting areas of elemental composition. BSE detectors are either semiconductors or scintillators.

An auger electron is emitted from an atom when an inner–shell vacancy is filled, this is called the auger effect. An inner–shell vacancy is produced via the removal of a core electron, this allows for a higher energy elecrton from a outer orbital to fall into the vacancy and results in the release of energy. This energy is mostly emitted in the form of a photon, however it can also be transferred to another electron in the same atom which is consequently ejected. This second emitted electron is the auger electron and auger electron spectroscopy can be used to study material surfaces.

X-rays can be produced when the electron beam interacts with the atomic 1s orbital (K shell) and an electron is emitted, an electron from a higher orbital (L, M or N shell) will be energetically favoured to fill the lower energy orbital, and so the excess energy is released in the form of an X–ray. These X–rays can be detected using energy–dispersive or wavelenth–dispersive X–ray spectroscopy (EDS, WDS).

Throughout this thesis a Carl Zeiss XB1540 focused-ion-beam microscope has been used for the characterisation of glass micropippetes and NCD diamond growth. Most frequently an accelerating voltage of 5 kV was used with the system imaging in the inlens mode.

4.9 Raman Spectroscopy

Raman spectroscopy is a technique which is used to obtain information about molecules and is often used to idenfity what is in a sample. It uses the inelastic scattering of photons from a monochromatic light source, to observe symmetric vibrational modes within a system. The light source is usually in the form of a near IR or near UV laser, this light interacts with vibrations within molecules, and information about present bonds is obtained. Inelastic scattering is a process where the kinetic energy of the incident particle, in this case a photon, is not conserved, elastic scattering in contrast occurs when the energy is conserved. When a photon interacts with matter (solid, liquid or gas) some of the kinetic energy may be lost, alternatively the kinetic energy might increase. The shift in energy observed is either red or blue, red shift is observed when the incident photon loses energy to the matter, the transfer of energy from matter to the incident photon is blue shift. Red shift is called Stokes scattering, and blue shift is anti–Stokes scattering. Elastic scattering is also called Rayleigh scattering, and this light is filtered out leaving only the inelastic scattered light to be detected. Peaks in the spectrum observed give information about the molecular strucure, and from this the identiy of the compound present can be found.

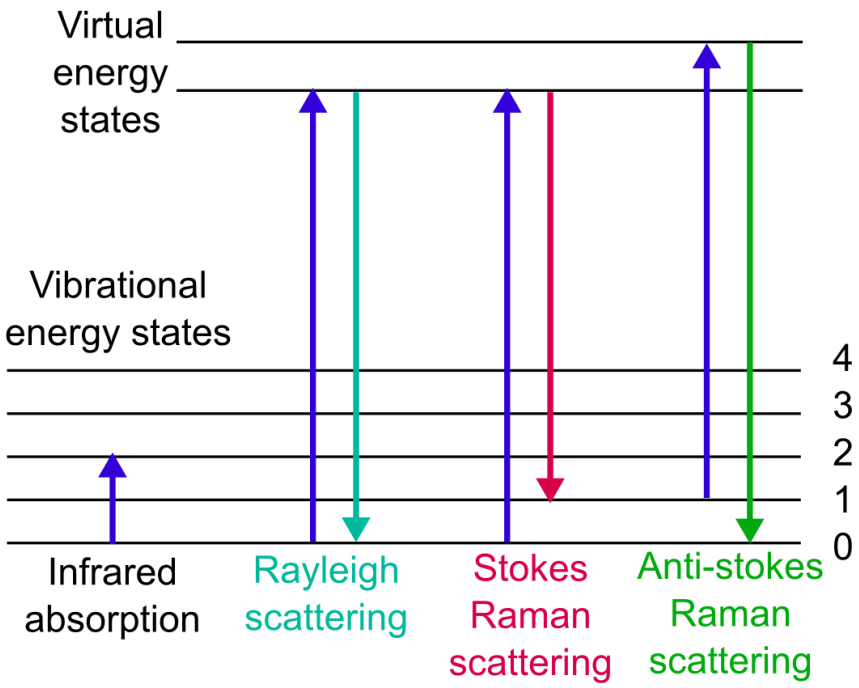

Figure 4.12 Energy level diagram showing the states involved in raman spectra.

The spectra detected show vibrational frequency of present bonds, in the form of wavenumbers (cm^{-1}), and peaks are used to identify chemical bonds present. The energy range is 200–4000 cm^{-1}.

An oscillating dipole is induced when a photon interacts with a molecule due to the caused movement of electrons and protons [185]. The dipole then radiates photons of varying yet specific frequencies. This mechanism can be understood from the time-dependent electric field of incident radiation (E) and the induced dipole moment of the molecule (P).

$$E = E_0 \cos(\omega_0 t) \tag{4.1}$$

Where E_0 is the amplitude of the $_{0th}$ component of the electric field and ω_0 is the frequency of E, the electric field. The induced dipole (P) will then look like:

$$P_\rho = \alpha_{\rho\sigma} E_\sigma = \alpha_{\rho\sigma} E_{\sigma 0} \cos(\omega_0 t) \tag{4.2}$$

Where $\alpha_{\rho\sigma}$ is the molecular polarizability which is a measure of how easily a molecule is polarized along a particular direction. As a molecule vibrates, the charge distribution and thus the moleculary polarizability $\alpha_{\rho\sigma}$ varies with time, and for small displacements it can be calculated using a Taylor series.

$$\alpha_{\rho\sigma}(Q) = (\alpha_{\rho\sigma})_0 + \sum_k \left(\frac{\partial \alpha_{\rho\sigma}}{\partial Q_k}\right)_0 Q_k + \dots \tag{4.3}$$

Where $(\alpha_{\rho\sigma})_0$ is the molecular polarizability at equilibrium, and Q_k is the κ^{th} normal modes value of equilibrium amplitude associated with ω_k, the vibrational frequency. Q_k, the time dependent amplitude of a normal vibrational mode is harmonic thus:

$$Q_k = Q_{k0} cos\,(\omega_k t) \tag{4.4}$$

Where Q_{k0} is the equlibrium amplitude, ω_k is the normal mode frequency and t is time. A combination of these equations yields a linear vector describing the induced dipole $P_\rho^{(0)}$:

$$P_\rho^{(0)} = \alpha_{\rho\sigma} E_{\sigma 0} \cos(\omega_0 t) + \sum_k \left(\frac{\partial_{\alpha_{\rho\sigma}}}{\partial Q_k}\right)_0 Q_{k0} E_{\sigma 0} \cos(\omega_\kappa t) \cos(\omega_0 t)$$

$$= \alpha_{\rho\sigma} E_{\sigma 0} \cos(\omega_0 t) + \sum_k \left(\frac{\partial_{\alpha_{\rho\sigma}}}{\partial Q_k}\right)_0 \frac{Q_{k0} E_{\sigma 0}}{2} [\cos(\mathrm{t}(\omega_0 - \omega_\kappa)) + \cos\big(t(\omega_0 + \omega_\kappa)\big)] \tag{4.5}$$

This shows that the induced dipole contains three frequencies; ω_0, $(\omega_0 - \omega_\kappa)$ and $(\omega_0 + \omega_\kappa)$, relating to the three types of inelastic scattering, Rayleigh, Stokes and Anit-stokes respectively [186].

The interaction between incoming photons and electrons present in a solid produces scattering because the electric field is able to induce a dipole moment, (M) present in the solid. This induced dipole moment varies with the frequency of the incident electric field and generates elastically scattered Rayleigh electrons, which have the same frequency as incident photons, yet produce a spherically symetrical distribution observed about the nucelus [187]. For inelastically scattered electrons, energy is removed from the induced dipole if a vibrational excitation can be prodced in the given solid. The vibration can be characterized by a dipole moment which is present during the vibration of the normal mode. During the vibration, a change in polarizability must be observed for the system to be Raman active. After the scattering process two states occur; a system left in a lower vibrational enery level resulting from anit–Stokes, and higher level from Stokes scattering [188].

4.10 NANODIAMOND MONOLAYER COATINGS

Nanodiamond (ND) monolayers have been deposited on a variety of substrates throughout this thesis, including Si, SiO and glass. A solution of monodisperesed NDs has been used as the source of NDs, and all methods of ND coating rely upon the electrostatic attractions that are present between the surface of the NDs and the surface of the substrate to be coated. Various abrasion techniques have previously been used to coat surfaces with diamond using diamond powder, ultrasonication has been used as the prefered method throughout this thesis [189]. The mechanism for ultrasonication coating is similar to that of abrasion but with a main advantage of uniform coverage, as a regular ND size is used as well as the sonication increase the kinetic energy of the NDs, and thus increases the collision rate with the substrate [76] ND solutions (0.05 gl^{-1}) were used for seeding, with substrates being degreased prior to a 10 minute ultrasonication. Substrates are then dried using a N_2 gun.

4.11 OZONE TREATMENT

One of the four sp^3 bonds at the diamond surface is dangling. This dangling bonds is terminated with various functional groups in high quality diamond, the functioning of the surface occurs naturally during MWPECVD growth, this is due to presence of hydrogen radicals in the plasma. Varying functional groups present at the surface changes properties including surface conductivity and hydrophobicity. Oxygen termination can be performed via various processes including acid cleaning, anodic oxidation, oxygen reactive ion etching (RIE) and ozone treatment. Throughout this thesis ozone treatment of NCD films and nanodiamonds has been used to oxygen terminate the diamond surface. This is because the etch rate of the diamond using ozone is much less than using RIE and the process is dry and facile. Ozone is a more powerful oxidising agent than oxygen due to the delocalised electron distribution over the two equivalent O–O bonds which in turn makes the electrons more avaliable to react and the easy dissociation into oxygen radicals ($O_3 \rightarrow O_2 + O\cdot$). The ozone treatment used throughout has been perfomed by: 1) placing samples on a heating stage inside a sealed chamber, UV ozone cleaner NL-UV253, 2) pumping down to evacuate chamber (10^{-6} mbar), 3) heating stage to 200°C for 30 minutes, 4) filling with O2

gas to reach 50 mbar pressure and then 5) generating O radicals using an ozone generator (10 g/h) for the desired length of time between 30 minutes and 2 hours.

4.12 HYDROGEN TREATMENT

Hydrogen termination of diamond has importance for stabilizing the structure of the surface [190]. MWPECVD treatment is frequently used for hydrogen termination as non–diamond carbon is etched at a greater rate than sp^3 carbon [191]. However, this was considered too harsh for the borosilicate glass slides used for cell culture and so a less harsh hydrogen environment was created. Throughout this these hydrogen treatment was used to ensure homogeneity of nanodiamond coated substrates after seeding and to ensure all oxygenated functional groups are removed from the surface. A custom made chamber was used to heat samples to 500°C in 10 Torr of hydrogen for 5 h and allowed to cool in hydrogen.

4.13 X–RAY PHOTOELECTRON SPECTROSCOPY

X–Ray Photoelectron Spectroscopy (XPS) is a quantitative, ultra–high vacuum (UHV) technique that measures elemental composition at the surface of various materials. XPS spectra are acquired by irradiating samples with an X–Ray beam and measuring the concentration and kinetic energy of electrons, which have been ejected from the surface (0 – 10 nm top layer) of a material. XPS spectra can give information about the elemental composition at the parts per thousand (ppt) range and more specifically details about the chemical and electronic state of elements present.

In XPS the kinetic energy of emitted electrons is measured using a spectrometer and the spectrum is displayed as intensity (yield) vs. binding energy of the electrons from the core orbital. A peak is observed if there are numerous electrons ejected with a particular characteristic energy. The intensity and energy of peaks provide suitable information in which surface elements can be identified and quantified. All elements can be detected apart from hydrogen and helium; this is because the core orbitals for both elements participate in chemical bonding. The signal produced from emitting electrons from the 1s orbital in

hydrogen or helium will overlap with kinetic energies observed from other valence electrons in the other surface atoms [192].

Performance materials are in increasing demand; therefore precisely engineered surfaces are of high importance. The surface chemistry of a material influences many factors including but not inclusive to adhesion, contact potential, wettability and corrosion. Therefore, XPS is a highly useful tool for understanding the chemical and physical interaction that occurs at the surface of a material. Throughout this thesis surface chemistry of nanodiamond samples were characterised using XPS, a Thermo K–alpha instrument was used, with a monochromated Al K_a(1486.6 eV) radiation source, alongside an internal flood gun to reduce charging.

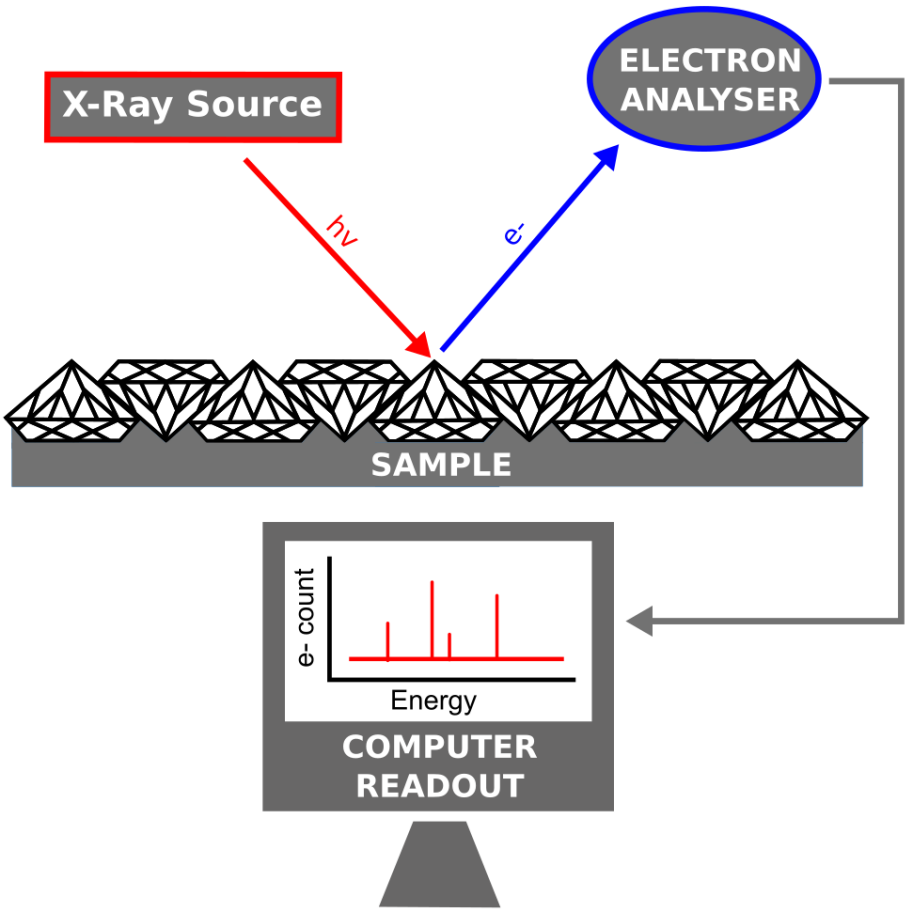

Figure 4.13 Schematic of a typical XPS instrument.

4.14 CONTACT ANGLE MEASURMENTS

The contact angle for a given material is the angle measured between a specific liquid and the interface of the solid. The corresponding angle is able to quantify the wettability of a surface via the Young equation. For a given system comprising of solid, liquid and vapour at a specific temperature and pressure there is a corresponding equilibrated contact angle. However, due to the small volumes of liquid used (1 µl – 10 µl) hysteresis of the contact angle is observed because of evaporation. The equilibrium contact angle is resultant from the relative strength of the solid, liquid and vapour molecular interactions. Wetting is a term used to describe the capacity of a liquid to sustain contact with the surface of a solid, and is the result of intermolecular interactions. The contact angle is determined by balancing out the adhesive and cohesive forces and is currently of particular attention in nanotechnology due to recent developments in new nanomaterials.

The Young–Laplace equation is used to determine the shape of a liquid–vapour interface, the contact angle being the boundary condition of the Young's equation:

$$\gamma_{sg} = \gamma_{sl} + \gamma_{lg} \cos\theta_c \quad (4.6)$$

Where γ_{sg} is the surface free energy of a solid, γ_{sl} the interfacial tension between liquid and solid, γ_{lg} the surface tension of a liquid and θ_c the contact angle.

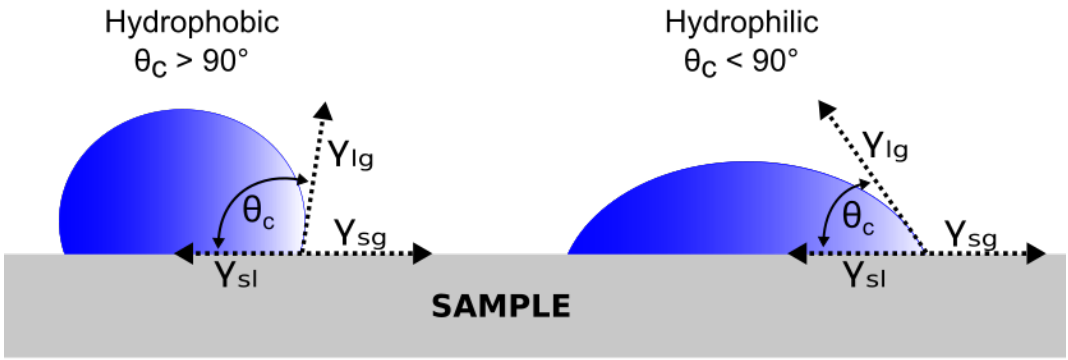

Figure 4.14 Schematic for two liquid drops displaying the values used in the Young's equation.

The value of the contact angle can give information about the wettability of a surface, i.e. how hydrophobic/hydrophilic something is. It has been shown that you can adjust the contact angle by roughening a surface, with rougher producing a smaller contact angle [193]. Throughout this thesis, contact angle measurements were taking using a Krűss Drop Shape Analysis system (DSA 10 MK2), values were calculated using Drop Shape Analysis software.

4.15 HUMAN NEURAL STEM CELLS (HNSCS)

All procedures involving human tissue were carried out in accordance to the Human Tissue Act 2006. The preparation of neural cell cultures was performed in close collaboration with the Developmental Biology Unit, Institute of Child Health, UCL by either Barbora Vagaska or Citlali Helenes Gonzalez.

The hNSCs were isolated and expanded by Kin Pong U according to the protocol described previously by Sun *et al.* (2008) [194]. Briefly, hindbrains from human embryos between 6–9 weeks old (Carnegie stage 18–22) were collected through Human Developmental Biology Resource (HDBR) and dissected in cold Neurobasal medium (Gibco). After complete removal of the meninges and blood vessels, the tissue was chopped into smaller pieces and digested in Accutase

solution at 37°C for 5–10 min with occasional trituration to obtain single cell suspension. Cells were then centrifuged and resuspended in growth medium composed of RHB–A medium (Stem Cell Sciences) supplemented with 1% (v/v) L–Glutamine, 1% (v/v) Penicillin/Streptomycin (both Gibco), 1% (v/v) 100x N2 supplement, 2% (v/v) 50x B27 supplement (both PAA), 10 ng/µl human recombinant FGF2, 10 ng/µl human recombinant EGF (both Peprotech), 50 µg/ml BSA fraction V and 5 µg/ml Heparin (both Sigma). Cells were plated on poly–L–lysine and laminin (10µg/ml, Sigma) coated dishes and grown for 7 days with media changed every 2 days to remove any dead cells or debris. To eliminate neurons from the primary cultures and get homogenous culture of neural stem cells, the cells were first transferred onto 0.1% (w/v) bovine gelatine (Sigma) coated dishes for 7 days and then re–plated onto laminin coated dishes for further expansion. The medium was changed every 2–3 days and after becoming confluent cells were split in ratio 1:2 to 1:3. For routine expansion and further experiments cells were grown in growth media composed of DMEM/F12 with Glutamax (Gibco) with same supplements (except of glutamine) and laminin was added to the medium instead of coating the dishes. Passages up to 30 were used for all experiments.

4.16 IMMUNOSTAINING

Immunostaining is a term used for a general method in which, antibodies are used to detect specific proteins. The most common immunostaining technique is immunocytochemistry (ICH), ICH is the staining of cells and first cases used fluorescent dyes. In ICH antibodies bind to antigens in a specific manner, the binding is highly selective and thus gives you spatial locations of particular anitgens. It is a technique which is used to identify, locate and label particular proteins and cellular components, and it can also be used to identify cellular events, for example apoptosis which is programmed cell death. Antibodies used are able to target specific antigens present in cell membranes, nuclei, cytoplasm as well as in lipids and proteins. ICH can be used not only to label and identify specific antigens, but is also used to examine structural components of the cell.

ICH can be performed on both live cells an fixed cells. An example of a live cell marker is CellTracker™ Green CMFDA which exhibits bright green fluorescence in the cytoplasm at all physiological pH levels; CellTracker™ Green CMFDA is

nonfluorescent until esterase cleavage occurs. Fixation of cells is a chemical process where biological tissue is preserved from decay, self-destruction and decomposition. By fixing cells, any biochemical reactions occuring are terminated, and it also may increase the stability and mechanical strength of the fixed tissue.

In chapter 6 subconfluent hNSCs were labelled with the vital cytoplasmic dye, CMFDA (5-chloromethylfluorescein diacetate, Cell Tracker, Invitrogen) in supplement–free culture media at 5 μM final concentration for 30 mins. After the incubation, the cells were washed twice with phosphate buffer solution (PBS), trypsinized and then plated on the different surfaces in the standard expansion media with laminin at a density of $3x10^4$ cells/cm^2. Cell attachment and morphology were assessed after 24 hrs using an Olympus IX70 inverted fluorescent microscope for one sample per substrate type. For each sample 6 randomly selected areas were imaged using monochromatic Hamamatsu – OrcaR2 camera/HCImage software at 10x and 40x magnification.

Staining for actin was performed on hNSCs, which were fixed after 48 hours *in vitro* in 4% (w/v) paraformaldehyde in PBS (pH 7.4) for 15 min and washed three times with PBS. Substrates were then incubated in blocking solution (10% fetal bovine serum, 3% bovine serum albumin in PBS with 0.2% Triton X100 for permeablization) for 30min at room temperature. Cells were stained with Phalloidin conjugated with Alexa Fluor® 488 diluted in blocking buffer (Invitrogen, 5U/ml) together with Hoechst 33258 (2 ug/ml) to counterstain nuclei for 1 hour at room temperature. After 3 washes with PBS to remove any excess die the samples were imaged using an inverted microscope Olympus IX71 (Carl Zeiss, Jena, Germany) equipped with a Hamamatsu ORCA-ER digital camera (Hamamatsu Corp., Bridgewater, NJ) and all the image processing was done in Image J/Fiji.

In chapter 7 and 8 permeablization was performed as previously stated. Primary and secondary antibodies were diluted in blocking solution and the incubation times were overnight at 4°C for primary, and 1h at RT for secondary antibodies. Hoechst 33258 (2 μg/ml) was added during secondary antibody incubation to counterstain cell nuclei. After final three washes in PBS the coverslips were mounted on slides with an aqueous based mounting medium (Hydromount, National Diagnostics). Specific antibodies used are highlighted in each results chapter. (Figure 4.15) shows an example of immunostaining for hNSCS which have been differentiated into neurons on TCPS and NDs. Neuronal specific

markers (BIII–Tub, DCX and Hoechst) are used to confirm the differentiation pathway, individual and stained images are shown.

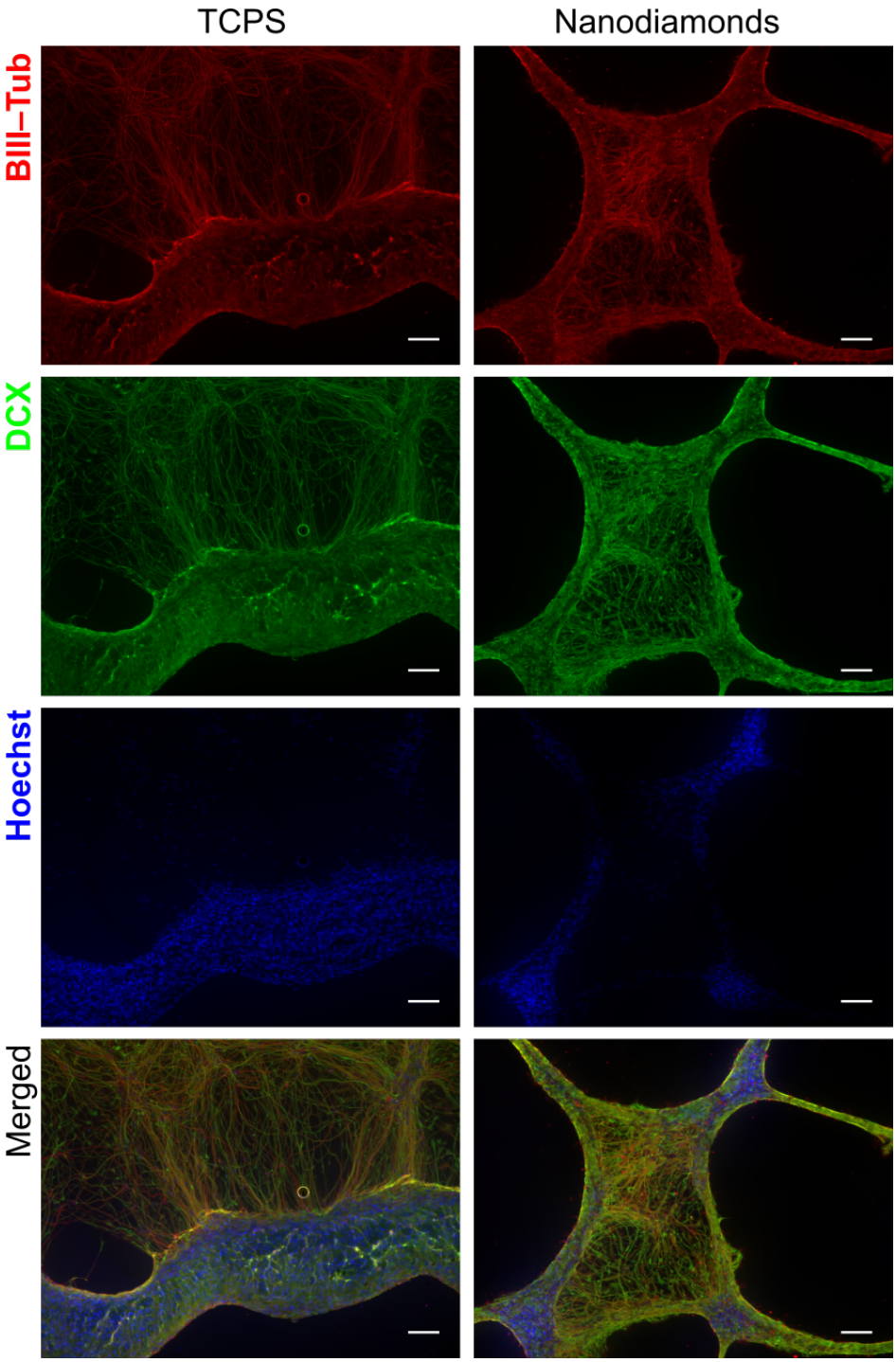

Figure 4.15 Example immunostained images. BIII–Tub (Red), DCX (green) and Hoechst (blue) labelled neurons, which have been differentiated from hNSCs on TCPS and nanodiamonds. Scale bar 100 μm.

4.17 BIO–LAYER INTERFEROMETRY

A Bio–layer Interferometry (BLI) system (ForteBio Octet ® RED96) was employed to compare protein–ND adhesion properties of NDs with O and H functionalisation. BLI is an optical technique in which white light is passed down an optical fibre and the reflected light is collected and measured. Proteins are covalently bound to the end of the optical fibre and the adhesion of molecules is measured in real–time. Interference patterns are observed in the reflected light, which is captured by a spectrometer. Molecules present in solution bind to the protein and as the adsorption increases, the interference pattern changes. Reflected light is measured from both the optical fibre and bio–layer interface and the interface between the bound molecules and the solution. The real–time interference pattern and subsequent wavelength shift is analysed and therefore the thickness of bound molecules can be calculated [195]. The detection is limited to molecules, which are binding to or dissociating from the optical fibre. Unbound molecules alter the refractive index of the solution but they do not affect the interference pattern. This allows for the BLI system to generate quantitation, affinity and kinetics information about protein: protein or protein: molecule binding. A schematic outlining how the thickness of bound molecules can be determined is shown in (Figure 4.16).

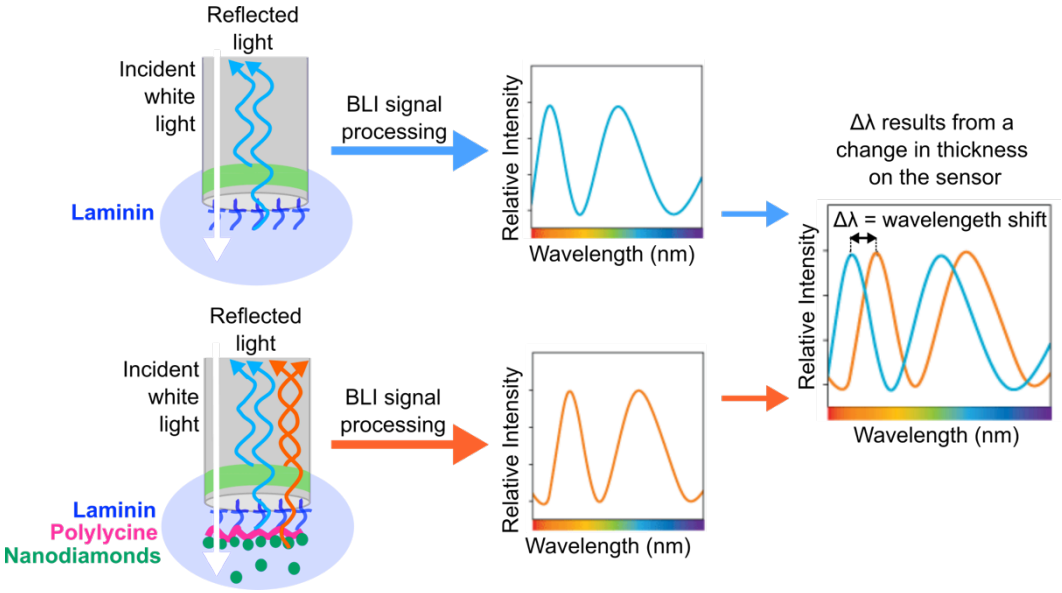

Figure 4.16 Schematic outlining how interferometry is used to measure binding thickness of proteins and nanoparticles on the end of an optical fibre (such as the ForteBio Octet ® RED96). White light is passed down the optical fibre, light waves are reflected from the sensor tip as well as from the bound proteins/nanoparticles. Phase difference between these two reflected light waves causes interference, which in turn is used to calculate quantitative thickness of adsorbate.

4.18 CELL COUNTING ANALYSIS

Matlab R2015a was used throughout this thesis for cell counting. (Figure 4.17) shows the code used cell counting and (Figure 4.18) shows corresponding images for the most important steps.

```
% Canny edge detection
BW=edge(I,'canny');
% Dilate edges of cells
se90=strel('line',3,90);
se0=strel('line',3,0);
Dil=imdilate(BW, [se90 se0]);

% Fill cells
BWfill=imfill(Dil, 'holes');
% Suppress cells on the border
BWcl=imclearborder(BWfill, 4);
% Erodes edges to seperate cells
sed=strel('diamond',1);
BWfin=imerode(BWcl,sed);
BWfin=imerode(BWfin,sed);

% Finds regions (cells) and numbers them
[B,N]=bwlabel(BWfin);
% Find areas of regions
Region=regionprops(B, 'Area')
region=[Region.Area];
% Anything below 0.2 and above 5 times the mean area is excluded
minimum=0.2*mean(region);
maximum=5*mean(region);
BWbrac1=bwareafilt(BWfin,[minimum maximum]);

% Finds regions (cells) in filtered images
[B,N]=bwlabel(BWbrac1);
% Find areas of regions
Region=regionprops(B, 'Area')
region=[Region.Area];
% Makes histogram of areas (50 bins)
h=histogram(region,50);
% Find most common area, which is likely to be a single cell
[m,i]=max(h.Values);
% Find centre of bin (corresponding area)
thresh=(h.BinEdges(i)+h.BinEdges(i+1))/2

% Select only regions of area 0.2-1.5 of eastimated area of single
% cell i.e. single cells
minimum=0.2*thresh;
maximum=1.5*thresh;
BWbrac=bwareafilt(BWfin,[minimum maximum]);
% Find regions (cells)
[B,N]=bwlabel(BWbrac);
% Set count to number of single cells
count=N

% Select regions of two cell area
minimum=1.5*thresh;
maximum=2.5*thresh;
BWbrac=bwareafilt(BWfin,[minimum maximum]);
[B,N]=bwlabel(BWbrac);
% Add number of newly counted cells to single cell count
count=count+(2*N)
% ...

% Output cell count
output2(n)=count;
```

Published with MATLAB® R2015a

Figure 4.17 Matlab code for cell counting (red numbers correspond to images in Figure 4.18).

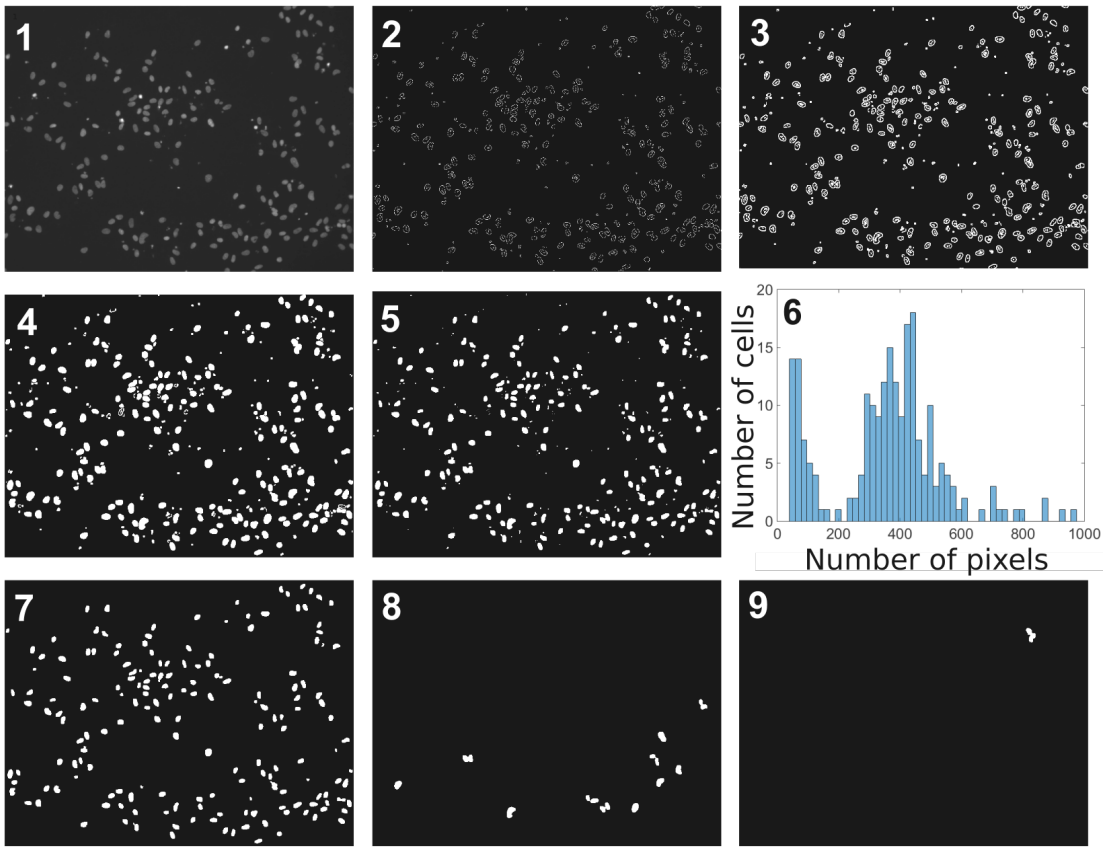

Figure 4.18 Showing each step of image manipulation required for cell counting. 1) Original fluorescent image of stained nuclei using Hoechst dye. 2) After edge detection function. 3) Dilation of edges of the cells. 4) Fill cells. 5) Eroding of the edges to assist the separation of cells and removes cells which are at the border of the image. 6) Plots a histogram showing the number of cells present for each given number of pixels (area). Assuming the smaller peak is resultant of noise and leftover non–specifically bound dye, the most common peak corresponds to the average number of pixels for a single cell. 7) Selects single cells, which are assumed to be between 0.2 and 1.5 times the average number of pixels for an individual cell. Counts these cells. 8) Repeat of step 7 but for two adjoining cells. 9) Repeat of step 7 but for three adjoining cells.

4.19 NEURITE TRACING

Techniques used for imaging neurons have improved due to advances in fluorescence microscopy. Demand has subsequently increased for accessible software, which is able to extract and analyse quantitative data about neuron morphology. Such neurite analysis is known as 'tracing'. Throughout this thesis, the Simple Neurite Tracer (SNT) has been used. SNT is a plugin available to use through open source Fiji software. It allows for semi–automated tracing of neurites and other tubular structures to be performed. The software allows for the analysis, reconstruction and visualisation of neuronal processes [196]. The plugin provides method for measuring neurite length and volume. SNT supports neurite tracing for 3D stacks, however this feature has not been utilised in the thesis. SNT is currently only one of a few open source neuron-tracing packages, others include: Neurolucida, hxskeletonize and Farsight, none of which were found to be as user friendly as SNT.

The user defines the neurite path; points along the middle of the process are selected and the software automatically finds the neurite connecting these points. When defining paths, the user confirms each segment, and so the probability of noise effecting traces is reduced. Neurites may start and end on other paths, creating branches. The paths between each point are found using a bidirectional A* search [197]. SNT was used to measure neurite length of neurons, which had been spontaneously differentiated from hNSCs (Chapter 8). An example of neurite tracing used in this thesis can be seen in (Figure 4.18) and corresponding neurite tracing data is shown in (Table 4.2).

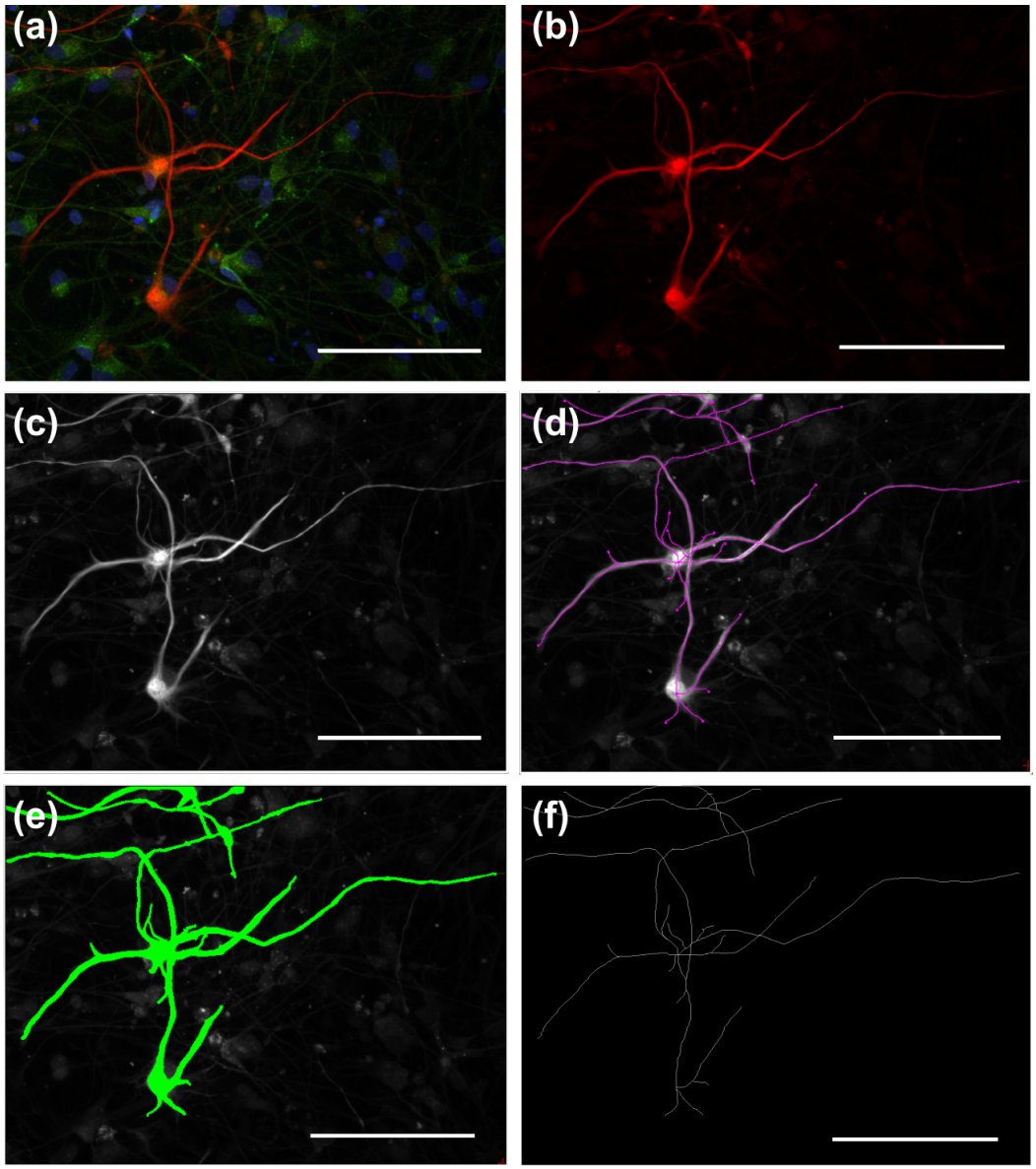

Figure 4.19 Example images produced whilst using the Simple Neurite Tracer of neurites stained for NF200. (a) Combined stack showing fluorescently stained neurons, which have been spontaneously differentiated from hNSCs on O–NDs. (b) Individual image taken from (a) showing the NF200 staining (red). (c) Grayscale image of fluorescent neuron used for neurite tracing analysis. (d) Neurites, which have been defined, are shown in pink, a high compliance of spatial resolution is observed. (e) Volume analysis (green) performed on the traced file from (d). (f) Length analysis (thin white lines) also performed on the trace file (d).

Path ID	Primary Path	Path Length µm	Starts On Path	Connected Path IDs	Child Path IDs
0	✓	235.84		1,4,16,17	1,4,16,17
1	✗	105.31	0	0,2,3	2,3
2	✗	21.46	1	1	
3	✗	193.77	1	1,15	15
4	✗	111.80	0	0,5,18,19	5,18,19
5	✗	11.17	4	4	
6	✓	245.46		7,8,9	7,8,9
7	✗	68.96	6	6,20	20
8	✗	25.50	6	6	
9	✗	21.92	6	6	
10	✓	154.17		11	11
11	✗	37.53	10	10	
12	✓	126.56		13,14	13,14
13	✗	29.58	12	12	
14	✗	12.37	12	12	
15	✗	31.36	3	3	
16	✗	21.91	0	0	
17	✗	18.34	0	0	
18	✗	12.15	4	4	
19	✗	33.84	4	4	
20	✗	10.82	7	7	
	Total Path Length	**1529.82 µm**			

Table 4.2 Example data acquired for neurite tracing, data shown corresponds to tracing done in (Figure 4.17).

4.20 CONCLUSION

This chapter contains information about experimental techniques used throughout this thesis. Equipment used has enabled diamond to be grown (MWPECVD), characterised (AFM, SEM, Raman, XPS) and employed in biological applications. The diversity in techniques used, highlight the interdisciplinary nature of research described throughout.

CHAPTER 5 – PATTERNING OF NANODIAMOND TRACKS AND NANOCRYSTALLINE DIAMOND FILMS USING A MICROPIPETTE FOR ADDITIVE DIRECT-WRITE PROCESSING

5.1 INTRODUCTION

The exceptional properties of diamond make it a desirable material for the fabrication of microelectromechanical systems (MEMS) devices [1,198] due to the attractive tribological [1,198] and mechanical properties of diamond, as well as high Q-factors being recorded on diamond micro resonators [199] . However, the chemical [200] and electrochemical inertness [201], and the extreme mechanical stability [24] of diamond make it a difficult material to process. Nanocrystalline diamond films (NCD) produced by chemical vapour deposition (CVD) posses the excellent properties of naturally occurring diamond [202,203], whilst offering the prospect for the selective growth of diamond in specific locations, avoiding the need for 3D pattern generation in thin film diamond layers. Patterned diamond at the micron scale would offer desirable properties for many applications: diamond bio-MEMs are highly desirably due to its biocompatibility [204] and diamonds strong resistance to bacterial colonization [205]. Other examples include diamond used for radio frequency resonators [206], scanning probe microscopy (SPM) probes as an all diamond cantilever [9], diamond electrodes for sensor applications [207], for patterning cells [42,166,208] and for the fabrication of diamond microelectrode arrays (MEAs) [209-211].

Currently there are several methods to pattern NCD films: top–down reactive ion etching (RIE) [209,212-218], laser ablation [42,219,220], photolithographic etchants [221] and bottom–up selective nanodiamond (ND) particle seeding, all of which have their own merits. RIE is a destructive process in which photolithographic methods are used in conjunction with typically oxygen / argon RF plasmas to remove unwanted areas of NCD film. RIE patterning is advantageous in that it fits into conventional CMOS processing work flows and can achieve sub–micrometre resolutions, however difficulties are encountered

when etching diamond due to the large resilience of diamond causing low etch selectivities for available hard masks, meaning only shallow diamond films can be easily patterned using such an approach. Furthermore, O_2/Ar RF plasmas can be damaging to the underlying substrate materials upon which NCD is deposited. More recently selective seeding has emerged as a solution to counter the low selectivity of diamond RIE processing to allow the bottom-up patterning of ND and NCD films. Various methodologies have been employed to pattern ND seeds, including inkjet printing of diamond inks [222,223], microcontact printing [224] and ND seeding via electrostatic self-assembly [225]. While these methods avoid the problems associated with mask selectivity in diamond etching, photolithography is still required and residual NDs can remain in nominally void pattern areas, leading to diamond growth in unwanted regions. To avoid this issue, Hébert *et al.* combine both processes by seeding with NDs, 'fixing' NDs with a short CVD plasma exposure, removing ND seeds from void pattern areas with RIE, and subsequently growing patterned NDs into NCD films [226].

Whilst all of these techniques have their merits, these processes still require photolithographic steps and the application of corrosive or reactive chemicals in processing, which could affect the surface chemistry of deposited NDs. Here a novel direct–write selective seeding method is described where no photolithographic steps or corrosive chemicals are required. ND patterns are deposited using a micropipette, which can print a variety of solutions onto desired substrates in picolitre volumes via ultrasonic ejection of liquid. 'Ink' constitution and printing parameters have been optimized, and the effect of varying micropipette diameter investigated. Post–printing, water and glycerol from the ink are evaporated at low pressures and temperatures to produce ND coatings of near monolayer thickness in any desired pattern. Subsequent CVD growth leads to patterned NCD layers. This direct–write additive method allows for facile microfabrication of nanodiamond patterns on a variety of substrates and topographies, unlike photolithographic techniques, which are limited to planar surfaces and require corrosive chemicals. Finally, this method has minimal wastage of NDs and can efficiently coat substrates using very small ND amounts, which is very important for applications where sample amounts are scarce, such as the positioning of NDs with colour centres (e.g. nitrogen–vacancy centres) on substrates.

5.2 EXPERIMENTAL METHODS

Alice Taylor performed all experimental activities presented in this chapter.

5.2.1 SELECTIVE PRINTING

A GIX II Microplotter (purchased from www.sonoplot.com) was used in ambient conditions for the selective seeding of ND inks. The microplotter is a computer–controlled micropipette fluid dispensing system for the deposition of picolitre volumes of liquid to 5μm precision. Liquids are drawn into the pipette from an ink well via capillary action and ejected via application of ultrasound to the pipette when in meniscal contact with a surface. The ultrasonic intensity is sufficiently low to avoid a spray ejection of liquid. The software programme SonoDraw was used to design the desired patterns in which the ink would be printed on the surface. An applied piezo-voltage of 20 V was used for every print as this was found produce the most reliable and consistent printing. Printing speeds were varied from 100 μm s^{-1} to 10000 μm s^{-1} depending on the substrate and tip; typically 2000 μm s^{-1} for silicon and 1000 μm s^{-1} for glass. Glass micropipettes were produced using a p-97 flaming/brown horizontal micropipette puller. Pulling parameters were optimised in order to produce a range of tips with inner diameters ranging between 1 μm to 30 μm.

5.2.2 CHEMICALS

Monodispersed detonation nanodiamonds (DNDs) (6–10 nm) were used throughout (New Metals & Chemicals Corporation, Japan). Various inks containing DNDs and glycerol (99.0% Sigma Aldrich, MW: 92.09 $gmol^{-1}$, 1414 cP) were produced and subjected to ultra-high power sonication using a VCX500 Vibra-cell sonicator with the cup horn accessory (100% amplitude, 3:2 duty cycle, water cooled and temperature controlled to be <28˚C, 5 hrs) to fully disperse the DNDs and to ensure a thorough glycerol / de–ionised water mix.

5.2.3 SUBSTRATE CLEANING

Substrates were degreased in acetone, IPA and then DI water (each for 5 mins sonication), to remove residues and dirt. Dust free surfaces allow for higher resolution printing, with reduced flow-back and also reduced contamination of particulates in the clean ND ink. With contamination, the NCD film quality suffers, as these particles act as re–nucleation sites and so the film contains more grain boundaries, and so all substrates are thoroughly cleaned before use.

5.2.4 INK EVAPORATION

A vacuum chamber (10^{-3} mbar, 50°C, 5mins) was used to evaporate the glycerol / de-ionised water ink and leave the printed NDs in the desired pattern on the surface of the substrate. Vacuum evaporation was used to allow glycerol evaporation at low temperatures as to not oxidise NDs through heating (oxidation onset ~ 250˚C). The boiling point of glycerol at 10^{-3} mbar is 40°C, and so a temperature of 50°C was used to ensure all glycerol had evaporated. In order to obtain a regular seeding of NDs on the surface, it is important that a quick evaporation of the ink is done. This helps to minimise the 'coffee-ring' effect, by where the ink dries towards the edge of the print, leaving a higher concentration of NDs around the ring.

5.2.5 ATOMIC FORCE MICROSCOPY

AFM measurements were carried out using a Veeco Dimension V using aluminium coated silicon AFM probes (resonant frequency 190 kHz). The system was operated in tapping mode with a VT-103-3K Acoustic/ Vibration Isolation System and the VT-102 Vibration Isolation Table at room temperature in air. AFM analysis was performed on ND patterns of varying ND concentrations, post–evaporation, with a scan size of 2 μm. AFM Images were post–processed with a median filter (3x3 kernel) using MATLAB 2012a software to remove noise and measurement artefacts. Surface coverage of NDs as a percentage was calculated using the threshold feature on ImageJ software.

5.2.6 PATTERNED NANOCRYSTALLINE DIAMOND GROWTH

Nanodiamond micro-patterns were printed on degreased Si (native oxide), SiO_2 (PECVD) and quartz wafers (5 mins acetone, 5 mins isopropanol alcohol, 5 mins deionised water with low power ultrasonication and N_2 gun drying). Print patterns were drawn on Sonodraw 1.1.3 software. Following ink evaporation, Microwave-plasma enhanced CVD (MPECVD) was performed using a SEKI Model AX5010 PECVD reactor. The parameters for growth were: 1500 W, 200 sccm H_2, 1.4 sccm CH_4 (0.7%), with 30 min and 4 hr growth times and a 5 minute 5% CH_4 initial incubation period.

5.2.7 SCANNING ELECTRON MICROSCOPY

Both the glass micropipettes and the NCD patterns were characterised using a Carl Zeiss XB1540 focussed-ion-beam microscope with an accelerating voltage of 5kV.

5.3 RESULTS AND DISCUSSION

5.3.1 OPTIMISING INK DEPOSITION

In order to achieve consistent and contiguous liquid deposition from a microplotter, optimisation of ink viscosity is essential. Various inks were prepared containing varying ratios of glycerol and de-ionised (DI) water and dynamic viscosities were calculated using the parameterisation stated by Cheng (2008) [227] . The viscosity of glycerol at 20°C is much greater than water (1414 cP compared to 1.75 cP), the optimum viscosity for printing was found to be a mixture of 50% volume glycerol, 50% de-ionised water (4.83 cP), as illustrated in (Figure 5.1 a), with the values for the dynamic velocity of the ink plotted in (Figure 5.1 b). This ink had a low enough viscosity to allow effective flows from the tip, high enough to prevent reflow and clumping of the ink at pattern vertices.

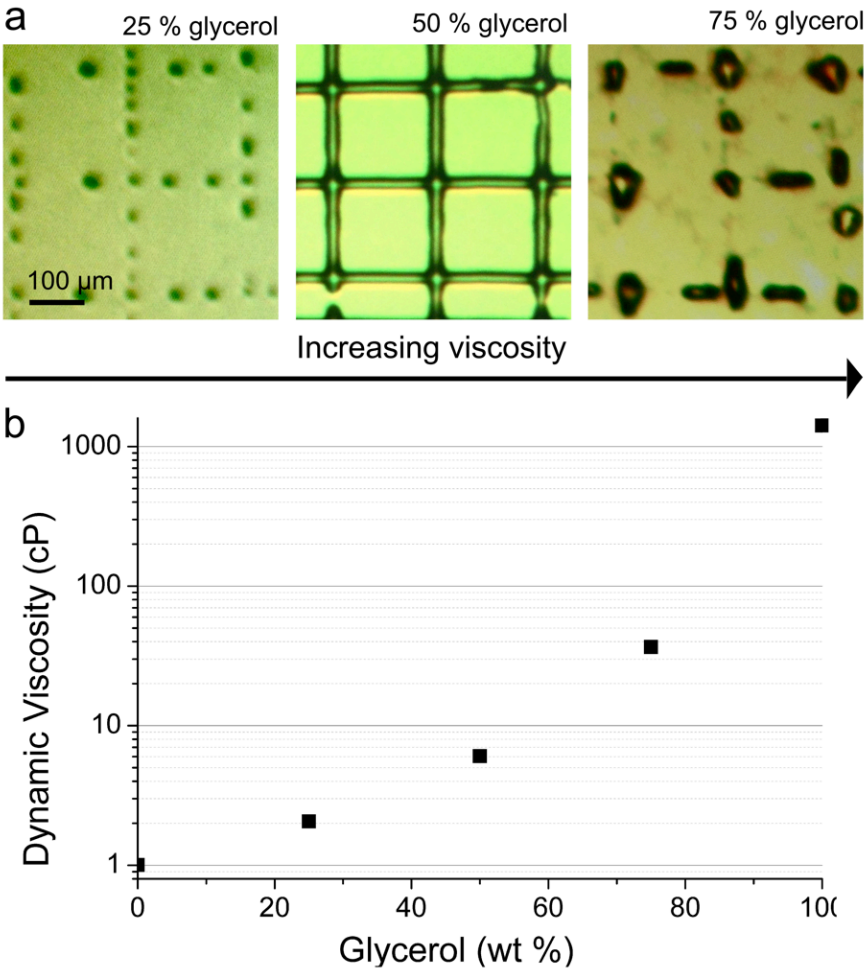

Figure 5.1 (a) Optical microscope images of grids printed using ND containing inks on a glass substrate. The three images are varying in glycerol percentage with it increasing from left to right. Optimum printing is observed using an ink containing 50 % glycerol. (b) The viscosity of the solution is calculated in related to the percentage weight of glycerol. Optimum viscosity was found to be 6.04 cP.

In addition to improving print quality, glycerol reduces the evaporation rate of water due to the increase in intermolecular forces, which avoids the premature evaporation of ink and the uneven deposition of NDs biased towards the edges of features where evaporation concludes, i.e. the ‘coffee–ring” effect. Whilst glycerol reduces premature evaporation of the ink, the boiling point of glycerol at room pressure is 290°C, such temperatures could cause substrate damage and there

have been reports of ND oxidation occurring at temperatures as low as 300°C [228] , which might lead to surface modification. Hence a custom vacuum chamber was built to enable the use of a lower vapour pressure of glycerol. A pressure of below 10^{-3} mbar was used to allow the evaporation of glycerol at 50˚C, being sufficiently low to avoid chemical modification of the NDs.

5.3.2 NANODIAMOND CONCENTRATION

Having established an optimum ink viscosity, the effect of changing concentration of the NDs was investigated. In order to grow high quality NCD patterns it is important that the ND assembly on the surface coverage is as confluent and as close to monolayer as possible, as small particles (rather than aggregates) results in better uniformity of the film [229]. Therefore it was important to ascertain which ND concentration produced confluent ND seeding and near monolayer coverage, as to optimise subsequent NCD film growth and minimise ND usage. The effect of ND concentration on seeding was investigated using AFM.

(Figure 5.2 a) shows AFM images of NDs seeded on silicon using a 30 µm tip and dot printing, with inks printed in concentrations of NDs ranging from 0.025 to 0.15 gL^{-1}, following glycerol-DI water evaporation. The corresponding graph, (Figure 5.2 b), shows the percentage coverage of the surface in relation to the ND concentration. It can be seen that for concentrations of 0.1 gL^{-1} and above, the coverage is 100%. For concentrations less than 0.1 gL^{-1} coverage is incomplete, for example, at 0.75 gL^{-1} coverage was 82%. The monolayer-type coverage observed shows evidence of the occasional small aggregate being present in the printed region, this is better than other reported attempts at printing ND patterns. For example, Zhuang *et al.* used a microcontact printing technique for producing ND patterns and the method was reported to only able to transfer ND agglomerates, and not individual ND particles [224]. As NCD quality is dependent on the size of the seed material and its uniformity, the method described here offers the prospect of better, denser, NCD films.

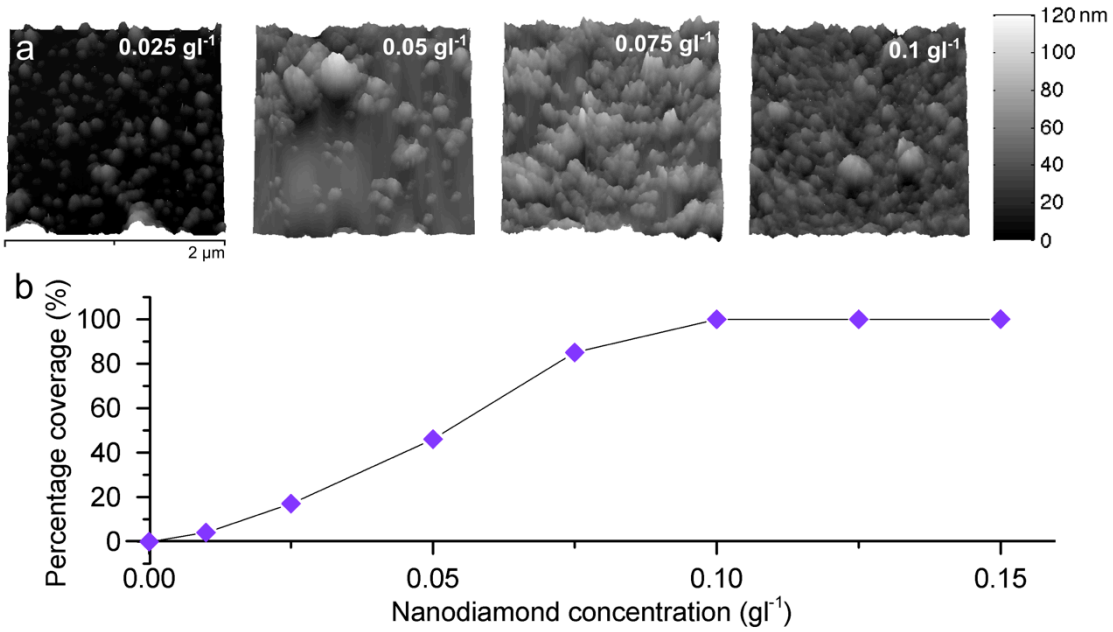

Figure 5.2 (a) 2 µm square AFM images of NDs seeded on silicon, each image is of NDs after evaporation of a glycerol de-ionised water ink, the resultant NDs are left seeded on the surface in varying coverage dependent on the concentration of NDs in the ink, concentrations shows are 0.025 gl^{-1}, 0.05 gl^{-1}, 0.075 gl^{-1}, 0.1 gl^{-1}. Scans are representative of the whole patterned area and were selected at random over each print. (b) Corresponding percentage coverage of NDs on Si in relation to concentration of NDs in the ink.

5.3.3 PATTERNED NANOCRYSTALLINE DIAMOND

(Figure 5.3) shows SEM images of CVD grown patterned NCD on silicon substrates with the ND seeds printed with a 0.1 gL^{-1} ND 50% wt glycerol / DI water ink. The ND patterns were grown for 30 minutes – 4 hours (see figure captions for duration) using previously stated conditions. (Figure 5.3 a) shows an array of lines printed using a tip with an inner diameter (ID) of 5µm, the lines are 200 µm spaced and their width is approx. 7µm. Consistent and clean printed lines are observed with a high level of pattern compliance and no residual NDs in void pattern regions. (Figure 5.3 b + c) show lines printed on Si using a 5 µm ID tip. It can be seen that the edge (Figure 5.3 d) of the lines are clean and no additional processes are needed for the removal of unwanted NCD. (Figure 5.3 e) The edge of a printed grid showing two intersecting lines, tip size 5 µm ID. (Figure 5.3 f) shows NCD printed with a void square in the middle, sharp lines and corners are

observed, highlighting the high resolution of the printing method. (Figure 5.3 g) shows the thinnest line achieved using this printing method, the line width is approximately 2 μm and was printed using a tip with an ID of 1.5 μm. (Figure 5.3 h) shows a 100 μm spaced array of printed NCD dots. (Figure 5.3 i) shows one printed dot, with a diameter of approximately 20 μm, which was achieved using a tip with an ID of 15 μm. (Figure 5.3 j) shows the edge of the printed dot shown in (Figure 5.3 i), clean printed edges are observed. The resolution of printing is limited to the mechanical movement of the machine, which has a 5 μm positioning resolution, and also to ID size of the pipette and ultrasonic power of the piezoelectric. Printed line artefacts are due to the slightly uneven motion of the tip during the print, but can be minimised by securing the substrate whilst printing and altering the speed of the print accordingly. SonoDraw 1.1.3 software allows for the patterning of lines, dots, arcs and filled regions, so any desired shape can be printed using this method. (Figure 5.3 k) SEM shows high quality NCD, verified by the faceted texture of the NCD film, as well as the confluent, pinhole–free nature of the film, all of which can be ascribed to high–density, homogenous seeding. (Figure 5.3 l) was grown from a printed region where the ND concentration in the ink was 0.001 gl^{-1}; this resulted in an individual ND being grown into a small (~500 nm) single crystal diamond. This capability is also of considerable interest since individually placed fluorescent NDs are key to several quantum information processing applications that are currently under investigation.

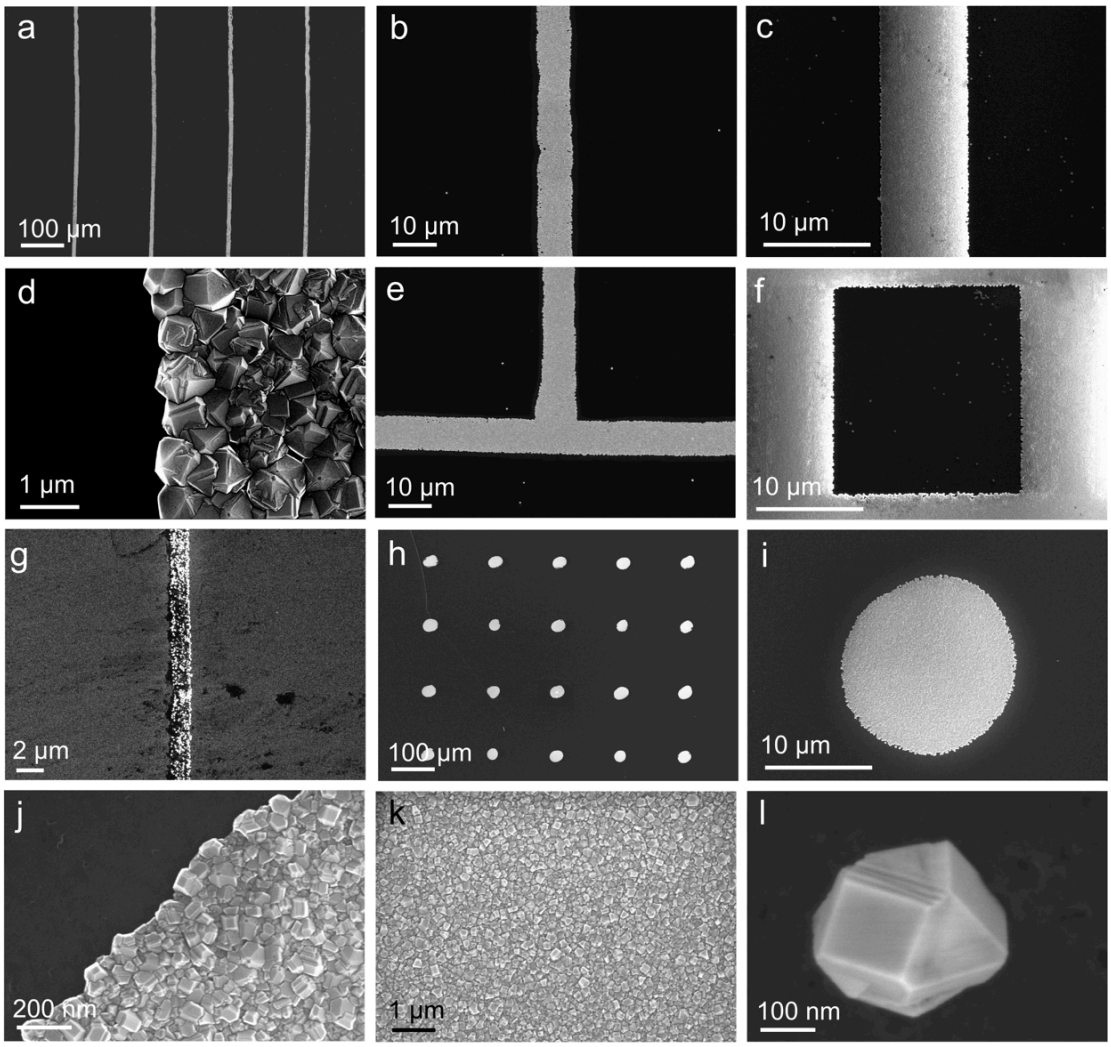

Figure 5.3 SEM images of patterned NCD which have been grown on silicon substrates using printed NDs as the seed and MWPECVD for the growth, all inks consisting of 50% wt glycerol and NDs at a concentration of 0.1 gl^{-1}, growth times varied from 30 minutes – 4 hours, 1500 W, 50 torr and 0.7 % CH_4. (a–c) A series of lines printed using a 5 µm ID tip, line width approx. 7 µm. Growth for 30 minutes. (d) The edge of the printed line shown in (c). (e) The edge of a printed grid showing two intersecting lines, tip size 5 µm ID, growth for 30 minutes. (f) NCD outline of square grown for 4 hours. (g) Line printed using 1.5 µm ID pipette, line width ≈ 2 µm. Grown for 30 minutes. (h) An array of dots printed using a 15 µm ID tip, grown for 1 hour. (i) An individual printed NCD dot from (h). (j) Edge of printed dot shown in (i). (k) Zoomed in SEM of the surface of a printed NCD region after 30 minute growth. (l) An ND seed grown into an individual NCD grain grown for 4 hours.

5.3.4 TIP DIAMETER VS. DOT DIAMETER

In order to investigate the effect of ID on dot deposition, a set of tips with varying diameter were prepared for printing. Different sized tips were pulled using a horizontal micropipette puller, whereby controlling the speed of the tip pull changes the ID. The ID of tips ranged from 1 to 30 μm. (Figure 5.4 a – d) show different tips of graded diameters alongside SEM images of their corresponding NCD dots on Si surfaces. All ND dots were subject to 30 mins growth using normal NCD conditions as previously stated. The minimum size of micropipette that can successfully print is 1.5 μm. When attempting to print smaller than this, ink did not enter the micropipette due to capillary action failing to load the pipette. (Figure 5.4 e) shows the relationship between tip ID and NCD dot diameter (DD). The relationship is approximately linear, where the printed dot is slightly larger than the tip ID ($DD \approx 3.15 + 1.40ID$). For a 30 μm tip, the dot is roughly 45 μm and so an ink spreading of ca. 40% is observed. Micropipettes with an inner diameter of 30 μm were found to produce the most consistent printing.

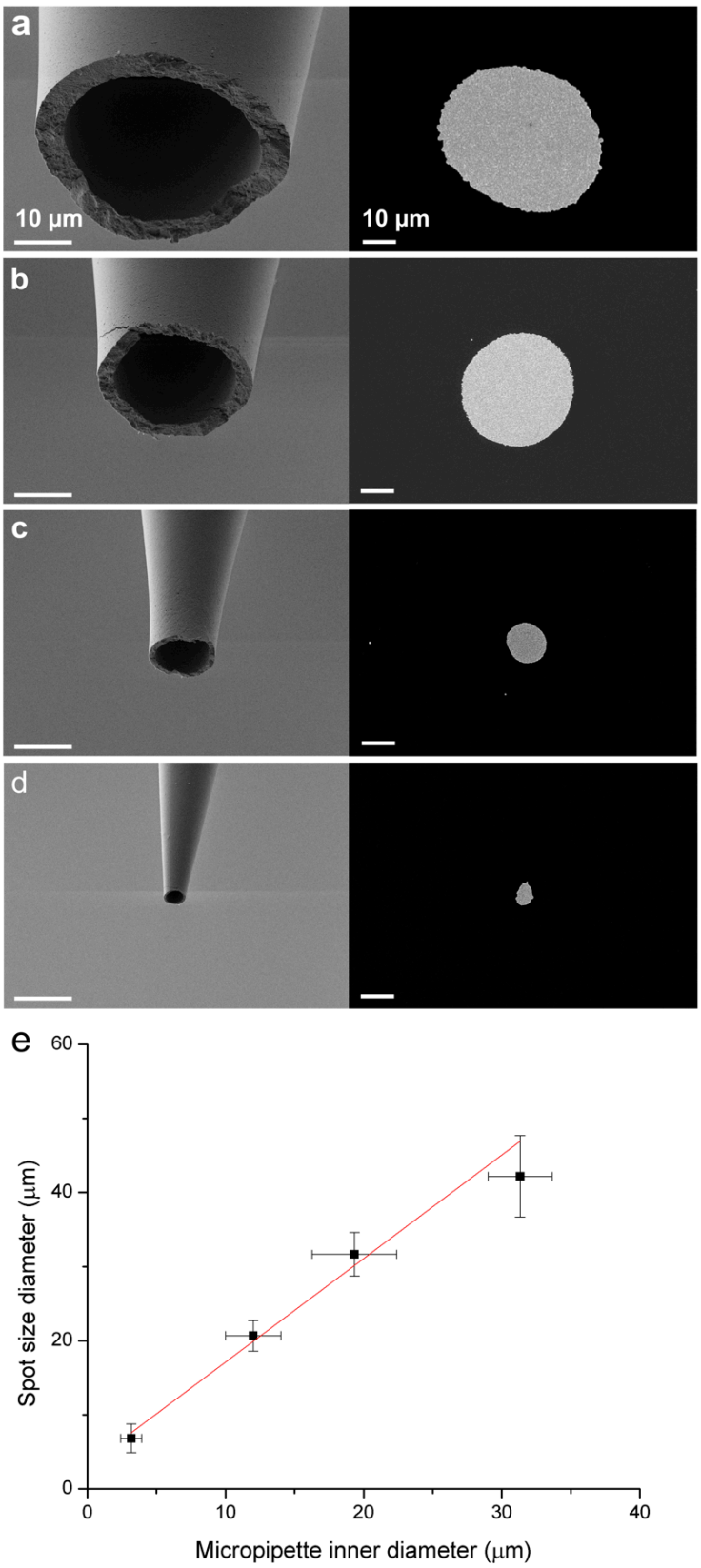

Figure 5.4 (a–d) SEM images of horizontally pulled glass micro-pipettes (left hand column) and the corresponding printed ND dot, which has been grown into

NCD (right hand column). Velocity of the pull was altered to produce micro-pipettes with the desired inner diameter. The velocity is in an arbitrary unit, but range from a) 8 a.u. to d) 14 a.u, producing tips with an inner diameter of around 40 µm to 5 µm respectively. (A tip with an ID of 1.5 µm has been pulled but SEM is not available). (e) Corresponding graph showing how the micropipette inner diameter affects the diameter of the NCD dot.

5.3.5 NANOCRYSTALLINE DIAMOND CHARACTERISATION

NCD quality was investigated by SEM and Raman spectroscopy. One of the most important factors in determining the quality of thin film diamond is surface roughness. The seeding quality and density of the nanodiamonds is paramount to this [76]. Various scratching and seeding techniques have been used to enhance ND nucleation density on foreign substrates. Scratching often results in a high nucleation density because the large diamond particles are imperfect and thus chip along grain boundaries leaving smaller diamond particles on the surface, which act as the nucleation site [230]. In order to obtain ND near–monolayer patterns it is important to sonicate the ink immediately before printing, this ensures that the NDs are fully dispersed in solution, and as few as possible aggregates are present. Best results were achieved when ND inks were sonicated for at least 8 hours immediately before printing. Nicely faceted NCD (4 hour growth) can be seen using SEM in (Figure 5.3 e), confirming the quality of the ND seeding.

The Raman spectra for the NCD grown can be seen in (figure 5.5), the diamond peak is observed at 1333 cm^{-1} for the 30 min growth, and 1329 cm^{-1} for the 4 hour growth. This peak corresponds to the zero–phonon line of diamond, indicative of a high content of sp^3–bonded carbon. Peak broadening can be observed in the sp^3 peak for the 30 min growth due to the low crystallite size of diamond grains and the thinness of the film [231]. and the redshift of the peak arises in phonon confinement in the NCD and is linear with grain size [232]. The narrowing of this peak at 4 hours growth suggest that the film grain size is approaching the micro-scale. The broad peak observed at 1560 cm^{-1} in the 30 min growth spectrum shows evidence of the non-diamond G-band, which arises from sp^2 carbon in-plane stretching mode, which can be assumed to be at the grain boundaries [233].

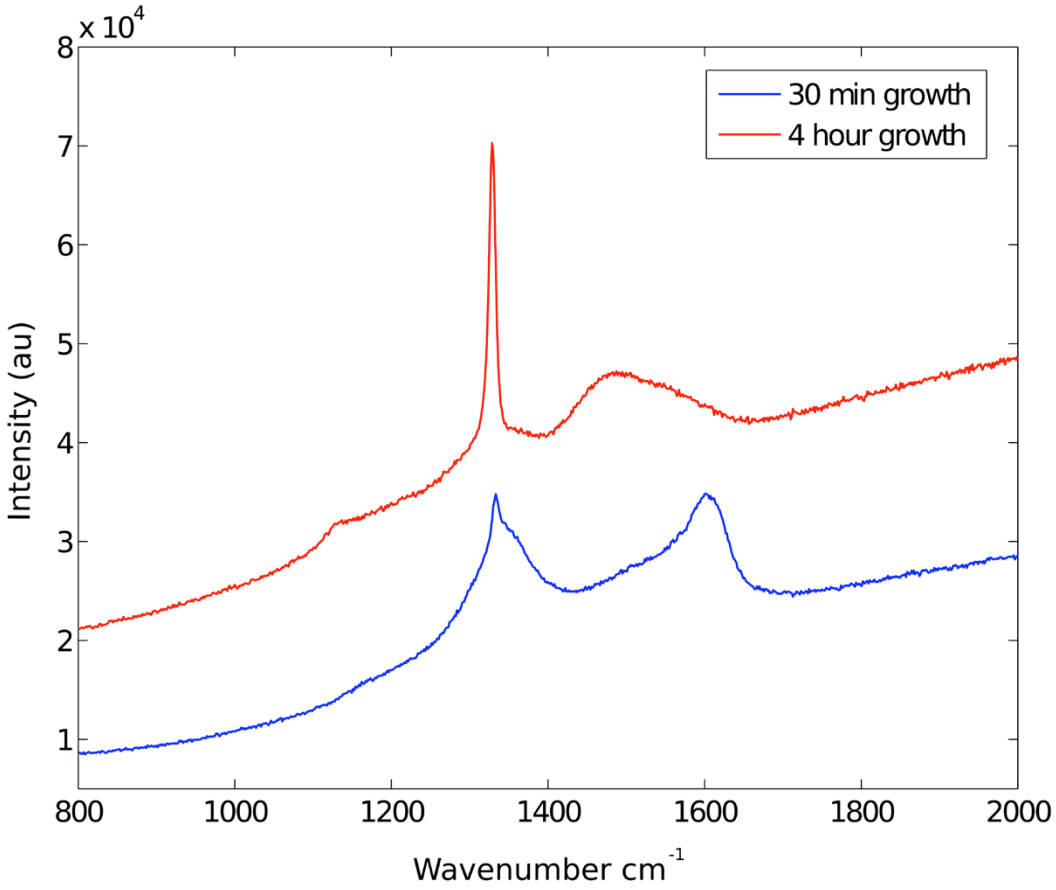

Figure 5.5 Raman spectra of NCD dots grown for 30 mins and 4 hours, both spectra showing the zero-phonon line for present in diamond thin films.

5.4 CONCLUSIONS

An additive, lithography–free, inert bottom-up technique for producing nanodiamond tracks and nanocrystalline diamond patterns with a high pattern compliance has been established, with a lateral resolution of 5μm and feature widths of ca. 2 μm. Patterning is achieved without the use of reactive chemicals, allowing for the preservation of ND surface chemistry. The patterning procedure has been developed using ultrasound driven plotter to deposit nanodiamond and glycerol / DI water inks. Printing has been optimised by tailoring ink constitution, hardware parameters and micropipette tip diameter to produce ND patterns with near–monolayer coatings with few agglomerates present. The effect of varying ND concentration upon ND seeding has been studied, and the relationship between tip diameter and dot size identified. Furthermore, low density ND patterning is demonstrated, which makes this process a valuable method for studying the individual properties of NDs on substrates, for example for quantum information processing applications. Post–printing, ink solvents are evaporated off using a low temperature vacuum evaporation to leave NDs in the desired pattern. The resultant ND patterns have been used as the nucleation site for NCD growth, and suspending the NDs in glycerol has no observable effects in the quality of the diamond film. Pertinently, this patterning technique allows for the selective seeding of NDs on a variety of substrates, including 3D substrates not compatible with conventional lithography techniques, and with a high degree of control over the nature of the ND monolayers deposited. This method for diamond patterning provides a material type that has lots of potential applications, which range from the use as a photonic crystal [234], to the use in bioelectronics [235] and MEMS applications including piezoelectric micro-resonators [236].

CHAPTER 6 – BIOCOMPATIBILITY OF NANOSTRUCTURED BORON DOPED DIAMOND FOR THE ATTACHMENT AND PROLIFERATION OF HUMAN NEURAL STEM CELLS

6.1 INTRODUCTION

Diamond is a material with extreme physical, chemical and electrical properties [24], it is inert [201], robust and has high longevity. Nanocrystalline diamond films (NCD) produced by chemical vapour deposition (CVD) displays very similar properties [202]. The passive chemical nature and the desirable tuneable electrical properties of diamond, including its wide electrochemical window make it a highly desirable material for many bio-applications, specifically for interfacing with electrical cells as electrodes. The main hindrance of using planar films of diamond as an electrode material is the relatively low capacitance values obtained; an ideal electrode material has a high capacitance and this can be increased in diamond by increasing the surface area of the electrode. This has been achieved via seeding nanodiamonds on carbon nanotubes (CNTs) [301] and thus nanostructuring the diamond films; such films have shown excellent electrical properties. Here, these substrates have been investigated to see if the inclusion of boron and the effect of increased surface area via the nanostructuring has any observable outcome on the biocompatibility of the diamond.

The superlative electrical properties of boron-doped diamond (BDD) make it a desired material of choice for many neural interface applications. BDD can be either p-type [237-239] in character or quasi-metallic at high boron concentrations ($>10^{20}$ cm^{-3}) [52,240,241]. In its quasi-metallic state it is a desirable choice of material for bio–electrochemical electrodes due to its chemical inertness [242], high structural stability at desired current charge densities [243] and low background current [244,245] compared to metal electrodes [246], both *in vivo* [247] and *in vitro* [248]. Moreover, the so-called electrochemical window of boron doped diamond electrodes, the voltage that can be applied before the onset of unwanted water redox reactions, is considerably higher than electrodes made for

metals or other forms of carbon [249]. Boron doped nanocrystalline diamond (BNCD) has also been used for bio–sensing, with H-terminated BNCD being used for the sensing of DNA [250,251] and glucose [252], and O-terminated BNCD for sensing dopamine [253] and uric acid [254]. BNCD has been used material of choice for the fabrication of diamond microelectrode arrays (MEAs) [210,211,216,255], in particular Piret et al. fabricated 3D-nanostructured BNCD MEAs with low level detection of neural activity, electrodes had a wide potential window and storage capacitance of 10 $mC.cm^{-2}$ [165]. BNCD is also a highly desirable material for neural prostheses and neural interfaces [256-258], as well as being used as a successful electrode material for neural stimulation [259].

For a material to be successful as a neural interface, it has to be both electrically active and biocompatible. The biocompatibility of un-doped CVD diamond, including NCD, has been investigated by cell viability and protein absorption methods, with most studies indicating that diamond is highly biocompatible [42,204,260]. Boron doped diamond offers properties required for many cell interfacing applications, including the recording of action potentials from electrogenic cells [216]. To date, the biocompatibility of BNCD materials, where the boron concentration is as high as $10^{21}\,cm^{-3}$ has not been explored, that is the subject of this study. Of particular note is the use of vertically aligned carbon nanotubes (CNTs) attached to substrates and subsequently overgrown with BNCD. This leads to a 3D structured BNCD material that can act as a scaffold for cellular attachment and outgrowth, and the biocompatibility of these novel 3D structures has also been explored. Planar thin films of BNCD can suffer from a relatively low double layer capacitance, and high impedance, reducing such electrodes performance for cell stimulation despite the attractive biocompatibility, 3D nanostructuring offers the prospect of overcoming this limitation.

The biocompatibility of diamond initiated a lot of work in which cells are grown on diamond, first reports of this occurred in 2004 by Specht *et al*. [167]; where neurons were successfully grown on single crystal diamond, and since this numerous reports have shown NCD positively supporting the adhesion and proliferation of many cell lines including osteoblasts [261-263], fibroblasts [264] and mesenchymal stem cells [265]. Patterned NCD films and nanodiamond layers have also been shown to direct neural adhesion and neurite outgrowth [42,73,266]. Here, the degree of human-neural stem cell (hNSC) adhesion and proliferation on diamond materials with these extreme levels of boron incorporation has been investigated via live cell staining using 5-

chloromethylfluorescein diacetate (CMFDA); a live cell fluorescent marker, along with the use of a methylene blue assay. hNSCs have been used for this biocompatibility study due to their sensitivity and highly responsive behaviour to external stimuli; this is in contrast to robust cancerous cells.

6.2 METHODS

Clement Hebert, CEA, performed diamond growth and Barbora Vagaska, UCL, plated and characterised hNSCs. Alice Taylor performed all other experimental activities and analysis presented in this chapter.

6.2.1 NCD AND BNCD GROWTH

Nanocrystalline diamond (NCD) films were grown on silicon substrates; growth was performed at CEA, by Clement Hebert. Prior to growth the Si substrates were seeded with diamond nanoparticles by spin coating. High Pressure High Temperature (HPHT) diamond nanoparticles with diameter approx. 25 nm (0.1% wt/wt, SYP GAF 0-0.05, Van Moppes) were dispersed in water (0.1% wt). The substrates were seeded by spin coating (2000 rpm for 20 s) and dried in N_2 gas (as previously reported by Girard et al.) [44]. NCD was grown in an AX6500X Microwave Plasma Enhanced Chemical Vapour Deposition (MPECVD) system (Seki Technotron Corp.). The growth was performed for 10 hours using the following parameters: MW power of 2.6 kW, pressure of 26 mbar, temperature of 650˚C, H_2 flow of 400 sccm, CH_4 flow of 4 sccm. Boron doped nanocrystalline diamond (BNCD) films were grown using these same growth parameters except trimethylborane (TMB, $B(CH_3)_3$) was added to the gas phase (2.4%TMB in CH_4). Such conditions lead to BNCD with a boron concentration of ca. 2 x 1021 cm-3, as described by Vanhove et al. [244]. NCD and BNCD surfaces were oxygenated using an ozone treatment (50mbar) for two hours, at 200˚C.

6.2.2 FABRICATION OF BNCD COATED CNTS

Vertically aligned CNTs (VACNTs) were deposited onto BNCD layers, prepared as described above. First, a 7 nm nickel layer was deposited on the diamond surface by e-beam evaporation and the sintered into ~50nm nanoparticles by

heating at 700°C for 3 minutes. The samples were then transferred into a plasma enhanced CVD reactor, ("Black Magic" AIXTRON) whereby the sintered nickel particles act as the catalyst site in which VACNTs are grown. CNTs of differing length were deposited by varying growth times; 1 μm and 2 μm for growths of 5 and 11 minutes respectively. The VACNTs were then coated with NDs via an electrostatic grafting method described by Girard *et al*. [267]. This step transforms the VACNTs into bundles of CNTs with densities of 9 and 4 bundles/μm^2 for CNTs of length 1 μm and 2 μm respectively. Finally, BNCD was grown in a MWPECVD (AX6500X) reactor until a BNCD thin film coating of ~50 nm was obtained upon the bundles. Boron incorporation was also optimised up to 2 x 10^{21} cm^{-3}. BNCD coated CNT surfaces were oxygenated using an ozone treatment as described above.

6.2.3 Atomic Force Microscopy

Atomic force microscopy (AFM) measurements were carried out using a Veeco Dimension V instrument with aluminum-coated silicon AFM probes (resonant frequency 190 kHz). The system was operated in tapping mode with a VT-103-3K acoustic/vibration isolation system and a VT-102 vibration isolation table at room temperature in air. AFM was performed on Tissue Culture Polystyrene (TCPS) and on NCD and BNCD films. Scan sizes of 2 μm for the TCPS and 5 μm for the NCD and BNCD films were taken and an arithmetic average of the roughness profile (R_a) was calculated using Nanoscope Software 6.1.3. AFM Images were post processed with a median filter (3 × 3 kernel) using MATLAB 2012a software to remove noise and measurement artifacts.

6.2.4 Scanning Electron Microscopy

The BNCD covered CNT bundles were characterized using a Carl Zeiss XB1540 focused-ion-beam microscope with an accelerating voltage of 5 kV, these images were used to calculate bundle density.

6.2.5 HUMAN NEURAL STEM CELLS (HNSCS) ISOLATION AND CULTURE

All procedures involving human tissue were carried out in accordance with the UKs Human Tissue Act 2006. The preparation of neural cell cultures was performed in close collaboration with the Developmental Biology Unit, Institute of Child Health, UCL by Barbora Vagaska.

The hNSCs were isolated and expanded according to the protocol described previously by Sun *et al*. [194]. Briefly, hindbrains from human embryos between 6–10 weeks old were collected through Human Developmental Biology Resource (HDBR) and dissected in cold Neurobasal medium (Gibco). After complete removal of the meninges and blood vessels, the tissue was chopped into smaller pieces and digested in Accutase (Gibco) solution at 37°C for 30 mins with occasional trituration to obtain single cell suspension. Cells were then centrifuged and re-suspended in growth medium composed of DMEM/F12 with Glutamax supplemented with 1% (v/v) Penicillin/Streptomycin, 1% (v/v) 100x N2 supplement, 2% (v/v) 50x B27 supplement (all Gibco), 20 ng/ml human recombinant FGF2, 20 ng/ml human recombinant EGF (both Peprotech), 50 µg/ml BSA fraction V and 5 µg/ml Heparin (both Sigma). Cells were plated on polylysine/laminin (10 µg/ml, Sigma) – coated dishes and grown for 7 days *in vitro* with the media changed every 2 days to remove any dead cells or debris. To eliminate neurons from the primary cultures and get a homogenous culture of neural stem cells, the cells were first transferred onto 0.1% (w/v) bovine gelatine (Sigma) –coated dishes for 7 days to form neurospheres, which were then re–plated onto laminin–coated dishes for further expansion. For routine expansion and further experiments, cells were grown in growth media supplemented with laminin instead of coating the dishes. Passages up to 30 were used for all experiments.

6.2.6 IMMUNOCYTOCHEMISTRY CHARACTERISATION OF HNSCS

For immunocytochemistry hNSCs were seeded either on poly-L-lysine/laminin coated glass cover slips or 8 well imaging chamber slides (PAA). The cells were fixed with 4% (w/v) paraformaldehyde (PFA) solution in PBS, pH=7.4 for 15 min at RT. After three rinses with PBS the cells were incubated with blocking solution composed of 10% (v/v) FBS, 3% (w/v) BSA in PBS with 0.2% (v/v) TritonX-100 for 1h at RT to permeabilize cell membranes. Primary and secondary antibodies

were diluted in blocking solution and the incubation times were overnight at 4°C for primary, and 1h at RT for secondary antibodies. Hoechst 33258 (2µg/ml) was added during secondary antibody incubation to counterstain cell nuclei. After final three washes in PBS the coverslips were mounted on slides with an aqueous based mounting medium (Hydromount, National Diagnostics). Primary and secondary antibodies used can be seen in the Table 6.1.

6.2.7 INDUCED HNSC DIFFERENTIATION

The controlled differentiation of hNSCs into astrocytes, oligodendrocytes and neurons has been adapted from Sun *et als.* Protocol, described in [45].

To induce astrocytic differentiation of hNSCs, the cells were cultured in media composed of DMEM/F12 medium, supplemented with 1% Penicillin /Streptomycin and 10% FBS for 2 weeks.

For neuronal differentiation hNSC were plated on laminin-coated plates in expansion medium without EGF supplement to induce differentiation. After 10 days in culture, FGF2 and heparin were also withdrawn from the media for another 4 days. Finally, neuron maturation was then induced by culturing in Neurobasal A medium supplemented with 1% Penicillin/Streptomycin, 1% L-Glutamine, 2% B27 and 10 ng/ml human recombinant βNGF with 10ng/ml human recombinant BDNF (both Peprotech) for another 2 weeks.

For oligodendrocytic differentiation cells were plated on laminin coated plates. The next day, the medium was changed to DMEM/F12 supplemented with 1% Penicillin/Streptomycin, 1% N2 supplement, 10 nM forskolin, 10ng/ml FGF2 and 10ng/ml PDGFaa (Peprotech) for 14 days. On day 15 the medium was switched to DMEM/F12 supplemented with 1% Penicillin/Streptomycin, 1% N2 supplement, 30 ng/ml tri-iodothyronine (T3), 200 µM ascorbic acid and 10ng/ml PDGFaa. After another 7 days, PDGFaa was withdrawn from the culture media to allow maturation of cells. hNSC isolation, confirmation and differentiation potential extremely important as it allows for the development of cell based therapies to continue [46].

a) Primary antibody staining:

Name	Host	Company	Cat. Number
GFAP	Rabbit	Millipore	AB1540
Nestin	Rabbit	Millipore	ABD69
SOX2	Rabbit	Millipore	AB5603
BIII Tubulin	Mouse	Promega	G712A
Vimentin	Mouse	Dako	M0725
BLBP (FABP7)	Rabbit	Chemical Signalling	D8N3N
MAP2	Mouse	Life Technologies	13–1500
A2B5	Mouse	R&D Systems	MAB1416

b) Secondary antibody staining:

Name	Host	Conjugated Flurochrome	Company	Cat. Number
anti rabbit	Donkey	Alexa568	Molecular Probes	A–110042
anti mouse IgG	Rabbit	Alexa488	Molecular Probes	A–21202
anti mouse IgM	Mouse	Alexa594	Molecular Probes	A–21044

Table 6.1 (a) Primary Antibodies and (b) Secondary Antibodies used throughout for specific hNSC, neuronal, oligodendrocytic and astrocytic fluorescent staining.

6.2.8 CELL ATTACHMENT AND MORPHOLOGY ASSAY

Prior to cell seeding, substrates were treated with ozone in a vacuum chamber for 30 mins, (200°C, 50 mbar) in order to increase homogeneity of surface chemistry between samples. Substrates were then placed in 24 well tissue culture plates, sterilized for 30 mins in 70% ethanol and washed three times in sterile distilled water. hNSCs were then plated at a density of 3 x 10^4 cells/cm^2. Subconfluent hNSCs were labelled with the vital cytoplasmic dye, CMFDA (5-chloromethylfluorescein diacetate, Cell Tracker, Invitrogen) in supplement–free culture media at 5 μM final concentration for 30 mins. After the incubation, the cells were washed twice with phosphate buffer solution PBS, trypsinized and then plated on the different surfaces in the standard expansion media with laminin at a density of 3x10^4 cells/cm^2. Cell attachment and morphology were assessed after 24 hrs using an Olympus IX70 inverted fluorescent microscope for one sample per substrate type. For each sample, 6 randomly selected areas were imaged using monochromatic Hamamatsu – OrcaR2 camera/HCImage software at x10 and x40 magnification.

For actin staining hNSCs were fixed after 48 hours *in vitro* in 4% (w/v) paraformaldehyde in PBS (pH7.4) for 15 min and washed three times with PBS. Substrates were then incubated in blocking solution (10% fetal bovine serum, 3% bovine serum albumin in PBS with 0.2% Triton X100 for permeablization) for 30min at room temperature. Cells were stained with Phalloidin conjugated with Alexa Fluor® 488 diluted in blocking buffer (Invitrogen, 5U/ml) together with Hoechst 33258 (2μg/ml) to counterstain nuclei for 1 hour at room temperature. After 3 washes with PBS to remove excess dye the samples were imaged using an inverted microscope Olympus IX71 (Carl Zeiss, Jena, Germany) equipped with a Hamamatsu ORCA-ER digital camera (Hamamatsu Corp., Bridgewater, NJ) and image processing was done using Image J and Fiji.

Culture confluence for both Phalloidin and CMFDA stained images were calculated in Matlab R2012b by applying an intensity threshold to the stained images and taking the average of the percentage area of each image above threshold (at least 6 images at varying magnification for one sample per substrate). Intensity thresholds were selected for each image by calculating the intensity level corresponding to the minimum value of the derivative of the intensity histogram of each image. This corresponded to the intensity boundary between the background and the cells. A 0.03 factor was added to this factor to

improve mapping precision. Confluency was displayed using box plots, (Figure 6.3 b) and (Figure 6.4 b) Cell counts were obtained for the Hoechst stained images in Matlab R2012b by applying an intensity threshold to the stained images and then using a find circular Hough transform to find the number of labelled nuclei per image, which was then scaled up accordingly (at least 6 images at varying magnification for one sample per substrate).

6.2.9 METHYLENE BLUE ASSAY (MB)

Cell viability of hNSCs was assessed by the methylene blue assay, which is a spectrophotochemically quantitative method for obtaining healthy cell counts [268]. Cell viability has been compared on NCD and BNCD using tissue culture polystyrene (TCPS) as the control throughout. hNSCs were plated on sterilized samples (3 samples per substrate) in 48 well plates, at a density of $3x10^4$ cells/cm^2. After 48 hrs in culture cells were fixed in 4% (w/v) paraformaldehyde in PBS (pH 7.4) for 15 mins, washed once with PBS and incubated with 1% (w/v) methylene blue in 0.01 M borate buffer (pH 8.5) solution at room temperature for 30 mins. Excess methylene blue in each well was washed off with 0.01 M borate buffer. The samples were then transferred to new wells and the dye was eluted in 1:1 (v/v) ethanol and 0.1 M HCl. The plates were gently shaken, then 100 µl of solution from each well were transferred to a 96 well plate and the absorbance was measured at 650 nm by a spectrophotometer (Revelation v4.21 Dynex Technologies, inc). The absorbance measurements were then normalized to the surface area of the samples and compared to cells grown in standard tissue culture polystyrene (TCPS).

6.3 RESULTS

6.3.1 SUBSTRATE CHARACTERIZATION

(Figure 6.1) shows the surface topography of substrates used throughout this investigation. (Figure 6.1 a) shows AFM images of NCD, BNCD and tissue culture polystyrene (TCPS) substrates accompanied by the root mean square (RMS) roughness for each substrate. The roughness of the NCD and BNCD is much grater than that of the TCPS, (being 85 nm and 38 nm respectively, vs. 3 nm). SEM has been used to show the structure of the BNCD CNT bundles, and (Figure 6.1 b) shows how the difference in length of the CNT alters the density of the bundles formed on the substrate. For CNTs of 1 μm length, the concentration of bundles is 9 μm^{-2} and for 2 μm long CNTs this decreases to an average of ca. 4 μm^{-2}.

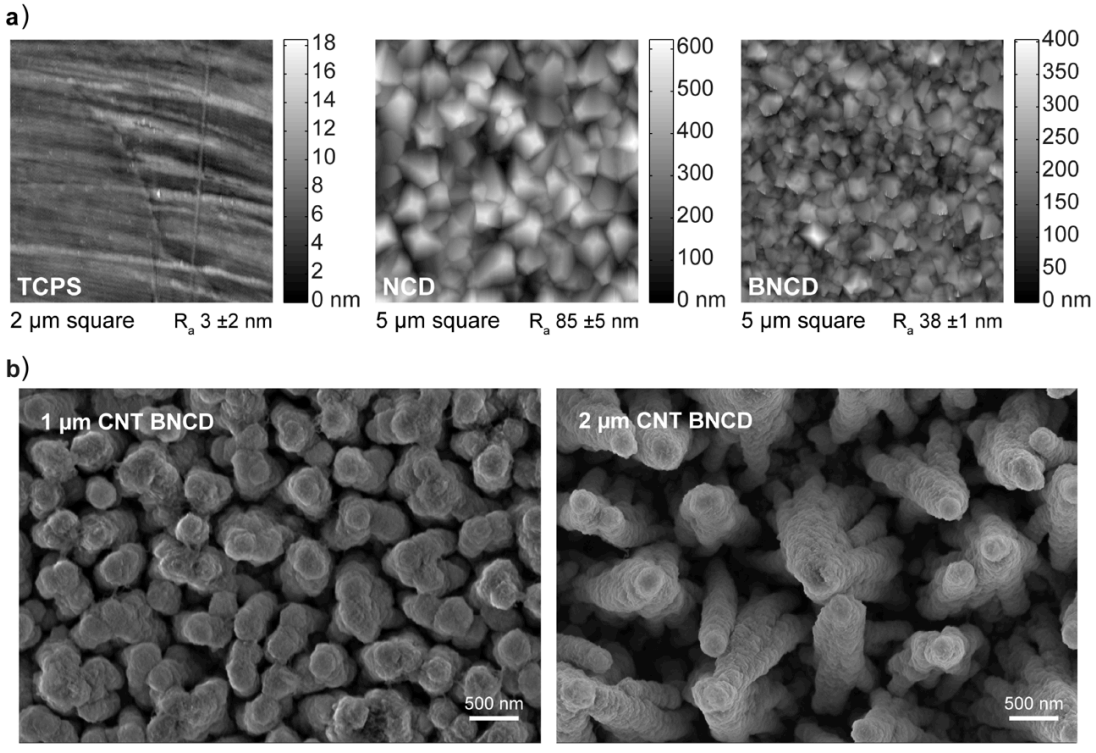

Figure 6.1 (a) From left to right: 2 μm square atomic force microscopy (AFM) scan of TCPS, and 5 μm square scans for both NCD and BNCD films. Ra: average roughness. Approximate values given, averaged over 3 AFM scans (b) Scanning electron microscopy (SEM) images of 1 μm and 2 μm CNT BCND nanostructures. 1 μm CNT BNCD has ca. 9 bundles/μm^2. 2 μm CNT BNCD has 4 bundles/μm^{-2}. Scale bar 500 nm. 5kV acceleration voltage.

6.3.2 CHARACTERISATION OF THE ISOLATED HNSCS

hNSCs have been isolated from human embryos aged between 6 – 10 weeks. Characterisation and confirmation of these cells has been summarised in (Figure 6.2), shows both the isolated hNSCs and the differentiation potential of cells from the same isolated batch. hNSCs have been successfully differentiated into neurons, astrocytes and oligodendrocytes, hereby proving the classification of the cells. Numerous NSC fluorescent markers have been used to clarify the identity of the isolated cells, including Nestin, GFAP, SOX2, Vimentin, TUBB3 and BLBP, and stained images expressing these proteins are shown in (Figure 6.2 a).

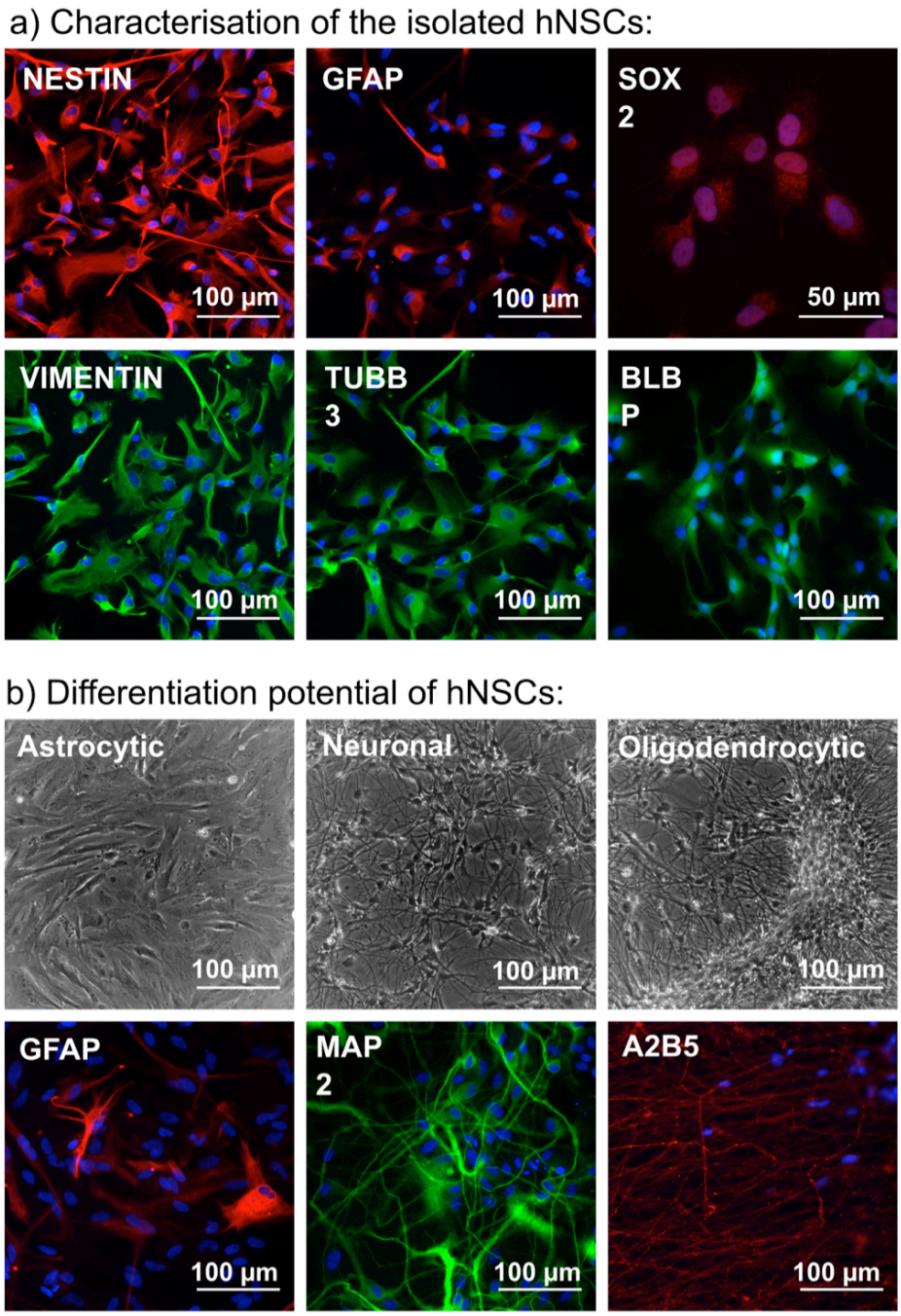

Figure 6.2 Characterization of isolated hNSCs. **(**a) Expression of neural stem/progenitor cells markers in isolated hNSCs as detected by immunocytochemistry. All cells show strong expression of cytoskeletal proteins such as nestin, vimentin and βIII tubulin (TUBB3), while GFAP staining shows heterogeneity in the population with both low and high expressing cells. hNSCs also express SOX2 and radial glial marker BLBP. Nuclei are counterstained with Hoechst 33258 in blue. (b) Trilineage differentiation potential of hNSCs towards

astrocytes, neurons and oligodendrocyte precursors. Top row: Phase contrast images of hNSCs morphology after 2 weeks of differentiation. Bottom: Expression of representative markers as detected by immunocytochemistry.

6.3.3 SURVIVAL OF HNSC ON NCD, BNCD AND 3D NANOSTRUCTURED BNCD

hNSCs were seeded onto ozone–treated NCD; BNCD; BNCD–coated CNTs of length 1 µm and 2 µm; and tissue culture polystyrene (TCPS), which was used as a control throughout. Cell attachment and morphology were assessed after 24 hours *in vitro* using CMFDA, after 48 hours via immunostaining using Phalloidin and Hoechst, and the methylene blue assay was used to evaluate cell viability on each substrate.

First of all the viability of hNSCs on planar substrates without CNT nanostructuring was investigated using immunohistochemical imaging. Fluorescent stained images in (Figure 6.3 a) show Phalloidin–labelled actin in green and nuclei stained by Hoechst in blue. The images are optically very similar and confluency percentage (Figure 6.3 b) shows that there is no statistical difference between the TCPS control, NCD and BNCD (37.6 ± 4.8 %, 37.2 ± 6.4 %, 37.1 ± 8.7 % respectively). Furthermore, no discernable differences were apparent in the morphology of adherent cells across each planar substrate. These similar confluency percentages and uniform cell morphology indicate that both NCD and BNCD are as good as the control for hNSC adhesion. Cell count data (Figure 6.3 c) for TCPS, NCD and BNCD substrates also confirms the similarity of hNSC adherence with cell counts (2.33 x 10^5 cells/cm^2, 1.85 x 10^5 cells/cm^2, and 2.09 x 10^5 cells/cm^2 respectively).

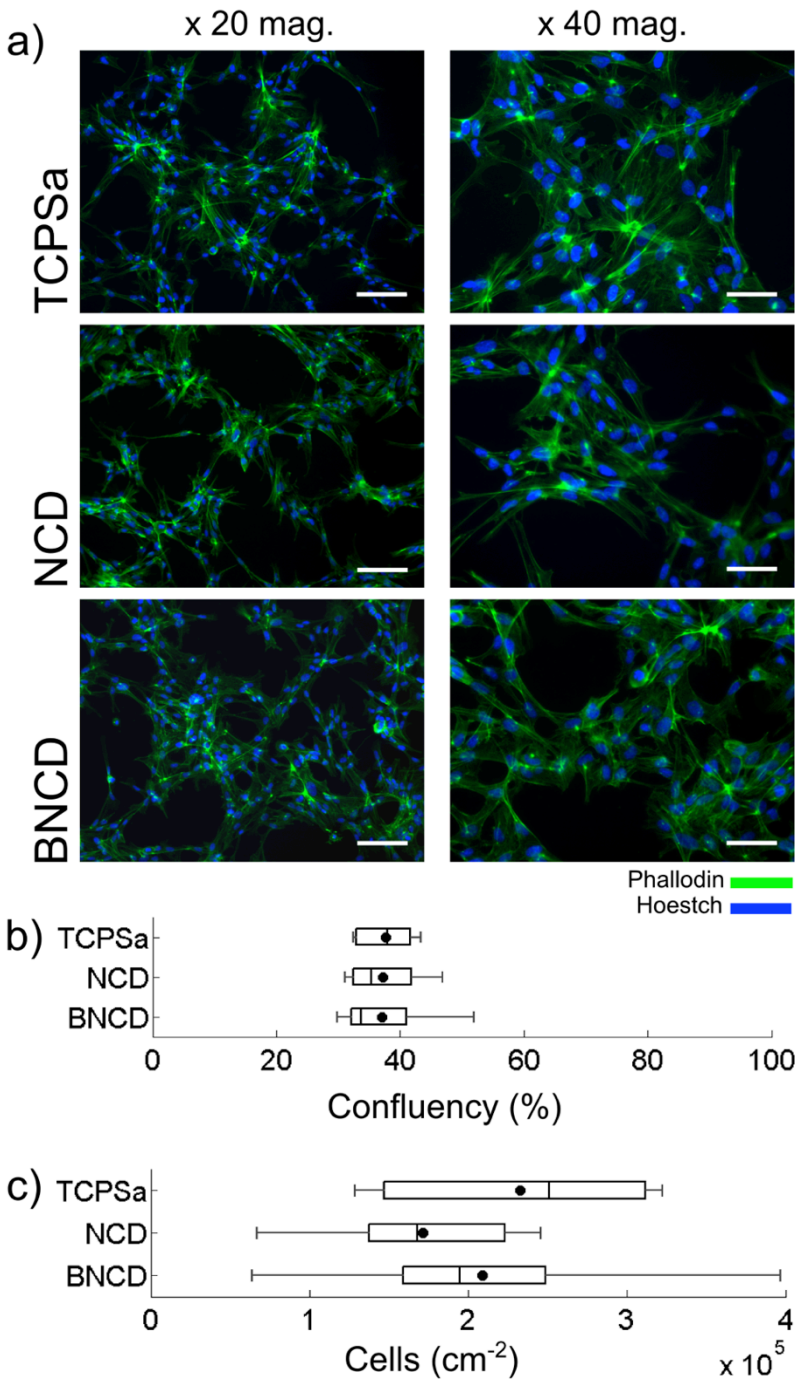

Figure 6.3 (a) show fluorescently labelled images of hNSCs using Alexa Fluor® 488 Phalloidin (green) and Hoechst (blue) after 48 hours *in vitro* on TCPS, NCD and BNCD. The scale bar is 100 µm and 50 µm for the x10 and x40 magnifications respectively. Panel (b) shows the confluency of each sample presented as a boxplot and mean of the data, panel (c) shows the boxplot and mean of cell concentration displayed as cells/cm^2 (black dot: mean, vertical bars from left to right: minimum value, lower quartile, median, upper quartile, maximum

value). Statistics performed using the threshold analysis on at least 6 images per sample.

Having established there to be no significant differences in hNSC viability between different substrate materials, cell viability was assessed for hNSC cultures upon CNT nanostructured substrates in comparison to planar substrates using live-cell staining and image analysis. CMFDA stained images in (Figure 6.4 a + c) show that the hNSCs have attached onto all surfaces, with a high confluence percentage and no indication of neurosphere formation, which can be indicative of hNSCs having poor adhesion to a biomaterial [269]. Further evidence of healthy attachment is demonstrated by the early formation of neurite processes after 24 hrs *in vitro* (Figure 6.4 a + c) 2nd columns). The similar sub-confluent attachment (20–50% mean confluence) of hNSCs over all substrates show that the cells are proliferating at similar rates. No significant change in confluence is observed between CNT BNCD substrates and the TCPSb control. In terms of the cells conforming to the BNCD-CNT structures, the grouping of cells is ascribed to fasciculation, rather than 3D structure obstruction, because the scale of fasciculation voids being considerably larger than the density of the 3D structures for both substrates (Figure 6.4 b), 1 μm CNT BNCD: 9 bundles μm^{-2}, 2 μm CNT BNCD: 4 bundles μm^{-2}. No differences in morphology are observed among hNSCs grown on the different substrates.

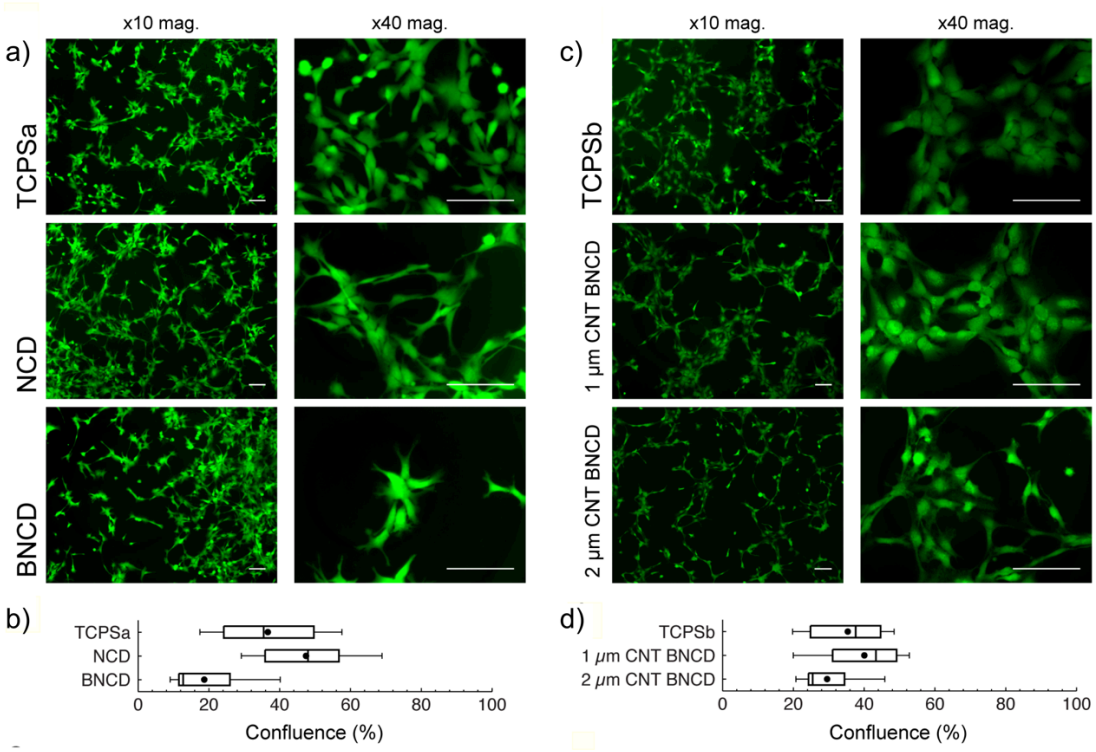

Figure 6.4 (a + c) show live staining of hNSCs using CMFDA; a vital cytoplasmic dye after 24h *in vitro,* on (a) TCPSa, NCD, BNCD and (c) TCPSb, 1 µm CNT BNCD and 2 µm CNT BNCD. The scale bar is 100 µm, with the left hand column at 10x magnification and the right 40x. Panels (b + d) show confluency of each sample presented as a boxplot and mean of the data (black dot: mean, vertical bars from left to right: minimum value, lower quartile, median, upper quartile, maximum value. Statistics performed using the threshold analysis on at least 6 images per sample).

The MB assay is a semi-quantitative method for indicating the relative number of healthy cells there are per substrate. (Figure 6.5 a) MB assays reveal a slightly reduced cell count on NCD and BNCD samples in comparison to the TCPSa control. Error bars show standard deviation of the absorbance for each sample set (4 substrates per sample), the larger error bars shown for NCD and BNCD result from using irregular sized substrates and so area calculations were not exact. Despite this, the cell counts for both NCD and BNCD are less than the TCPSa control. However, (Figure 6.5 b) shows very comparable cell counts between NCD and BNCD substrates, showing hNSCs to have a similar viability and propensity to attach and proliferate to NCD and BNCD surfaces. The

nanostructured CNT BNCD samples showed significantly increased attachment of hNSCs in comparison to the TCPSb control, and moreover an increased cell count with increasing CNT length / reduced 3D structure density, (1 µm CNT 1.35 a.u, 2 µm CNT 1.55 a.u, TCPSb 1.1 a.u) was observed.

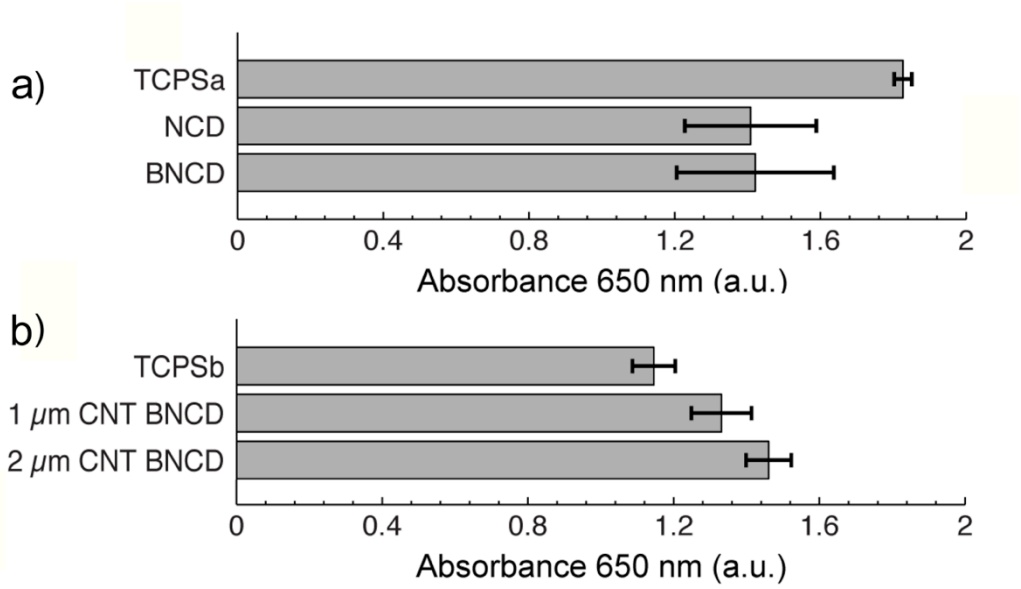

Figure 6.5 (a + b) show the MB assay indicative of vital cell count for each sample at an absorbance of 650 nm. Statistics performed using 4 substrates per sample set, the mean absorbance is plotted standard deviation error bars.

6.4 DISCUSSION

Nanoscale topography has been shown to influence neuronal adhesion upon diamond [208], whereby surfaces with features of higher curvature promote neuronal adhesion. In nanocrystalline diamond films curvature manifests in the size of grain boundaries, which in turn determines the roughness of substrates. The inclusion of boron in the diamond lattice during MWPECVD growth causes increased re–nucleation, resulting in smaller grains with higher curvature within BNCD materials, unlike intrinsic NCD materials which evolve larger grains during growth. In this case the reduced grain sizes of BNCD in comparison to NCD are still in excess of the dimensions that are conducive to nanotopographical enhancement of cellular adhesion (Figure 6.1 a). The similar values obtained

from the MB assays for NCD and BNCD substrates (Figure 6.5 a + b) and the similar morphology of cells show the inclusion of boron within the diamond lattice not to be detrimental to hNSC adhesion, and that the reduced grain size of BNCD does not effect hNSC adhesion. The cell counts recorded here are comparable to murine NSCs grown on oxygenated ultrananocrystalline diamond (UNCD) [256]. Furthermore, the observation of initial process extension of hNSCs on all substrates (Figure 6.3 a) and (Figure 6.4 a + c), high confluency percentages (Figure 6.2 b) and (Figure 6.3 b + d) and similar cell counts for each substrate (Figure 6.3 c) are a promising indicator of healthy hNSCs and of subsequent neuronal network formation.

Upon 3D nanostructuring of BNCD substrates, the increased MB assay value of the CNT BNCD samples with respect to the TCPSb control substrate suggests nanostructuring enhances cell proliferation. Such an effect could be due to the increased surface area or enhanced local curvature of substrates. Given the monotonic increase in MB assay with respect to the length of CNTs, and the corresponding increase in sample surface area, this aspect of the substrate morphology could be ascribed to increasing cell proliferation. However, it has been shown that cardiomyocytes cells preferentially sit atop of nanopillar features when spaced at a pitch of 2 μm spacing [270] . Herein, the spacing of the 3D structures is less than 2 μm (Figure 6.1 b), hence, assuming hNSCs are of comparable size to cardiomyocyte cells, they are expected to be residing on top of the structures, thus surface area should not directly dictate cell count.

6.5 CONCLUSIONS

It has been found that the inclusion of boron in diamond has no observable effect of the proliferation and adherence of human neural stem cells. These results have been shown using image analysis of hNSCs grown on NCD and BNCD with TCPS as the control. Percentage confluency and cell count / MB data suggest that there is minimal difference between all three planar substrates. In addition to the assessment of BNCD vs. NCD vs. TCPS biocompatibility towards hNSCs, the impact of nanostructuring the BNCD using CNTs as scaffolds upon hNSC adherence and proliferation has been investigated. Herein it has been shown that increasing surface nanostructuring via CNT scaffolds has a positive effect on cell viability. Given the enhanced capacitance of such nanostructured electrodes, this result of increased cell viability of hNSCs on CNT–nanostructured BNCD is very promising for improving the performance of electrodes at the brain–machine interface, micro–electrode arrays and in lab–on–chip devices.

CHAPTER 7 – OXYGEN VS. HYDROGEN FUNCTIONALISED NANODIAMONDS FOR HUMAN NEURAL STEM CELL ADHESION AND PROLIFERATION

7.1 INTRODUCTION

Nano–bio interfaces encompass kinetic, physiochemical and thermodynamic interactions between the surfaces of nanomaterials and numerous biological components including proteins, cell membranes and DNA [271]. Cells are surrounded by extra cellular matrixes (ECMs) in their natural environment [272], nanoscale topography is observed on the ECM surface. The understanding of these nano–cell interactions is essential if advances in knowledge about cell motility, morphology, proliferation and differentiation are to occur [273]. It has been hypothesised that nanostructured surfaces are able to mimic live tissue [274] as they have similar physical properties to the naturally occurring ECM [275]. Therefore, interest into studying the interactions of cells with nanostructured materials is increasing. Ideally, nanomaterials will be designed with precise biological functionality in order to control cell behaviour via external cues. This will be achieved by modifying chemical and physical properties of nano–scale materials [276]. It has been demonstrated that cellular behaviour is manipulated by a variety of substrate factors including rigidity [277,278], surface charge [279,280], topography [281,282] and wettability [283,284]. Focal adhesions are molecular assemblies in which regulatory signals and mechanical forces can be transmitted between the ECM and cells [285]. They are generally between 5–200 nm in size, and it has been shown that these adhesion sites are greatly influenced by complex mechanisms which occur at the nano– rather than micro–scale [286].

Stem cells have vast potential as treatment and prevention tools in regenerative medicine. However, it is essential that we are capable of introducing cells into foreign environments where natural cell behaviour is maintained [287]. Neural Stem Cells (NSCs) are able to proliferate, self–renew and differentiate into the three main cell types present in the central nervous system: neurons, astrocytes and oligodendrocytes [288]. Understanding the differentiation into these specific

cells is vital for advances in the treatment of neurological diseases such as Parkinson's [289] and Alzheimer's [290] to be made [291]. In order to utilise the regenerative potential of stem cells in treating neurodegenerative diseases, the stem cell 'niche' must be found. The niche is the specific microenvironment in which stem cells naturally occur. The interaction of cells with this exterior niche environment influences stem cell fate [292]. In order to mimic this niche, nano–biomaterials are being precisely engineered to enable specific stem cell manipulation and interaction. Examples include but are not limited to: graphene and graphene foams [293,294], carbon nanotubes [295,296], and various nanofibers [297-299].

Diamond is biocompatible [42,74,204,260,300], this along with the excellent electrical properties of diamond [237,301] make it an exciting material for electrically interfacing with neurons. Detonation nanodiamonds (DNDs) were first synthesised at the beginning of the 1960s [65]. Typically between 5–10 nm in diameter, these nanoparticles naturally aggregate into micro sized particles due to high Van der Waals (VdW) intermolecular forces. Developments in the dispersion of DNDs has enabled monolayers of DNDs to be produced, utilising these strong VdW force [302]. Neurons have been successfully grown on single crystal [167], micro–crystalline [42,166] and nanocrystalline diamond (NCD) films [303]. Nanodiamonds (NDs) have been shown to promote neurite outgrowth from neurons [73] and patterned neural networks have been created by culturing neurons on nanodiamond tracks [208].

NSCs are more sensitive than neurons. They are extremely responsive to external stimuli, and can readily form neurospheres; when the cells cluster together. Neurosphere formation is indicative of poor NSCs adhesion to the biomaterial [269]. The interaction of NSCs with diamond has been reported: ultra–nanocrystalline diamond has shown to be a promising biomaterial of choice for NSC adhesion and differentiation [256], with tunable cell adhesion being observed [257]. Microcrystalline diamond has also shown to be a successful platform for neuronal induced differentiation from pluripotent stem cells [304]. We previously reported that boron doped diamond successfully supports the adhesion and proliferation of human NSCs (hNSCs) with an increase in adhesion being observed with increasing nanostructuring [300]. Herein, the interaction between ND monolayers and hNSCs has been investigated for the first time. Specifically, the effect of altering ND surface functionalisation on hNSC adhesion and proliferation after 7 DIV has been explored. It has been shown that NDs with

oxygen containing groups on the surface allow for a significantly better hNSC attachment over hydrogen functionalisation. Contact angle measurements and protein adsorption experiments have enabled the development of a possible explanation to why this difference is observed.

7.2 Materials and Methods

Citlali Helenes Gonzalez, UCL, plated the hNSCs. Alice Taylor performed all other experimental activities and analysis presented in this chapter.

7.2.1 Chemicals

Monodispersed detonation nanodiamonds (DNDs) (5 − 10 nm) were used throughout (New Metals & Chemicals Corporation, Tokyo, Japan). This form of DND has been subjected to a deagglomeration process utilising wet milling with zirconia [305].

7.2.2 Nanodiamond monolayer coatings

Nanodiamond monolayer coatings are obtained by ultrasonicating substrates in the H–ND solution (0.05 g/L of NDs) (described below) for 10 min (excess time). Glass (Cover glass, VWR, UK) was used throughout as the substrate for ND attachment as the transparency allowed for easy optical and fluorescent imaging. Prior to seeding substrates are degreased in acetone, IPA and then DI water (each for 5 mins sonication), to remove residues and dirt.

7.2.3 Hydrogen termination

DNDs were dried by evaporating off excess water at 80 C for 30 mins. Hydrogen functionalization of these DNDs was achieved using a hydrogen anneal process. A custom–made chamber was used to heat samples to 600 C in 25 Torr of hydrogen for 5 h and allowed to cool in hydrogen. H–NDs were then re–suspended in DI water (0.05 g/L) and subjected to ultra-high power sonication using a VCX500 Vibra-cell sonicator with the cup horn accessory (100%

amplitude, 3:2 duty cycle, water cooled and temperature controlled to be <30˚C, 5 hrs) to fully disperse the NDs.

7.2.4 OXYGEN TERMINATION

Oxygen functionalization of the NDs was achieved using an ozone treatment on H–ND monolayers. A custom built chamber was used in conjunction with a commercially available ozone generation unit (Ozonia TOGC2–100201). Here, samples were subjected to ozone flow at a pressure of 50 mbar, at 200 C for 1 hour. After which the sample was allowed to cool in ozone before being removed.

7.2.5 ATOMIC FORCE MICROSCOPY

Atomic force microscopy (AFM) measurements were carried out using a Veeco Dimension V instrument with aluminum-coated silicon AFM probes (resonant frequency 190 kHz). The system was operated in tapping mode with a VT-103-3K acoustic/vibration isolation system and a VT-102 vibration isolation table at room temperature in air. AFM was performed on Tissue Culture Polystyrene (TCPS), glass H–ND monolayers. Scan sizes of 2 μm were taken and root mean square of the roughness (Rq) was calculated using Nanoscope Software 6.1.3. AFM Images were post processed with a median filter (3 × 3 kernel) using MATLAB 2012a software to remove noise and measurement artifacts.

7.2.6 X-RAY PHOTOELECTRON SPECTROSCOPY

Surface chemistry of the nanodiamond samples were characterised by X-ray photoelectron spectroscopy (XPS) was done using a Thermo K–alpha instrument, a monochromated Al K_a(1486.6 eV) radiation source was used, alongside an internal flood gun to reduce charging. Data was processed and analysed using CasaXPS (version 2.3.12, Casa Software Ltd).

7.2.7 CONTACT ANGLE MEASUREMENTS

Contact angle measurements were taking using a Krűss Drop Shape Analysis system (DSA 10 MK2), values were calculated using Drop Shape Analysis software. Contact angles of the DI water droplet were measured immediately, with a constant volume of 3 µl used for all samples. Three repeats were done for each substrate.

7.2.8 HUMAN NEURAL STEM CELL ISOLATION AND CULTURE

(Previously described in section 6.2.5 Human Neural Stem cell Isolation and Culture). The preparation of neural cell cultures was performed in close collaboration with the Developmental Biology Unit, Institute of Child Health, UCL by Citlali Helenes Gonzalez.

7.2.9 CELL ATTACHMENT AND MORPHOLOGY ASSAY

Substrates were then placed in 24 well tissue culture plates, sterilized for 30 mins in 70% ethanol and washed three times in sterile distilled water. Prior to cell culture, some substrates were coated with poly–L–lysine (PL) (Sigma 1 mg/ml) and Laminin (LN) (Sigma, L2020, 1 mg/ml). PL was diluted to 0.1 mg/ml in Phosphate Buffer Saline (PBS). Sufficient solution was then placed into each well to ensure even coating of surface for 1hr at RT. Wash 3 times with water and leave in hood over night or until dry. After PL coating, LN solution was diluted to 10µg/ml in PBS. Sufficient solution was added to each well to ensure even coating of surface and incubated for one hour at 37°C. Excess Lam was then removed and used without washing. hNSCs were then plated at a density of 3×10^4 cells/cm^2 and were grown in humidified incubators at 37°C with 5% CO_2. For actin staining hNSCs were fixed after 7 *days in vitro* (DIV*)* in 4% (w/v) paraformaldehyde in PBS (pH 7.4) for 15 min and washed three times with PBS. Substrates were then incubated in blocking solution (10% fetal bovine serum, 3% bovine serum albumin in PBS with 0.2% Triton X100 for permeablization) for 30min at room temperature. Cells were stained with Phalloidin conjugated with Alexa Fluor® 488 diluted in blocking buffer (Invitrogen, 5 U/ml) together with Hoechst 33258 (2 µg/ml) to counterstain nuclei for 1 hour at room temperature.

After 3 washes with PBS to remove excess dye the samples were imaged using an inverted microscope Olympus IX71 (Carl Zeiss, Jena, Germany) equipped with a Hamamatsu ORCA-ER digital camera (Hamamatsu Corp., Bridgewater, NJ) and image processing was done using Image J and Fiji. Cell counts were obtained for the Hoechst stained images in Matlab R2015a by applying an intensity threshold to the stained images and then using an edge finding transform to find the number of labeled nuclei per image, which was then scaled up accordingly (at least six images at varying magnification for one sample per substrate).

7.2.10 BIO–LAYER INTERFEROMETRY

Bio–layer Interferometry (BLI) was performed using a (ForteBio Octet ® RED96) to observe the adsorption of NDs onto proteins.

7.2.10.1 PREPARATION OF LAMININ AND POLY–L–LYSINE

Laminin (LN) (Sigma, L2020, 1 mg/ml) was diluted to 25 µg/ml in 10mM sodium acetate buffer pH 4.0. Previous pH scouting experiments showed pH4 to achieve optimal LN immobilization. Poly–L–lysine (PL) (Sigma 1 mg/ml) was diluted to 0.1 mg/ml in PBS.

7.2.10.2 IMMOBILIZATION OF LAMININ VIA AMINE COUPLING ON AR2G BIOSENSORS

Amine Reactive 2nd Generation (AR2G) biosensors are used to immobilize LN onto the end of an optical fibre. The immobilization is achieved via a standard amide bond formation via EDC catalysis, which results in a covalent bond between the carboxylic acid terminated biosensor and a reactive amine on the LN. The biosensors were pre–hydrated in DI water for 10 min and then the AR2G surface is activated by reaction with 20 mM EDC (1-Ethyl-3-[3-dimethylaminopropyl] carbodiimide hydrochloride) and 10 mM s-NHS (N-hydroxysulfosuccinimide) in DI water for 5 min. LN (25 µg/ml, pH 4) is immobilized onto the surface for 15 min, which results in covalently bonding

between the activated AR2G and amine groups on the LN. The immobilization was performed at 30°C, and agitation speeds of 1000 rpm were used. The activated carboxylic groups are then quenched in 1 M ethanolamine for 5 min. A schematic of the immobilization can be seen in (Figure 7.1). Experimental definition and execution was performed using Data Acquisition software 7.1.0.92 (ForteBio).

7.2.10.3 ASSOCIATION OF POLYLYSINE AND NANODIAMONDS

After activation of AR2G and immobilization of LN, the biosensors are buffered in PBS for 180 s to equilibrate. Sensors are then immersed in PL (0.1 mg/ml in PBS) for 30 min. Equilibration in DI water for 300 s showed minimal PL dissociation. The subsequent association of NDs (0.5 mg/ml) with both H– and O–functionalisation onto the PL was investigated for 30 min. Following association, dissociation in DI water was performed to gauge stability of adsorbed NDs. Both ND types were tested in triplicate.

7.2.10.4 ASSOCIATION OF NDS ONTO NON–FUNCTIONALISED BIOSENSORS

The association of H– and O–NDs (0.5 mg/ml) onto quenched sensors (without LN and PL) was simultaneously investigated as a control.

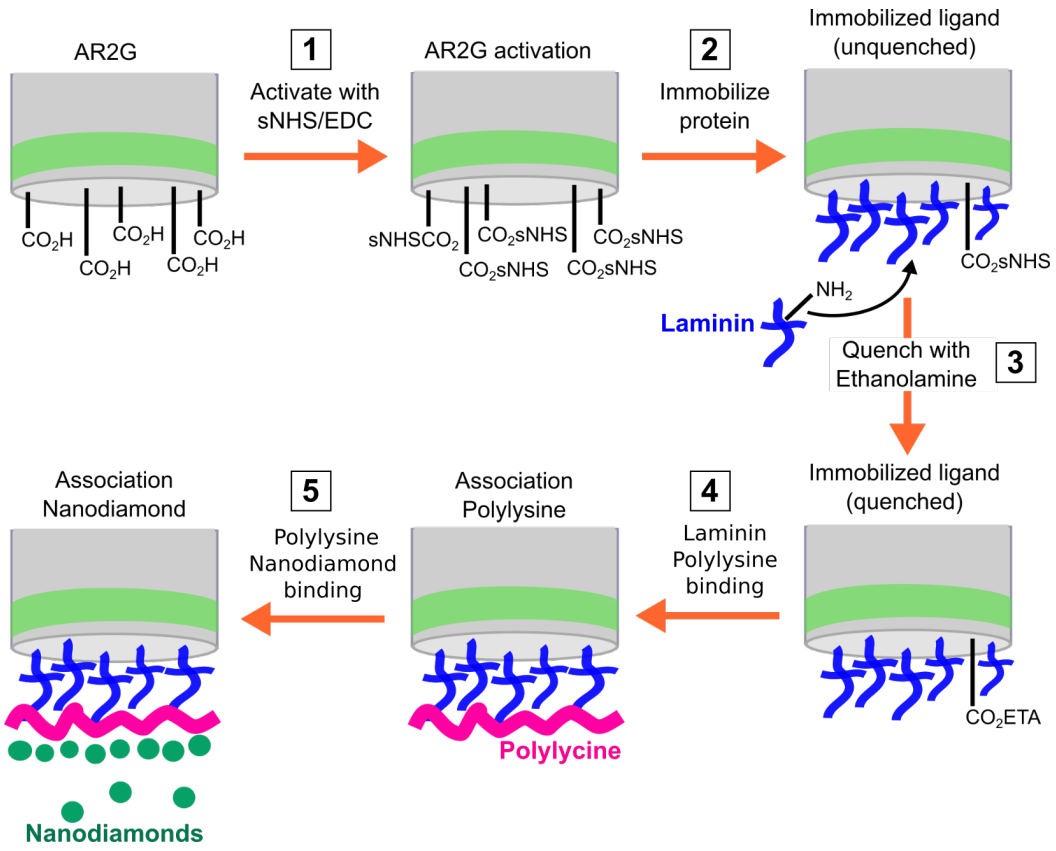

Figure 7.1 Schematic outlining the covalent immobilization process of laminin onto AR2G coated biosensors, and subsequent binding of poly–L–lysine and nanodiamonds. Step 1: EDC catalysis activates carboxylic acid coated sensor by facilitating the reaction with sNHS, resulting in a more reactive carboxylic acid site. Step 2: LN is covalently immobilized onto the sensor. The covalent bond is formed between a reactive amine group on the laminin and the carboxy–functionalisaed surface of the biosensor. Step 3: ethanolamine is used to quench all remaining carboxylic activated groups on the sensor head to prohibit non–specific binding. Step 4: poly–L–lysine is bound to the laminin coated sensor, the thickness of this is measured using Bio–layer Interferometry. Step 5: nanodiamonds are bound to the poly–L–lysine, the binding thickness is also measured using Bio–layer Interferometry.

7.3 RESULTS

7.3.1 ROUGHNESS MEASUREMENTS

AFM topographical images of the three different types of substrate used throughout is shown in (Figure 7.2). The AFM data files were used to calculate root mean squared roughness (R_q) measurements for each substrate. The roughness of the TCPS and ND monolayer were very similar (3.84 nm and 3.74 nm respectively), with the glass being much flatter at 0.26 nm. The AFM images also show that the NDs have adhered to the glass cover slips homogeneously in an apparent monolayer formation.

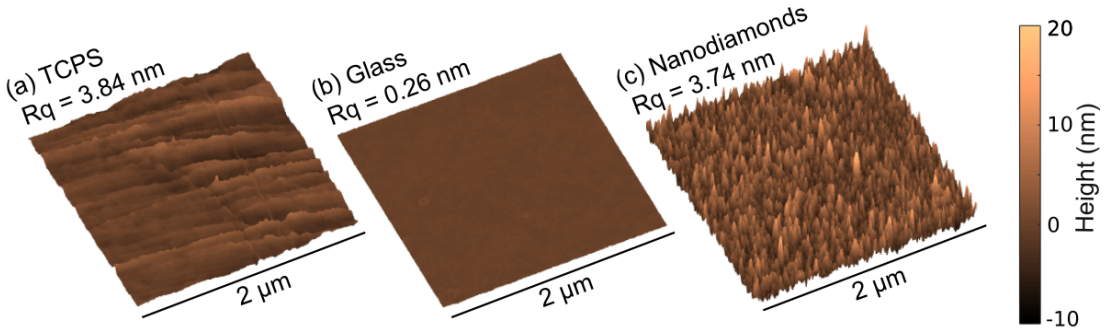

Figure 7.2 From left to right: 2 µm square atomic force microscopy (AFM) scan of (a) TCPS, (b) Glass and (c) Nanodiamonds. R_q = root mean square roughness.

7.3.2 XPS SPECTRA

(Figure 7.3) shows the XPS spectra for Hydrogen (a) and Oxygen (b) terminated nanodiamonds taken on Indium tape. For both samples the nitrogen percentage composition is very similar (H–NDs 1.04 % and O–NDs 0.94%), which suggest that the Nitrogen present is within the nanodiamond. The main difference in elemental composition between samples is the difference in percentage attribution of the Carbon and Oxygen. H–NDs are 4.04 % Oxygen and 94.92 % Carbon, compared to O–NDs which are 6.85 % Oxygen and 92.21 % Carbon, this

corresponds to a 70% increase in Oxygen and a 3 % reduction in Carbon after O–termination.

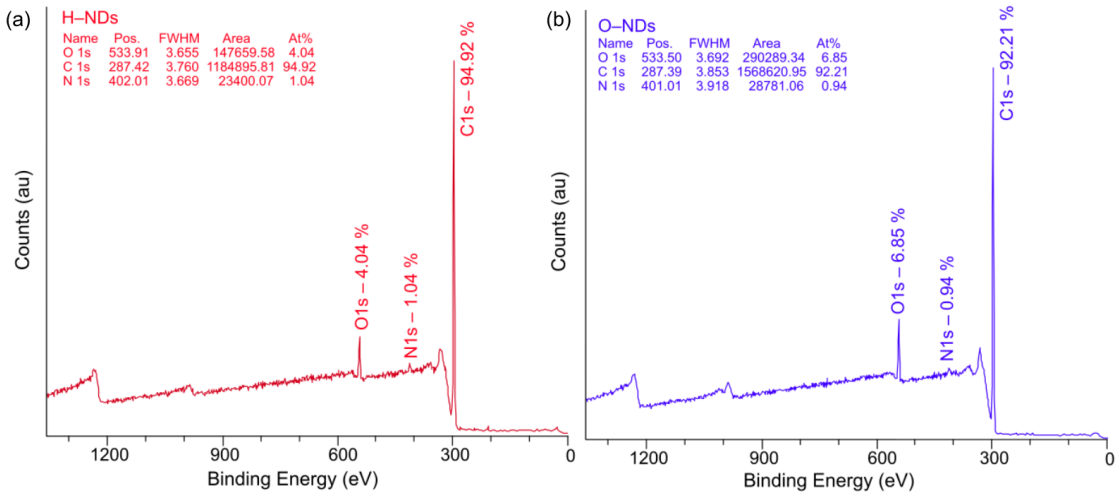

Figure 7.3 XPS spectra for (a) H–NDs and (b) O–NDs. Highlighted peaks are the C1s, O1s and N1s.

7.3.3 Optical Images

(Figure 7.4 a) shows optical images taken at 4 DIV of the hNSC culture. The optical images are useful to look at how the cells are adhering to each surface and it can be seen that full confluent cells can be observed for both the TCPS control and O–NDs, showing that they are ideal for hNSC attachment. In the glass control images, patchy, non–confluent adhesion of hNSCs to the surface is observed, indicating that glass is a non–ideal biomaterial for hNSC growth. The H–NDs appear to be the least suitable substrate for hNSC adhesion, with the lowest coverage of hNSCs observed. In fact, it appears that the hNSCs are opting to adhere to themselves instead of the substrate with early signs of neurosphere formation prominent.

7.3.4 Fluorescently Stained hNSCs

Phalloidin and Hoechst fluorescent dyes were used to selectively stain the F–actin of the microfilament in the cytoskeleton (green) and nuclei (blue)

respectively in hNSCs after 7 DIV. F–actin is present in all types of eukaryotic cells, where it forms networks that support the mechanical structure, determine shape and facilitate movement of cells, enabling cell migration and division [306]. (Figure 7.4 b) shows the fluorescent staining of hNSCs cultured on TCPS, glass and H– and O–NDs. It can be seen that both the TCPS control and O–NDs are highly suitable substrates for hNSC adhesion as confluent attachment is again observed, consistent with the optical images. Further patchy adhesion is observed on both the glass control and H–NDs, with glass showing signs of preferential neural–neural adhesion, which suggests neurosphere formation. A neurosphere is observed in (Figure 7.4 b) showing that the hNSCs prefer to adhere to other hNSCs and not the H–ND surface.

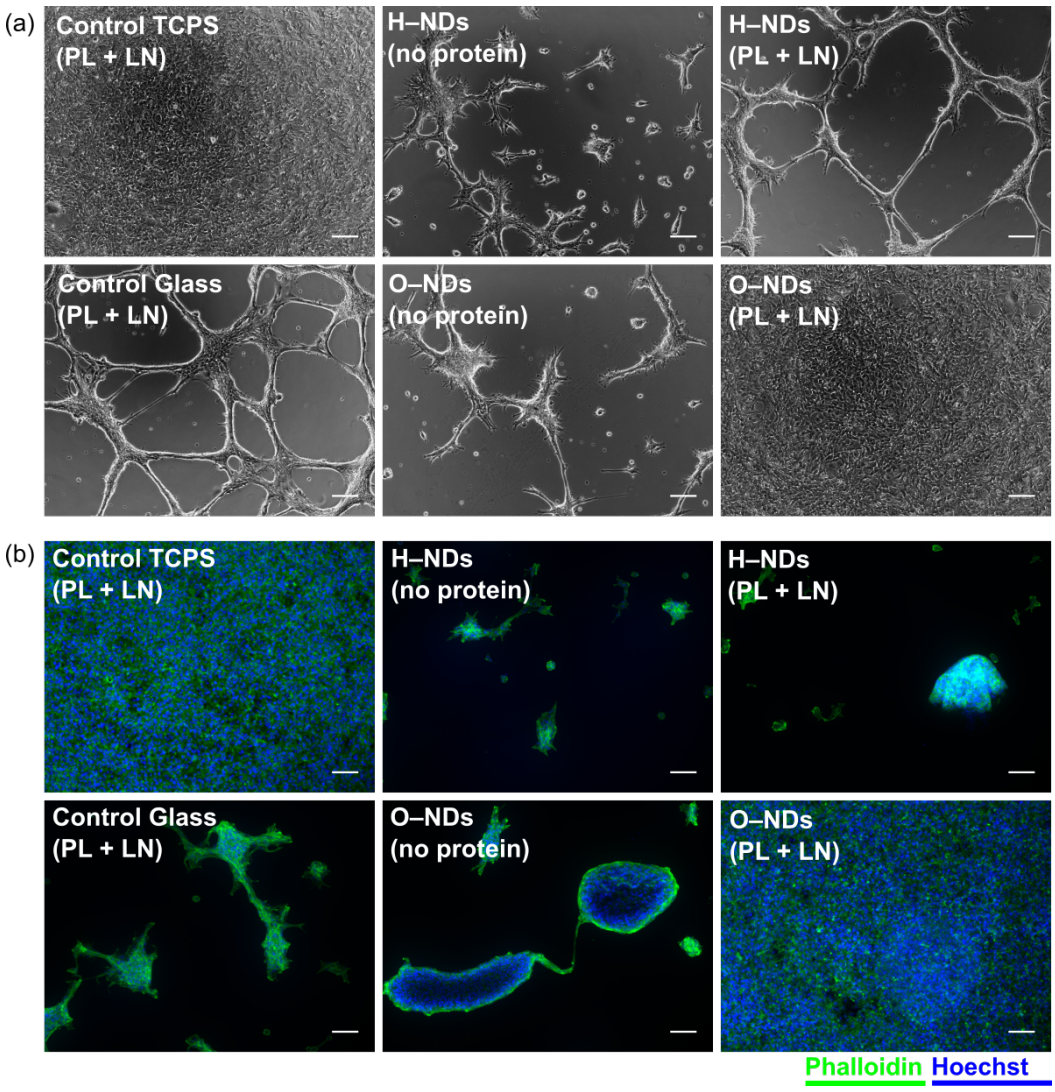

Figure 7.4 (a) Shows optical images of hNSCs after 4 DIV which have been cultured on Control TCPS, Control Glass H–NDs and O–NDs, with and without PL + LN coating. (b) Shows fluorescently labelled images of hNSCs using Alexa Fluor® 488 Phalloidin (green) and Hoechst (blue) after 7 DIV on Control TCPS, Control Glass H–NDs and O–NDs, with and without PL + LN coating. Images were taken at random over each substrate. The scale bar is 100 µm.

7.3.5 CELL COUNT DATA

Cell counts, shown in (Figure 7.5), were performed after 7 DIV. The highest cell count was observed on the TCPS (2546 cells/mm^2) with O–NDs only slightly less (2265 cells/mm^2). Glass had the fewest cells (134 cells/mm^2), and H–NDs had a cell count of 570 cells/mm^2.

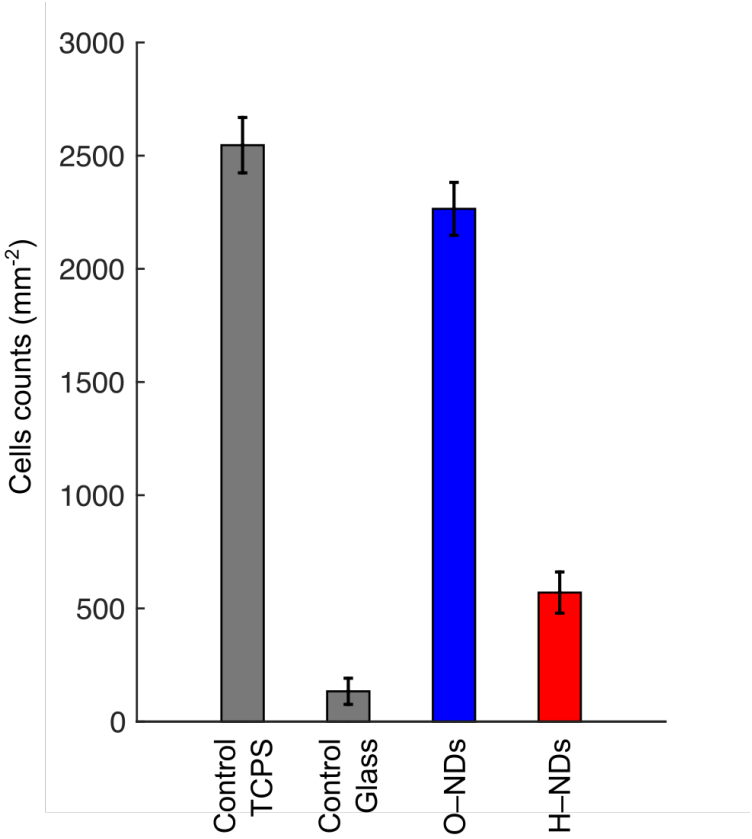

Figure 7.5 Shows the mean of cell concentration on Control TCPS, Control Glass, O–NDs and H–NDs, displayed as cell nuclei per (mm^2). Cell counts were obtained using image analysis on Hoechst stained nuclei on at least 4 images per sample.

7.3.6 CONTACT ANGLE

Contact angle measurements (Figure 7.6) were performed on TCPS, glass, ONDs and HNDs, with and without protein coating. Three comparisons have been made, the first is between the four un–coated substrates, the second between the four protein coated substrates and the third between each substrate type with and without protein coating. Without coating the O–NDs produce the smallest contact angle of all substrates (21.9°), then glass (25.8°), then H–NDs (54.7°), with TCPS having the largest contact angle of (89.3°). A smaller contact angle is indicative of a more hydrophilic surface, and thus H–NDs are more hydrophobic than O–NDs, and TCPS is significantly more hydrophobic than the three other substrates. Poly-L-lysine and Laminin (PL+LN) coating increased the contact angle on all substrates except for the TCPS. The most hydrophobic substrate observed after coating was the glass (79.6°), but the contact angle of the coated TCPS (75.6°) and the (PL+LN) H–NDs (69.1°) was comparable. The contact angle of the (PL+LN) O–NDs is significantly less than the other three (50.4°). The largest increase in contact angle upon protein coating is observed on glass (+53.8°), then O–NDs (+28.5°) and then H–NDs (+14.4°) and the TCPS is the only substrate in which a decrease in contact angle is observed.

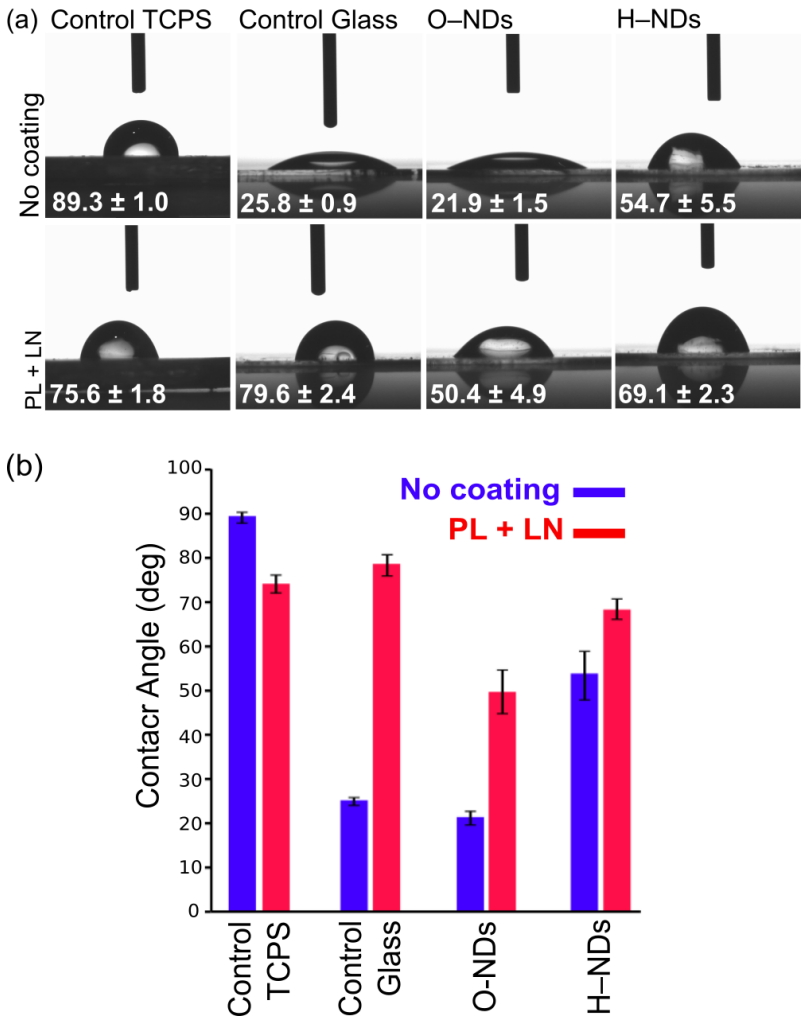

Figure 7.6 (a) Optical images showing contact angle values for 3 µl of DI water shown on (from left to right) Control TCPS, Control Glass, O–NDs and H–NDs. The top row is without any protein coating, and the bottom row is after (PL+LN) coating. (b) Shows the values obtained from triplicate drops, highlighting the difference with and without coating. Error bars show one standard deviation.

7.3.7 Bio–layer Interferometry

The binding of NDs with H– and O– surface functionalisation to sensors coated with (LN+PL) showed O–NDs to adhere considerably better then H–NDs. This is shown in (Figure 7.7); the red solid line remains at 0 nm of binding for the duration of the association, showing that the H–NDs are not binding to the protein coated sensor at all. The opposite can be seen for the O–NDs, (blue line) which clearly shows fast binding. After 10 minutes a binding thickness of around 12 nm

can be seen. The size of the O–NDs is approx. between 5–10 nm and so this observed thickness indicates NDs are completely covering the sensor and few aggregates are present. After 30 minutes the sensors are placed in DI water. The lack of any dissociation shows the stability of these O–NDs bound to the (LN+PL). The dashed lines in (Figure 7.7) show the binding of H– and O–NDs to blank sensors; without protein coating. Here the opposite effect is observed; the H–NDs adsorb onto the sensor and the O–NDs do not. The binding rate is similar, and the stability of the ND–sensor interaction remains.

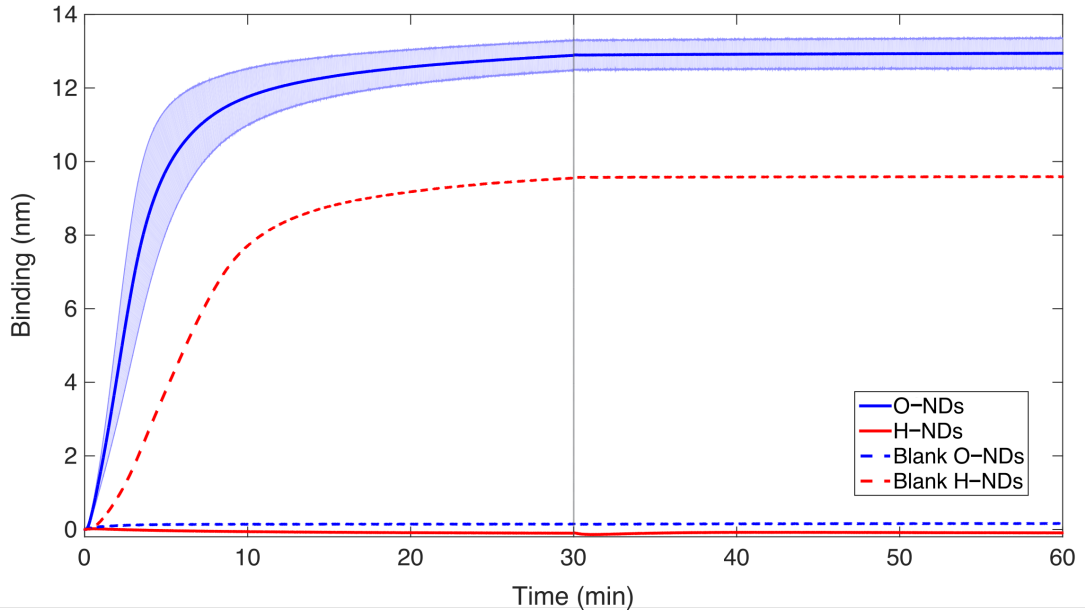

Figure 7.7 Bio–layer Interferometry data showing the difference in binding of H– and O–NDs to PL coated LN. The solid lines show the mean binding thickness of NDs onto the protein–coated sensor (O blue and H red). The pale blue and pale red block areas show the standard deviation from the mean. The dashed lines show the binding thickness of NDs (O blue and H red) of the blank sensors without any protein coating. The grey line at 30 minutes shows the transition of the biosensor from the ND coating solutions into DI water.

7.4 DISCUSSION

The adhesion and cell count of hNSCs after 7 DIV on (PL+LN) coated O–NDs has been shown to be as high as when cultured on TCPS. This can be seen in optical and fluorescently labelled hNSCs (Figure 7.4 a + b) and via cell counting data (Figure 7.5). The adhesion and cell counts for hNSCs cultured on both glass and H–NDs is significantly lower. The surface functionalisation of NDs is therefore paramount in controlling cell behaviour.

Surface properties including wettability and roughness play a very important role in manipulating cellular adhesion. Modifications to surface properties can lead to improved biocompatibility [307,308], and it is very important that optimal conditions for specific cellular adhesion are realised. Nanotopography of surfaces greatly influences cellular adhesion, spreading [309] and fate [310]. Nanometer rough scaffolds have shown to promote the adhesion and proliferation of nerve cells due to their high surface area [274]. Very similar roughness values for TCPS and ND monolayers are observed (Figure 7.2), with glass being much smoother (TCPS: R_q = 3.84 nm, NDs: R_q = 3.74 nm, glass = 0.26 nm). O–NDs provide an excellent surface for hNSCs adhere to. The naturally occurring ECM of the stem cell niche is enriched with nanotopographical cues that manipulate cell fate and function [311]. It is hypothesised that the nano–scale roughness of ND monolayers is comparable to the ECM in the stem cell niche, which suggests why excellent hNSC adhesion is observed. The increase in surface area upon nanostructuring leads to more available sites for focal adhesion to occur [312]. It has previously been demonstrated that the focal adhesion activation of Human fetal osteoblastic cells were significantly enhanced on PLLA plastic with approx. 5 nm R_q roughness [313], comparable to ND monolayers (R_q = 3.74 nm) and TCPS (R_q = 3.84 nm).It is therefore suggested that the nano–scale roughness of NDs and TCPS promotes the formation of focal adhesions and thus enhances hNSC attachment.

Many chemical properties of a material including composition and hydrophilicity [314] affect cellular adhesion. Typically, hydrophilic surfaces enable better adhesion despite having a lower affinity for protein adsorption than hydrophobic surfaces [315]. Contact angle results herein show the contact angle of O–NDs to be much less than TCPS, glass and H–NDs, both with and without PL + LN coating (Figure 7.6). This increase in hydrophilicity of the O– functionalisation has transformed the surface from one that is not suited to hNSC adhesion, into one

that is. The similarity in contact angle after coating with (PL+LN) for TCPS, glass and H–NDs suggests that the proteins are adhering to the surfaces similarly. The significant difference observed between O–NDs and the other three substrates with (PL+LN) coating, suggests that oxygen–containing groups on the surface of the NDs are interacting differently with the proteins. H– and O–NDs have positive and negative surface charges respectively [316]. PL has many available amino groups, which are hydrophilic in nature and are positively charged [317]. It is hypothesised that the negatively charged O–NDs are electrostatically attracting the positively charged PL, resulting in a stronger PL binding with better coverage. This increased coverage of positively charged PL subsequently promotes uniform coating of LN, which is negatively charged [318]. Laminin enhances adhesion and growth of NSCs [319], therefore uniform coverage results in a more confluent attachment of cells. The surface of TCPS is also negatively charged [320]. hNSC adhesion is high on (PL+LN) coated TCPS, this may also be a result of the electrostatic interactions between the negatively charged surface and the positively charged PL. It is suggested that the positively charged surface of the H–NDs electrostatically repulses the PL inducing a non–uniform coating of LN, which results in the reduced and patchy cell adhesion observed.

BLI results show that O–NDs bind readily to PL coated LN, compared to H–NDs which showed no binding. Surface charge of NDs has shown to have a substantial affect on protein adsorption [316]. Contact angle results suggest that electrostatic interactions of the H– and O–NDs are responsible differences in protein adsorption. This explains why the negative O–ND surface binds readily to the positively charged PL, whereas the positive H–NDs do not. Suggested electrostatic interactions occurring between PL and H– and O–NDs can be seen in (Figure 7.8). It is believed that the positive NH_3^+ groups on the PL are non–covalently bonding to the stable negatively charged resonant carboxyl groups present on the surface of the O–NDs.

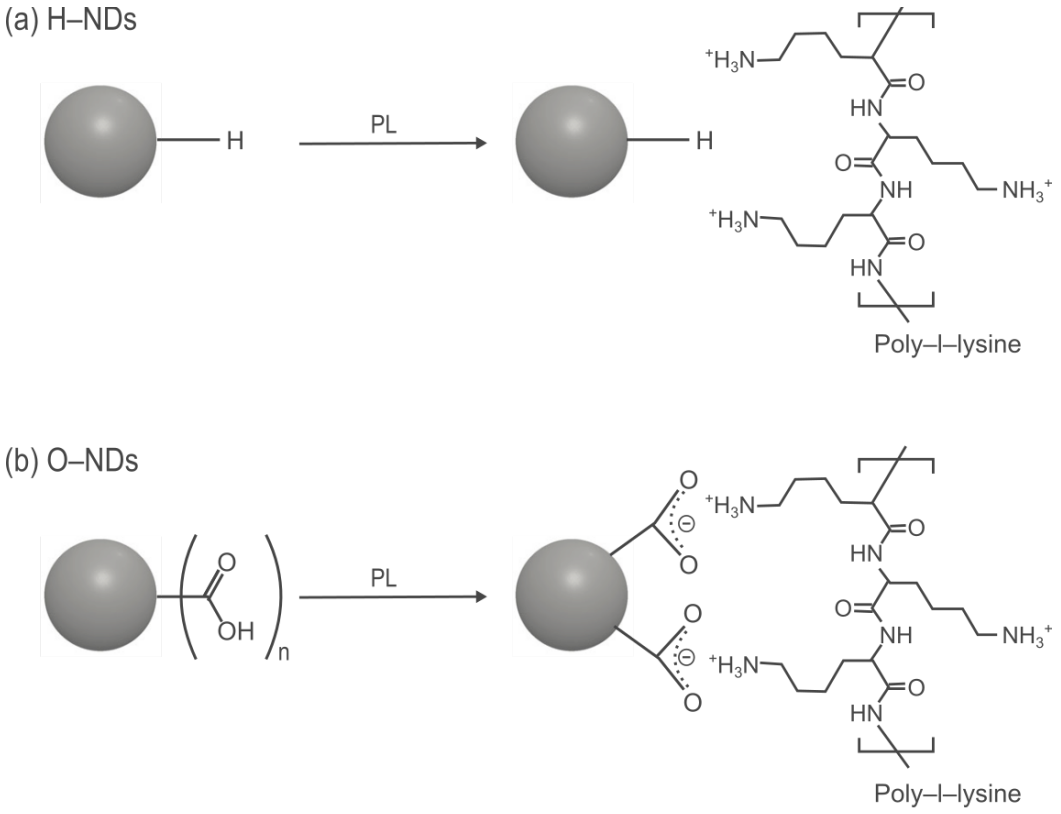

Figure 7.8 Schematic outlining the bonding of H– and O–NDs with poly–L–lysine. (a) Shows the lack of binding interactions occurring between H–NDs and PL. (b) Surface modification of O–NDs with PL, resonant negatively charged structures on the surface of the O–ND conjugate with the positively charged PL. Adapted from [94].

NSC cultures typically employ large ECM proteins such as LN to coat culture surfaces, the large size results in engagement with numerous integrin receptors on the NSC surface [321]. Evidence suggests that negatively charged oligosaccharides groups present in LN are responsible for protein–protein bonds [322]. This has been confirmed using BLI, where binding between LN and PL is observed, remaining stable after placing the biosensor in DI water. The stability of the binding between O–NDs and PL suggests that the electrostatic interactions occurring are strong. It is hypothesised that the monolayer coverage of NDs and the protein adsorption affinity of O–NDs is facilitating the uniform coverage of PL. The lack in binding of H–NDs with PL suggests that the coating procedure is

resulting in uneven PL coverage. This supports hNSC adhesion observations, where minimal attachment occurs.

Contact angle and protein adsorption results reported; suggest why excellent adhesion and high cell counts of hNSCs cultured on O–NDs is observed.

7.5 CONCLUSIONS

Good adhesion of cells onto biomaterials is paramount in enabling the proliferation and maintaining cellular functions [294]. The dangling sp^2 bonds on the surface of NDs enable precise control over termination [323]. It has been shown that the presence of oxygen containing groups on the surface of NDs has increased hNSC adhesion compared to NDs with hydrogen–termination. A number of factors have been suggested as to why hNSCs have such pronounced adhesion to O–NDs. These include: topography, wettability, surface charge and protein ordering. Modifying biomaterial surfaces in order to create nano–roughness has previously resulted in an increase in cellular adhesion on plastic with an R_q of 5nm [313], the R_q value for ND monolayers is approx. 4 nm. This similarity in nano–roughness is proposed to be ideal for hNSC adhesion. Contact angle values for O–NDs were much lower than TCPS, glass and H–NDs, with and without protein coating. This increase in hydrophilicity is also responsible for the increase in hNSC attachment.

hNSC culture substrates are typically coated in laminin; a large ECM protein. The large size results in engagement with numerous integrin receptors on the NSC surface [321], and therefore an increase in focal adhesion sites. The O–NDs have shown to promote adhesion via an increase in protein adsorption, and it is hypothesised that this increase in LN and PL coverage has led to the development of more available focal adhesion sites. Typically, an increase in hydrophilicity corresponds to a decrease in protein adsorption [315]. Despite this, O–NDs enable the simultaneous increase in hydrophilicity and protein adsorption affinity.

These results suggest that modifications to ND functionalisation provides extensive potential for discovering and exploiting NDs as a bio–material. It is proposed that the interactions of cells with NDs can be controlled via precisely tuning surface functionalisation. The simple sonication process in which objects

are coated, promotes the use of NDs as an *in vivo* biomaterial. Specifically, it is hypothesised that O–NDs are an ideal material choice for the coating of neurological implants in which NSC adhesion is paramount.

CHAPTER 8 – DIFFERENTIATION OF HUMAN NEURAL STEM CELLS ON NANODIAMOND

8.1 INTRODUCTION

Neurodegenerative diseases are acute and chronic conditions, which originate from the death of neurons in the central nervous system (CNS). Conventional treatment for many neurological degenerative diseases may relieve symptoms but rarely terminates the condition [324]. Stem–cell based therapy has the potential to be beneficial for the repair of the CNS through cell replacement and by promoting the survival of affected neurons [325]. The use of human neural foetal tissue in cell–based therapy has been used to treat Parkinson's [289] and Huntington's [326] disease in patients. This approach doesn't provide a practical route to CNS therapeutics due to both the limited availability of human foeti and ethical restrictions. Consequently, extensive research into the use of human neural stem cells (hNSCs) for cell replacement therapies is being undertaken. Stem–cell based therapy is the present standard for the treatment of blood tumours. However, the application of using hNSCs replacement for diseases affecting the CNS is not yet developed and is currently being clinically scrutinised. Despite significant scientific progress since the discovery of hNSCs in 1989 [327], a profound understanding of the basic biology of NSCs is lacking.

Along with increased knowledge, it is imperative that we learn how to manipulate the fate of hNSCs. In order to utilise the potential of stem cells in the field of regenerative medicine, it is essential that we are able to isolate the cells from their natural setting, propagate the cells in culture, and introduce the cells to a foreign environment [287]. To do this, the understanding of how stem cells interact with their natural environment is essential; such environments are termed the stem cell 'niche'. The niche controls stem cell fate [328] through signalling, and by interacting with the support tissue and the extracellular matrix (ECM) [329]. In order to continue developing stem cell therapies, it is critical that stem cell fate can be controlled outside of its natural environment by replicating conditions *in vitro* using model systems [330,331]. An importance of using model systems is the resultant tractability in testing hypotheses for both biomedical applications and fundamental stem cell biology [332]. In order to recreate the stem cell niche, materials which can be precisely controlled are required, with a

broad range of materials being investigated for their stem cell interactions [294,333-335].

As a cell line, hNSCs also offer an irreplaceable resource for studying neurodegenerative diseases, and so it is of uttermost importance that we understand the intra– and extra–cellular mechanisms, which govern the fate of such cells. The central nervous system (CNS) consists of neurons, astrocytes, oligodendrocytes and microglia, all of which are important for maintaining function in the CNS. However, the neuron is often deemed the 'building block' of the CNS due to its role in neurotransmission. Neurons are able to transmit and receive electrical signals, and countless aspects of physiology, behaviour and emotion result from this electrical activity. Therefore, the *in vitro* production of human neurons from hNSCs is fundamental for advances in neuro–regenerative medicine to take place. The potential for expanding foetal derived hNSCs in suspension cultures containing specific growth factors has been explored [336-338]. Growth Factors, which are naturally occurring, stimulate growth, proliferation and differentiation of cells by supporting the transfer of electrical and chemical signals [339]. However, early experiments resulted in the production of neuronal cell neurospheres due to inadequate substrates giving rise to a lack in cellular adhesion. Neurosphere formation is often accompanied by the loss of capacity in which such cells can self–renew and differentiate [340]. Additionally, the identity and quantity of cells inside a neurosphere is unknown which provides difficulties in quantifying results [341]. The long–term differentiation capacity of hNSCs has since been demonstrated [194] and such findings provide a platform in which a range of neurobiological conditions can be studied.

Biomaterials must be biocompatible, they are used to improve function, promote recovery and treat neurological disorders in the CNS. Ideal neural scaffolds are both supportive and bio–active; the engineered tissue should have the capacity to modify function of the implanted cells [342]. In order to greatly improve tissue regrowth in damaged areas of the brain, the biomaterial must induce both endogenous and transplanted NSCs differentiation into neural cells [343]. Diamond has previously shown to be biocompatible and supportive of neuronal cell growth [42,166,167,300]. Nanocrystalline diamond (NCD) films and nanodiamond particles have both shown to be bio–active [73,88]. NCD films have been shown to support hNSC proliferation and differentiation [344]. The interaction of living systems with macroscopic and nanostructured materials is not comparable [271]. Herein, the use of nanodiamond monolayers for the support of

hNSC differentiation has been investigated. Differentiation of the hNSCs has been induced on nanodiamond (ND) monolayers of with different functionalisation. The bio–activity of these ND monolayers has also been scrutinised, with their effect on the spontaneous differentiation of hNSCs being examined. The results show that both hydrogen and oxygen functionalised NDs (H–NDs + O–NDs) support the differentiation of hNSCs into neurons, with attachment significantly higher on O–NDs. The induced differentiation was less successful into oligodendrocytes on both substrates, with very little attachment being observed. Spontaneous differentiation of hNSCs on nanodiamond monolayers yielded neuronal cells on both H–NDs and O–NDs, this is the first time this has been observed. Encouraging the differentiation of hNSCs into neurons is important for applications where conditions mimicking the stem cell 'niche' are required. Neurite extension of differentiated neurons was considerably higher on O–NDs, complimenting results obtained in Chapter 7. The demonstrated capacity of O–NDs for increasing adhesion, encouraging neuronal differentiation and stimulating neuronal network formation, promotes their use as a biomaterial for neurological applications.

8.2 METHODS

Citlali Helenes Gonzalez, UCL, plated the hNSCs. Alice Taylor performed all other experimental activities and analysis presented in this chapter.

8.2.1 SUBSTRATE PREPARATION

Chemicals used, monolayer nanodiamond diamond coatings and the methods for producing hydrogen and oxygen–terminated surfaces are as previously described in Chapter 7 (section 7.2.1 – 7.2.4). Nanodiamond and glass substrates were then coated with poly–L–lysine (PL) and laminin (LN) prior to cell culture. (As previously described in section 7.2.9 – Cell attachment and morphology assay).

8.2.2 hNSC Isolation and Culture

(As previously described in section 6.2.5 – hNSC Isolation and Culture). All procedures involving human tissue were carried out in accordance to the Human Tissue Act 2006. The preparation of neural cell cultures was performed in close collaboration with the Developmental Biology Unit, Institute of Child Health, UCL by Citlali Helenes Gonzalez.

8.2.3 Inducing the differentiation of hNSCs into neurons

For neuronal differentiation hNSC were plated on the (PL + LN) coated glass and ND substrates in normal expansion medium. After 3 DIV EGF, FGF2 and herapin is removed from the medium, this removal inhibits self–renewal and induces differentiation. Neuron maturation was then induced by culturing in Neurobasal A medium supplemented with 1% Penicillin/Streptomycin, 1% L-Glutamine, 2% B27 and 10ng/ml human recombinant βNGF with 10 ng/ml human recombinant BDNF (both Peprotech) for another 2 weeks. The change in medium composition for inducing neuronal differentiation is summarised in Table 8.1 below.

hNSC medium	3 DIV	12 DIV
1% P/S	DMEM/F12	
1% N2	10uM Forskolin	
2% B27	2mM VPA	Neurobasal medium
1% BSA5	5mM KCL	1% P/S
0.05% Hep	1uM Hydrocortisone	2% B27
0.025% FGF2	5ug/ml Insulin	1% L-Glu
0.025% EGF		
1% Laminin	1% P/S	

Table 8.1 Showing the standard medium for hNSC culture, along with the medium change and the corresponding DIV for inducing neuronal differentiation.

8.2.4 INDUCING THE DIFFERENTIATION OF HNSCS INTO OLIGODENDROCYTES

For oligodendrocytic differentiation hNSC were plated on the (PL + LN) coated glass and ND substrates in normal expansion medium. The next day, the medium was changed to DMEM/F12 supplemented with 1% Penicillin/Streptomycin, 1% N2 supplement, 10 nM forskolin, 10 ng/ml FGF2 and 10 ng/ml PDGFaa (Peprotech) for 14 days. On day 15 the medium was switched to DMEM/F12 supplemented with 1% Penicillin/Streptomycin, 1% N2 supplement, 30ng/ml tri-iodothyronine (T3), 200 µM ascorbic acid and 10 ng/ml PDGFaa. After another 7 days, PDGFaa was withdrawn from the culture media to allow maturation of cells. hNSC isolation, confirmation and differentiation potential extremely important as it allows for the development of cell based therapies to continue [46]. The change in medium composition for inducing oligodendrocyte differentiation is summarised in Table 8.2 below.

hNSC medium	1 DIV	15 DIV	22 DIV
1% P/S	DMEM/F12	DMEM/F12	DMEM/F12
1% N2	1% P/S	1% P/S	1% P/S
2% B27	1% N2	1% N2	1% N2
1% BSA5	10 µM Forskolin	30 ng/ml T3	30 ng/ml T3
0.05% Hep	10 ng/ml FGF2	200 µM ascorbic acid	200 µM ascorbic acid
0.025% FGF2	10 ng/ml PDGFaa	10 ng/ml PDGFaa	
0.025% EGF			
1% Laminin			

Table 8.2 Showing the standard medium for hNSC culture, along with the medium change and the corresponding DIV for inducing oligodendrocytic differentiation.

8.2.5 SPONTANEOUS DIFFERENTIATION OF HNSCS

For enabled spontaneous differentiation of hNSCs the assay commences with normal culture conditions until day 3 when, when the growth factors and herapin are removed. The new growth factor free medium is changed every 3–4 days, and the cells were left to develop for 25 days in total. This is summarised in Table 8.3 below:

hNSC medium	3 DIV
1% P/S	1% P/S
1% N2	1% N2
2% B27	2% B27
1% BSA5	1% BSA5
0.05% Hep	1% Laminin
0.025% FGF2	
0.025% EGF	
1% Laminin	

Table 8.3 Outlining the medium change used for the spontaneous differentiation culture.

8.2.6 IMMUNOCYTOCHEMISTRY

For immunocytochemistry hNSCs were seeded on glass cover slip controls or ND monolayers with both H–and O–termination. The cells were fixed with 4% (w/v) paraformaldehyde (PFA) solution in PBS, pH=7.4 for 15 min at RT prior to immunocytochemical protein detection. After three rinses with PBS the cells were incubated with blocking solution composed of 10% (v/v) FBS, 3% (w/v) BSA in PBS with 0.2% (v/v) TritonX-100 for 1h at RT to permeabilize cell membranes. Primary and secondary antibodies were diluted in blocking solution and the incubation times were overnight at 4°C for primary, and 1h at RT for secondary antibodies. Hoechst 33258 (2µg/ml) was added during secondary antibody

incubation to counterstain cell nuclei. After final three washes in PBS the coverslips were mounted on slides with an aqueous based mounting medium (Hydromount, National Diagnostics). Primary and secondary antibodies used can be seen in Table 8.4 below. Images were acquired using an inverted microscope Olympus IX71 (Carl Zeiss, Jena, Germany) equipped with a Hamamatsu ORCA-ER digital camera (Hamamatsu Corp., Bridgewater, NJ). Image processing was done using Fiji.

a) Primary antibody staining:

Name	Host	Company	Cat. Number
MAP2	Mouse	Life Technologies	13–1500
NF200	Rabbit	Sigma	N4142
NEUN	Mouse	Millipore	MAB377
DCX	Rabbit	Invitrogen	48–1200
Nestin	Rabbit	Millipore	ABD69
βIII–Tub	Mouse	Promega	G712A
O4	Mouse	Millipore	MAB345

b) Secondary antibody staining:

Name	Host	Conjugated Flurochrome	Company	Cat. Number
anti rabbit	Donkey	Alexa568	Molecular Probes	A–110042
anti mouse IgG	Rabbit	Alexa488	Molecular Probes	A–21202
anti mouse IgM	Mouse	Alexa594	Molecular Probes	A–21044

Table 8.4 (a) Primary Antibodies and (b) Secondary Antibodies used throughout for specific hNSC, neuronal and oligodendrocytic fluorescent staining.

8.2.7 NEURITE TRACING

Simple Neurite Tracer (SNT) software was used for the analysis of neurite length after the spontaneous differentiation culture of hNSCs on glass, O–NDs and H–NDs. SNT is a semi automated application which is able to trace neurites, construct complex neuronal topology and provide quantitative data on morphology [196]. The software is available as a plugin in open source Fiji. The SNT was used to measure neurite length precisely on fluorescently stained images. Three fluorescently tagged proteins were use to compare the maturity of the differentiation on the three substrates. MATLAB 2012a software was used to perform ANOVA analysis on the neurite lengths of each substrate. Neurite tracing was performed on at least 10 images per sample set, taken at random for all fluorescent stains for each substrate type. The images used were at a magnification of 40x. due the increased accuracy of tracing neurite length at a higher magnification.

8.3 RESULTS

8.3.1 INDUCED DIFFERENTIATION OF HNSCS INTO NEURONS

Fluorescently stained images of neurons, which have been subject to induced differentiation from hNSCs after 25 DIV can be seen in (Figure 8.1). Monolayers of untreated NDs are used for the initial culture, with TCPS being the control. Neurons in (Figure 8.1) have been stained for Nestin, MAP2 and Hoechst. Nestin is a protein abundant in nerve cells, especially during the radial growth of axons, MAP2 is a neuronal specific marker enriched in dendrites and Hoechst is used to stain DNA in the nuclei of cells. Neurons differentiated on both substrates have developed extended neurite processes, however a higher confluency is observed on the NDs compared to the TCPS. The neuronal adhesion on the TCPS is not confluent; neurons are adhering to themselves in a patchy conformation. The presence of MAP2 and Hoechst is more uniform on neurons that have been differentiated on NDs (Figure 8.1 right column). The confluent attachment of neurons and neurites on NDs indicates that it is a substrate suitable for the differentiation of hNSCs into neurons. Fluorescently labelled images suggest that the NDs are promoting neural extension to occur over the surface, as neurites

developed is uniform and pronounced. It is suggested that bio–active nature of the NDs is encouraging neurite outgrowth.

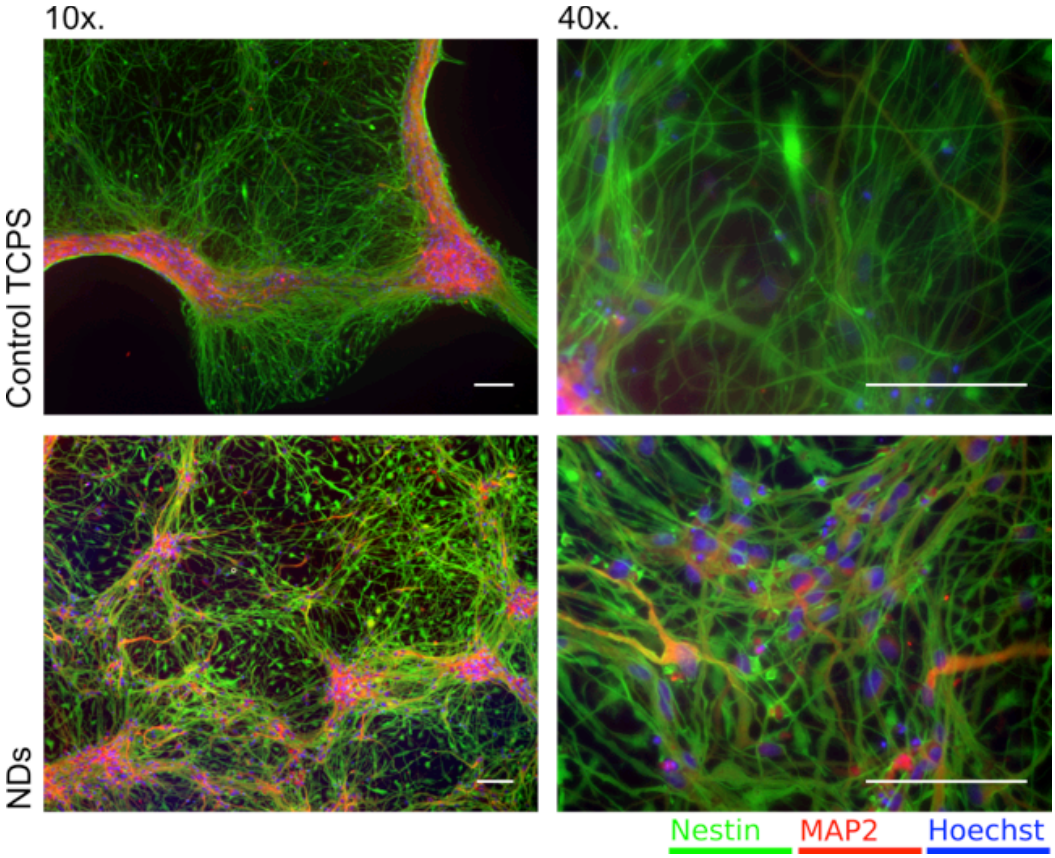

Figure 8.1 Fluorescently stained images of neurons, which have been inductively differentiated from hNSCs after 25 DIV on NDs and TCPS (control). Various growth factors are used to manipulate cell fate (Table 8.1). Successful neuronal differentiation is observed, and neurons have been stained using Nestin, MAP2 and Hoechst. The neuronal attachment is confluent on the NDs, clustering of neurons is observed on the TCPS control, indicating poor adhesion. Scale bar 100 µm.

The induced differentiation of hNSCs into neurons was then performed on functionalised NDs (O and H). Images shown in (Figure 8.2) show differentiated neurons which have been stained for NF200, MAP2 (Figure 8.2 a) and Hoechst and NeuN, DCX and Hoechst (Figure 8.2 b). NF200 is present in neural

processes; specifically axons, MAP2 is abundant in dendrites and Hoechst is used to stain DNA in the nuclei. A large difference is observed between neurons that have been cultured on all three substrates. Complimenting results obtained in Chapter 7, the O–NDs are the most suitable platform for hNSCs to adhere and differentiate. Neurons were successfully differentiated from hNSCs and process extension of neurites containing MAP2 and NF200 is significantly more pronounced on O–NDs, compared to TCPS and H–NDs (Figure 8.2 a).

NeuN is present in mature neurons, whereas DCX is expressed during the division of neural precursor cells and so is observed at a much earlier stage of neuron development. DCX presence is not observed in neurons differentiated from hNSCs on TCPS or H–NDs; however, small quantities of DCX are present in neurites developed on O–NDs (Figure 8.2 b). NeuN has not been detected on any substrate, indicating that the differentiated neurons are lacking in maturity even after 25 DIV.

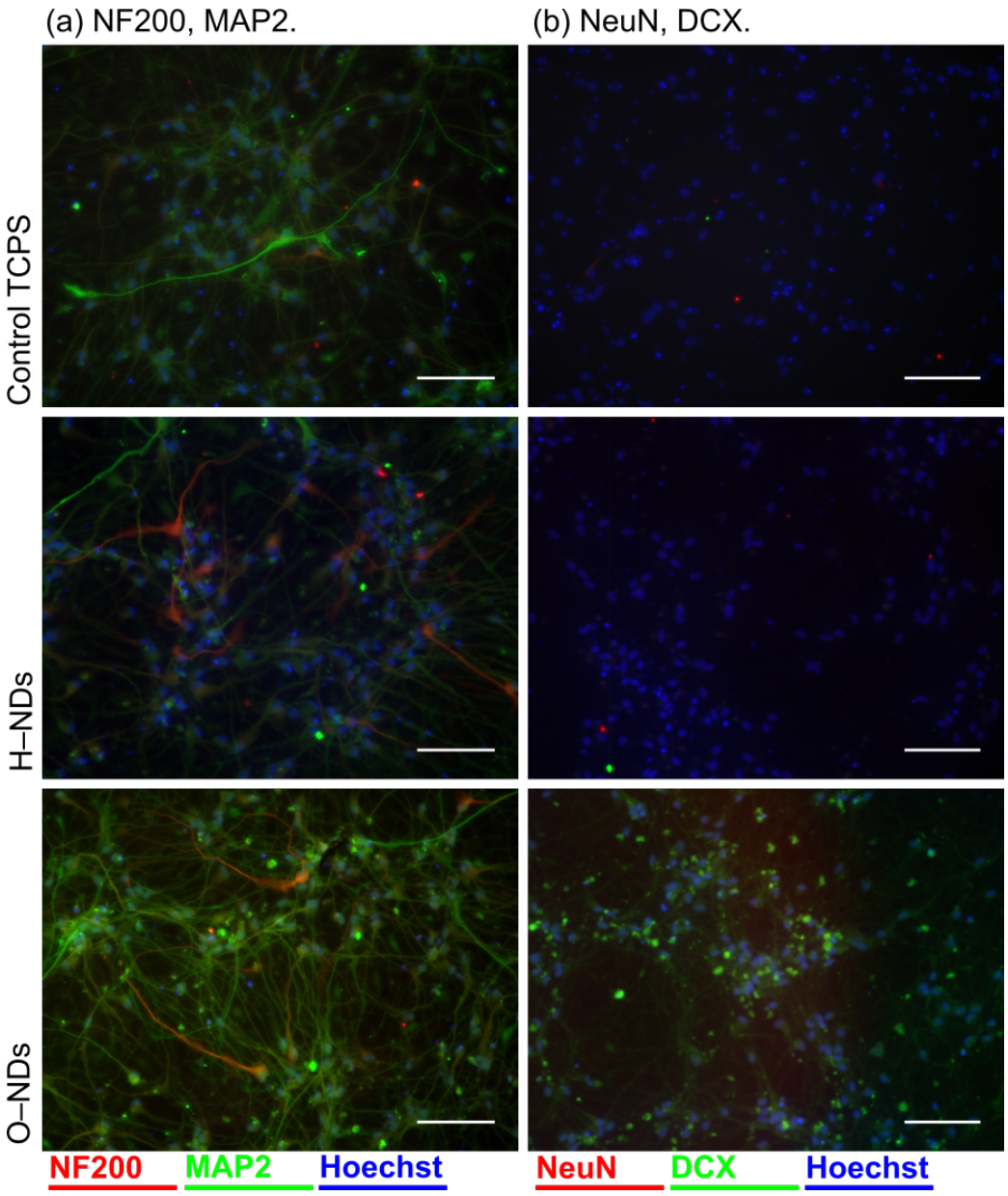

Figure 8.2 Fluorescently stained images of neurons, which have been inductively differentiated from hNSCs after 25 DIV. Growth factors used to manipulate cell fate can be found in (Table 8.1). Cells have been cultured on H–NDs, O–NDs and a TCPS control. Successful differentiation into neurons is observed on all three substrates, however maximum coverage and neurite extension is present on O–NDs. Differentiated neurons have been stained using neuronal markers NF200, MAP2 and Hoechst, and NeuN, DCX and Hoechst. Scale bar 100 μm.

8.3.2 INDUCED DIFFERENTIATION OF HNSCS INTO OLIGODENDROCYTES

Fluorescently stained images showing the induced differentiation of hNSCs into oligodendrocytes after 25 DIV, on TCPS and ND substrates, with and without (PL+LN) protein coating, are shown in (figure 8.3). All substrates show positive O4 staining, which is frequently used for oligodendrocyte marking as it is often the earliest recognised protein present in oligodendrocytic cells. TCPS (PL+LN) is the best substrate for supporting oligodendrocytic differentiation, as confluent oligodendrocyte adhesion is observed. Non–confluent attachment can be seen on the other three substrates (NDs with and without (PL+LN) and TCPS (no coating)). This increased attachment on TCPS (PL+LN) demonstrates that the protein coating is promoting oligodendrocyte adhesion. The attachment of oligodendrocytes on TCPS (no coating) and ND (PL+LN) is comparable. Despite the coverage on TCPS (no coating) being more than ND (PL+LN), there is evidence that the oligodendrocytes are extending their processes over both surfaces despite the patchy adhesion. The least supportive substrate is ND (no coating), as the oligodendrocytes have formed a sphere of cells, indicating minimal adhesion to substrate. DCX is a protein associated with immature neuronal cells; mature oligodendrocytes don't contain DCX. There is much less DCX present on the TCPS (PL+LN) compared to the other three substrates, this indicated that not only are the oligodendrocytes adhering better to this substrate, they are also more mature.

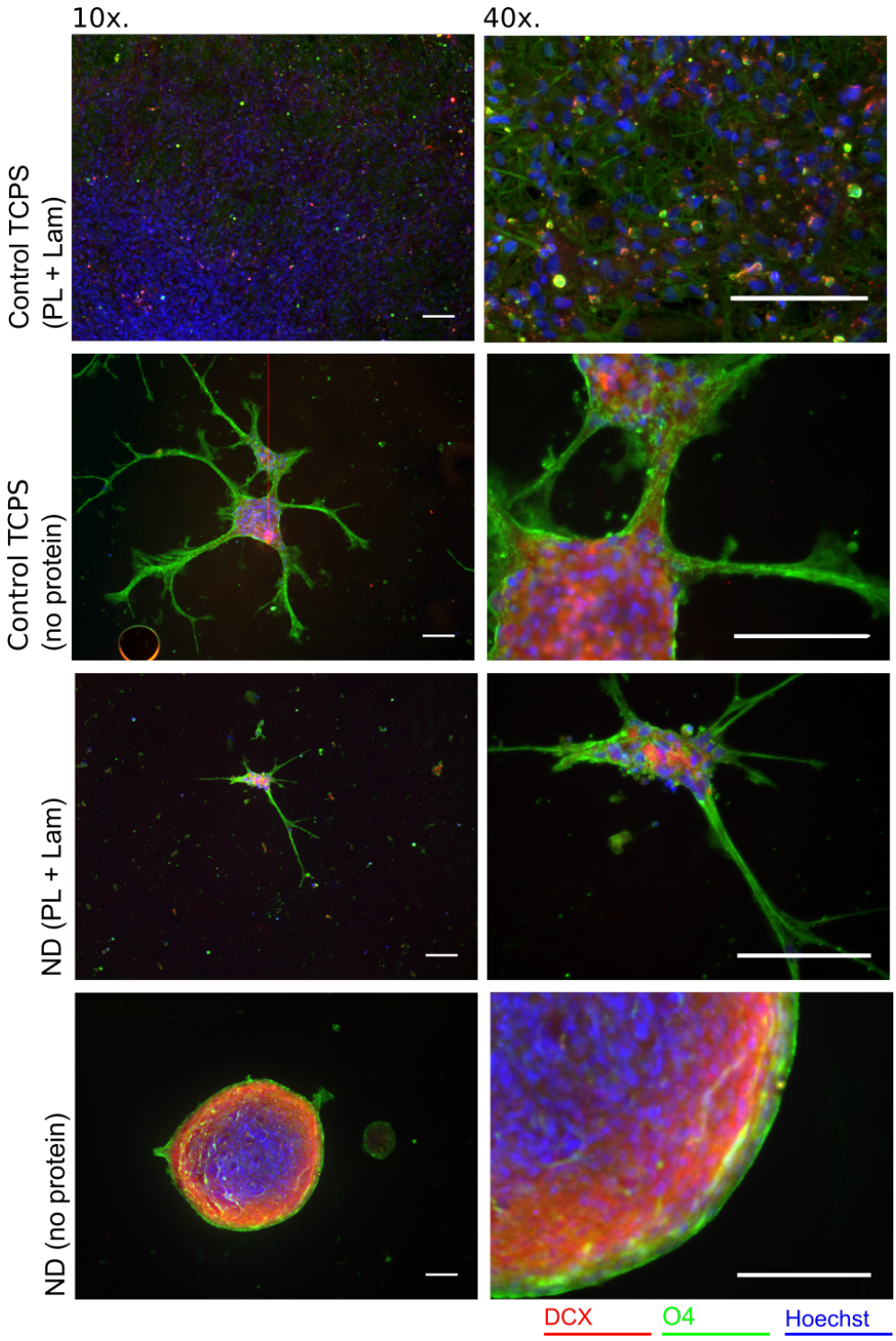

Figure 8.3 Induced oligodendrocyte differentiation from hNSCs on TCPS and ND substrates with and without poly-L-lysine and laminin (PL+LN) coating. DCX is stained in red, O4 in green and Hoechst in blue. A confluent attachment is observed on Control TCPS (PL+LN), highlighting a substrate, which is suitable for oligodendrocyte adhesion, the other three substrates have patch coverage, being less suited. Scale bar 100 µm.

8.3.3 SPONTANEOUS DIFFERENTIATION OF HNSCS ON NANODIAMOND MONOLAYERS

After 25 DIV without differentiation inducing reagents, hNSCs were fixed and stained with two combinations of fluorescent markers. The first are labelled with NeuN, DCX and Hoechst (Figure 8.4) and the second NF200, MAP2 and Hoechst (Figure 8.5). These fluorescent images were subsequently used for neurite tracing using the Simple Neurite Tracer (SNT), a plugin of Fiji software. Statistical analysis was performed using the one–way analysis of variance (ANOVA) test, which is shown in (Figure 8.6).

Fluorescently stained images of hNSCs after 25 DIV are shown using immunostaining of NeuN (red), DCX (green) and Hoechst (blue) (Figure 8.4 a) on the glass control and both H– and O–NDs. NeuN is expressed in neural cells with significantly more maturity than neural precursor cells. Hoechst is used to stain DNA in the nuclei. DCX is expressed during the division of immature neural precursor cells. The obvious presence of NeuN on the glass control and both H– and O–NDs implies that the hNSCs have spontaneously differentiated into neurons without any inducing factors being present in the medium. The small quantities of DCX expressed on all three substrates suggest that the hNSCs are mature in their development with minimal division of precursor cells occurring.

Similarly, images in (Figure 8.5 a) show the presence of NF200, MAP2 and Hoechst on same three substrates. NF200 is a protein present in neurofilaments and is expressed mature axons; it is responsible for the regulation of axonal width. MAP2 is a protein associated with the crosslinking of microtubules, and is enriched in dendrites. The presence of both MAP2 and NF200 suggests that the spontaneously differentiated hNSCs are neurons, which after 25 DIV are already expressing signs of maturity.

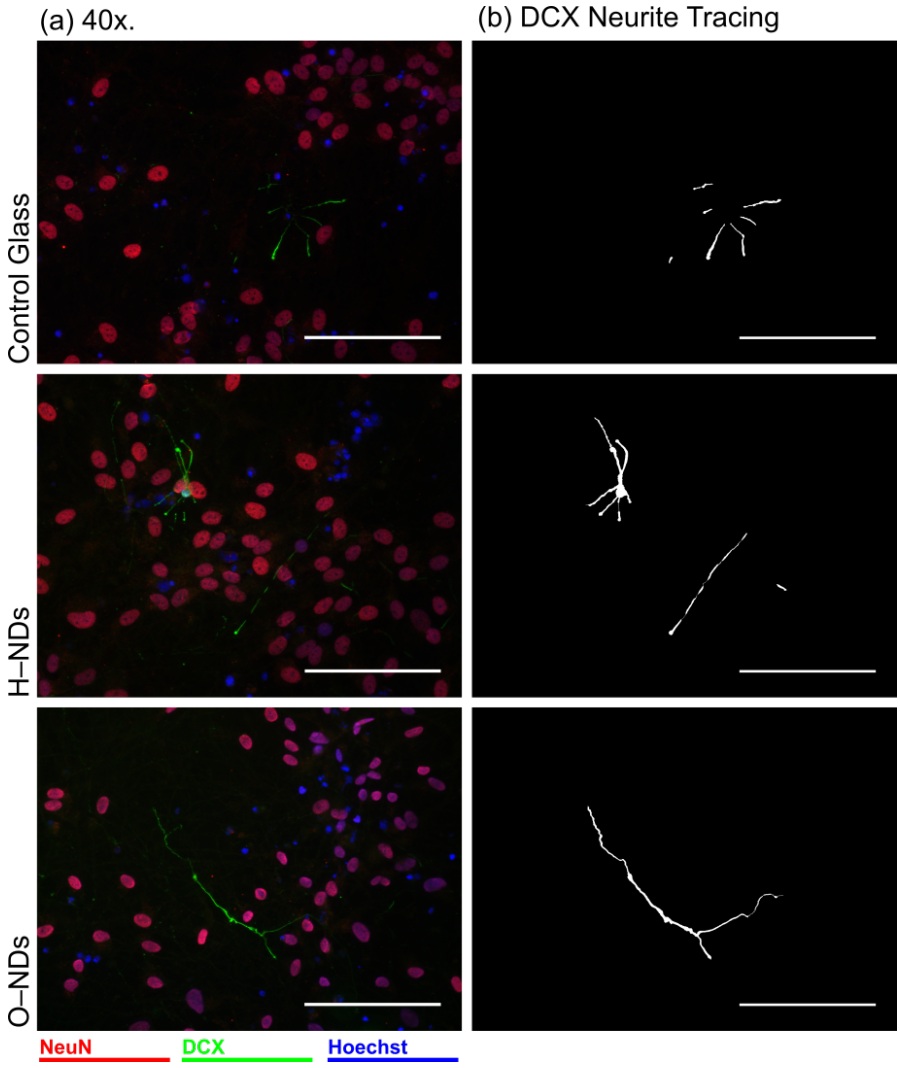

Figure 8.4 (a) Fluorescently stained images of neurons, which have been spontaneously differentiated from hNSCs after 25 DIV. Neurons have been stained using NeuN (red), DCX (green) and Hoechst (Blue). (b) Example images after neurite–tracing analysis that has been performed on neurites that have been stained for DCX. Scale bar 100 μm.

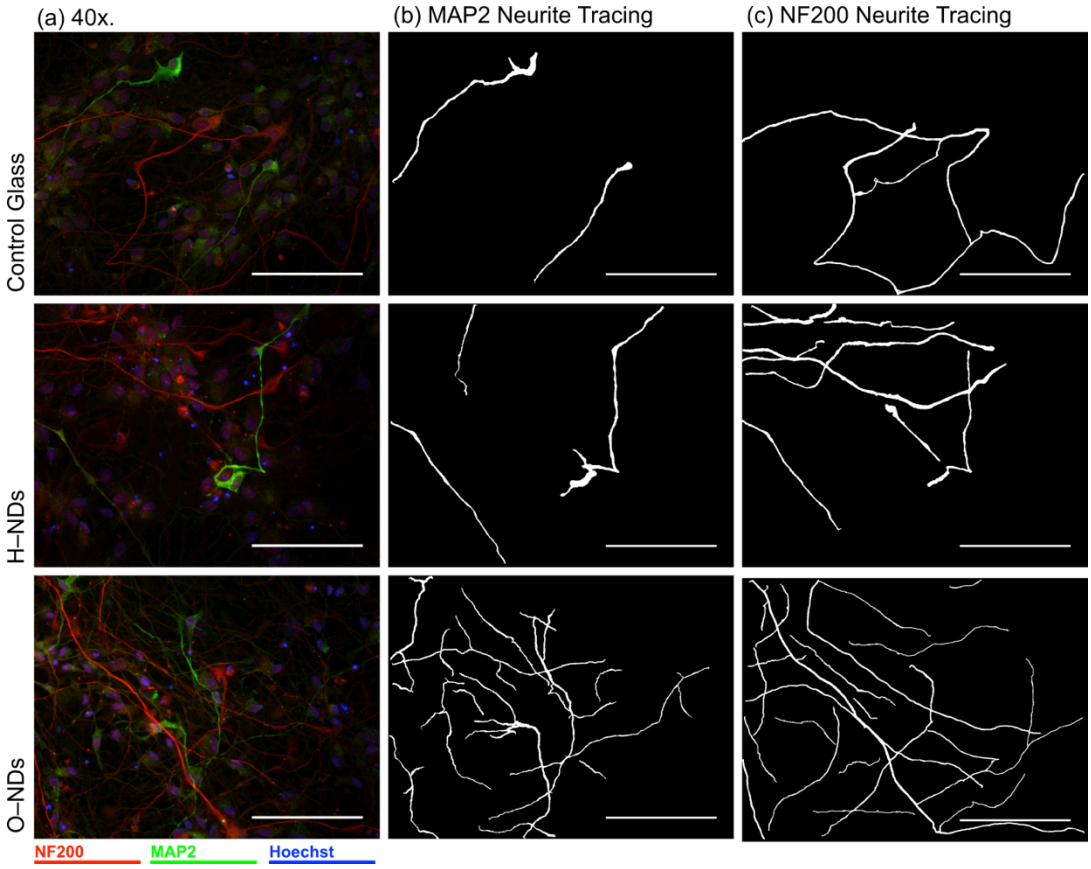

Figure 8.5 (a) Fluorescently stained images of neurons, which have been spontaneously differentiated from hNSCs after 25 DIV. Neurons have been stained using NF200 (red), MAP2 (green) and Hoechst (Blue). (b + c) Example images after neurite–tracing analysis that has been performed on neurites that have been stained for: MAP2 (b) and NF200 (c). Scale bar 100 µm.

ANOVA analysis of tracing revealed that neurite extension and length was significantly higher on O–NDs than the glass control and H–NDs. DCX expression was calculated to be (2.47×10^3 µm/mm) on O–NDs compared to (2.11×10^3 µm/mm) H–NDs and (1.10×10^3 µm/mm) glass control, obtaining a p–value of 0.0475. Multicompare analysis concluded that a statistical difference was observed between the O–NDs and glass control only (Figure 8.6 a + d).

Neurite length expressing MAP2 was calculated to be (1.61×10^4 µm/mm) on O–NDs compared to H–NDs (1.20×10^4 µm/mm) and glass control (3.05×10^3 µm/mm), with an extremely low p–value of 5.77×10^{-4} being observed. Statistical difference

was shown between the glass control and both H– and O–NDs, but no difference in H– and O–NDs was shown (Figure 8.6 b + d).

Neurite length expressing NF200 was again highest on O–NDs ($2.30x10^4$ µm/mm) compared to glass ($1.28x10^4$ µm/mm) and H–NDs ($8.59x10^3$ µm/mm), p–value $1.48x10^{-5}$. Statistical difference observed between neurite length of NF200 on O–NDs with the glass control and H–NDs (Figure 8.6 c + d).

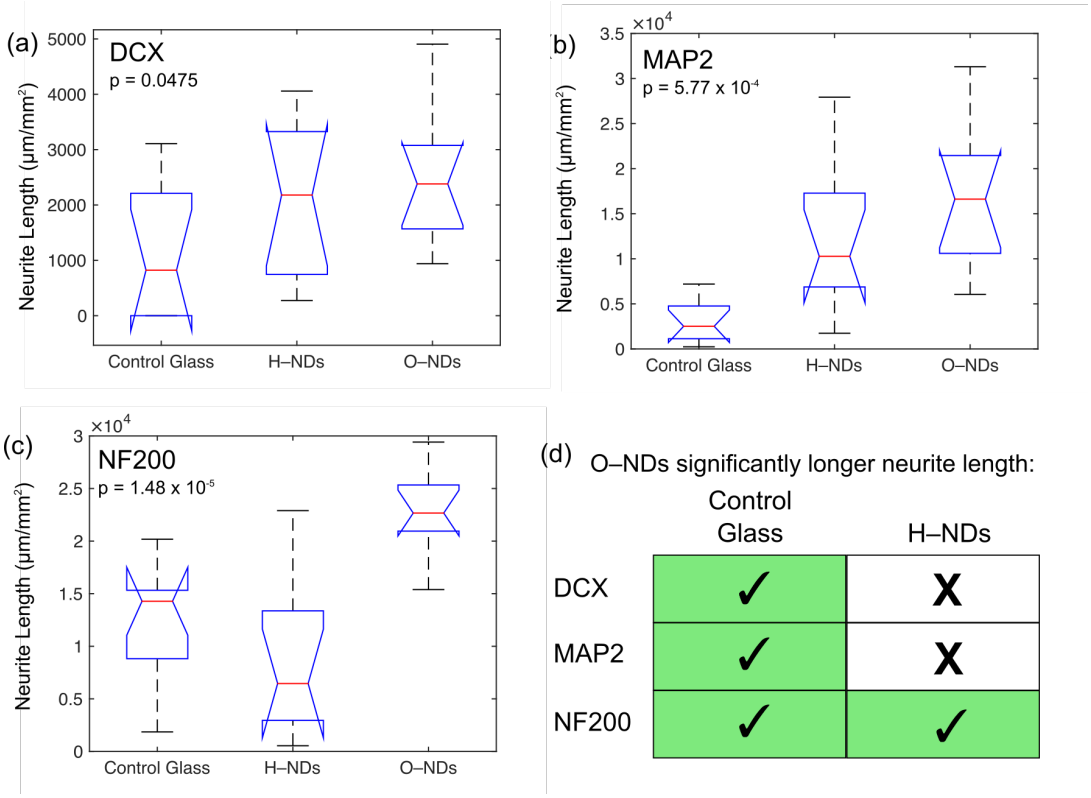

Figure 8.6 ANOVA analysis displayed as a boxplot for the length of neurites calculated using SNT on glass, H–NDs and O–NDs for: (a) DCX, (b) MAP2 and (c) NF200 staining. The medians are shown as a red horizontal line, blue horizontal lines represent upper and lower quartiles, with blue notches signifying confidence interval around the median. Black lines show the range of neurite lengths per stain. p–values for calculated neurite length are shown in the top left corner. (d) Multicompare analysis shown in a table, which highlights whether a statistically significant higher value has been observed for neurite extension expressed using DCX, MAP2 and NF200 markers, on O–NDs compared to both

Control Glass and H–NDs. Confirmation of this significant difference is shown as a green ticked box, a cross marking that no significance was observed.

8.4 DISCUSSION

The ECM environment within the CNS is responsible for many regulatory functions during development and adulthood. The interaction of the ECM and NSCs is critical for cell growth, migration and differentiation, and this is regulated through ECM signalling [345] and changes to matrix stiffness [346]. Therefore, the specific composition and structure of the ECM is vital in controlling the differentiation of NSCs. Cellular adhesion is fundamental in many biological processes as adhered cells are able to sense, interpret and respond to ECM signalling through interactions between focal adhesion sites and receptors at the cell surface [347,348]. Chemical and physical signals such as: topography, electrostatic charge, hydrophobicity and protein adsorption have critical roles in regulating cell behaviour. Herein, NDs produced by a detonation process [323] have shown to be an excelled substrate for hNSC adhesion, proliferation and differentiation.

8.4.1 NEURONAL DIFFERENTIATION:

Untreated NDs have shown to support the induced differentiation of hNSCs into neurons (Figure 8.1). The adhesion of neural cells is higher and neurite extension is more uniform than on NDs compared to the TCPS control. NDs have previously been classified as bio–active, they have shown to promote the adhesion of neurons without the presence of LN [73], and results obtained in Chapter 7 show that the roughness of NDs contributes towards a material which promotes hNSC adhesion. The confluency and increased adhesion of differentiated neurons on NDs supports the bio–active classification of NDs. Next, the effect of varying ND functionalisation of the differentiation of hNSCs into neurons was investigated. An increased neurite extension was observed on O–NDs compared to H–NDs (Figure 8.2). This also compliments results obtained in Chapter 7 and suggests that the functionalised surface of the NDs are strongly affecting the neural behaviour. O–NDs are encouraging hNSC adhesion and also promoting the neurite outgrowth of differentiated neurons. This demonstrated capacity for

supporting hNSC growth and promotes the use of O–NDs as a coating for neurological implants.

8.4.2 OLIGODENDROCYTIC DIFFERENTIATION:

A major problem encountered whilst using neurological implants is gliosis. Gliosis is the immune response of glial cells that occurs after foreign bodies are discovered in the brain, it is an aggressive immune reaction and leads to glial scarring [156]. Gliosis often occurs on implants in the CNS, and the insulating nature of oligodendrocytes can lead to the failure of such neural prosthetics [158]. It is therefore important that the proliferation of oligodendrocytes is kept to a minimum in order to increase the lifetime of neurological implants whilst simultaneously providing support for electrically active neuronal networks. Unlike NCD which has been shown to promote hNSC differentiation into oligodendrocytes [256], the adhesion of oligodendrocytes on NDs is poor both with and without (PL+LN). TCPS with protein coating (PL+LN) supported the adhesion of differentiated oligodendrocytes (Figure 8.3). The reduction of oligodendrocytic adhesion and differentiation when hNSCs are cultured on NDs also supports their use as a material for coating CNS implants. It is suggested that O–ND coated implants would result in good neuronal adhesion and poor glial cell adhesion, reducing gliosis and therefore, maintaining the performance and increasing lifetime of neurological prosthetic devices.

8.4.3 SPONTANEOUS DIFFERENTIATION:

During the differentiation of hNSCs into neurons, extensive morphological changes occur. As the cells mature neurites emerge, outgrow, branch and connect with other neurites [349]. This series of morphological changes is vital for facilitating neural network function [350]. Directed and intentional axonal and dendritic outgrowth of neuronal processes is imperative in creating new connection pathways in the CNS [351]. Results show that the spontaneous differentiation of hNSCs on glass, H– and O–NDs resulted in neuron formation. Here, SNT analysis was used to determine that neurite extension was significantly higher for neurons, which spontaneously differentiated on O–NDs. Despite the presence of neurite extension on all three substrates, a significant

increase in length of dendrites and axons was observed on O–NDs. This implies that the functional surface is interacting with the neurons and promoting neurite extension, whilst simultaneously maintaining neuron proliferation. Greater neurite length was discovered whist staining for MAP2, NF200 and DCX, and for all three proteins O–NDs resulted in a higher length of neurites per mm^2 (Figure 8.6).

It has been shown that O–NDs monolayers promote the differentiation of hNSCs into neurons with increased neurite length. Results obtained in Chapter 7 demonstrate the importance of ND surface hydrophilicity, topography, protein adhesion and surface charge in manipulating hNSC behaviour. O–NDs have successfully induced the differentiation of hNSCs into neurons by mimicking the natural environment of NSCs. It is hypothesised that the NDs have become bio–active upon oxidation and have facilitated extra–cellular signalling between its surface and the hNSCs, mimicking the stem cell niche and promoting neuronal differentiation.

8.5 CONCLUSION

In order to greatly improve tissue regrowth in damaged areas of the brain, implanted materials must induce both endogenous and transplanted NSCs differentiation into neural cells [343]. When stem cells are removed from their *in vivo* niche, they often differentiate spontaneously inefficiently and uncontrollably when subsequently cultured *in vitro* [352]. The potential for use of stem cells in regenerative medicine lies in the ability to be able to control stem cell fate. This can be done via mimicking the microenvironment in which such cells naturally occur [292]. Topography has been demonstrated to be an important factor in regulating stem cell fate. Herein, a facile method for coating glass with nanodiamonds has been described, and the effect of varying surface functionalisation on hNSC adhesion and differentiation has been investigated. It has been shown that the topography of ND monolayers is an exceptional platform for hNSC adhesion, proliferation and differentiation.

Induced differentiation of hNSCs into neurons was successful on NDs, whereas the conversion of hNSCs into oligodendrocytes was accompanied by cell–sphere formation. This preference for neuronal adhesion was then confirmed via spontaneous differentiation of hNSCs, where inducing factors were removed from the culture medium. This is the first time NDs have been used to investigate the spontaneous differentiation of hNSCs, with extremely promising results being shown.

It was discovered that NDs with oxygen functionalisation promoted adhesion and encouraged the differentiation of hNSCs into neurons without exterior factors. A statistically significant difference was observed in neurite extension on O–NDs over both H–NDs and the glass control. This along with the simple process in which monolayers of NDs are formed, provides promise for the application of coating neural implants with O–NDs. It is hypothesised that O–ND coated implants would promote neurite extension, whilst simultaneously reducing gliosis and thus increasing lifetime and maintaining performance of implanted electrodes in the CNS.

CHAPTER 9 – CONCLUSION

This thesis has demonstrated the potential for diamond as an invaluable material for prosthetic neurological applications. Various forms of diamond have shown to be exceptional at promoting human Neural Stem Cells (hNSC) adhesion, proliferation and differentiation *in vitro*. Boron–doped nanocrystalline diamond (BNCD) has been shown to be biocompatible, and this form of diamond holds great promise for use as a material for *in vivo* applications in the Central Nervous System (CNS). Furthermore, hNSCs have been cultured and differentiated on nanodiamonds (NDs) for the first time. Results obtained emphasize the potential of NDs for interfacing with neural cells. Overall, the use of diamond as a substrate for stem cell biotechnology has been presented.

In Chapter 5 a novel, additive, lithography–free, inert, bottom–up technique for producing ND tracks and nanocrystalline diamond (NCD) patterns with high pattern compliance was described. A lateral patterning resolution of 5 μm and feature widths of 2 μm was achieved without the use of reactive chemicals, allowing for the preservation of ND surface chemistry. The patterning procedure was developed using an ultrasound driven plotter to deposit nanodiamond in glycerol/DI water inks. Printing was optimized by tailoring ink composition, hardware parameters, and micropipette tip diameter in order to produce ND patterns with near–monolayer configuration. The effect of varying ND concentration on ND seeding was studied, and the relationship between tip diameter and dot size identified. Furthermore, low-density ND patterning was demonstrated, which makes this process a valuable method for studying the individual properties of NDs on substrates, for example, in quantum information processing applications, and measuring electrical and physical properties of individual NDs. Post–printing, ink solvents were evaporated off using low-temperature vacuum evaporation to realise NDs in the desired pattern. The resultant ND patterns were used as the nucleation sites for NCD growth; suspending the NDs in glycerol had no observable effects on NCD quality. Pertinently, this patterning technique allows for the selective seeding of NDs on a variety of substrates, including three-dimensional substrates that are not compatible with conventional lithography techniques, with a high degree of control

over the nature of the ND monolayers deposited. This bottom–up method for patterning diamond encourages its potential as an indispensable material for many applications. These include applications in bioelectronics [235], piezoelectric microresonators [236] and photonic crystals [234]. NCD and NDs have been used to pattern neuron adhesion and neurite outgrowth [42,73], and the technique described here provides a simple, high resolution method for spatially controlling neural network formation.

Chapter 6 described the findings of a biocompatibility study, investigating if the inclusion of boron into diamond has any observable effect on human neural stem cell attachment and proliferation. Neurological implants require a material that is both electrically conductive and biocompatible. Boron–doped diamond achieves both of these requirements, as it is semi–conductive and no difference in cell viability upon boron inclusion was observed. These results were confirmed by analysis of immunostained images and the quantitative Methyl Blue (MB) assay. The MB assay allows a specific dye to enter healthy cells; the dye is then eluted and spectrophotometrically measured. Percentage confluency, cell counts and MB data suggest that there is minimal difference between the biocompatibility of TCPS, NCD and BNCD. Furthermore, the impact of nanostructuring the BNCD using CNTs as scaffolds upon hNSC adherence and proliferation was investigated. Herein, it has been shown that nanostructuring of BNCD has a positive effect on cell viability. Given the enhanced capacitance of such nanostructured BNCD electrodes [301], this increase in hNSC viability is very promising for improving the performance of electrodes at the brain–machine interface. Specifically, micro–electrode arrays [165,209,216] and neurological implants [210,259,353] will benefit from this novel material, where high double layer capacitance, low impedance, robust, stable and biocompatible electrodes are desired for investigating the electrical activity of neurons.

Results in Chapter 7 highlighted the potential of ND monolayers as a biomaterial for interfacing with neurological cells. The adhesion of hNSCs on hydrogen and oxygen functionalised NDs was investigated for the first time. It was discovered that O–NDs are superb at supporting hNSC attachment; H–NDs on the other hand, are not. O–NDs promoted hNSC attachment, with near confluent adhesion,

whereas H–ND monolayers resulted in the sporadic adhesion of much fewer cells. Contact angle and protein adsorption measurements were employed to investigate the significant difference observed when culturing hNSCs on H– and O–NDs. It was discovered that the O–NDs were considerably more hydrophilic than H–NDs both with and without protein coating. Protein adsorption showed O–NDs bind readily to poly–L–lysine–coated laminin, whereas H–NDs showed no binding. It is hypothesised that the nano–roughness, hydrophilicity, surface charge and protein adsorption affinity of O–NDs facilitates hNSC adhesion via mimicking the environment in which hNSCs naturally occur. NDs have an sp^3 diamond core, which is surrounded by dangling sp^2 bonds, which can be easily modified by bonding with functional groups of great versatility. The difference in surface functionalisation preference observed herein, suggests that ND surface modification provides extensive potential for discovering and exploiting NDs as a bio–material. It is proposed that the interactions of cells with NDs can be controlled via precisely tuning surface functionalisation. Looking forward, the incorporation of O–NDs into three–dimensional cellular matrixes will be investigated. It is hypothesised that the superior protein adsorption affinity of O–NDs will encourage hNSCs to grow with three dimensional confluence, which is currently proving difficult due to the sensitive nature of the cells. Three dimensional growth is a more accurate representation of how cells grow *in vivo*, which is important when building models of native tissue growth [354]. Encouraging hNSCs to grow evenly throughout ND matrigels will facilitate more accurate research into the modelling of neurological diseases such as Alzheimer's [355] and Parkinson's [356] to take place.

Chapter 8, the final results chapter, demonstrated the capacity of ND monolayers as a substrate for supporting hNSC differentiation. hNSCs were subject to induced differentiation into neurons and oligodendrocytes on NDs. NDs were shown to successfully promote neuronal differentiation, with confluent attachment and extensive neurite formation observed after 25 DIV. Differentiation into oligodendrocytes led to cellular clustering. This preference for neuronal adhesion was then confirmed via a spontaneous differentiation assay. hNSCs were subject to 25 DIV and inducing factors were removed from the culture medium. It was discovered that both H– and O–NDs promoted the spontaneous differentiation of hNSCs into neurons without exterior manipulation. Neurons communicate through complex, electrically active neural networks. Neurite outgrowth is essential for the

facilitation of electrical communication, which is responsible for many invaluable functions including memory, movement and emotion. A statistically significant difference was observed in neurite extension on O–NDs compared to H–NDs and the control. O–NDs promoted excessive neurite extension, implying that the differentiated neurons were electrically communicating. Therefore, O–NDs are proposed to be an excellent substrate for stimulating neural network formation, complimenting results obtained in Chapter 7. The absence in adhesion of oligodendrocytes on NDs suggests that gliosis would be reduced if neurological implants were coated in O–NDs, thus prolonging the lifetime of such implants. Stem cell–based therapy has the potential to be hugely beneficial for the repair of the CNS after injury. For this to happen, it is critical that stem cell fate is controlled. The potential of O–NDs for the treatment of neurological trauma will be investigated.

The constricting blood–brain barrier (BBB) prevents conventional drug delivery systems and the normal immune response of the body from functioning in the CNS. Electronic neurological implants are used in the CNS to help manage symptoms and improve the patient's quality of life. They offer hope to patients who are suffering from debilitating effects of neurological diseases including Parkinson's, Huntington's, macular degeneration and numerous other medical conditions. This thesis has confirmed the biocompatibility of BNCD, presented a novel, simple method for patterning diamond and shown how nanodiamonds fail to support glial cell attachment. These results support the use of diamond, as a material in which neurological implants should be fabricated. Also, the continuous increase in life expectancy is resulting in a population where neurodegenerative diseases are more common. Extensive research is currently being performed to provide treatment and prevention of these diseases. Herein, nanotechnology has been employed as a tool to investigate the effect of treating various neurodegenerative diseases via manipulating cellular behaviour whilst simultaneously minimizing side effects. Throughout this thesis, nanodiamonds have been used as a substrate for interfacing with hNSCs. O–NDs have shown to promote hNSC adhesion and neuronal differentiation, highlighting them as promising material for treating neurodegenerative diseases, and further investigation into their cellular interactions will be conducted.

This work represents the first comprehensive study of the interaction of NDs with human neural stem cells with an emphasis on the biotechnological applications of this system. A combination of the novel method described for patterning diamond and the quantification that BNCD is biocompatible confirm the promise of diamond for neuronal implants. The ability of NDs for manipulating hNSC adhesion and differentiation also promote diamond as an indispensable material for stem cell–based treatment and the study of neurological diseases.

FUTURE WORK

Results achieved and presented in this thesis promote the use of diamond in biotechnological applications. A novel technique for patterning nanodiamond (ND) tracks and nanocrystalline diamond (NCD) films has been described. The biocompatibility of NCD has demonstrated retention after boron incorporation. NDs surface functionalisation has shown to significantly affect hNSC adhesion and, the spontaneous differentiation of hNSCs into neurons on NDs has been observed for the first time. Here, a list of future experiments that would lead to exciting extensions to the current study are proposed:

The potential of diamond for patterning neuron adhesion and neurite outgrowth has been shown by others [42,73]. The technique described in Chapter 5 offers the potential to considerably extend this previous work by depositing ND tracks of varying functionalisation on planar Micro–electrode Arrays (MEAs). The aim would be to direct neurite extension over the planar electrodes, to increase the probability of being able to record neuronal electrical activity.

Individual CNTs coated with BNCD electrodes are desired for enabling intra–cellular recording of individual neurons. Forests of CNTs have been successfully grown from 5 nm Ni films using DC plasma CVD (at UCL). However, reliable growth of individual CNTs growth has not yet been achieved. The use of Ni nanoparticles (NiNP) (50 nm) should be investigated for CNT growth. If successful, NiNP should be be dispersed in a DI water ink and subject patterning via microplotting. NiNP concentration would then be investigated, as individual NiNPs are desired in order to grow single CNTs. The SonoPlot® Microplotter will be used to facilitate spatial deposition of NiNPs onto the planar electrodes of MEAs. Results given in Chapter 5 offer the subsequent potential to deposit NDs on top of the CNT, which could then be grown into an NCD film using Microwave Plasma Enhanced CVD (MPECVD) into 3D BNCD nanopillars. The biocompatible, high aspect ratio electrodes would then be used for intra–cellular recording of neurons.

Geometric cues have been shown to influence differentiation of stem cells by altering the focal adhesion sites [357]. The technique developed in Chapter 5 could be used to pattern O–NDs in an array of shapes. The effect of hNSCs differentiation on these geometric forms could then be investigated. O–NDs could also be used to pattern lines of different width, and these used to investigate the relationship between thickness of ND track and neurite outgrowth.

Work in this thesis has shown that O–NDs are a superior material for interfacing with hNSCs and initial results suggest that H–NDs are more suited for Adipose Stem Cell (ASC) adhesion. ASCs are stem cells that can be harvested directly from adult adipose tissue, more commonly known as body fat. They were discovered in 2002 [358] and have the capacity to differentiate into a diverse array of adult cells including: bone, cardiac, cartilage and neurons [359]. All adults have adipose tissue and an advantage for using ASCs in stem cell therapy is that the patient's own cells can be used; therefore reducing the probability of tissue rejection. Further research should take place investigating the adhesion, proliferation and differentiation of ASCs with H– and O–NDs.

The success in using Bio–layer Interferometry (BLI) for investigating ND–protein binding will lead to further exciting experiments. Preliminary experiments have shown that H–NDs bind to laminin (LN) coated sensors (without poly–L–lysine (PL)), whereas O–NDs do not. This difference in binding suggests that H–NDs will promote the uniform attachment of LN without PL being present. Therefore, it is hypothesised that the adhesion of hNSCs will be significantly higher for laminin coated substrates on H–NDs than O–NDs The removal of PL from the culture protocol is beneficial for experimental simplicity: this should be investigated. The binding of amino functionalised NDs and (PL/LN) will also be explored.

The reported success of O–NDs for hNSC adhesion and neurite extension should promote the use of O–NDs for stem cell therapy applications. In order to increase knowledge about various neurodegenerative diseases, three–dimensional modelling *in vitro* is required. At present, the three–dimensional culture of hNSCs is proving difficult due to their sensitive nature and their preference to form

neurospheres when subject to various matrigels. O–NDs should be employed to encourage uniform spatial growth of hNSCs in three–dimensional environments by conjugating the O–NDs with PL and LN, and then dispersing these throughout the cell support scaffold. The use of NDs in matrigels will also be used to investigate ASC adhesion and differentiation in a three–dimensional environment. Indeed, initial experiments have begun at UCL.

The future work stemming from the thesis will be challenging, but successful results obtained demonstrate the exciting potential for diamond in biotechnological applications.

REFERENCES

[1] Pauling L 1931 The nature of the chemical bond. Application of results obtained from the quantum mechanics and from a theory of paramagnetic susceptibility to the structure of molecules *J. Am. Chem. Soc.* **53** 1367–400

[2] Hom T, Kiszenik W and Post B 1975 Accurate lattice constants from multiple reflection measurements. II. Lattice constants of germanium silicon, and diamond *J Appl Crystallogr* **8** 457–8

[3] Sussmann R S 2009 CVD *Diamond for Electronic Devices and Sensors* (Wiley)

[4] Davis R F 1993 *Diamond Films and Coatings* (Noyes Publications)

[5] Dundek M 2009 *Diamonds* (Marijan Dundek)

[6] Pierson H O 2012 *Handbook of Carbon, Graphite, Diamonds and Fullerenes* (William Andrew)

[7] Zazula JM. Http://LBruno.web.cern.ch/lbruno/documents/bibliography/lhc_note_78.pfd, 1997

[8] Hannay J B 1879 On the artificial formation of the diamond *Proceedings of the Royal Society of London* **30** 450–461

[9] Malavé A and Oesterschulze E 2006 All-diamond cantilever probes for scanning probe microscopy applications realized by a proximity lithography process *Rev. Sci. Instrum.* **77** 043708

[10] Grotjohn T A, Becker M, Yaran M K and Schuelke T Fabrication and properties of ultranano, nano, and microcrystalline diamond membranes and sheets. *J. Vac. Sci. Technol.* **22** 2811

[11] Hall H T 1958 Ultrahigh-Pressure Research: At ultrahigh pressures new and sometimes unexpected chemical and physical events occur. *Science* **128** 445–9

[12] Bundy F P, Hall H T, Strong H M and Wentorf R H 1955 Man–made Diamonds *Nature* **176** 51–55

[13] Bovenkerk H P, Bundy F P, Hall H T and Strong H M 1959 Preparation of diamond *Nature* **184** 1094–1098

[14] Angus J C, Wang Y and Sunkara M 1991 Metastable growth of diamond and diamond-like phases *Annual Review of Materials Science* **21** 221–48

[15] Naamoun M, Tallaire A, Silva F and Achard J 2012 Etch-pit formation mechanism induced on HPHT and CVD diamond single crystals by H2/O2 plasma etching treatment *Phys. Status Solidi A.* **209** 1715–1720

[16] Eversole W. Synthesis of diamond. US Patent Office. 3,030,187 and 3,003,188.

[17] Angus J C, Argoitia A, Gat R, Li Z, Sunkara M, Wang L and Wang Y 1993 Chemical Vapour Deposition of Diamond *Philosophical Transactions of the Royal Society of London A: Mathematical, Physical and Engineering Sciences* **342** 195–208

[18] Angus J C 1968 Growth of Diamond Seed Crystals by Vapor Deposition *J. Appl. Phys.* **39** 2915

[19] Deryagin B V, Spitsyn B V, Builov L L, Klochkov A A, Gorodetskii A E and Smol'Yaninov A V 1976 Diamond crystal synthesis on nondiamond substrates *Soviet Physics Doklady* **21** 676

[20] Spitsyn B V, Bouilov L L and Derjaguin B V 1981 Vapor growth of diamond on diamond and other surfaces *Journal of Crystal Growth* **52** 219–226

[21] Matsumoto S, Sato Y, Kamo M and Setaka N 1982 Vapor Deposition of Diamond Particles from Methane *Jpn. J. Appl. Phys.* **21** L183–5

[22] Kamo M, Sato Y, Matsumoto S and Setaka N 1983 Diamond synthesis from gas phase in microwave plasma *Journal of Crystal Growth* **62** 642–4

[23] Matsumoto S 1985 Chemical vapour deposition of diamond in RF glow discharge *J Mater Sci Lett* **4** 600–2

[24] May P W 2000 Diamond thin films: a 21st-century material *Philosophical Transactions of the Royal Society A: Mathematical, Physical and Engineering Sciences* **358** 473–95

[25] Liu H and Dandy D S 1996 *Diamond Chemical Vapor Deposition: Nucleation and Early Growth Stages* (Noyes)

[26] Morrish A A and Pehrsson P E 1991 Effects of surface pretreatments on nucleation and growth of diamond films on a variety of substrates *Applied Physics Letters* **59** 417

[27] Ravi K V and Koch C A A P L Nucleation enhancement of diamond synthesized by combustion flame techniques *Applied Physics Letters* **57** 348

[28] Robertson J 1995 Mechanism of bias-enhanced nucleation and heteroepitaxy of diamond on Si *Diamond & Related Materials* **4** 549–52

[29] Iijima S, Aikawa Y and Baba K Early formation of chemical vapor deposition diamond films *Applied Physics Letters* **57** 2646–2648

[30] Kim J H, Lee S K, Kwon O M and Lim D S 2009 Ultra thin CVD diamond film deposition by electrostatic self-assembly seeding process with nano-diamond particles. *J. Nanosci. Nanotech.* **9** 4121–7

[31] Field J E 1992 *The Properties of Natural and Synthetic Diamond* (Academic Press)

[32] Wörner E, Wild C, Müller-Sebert W, Locher R and Koidl P 1996 Thermal

conductivity of CVD diamond films: high-precision, temperature-resolved measurements *Diamond & Related Materials* **5** 688–92

[33] Sussmann R S 2009 *CVD Diamond for Electronic Devices and Sensors* (John Wiley & Sons)

[34] Isberg J, Hammersberg J, Johansson E, Wikström T, Twitchen D J, Whitehead A J, Coe S E and Scarsbrook G A 2002 High carrier mobility in single-crystal plasma-deposited diamond. *Science* **297** 1670–2

[35] Wild C, Wörner E. The CVD diamond booklet. Diamond materials. 2008.

[36] Khounsary A M and Kuzay T M 1992 On diamond windows for high power synchrotron X-ray beams *Nuclear Instruments and Methods in Physics* **319** 233–239

[37] Hazen R M 1999 *The Diamond Makers* (Cambridge University Press)

[38] Szunerits S and Boukherroub R 2007 Different strategies for functionalization of diamond surfaces *J Solid State Electrochem* **12** 1205–18

[39] Pleskov Y V 2002 Electrochemistry of Diamond: A Review - Springer *Russian Journal of Electrochemistry* **38** 1275–1291

[40] Rezek B, Ukraintsev E, Michalíková L, Kromka A, Zemek J and Kalbacova M 2009 Adsorption of fetal bovine serum on H/O-terminated diamond studied by atomic force microscopy *Diamond & Related Materials* **18** 918–22

[41] Grieten L, Janssens S D, Ethirajan A, Bon N V, Ameloot M, Michiels L, Haenen K and Wagner P 2011 Real-time study of protein adsorption on thin nanocrystalline diamond *phys. stat. sol. (a)* **208** 2093–8

[42] May P W, Regan E M, Taylor A, Uney J, Dick A D and Mcgeehan J 2012 Spatially controlling neuronal adhesion on CVD diamond *Diamond & Related Materials* **23** 1–5

[43] Rezek B, Michalíková L, Ukraintsev E and Kromka A 2009 Micro-pattern guided adhesion of osteoblasts on diamond surfaces *Sensors* **5** 3549–3562

[44] Hopper A P, Dugan J M, Gill A A and Fox O 2014 Amine functionalized nanodiamond promotes cellular adhesion, proliferation and neurite outgrowth *Biomedical Materials* **9** 045009

[45] Teraji T 2006 Chemical vapor deposition of homoepitaxial diamond films *phys. stat. sol. (a)* **203** 3324–57

[46] Kalish R 1999 Doping of diamond *Carbon* **37** 781–785

[47] Borst T H and Weis O 1996 Boron-Doped Homoepitaxial Diamond Layers: Fabrication, Characterization, and Electronic Applications *phys. stat. sol. (a)* **154** 423–44

[48] Wentorf R H Jr and Bovenkerk H P 1962 Preparation of Semiconducting

Diamonds *The Journal of Chemical Physics* **36** 1987–1990

[49] Yamanaka S, Watanabe H and Masai S 1998 High-Quality B-Doped Homoepitaxial Diamond Films using Trimethylboron *Japanese Journal of Applied Physics* **37** 1129–1131

[50] Mortet V, Daenen M, Teraji T, Lazea A, Vorlicek V, D'Haen J, Haenen K and D'Olieslaeger M 2008 Characterization of boron doped diamond epilayers grown in a NIRIM type reactor *Diamond & Related Materials* **17** 1330–4

[51] Volpe P-N, Pernot J, Muret P and Omnes F 2009 High hole mobility in boron doped diamond for power device applications *Appl. Phys. Lett.* **94** 092102

[52] Bustarret E, Achatz P, Sacépé B, Chapelier C, Marcenat C, Ortéga L and Klein T 2008 Metal-to-insulator transition and superconductivity in boron-doped diamond *Philosophical Transactions of the Royal Society A: Mathematical, Physical and Engineering Sciences* **366** 267–79

[53] Nishimura K, Das K and Glass J T 1991 Material and electrical characterization of polycrystalline boron-doped diamond films grown by microwave plasma chemical vapor deposition *J. Appl. Phys.* **5** 3142–3148

[54] Ushizawa K, Watanabe K, Ando T, Sakaguchi I, Nishitani-Gamo M, Sato Y and Kanda H 1998 Boron concentration dependence of Raman spectra on {100} and {111} facets of B-doped CVD diamond *Diamond & Related Materials* **7** 1719–22

[55] Saha P, Kundoo S, Banerjee A N and Chattopadhyay K K 2003 Synthesis of boron–doped diamond films by DC plasma CVD using a CH4+CO2+H2 gas mixture at lower substrate temperature and formation of an n-Si/p-diamond heterojunction *Vacuum* **72** 129–34

[56] Kalish R 1997 Ion-implantation in diamond and diamond films: doping, damage effects and their applications *Applied Surface Science* **117** 558–569

[57] Kalish R 2001 The search for donors in diamond *Diamond & Related Materials* **10** 1749–55

[58] Popovici G and Prelas M A 1995 Prospective n-type impurities and methods of diamond doping *Diamond & Related Materials* **4** 1305–1310

[59] Nesládek M 2005 Conventional n-type doping in diamond: state of the art and recent progress *Semicond. Sci. Technol.* **20** 19–27

[60] Koizumi S, Kamo M, Sato Y, Mita S and Sawabe A 1999 Growth and characterization of phosphorus doped n-type diamond thin films *Diamond and Related Materials* **172** 71–78

[61] Kajihara S A, Antonelli A, Bernholc J and Car R 1991 Nitrogen and potential n-type dopants in diamond *Physical Review Letters* **66** 2010–2013

[62] Saada D, Adler J and Kalish R 2000 Sulfur: A potential donor in diamond

Applied Physics Letters **77** 878

[63] Haenen K, Meykens K and Nesladek M 2000 The Electronic Structure of Phosphorus in n-Type CVD Diamond Films: Revised *phys.status solidi (a)* **181** 11–16

[64] Kennett D J, Kennett J P, West A, Mercer C, Hee S S Q, Bement L, Bunch T E, Sellers M and Wolbach W S 2009 Nanodiamonds in the Younger Dryas boundary sediment layer. *Science* **323** 94

[65] Shenderova O A, Zhirnov V V and Brenner D W 2002 Carbon Nanostructures *Critical Reviews in Solid State and Materials Sciences* **27** 227–356

[66] Shenderova O, Koscheev A, Zaripov N, Petrov I, Skryabin Y, Detkov P, Turner S and Van Tendeloo G 2011 Surface Chemistry and Properties of Ozone-Purified Detonation Nanodiamonds *J. Phys. Chem. C* **115** 9827–37

[67] Krüger A, Kataoka F, Ozawa M, Fujino T, Suzuki Y, Aleksenskii A E, Vul A Y and Osawa E 2005 Unusually tight aggregation in detonation nanodiamond: Identification and disintegration *Carbon* **43** 1722–30

[68] Krueger A 2008 The structure and reactivity of nanoscale diamond *Journal of Materials Chemistry* **18** 1485–92

[69] Batsanov S S, Gavrilkin S M, Batsanov A S, Poyarkov K B, Kulakova I I, Johnson D W and Mendis B G 2012 Giant dielectric permittivity of detonation-produced nanodiamond is caused by water *Journal of Materials Chemistry* **22** 11166–72

[70] Baidakova M and Vul A 2007 New prospects and frontiers of nanodiamond clusters *J. Phys. D: Appl. Phys.* **40** 6300–11

[71] Bevilacqua M, Patel S, Chaudhary A, Ye H and Jackman R B 2008 Electrical properties of aggregated detonation nanodiamonds *Applied Physics Letters* **93** 132115

[72] Schrand A M, Huang H, Carlson C, Schlager J J, Omacr Sawa E, Hussain S M and Dai L 2007 Are diamond nanoparticles cytotoxic? *J Phys Chem B* **111** 2–7

[73] Thalhammer A, Edgington R J, Cingolani L A, Schoepfer R and Jackman R B 2010 The use of nanodiamond monolayer coatings to promote the formation of functional neuronal networks. *Biomaterials* **31** 2097–104

[74] Liu K-K, Cheng C-L, Chang C-C and Chao J-I 2007 Biocompatible and detectable carboxylated nanodiamond on human cell *Nanotechnology* **18** 325102

[75] Prelas M A, Popovici G and Bigelow L K 1997 *Handbook of Industrial Diamonds and Diamond Films* (CRC Press)

[76] Williams O A 2011 Nanocrystalline diamond *Diamond & Related Materials* **20** 621–40

[77] Butler J E and Sumant A V 2008 The CVD of nanodiamond materials *Chem. Vap. Deposition*

[78] Fries M D and Vohra Y K 2002 Nanostructured diamond film deposition on curved surfaces of metallic temporomandibular joint implant *J. Phys. D: Appl. Phys.* **35** L105–7

[79] Bajaj P, Akin D, Gupta A, Sherman D, Shi B, Auciello O and Bashir R 2007 Ultrananocrystalline diamond film as an optimal cell interface for biomedical applications *Biomed Microdevices* **9** 787–94

[80] Jozwik K and Karczemska A 2007 The new generation Ti6Al4V artificial heart valve with nanocrystalline diamond coating on the ring and with Derlin disc after long-term mechanical fatigue examination *Diamond & Related Materials* **16** 1004–9

[81] Papo M J, Catledge S A, Vohra Y K and Machado C 2004 Mechanical wear behavior of nanocrystalline and multilayer diamond coatings on temporomandibular joint implants *J Mater Sci: Mater Med* **15** 773–7

[82] Fineberg J 2011 Diamonds are forever – or are they? *Nature Materials* **10** 3–4

[83] Krauss A R, Auciello O, Gruen D M, Jayatissa A, Sumant A, Tucek J, Mancini D C, Moldovan N, Erdemir A, Ersoy D, Gardos M N, Busmann H G, Meyer E M and Ding M Q 2001 Ultrananocrystalline diamond thin films for MEMS and moving mechanical assembly devices *Diamond & Related Materials* **10** 1952–61

[84] Khanna P, Villagra A, Kim S, Seto E, Jaroszeski M, Kumar A and Bhansali S 2006 Use of nanocrystalline diamond for microfluidic lab-on-a-chip *Diamond & Related Materials* **15** 2073–7

[85] Dankerl M, Eick S, Hofmann B, Hauf M, Ingebrandt S, Offenhäusser A, Stutzmann M and Garrido J A 2009 Diamond Transistor Array for Extracellular Recording From Electrogenic Cells *Adv. Funct. Mater.* **19** 2915–23

[86] Xiao X, Wang J, Liu C, Carlisle J A, Mech B, Greenberg R, Guven D, Freda R, Humayun M S, Weiland J and Auciello O 2006 In vitro and in vivo evaluation of ultrananocrystalline diamond for coating of implantable retinal microchips *Journal of Biomedical Materials Research Part B: Applied Biomaterials* **77B** 273–81

[87] Chen Y C, Tsai C Y, Lee C Y and Lin I N 2014 In vitro and in vivo evaluation of ultrananocrystalline diamond as an encapsulation layer for implantable microchips *Acta Biomaterialia* **10** 2187–99

[88] Yang W, Auciello O, Butler J E, Cai W, Carlisle J A, Gerbi J E, Gruen D M, Knickerbocker T, Lasseter T L, Russell J N, Smith L M and Hamers R J 2002 DNA-modified nanocrystalline diamond thin-films as stable, biologically active substrates *Nat Mater* **1** 253–7

[89] Härtl A, Schmich E, Garrido J A, Hernando J, Catharino S C R, Walter S, Feulner P, Kromka A, Steinmüller D and Stutzmann M 2004 Protein-

modified nanocrystalline diamond thin films for biosensor applications *Nat Mater* **3** 736–42

[90] Rubio-Retama J, Hernando J, López-Ruiz B, Härtl A, Steinmüller D, Stutzmann M, López-Cabarcos E and Garrido J A 2006 Synthetic Nanocrystalline Diamond as a Third-Generation Biosensor Support *Langmuir* **22** 5837–5842

[91] Neugart F, Zappe A, Jelezko F, C Tietz, Boudou J P, Krueger A, Wrachtrup J 2007 Dynamics of Diamond Nanoparticles in Solution and Cells *Nano Letters* **7** 3588–3591

[92] Martín R, Álvaro M, Herance J R and García H 2010 Fenton-Treated Functionalized Diamond Nanoparticles as Gene Delivery System *ACS Nano* **4** 65–74

[93] Nguyen T T-B, Chang H-C and Wu V W-K 2007 Adsorption and hydrolytic activity of lysozyme on diamond nanocrystallites *Diamond & Related Materials* **16** 872–6

[94] Krueger A 2008 New Carbon Materials: Biological Applications of Functionalized Nanodiamond Materials *Chemistry – A European Journal* **14** 1382–90

[95] Huang H, Pierstorff E, Osawa E and Ho D 2007 Active Nanodiamond Hydrogels for Chemotherapeutic Delivery *Nano Lett.* **7** 3305–14

[96] Liu K K, Zheng W W, Wang C C, Chiu Y C, Cheng C L, Lo Y S, Chen C and Chao J I 2010 Covalent linkage of nanodiamond-paclitaxel for drug delivery and cancer therapy *Nanotechnology* **21** 315106

[97] Narayan R J, Boehm R D and Sumant A V 2011 Medical applications of diamond particles & surfaces *Materials Today* **14** 154–63

[98] Barnard A S 2009 Diamond standard in diagnostics: nanodiamond biolabels make their mark *Analyst* **134** 1751–64

[99] Hui Y Y, Cheng C L and Chang H C 2010 Nanodiamonds for optical bioimaging *J. Phys. D: Appl. Phys.* **43** 374021

[100] Yu S J, Kang M W, Chang H C, Chen A and Yu Y C 2005 Bright Fluorescent Nanodiamonds: No Photobleaching and Low Cytotoxicity *J. Am Chem. Soc.* **127** 17604–17605

[101] Fu C-C, Lee H-Y, Chen K, Lim T-S, Wu H-Y, Lin P-K, Wei P-K, Tsao P-H, Chang H-C and Fann W 2007 Characterization and application of single fluorescent nanodiamonds as cellular biomarkers *PNAS* **104** 727–32

[102] Chang Y-R, Lee H-Y, Chen K, Chang C-C, Tsai D-S, Fu C-C, Lim T-S, Tzeng Y-K, Fang C-Y, Han C-C, Chang H-C and Fann W 2008 Mass production and dynamic imaging of fluorescent nanodiamonds *Nature Nanotechnology* **3** 284–8

[103] Yuan Y, Chen Y, Liu J-H, Wang H and Liu Y 2009 Biodistribution and fate of nanodiamonds in vivo *Diamond & Related Materials* **18** 95–100

[104] Reed J C 2000 *Apoptosis* (Elsevier)

[105] Li S, L'Heureux N and Elisseeff J H 2011 *Stem Cell and Tissue Engineering* (World Scientific)

[106] Turrigiano G G and Nelson S B 2004 Homeostatic plasticity in the developing nervous system *Nat Rev Neurosci* **5** 97–107

[107] Wilson A, Laurenti E, Oser G, van der Wath R C, Blanco-Bose W, Jaworski M, Offner S, Dunant C F, Eshkind L, Bockamp E, Lió P, MacDonald H R and Trumpp A 2008 Hematopoietic Stem Cells Reversibly Switch from Dormancy to Self-Renewal during Homeostasis and Repair *Cell* **135** 1118–29

[108] Miller S J, Lavker R M and Sun T-T 1993 Keratinocyte stem cells of cornea, skin and hair follicle: common and distinguishing features *Seminars in Developmental Biology* **4** 217–40

[109] Miller S J, Lavker R M and Sun T-T 2005 Interpreting epithelial cancer biology in the context of stem cells: Tumor properties and therapeutic implications *Biochimica et Biophysica Acta (BBA) - Reviews on Cancer* **1756** 25–52

[110] Clarke D L, Johansson C B, Wilbertz J, Veress B, Nilsson E, Karlström H, Lendahl U and Frisén J 2000 Generalized Potential of Adult Neural Stem Cells *Science* **288** 1660–3

[111] Takahashi K and Yamanaka S 2006 Induction of Pluripotent Stem Cells from Mouse Embryonic and Adult Fibroblast Cultures by Defined Factors *Cell* **126** 663–76

[112] Meyers R A 2013 *Stem Cells* (John Wiley & Sons)

[113] Slack J M W 2007 Metaplasia and transdifferentiation: from pure biology to the clinic. *Nat Rev Mol Cell Biol* **8** 369–78

[114] Bajénoff M, Wurtz O and Guerder S 2002 Repeated Antigen Exposure Is Necessary for the Differentiation, But Not the Initial Proliferation, of Naive CD4+ T Cells *J Immunol* **168** 1723–9

[115] Tofighi R, Tamm C, Moors M, Ibrahim W N W and Ceccatelli S 2011 *Neuromethods* vol 56, ed M Aschner, C Suñol and A Bal-Price (Totowa, NJ: Humana Press)

[116] Buylla A A and Temple S 1998 Stem cells in the developing and adult nervous system *Journal of neurobiology* **36** 105–110

[117] Uchida N, Buck D W, He D, Reitsma M J, Masek M, Phan T V, Tsukamoto A S, Gage F H and Weissman I L 2000 Direct isolation of human central nervous system stem cells *PNAS* **97** 14720–14725

[118] Messam C A, Hou J and Major E O 2000 Coexpression of Nestin in Neural and Glial Cells in the Developing Human CNS Defined by a Human-Specific Anti-nestin Antibody *Experimental Neurology* **161** 585–96

[119] Johe K K, Hazel T G, Muller T, Dugich-Djordjevic M M and McKay R D 1996 Single factors direct the differentiation of stem cells from the fetal and adult central nervous system. *Genes & Development* **10** 3129–40

[120] Alvarez-Buylla A and García-Verdugo J M 2002 Neurogenesis in Adult Subventricular Zone *Journal of Neuroscience* **22** 629–634

[121] Doetsch F, Caillé I, Lim D A, García-Verdugo J M and Alvarez-Buylla A 1999 Subventricular Zone Astrocytes Are Neural Stem Cells in the Adult Mammalian Brain *Cell* **97** 703–16

[122] Kazanis I 2009 The subependymal zone neurogenic niche: a beating heart in the centre of the brain: how plastic is adult neurogenesis? Opportunities for therapy and questions to be addressed. *Brain* **132** 2909–21

[123] Seri B, García-Verdugo J M, McEwen B S and Alvarez-Buylla A 2001 Astrocytes give rise to new neurons in the adult mammalian hippocampus. *Journal of Neuroscience* **21** 7153–60

[124] Seri B, Herrera D G, Gritti A, Ferron S, Collado L, Vescovi A, García-Verdugo J M and Alvarez-Buylla A 2006 Composition and organization of the SCZ: a large germinal layer containing neural stem cells in the adult mammalian brain. *Cereb. Cortex* **16 Suppl 1** i103–11

[125] Pencea V, Bingaman K D, Freedman L J and Luskin M B 2001 Neurogenesis in the Subventricular Zone and Rostral Migratory Stream of the Neonatal and Adult Primate Forebrain *Experimental Neurology* **172** 1–16

[126] Lee A, Kessler J D, Read T-A, Kaiser C, Corbeil D, Huttner W B, Johnson J E and Wechsler-Reya R J 2005 Isolation of neural stem cells from the postnatal cerebellum. *Nat Neurosci* **8** 723–9

[127] Sutter R, Yadirgi G and Marino S 2007 Neural stem cells, tumour stem cells and brain tumours: dangerous relationships? *Biochim. Biophys. Acta* **1776** 125–37

[128] Kazaniz I, Lathia J, Moss L, ffrench–Constant C 2008 The neural stem cell microenvironment (*StemBook.org)*

[129] Azevedo F A C, Carvalho L R B, Grinberg L T, Farfel J M, Ferretti R E L, Leite R E P, Filho W J, Lent R and Herculano Houzel S 2009 Equal numbers of neuronal and nonneuronal cells make the human brain an isometrically scaled‐up primate brain *Journal of Comparative Neurology* **513** 532–41

[130] David J Maloney Professor and Chair of Neuroscience Irwin B Levitan P D, Levitan I B, Kaczmarek L K and Professor of Pharmacology and Cellular and Molecular Physiology Leonard K Kaczmarek P D 2015 *The Neuron* (Oxford University Press, USA)

[131] Scott S A 1992 *Sensory Neurons* (Oxford University Press, USA)

[132] Stein P S G 1999 *Neurons, Networks, and Motor Behavior* (MIT Press)

[133] Stiles J 2008 *The Fundamentals of Brain Development* (Harvard University Press)

[134] Hülsmann S, Oku Y, Zhang W and Richter D W 2000 Metabolic coupling between glia and neurons is necessary for maintaining respiratory activity in transverse medullary slices of neonatal mouse *European Journal of Neuroscience* **12** 856–62

[135] Magistretti P J and Pellerin L 1999 Cellular mechanisms of brain energy metabolism and their relevance to functional brain imaging *Philosophical Transactions of the Royal Society of London B: Biological Sciences* **354** 1155–63

[136] Newman E and Reichenbach A 1996 The Müller cell: a functional element of the retina *Trends in Neurosciences* **19** 307–12

[137] Fawcett J W and Asher R A 1999 The glial scar and central nervous system repair *Brain Research Bulletin* **49** 377–91

[138] Thomas J L, Spassky N, Perez Villegas E M, Olivier C, Cobos I, Goujet Zalc C, Martínez S and Zalc B 2000 Spatiotemporal development of oligodendrocytes in the embryonic brain *J. Neurosci. Res.* **59** 471–6

[139] Dai X, Lercher L D, Clinton P M, Du Y, Livingston D L, Vieira C, Yang L, Shen M M and Dreyfus C F 2003 The Trophic Role of Oligodendrocytes in the Basal Forebrain *J. Neurosci.* **23** 5846–53

[140] Banati R B 2003 Neuropathological imaging: in vivo detection of glial activation as a measure of disease and adaptive change in the brain *Br Med Bull* **65** 121–31

[141] Gehrmann J, Matsumoto Y and Kreutzberg G W 1995 Microglia: intrinsic immuneffector cell of the brain. *Brain Res. Brain Res. Rev.* **20** 269–87

[142] Kreutzberg G W 1996 Microglia: a sensor for pathological events in the CNS. *Trends in Neurosciences* **19** 312–8

[143] Dissing-Olesen L, Ladeby R, Nielsen H H, Toft-Hansen H, Dalmau I and Finsen B 2007 Axonal lesion-induced microglial proliferation and microglial cluster formation in the mouse. *Neuroscience* **149** 112–22

[144] Giordana M T, Attanasio A, Cavalla P, Migheli A, Vigliani M C and Schiffer D 1994 Reactive cell proliferation and microglia following injury to the rat brain *Neuropathology and Applied Neurobiology* **20** 163–74

[145] Storb R and Thomas E D 1983 Allogeneic Bone-Marrow Transplantation *Immunological Reviews* **71** 77–102

[146] Thomas E D, Buckner C D, Banaji M, Clift R A, Fefer A, Flournoy N, Goodell B W, Hickman R O, Lerner K G, Neiman P E, Sale G E, Sanders J E, Singer J, Stevens M, Storb R and Weiden P L 1977 One hundred patients with acute leukemia treated by chemotherapy, total body irradiation, and allogeneic marrow transplantation *Blood* **49** 511–33

[147] Tyndall A, Fassas A, Passweg J, Ruiz de Elvira C, Attal M, Brooks P, Black

C, Durez P, Finke J, Forman S, Fouillard L, Furst D, Holmes J, Joske D, Jouet J, Kötter I, Locatelli F, Prentice H, Marmont A M, McSweeney P, Musso M, Peter H H, Snowden J A, Sullivan K and Gratwohl A 1999 Autologous haematopoietic stem cell transplants for autoimmune disease--feasibility and transplant-related mortality. Autoimmune Disease and Lymphoma Working Parties of the European Group for Blood and Marrow Transplantation, the European League Against Rheumatism and the International Stem Cell Project for Autoimmune Disease. *Bone Marrow Transplant* **24** 729–34

[148] Rossi F and Cattaneo E 2002 Neural stem cell therapy for neurological diseases: dreams and reality *Nat Rev Neurosci* **3** 401–9

[149] Abe K 2000 Therapeutic Potential of Neurotrophic Factors and Neural Stem Cells Against Ischemic Brain Injury *Journal of Cerebral Blood Flow & Metabolism* **20** 1393–408

[150] Liu J, Solway K, Messing R O and Sharp F R 1998 Increased Neurogenesis in the Dentate Gyrus After Transient Global Ischemia in Gerbils *J. Neurosci.* **18** 7768–78

[151] Kennea N L and Mehmet H 2002 Neural stem cells *Small* **197** 536–50

[152] Olanow C W, Kordower J H and Freeman T B 1996 Fetal nigral transplantation as a therapy for Parkinson's disease *Trends in Neurosciences* **19** 102–9

[153] Bjorklund A and Lindvall O 2000 Cell replacement therapies for central nervous system disorders *Nat Neuroscience* **3** 537–544

[154] Abbott N J 2005 Dynamics of CNS Barriers: Evolution, Differentiation, and Modulation *Cell Mol Neurobiol* **25** 5–23

[155] Streit W J 2000 Microglial Response to Brain Injury: A Brief Synopsis *Toxicol Pathol* **28** 28–30

[156] Polikov V S, Tresco P A and Reichert W M 2005 Response of brain tissue to chronically implanted neural electrodes *Journal of Neuroscience Methods* **148** 1–18

[157] Jessen K R 2004 Glial cells *The International Journal of Biochemistry & Cell Biology* **36** 1861–7

[158] Cheung K C 2007 Implantable microscale neural interfaces *Biomed Microdevices* **9** 923–38

[159] Wise K D 2005 Silicon microsystems for neuroscience and neural prostheses *Engineering in Medicine and Biology Magazine, IEEE* **24** 22–9

[160] Moxon K A, Leiser S C, Gerhardt G A, Barbee K A and Chapin J K 2004 Ceramic-based multisite electrode arrays for chronic single-neuron recording *IEEE Trans Biomed Eng* **51** 647–56

[161] Hassler C, Guy J, Nietzschmann M, Staiger J F and Stieglitz T 2011 Chronic intracortical implantation of saccharose-coated flexible shaft

electrodes into the cortex of rats *IEEE* **33** 644–647

[162] Rousche P J, Pellinen D S, Pivin D P, Williams J C, Vetter R J and Kipke D R 2001 Flexible polyimide-based intracortical electrode arrays with bioactive capability. *IEEE Trans Biomed Eng* **48** 361–71

[163] Prohaska O J, Olcaytug F, Pfundner P and Dragaun H 1986 Thin-film multiple electrode probes: possibilities and limitations. *IEEE Trans Biomed Eng* **33** 223–9

[164] Blum N A, Carkhuff B G, Charles H K, Edwards R L and Meyer R A 1991 Multisite microprobes for neural recordings. *IEEE Trans Biomed Eng* **38** 68–74

[165] Piret G, Hebert C, Mazellier J P, Rousseau L, Scorsone E, Cottance M, Lissorgues G, Heuschkel M O, Picaud S, Bergonzo P and Yvert B 2015 3D-nanostructured boron-doped diamond for microelectrode array neural interfacing *Biomaterials* **53** 173–83

[166] Regan E, Taylor A, Uney J B, Dick A D and May P W 2011 Spatially Controlling Neuronal Adhesion and Inflammatory Reactions on Implantable Diamond *IEEE Emerging Topics in Circuits and Systems* **1** 577–565

[167] Specht C, Williams O, Jackman R and Schoepfer R 2004 Ordered growth of neurons on diamond *Biomaterials* **25** 4073–4078

[168] Fattahi P, Yang G, Kim G and Abidian M R 2014 A Review of Organic and Inorganic Biomaterials for Neural Interfaces *Adv. Mater. Weinheim* **26** 1846–85

[169] Ke Wang, Harvey A Fishman, Hongjie Dai AJames S Harris 2006 Neural Stimulation with a Carbon Nanotube Microelectrode Array *Nano Lett.* **6** 2043–2048

[170] Heim M, Yvert B and Kuhn A 2012 Nanostructuration strategies to enhance microelectrode array (MEA) performance for neuronal recording and stimulation *Journal of Physiology-Paris* **106** 137–45

[171] Abidian M R, Corey J M, Kipke D R and Martin D C 2010 Conducting-Polymer Nanotubes Improve Electrical Properties, Mechanical Adhesion, Neural Attachment, and Neurite Outgrowth of Neural Electrodes *Small* **6** 421–9

[172] Piret G, Perez M T and Prinz C N 2012 Neurite outgrowth and synaptophysin expression of postnatal CNS neurons on GaP nanowire arrays in long-term retinal cell culture *Biomaterials* **34** 875–887

[173] McKenzie J L, Waid M C, Shi R and Webster T J 2004 Decreased functions of astrocytes on carbon nanofiber materials *Biomaterials* **25** 1309–17

[174] Ereifej E S, Matthew H W, Newaz G, Mukhopadhyay A, Auner G, Salakhutdinov I and VandeVord P J 2013 Nanopatterning effects on astrocyte reactivity *J Biomed Mater Res A* **101A** 1743–57

[175] Tysseling-Mattiace V M, Sahni V, Niece K L, Birch D, Czeisler C, Fehlings

M G, Stupp S I and Kessler J A 2008 Self-Assembling Nanofibers Inhibit Glial Scar Formation and Promote Axon Elongation after Spinal Cord Injury *J. Neurosci.* **28** 3814–23

[176] Brown K T 1986 *Advanced Micropipette Techniques for Cell Physiology* (John Wiley & Sons)

[177] http://www.sutter.com/manuals/P-97-DOM_OpMan.pdf

[178] May P W 1995 CVD diamond: a new technology for the future? *Endeavour* **19** 101–106

[179] Butler J E, Mankelevich Y A, Cheesman A, Ma J and Ashfold M N R 2009 Understanding the chemical vapor deposition of diamond: recent progress *J. Phys.: Condens. Matter* **21** 364201

[180] Cicala G, Bruno P, Bénédic F, Silva F, Hassouni K and Senesi G S 2005 Nucleation, growth and characterization of nanocrystalline diamond films *Diamond & Related Materials* **14** 421–5

[181] Smith H 1994 Computational Studies of an Asymmetric Rf Plasma Using Particle-in-cell Techniques (http://plasma.kulgun.net/HBS/)

[182] Binning G, Quate C F, Gerber C 1989 Atomic Force Microscope *Physical Review Letters* **56** 930

[183] Binnig G, Gerber C, Stoll E, Albrecht T R and Quate C F 1987 Atomic resolution with atomic force microscope *Surface Science* **180** 1–6

[184] Everhart T E and Thornley R F M 2002 Wide-band detector for micro-microampere low-energy electron currents *J. Sci. Instrum.* **37** 246–8

[185] Larkin P 2011 *Infrared and Raman Spectroscopy; Principles and Spectral Interpretation* (Elsevier)

[186] Colthup N 2012 *Introduction to Infrared and Raman Spectroscopy* (Elsevier)

[187] Cormack A 1955 Internal Rayleigh Scattering *Physical Review* **97** 986–6

[188] Kuzmany H 2009 *Solid-State Spectroscopy* (Springer)

[189] Daenen M, Williams O A, D'Haen J, Haenen K and Nesladek M 2006 Seeding, growth and characterization of nanocrystalline diamond films on various substrates *phys. stat. sol. (a)* **203** 3005–10

[190] Kawarada H 1996 Hydrogen-terminated diamond surfaces and interfaces *Surface Science Reports* **26** 205–6

[191] Donnelly C M, McCullough R W and Geddes J 1997 Etching of graphite and diamond by thermal energy hydrogen atoms *Diamond & Related Materials* **6** 787–90

[192] Stojilovic N 2012 Why Can't We See Hydrogen in X-ray Photoelectron Spectroscopy? *Journal of Chemical Education* **89** 1331–1332

[193] Chow T S 1998 Wetting of rough surfaces *J. Phys.: Condens. Matter* **10**

L445–51

[194] Sun Y, Pollard S, Conti L, Toselli M, Biella G, Parkin G, Willatt L, Falk A, Cattaneo E and Smith A 2008 Long-term tripotent differentiation capacity of human neural stem (NS) cells in adherent culture *Molecular and Cellular Neuroscience* **38** 245–58

[195] Matthew A 2006 Current biosensor technologies in drug discovery (*Drug Discovery)*

[196] Longair M H, Baker D A and Armstrong J D 2011 Simple Neurite Tracer: open source software for reconstruction, visualization and analysis of neuronal processes *Bioinformatics* **27** 2453–4

[197] Hart P E, Nilsson N J and Raphael B 1968 A Formal Basis for the Heuristic Determination of Minimum Cost Paths *IEEE Transactions on Systems Science and Cybernetics* **4** 100–7

[198] Williams J A and Le H R 2006 Tribology and MEMS *J. Phys. D: Appl. Phys.* **39** R201–14

[199] Lu J, Cao Z, Aslam D M, Sepulveda N and Sullivan J P Diamond micro and nano resonators using laser, capacitive or piezoresistive detection *IEEE proceedings* **3** 873–876

[200] Krueger A 2011 Beyond the shine: recent progress in applications of nanodiamond *Lab Chip* **21** 12571

[201] Fries M D and Vohra Y K 2004 Properties of nanocrystalline diamond thin films grown by MPCVD for biomedical implant purposes *Diamond & Related Materials* **13** 1740–3

[202] Williams O A and Nesladek M 2006 Growth and properties of nanocrystalline diamond films *phys. stat. sol. (a)* **203** 3375–3386

[203] Philip J, Hess P, Feygelson T and Butler J E 2003 Elastic, mechanical, and thermal properties of nanocrystalline diamond films *Journal of Applied Physics* **93** 2164–2171

[204] Tang L, Tsai C, Gerberich W W, Kruckeberg L and Kania D R 1995 Biocompatibility of chemical-vapour-deposited diamond *Journal of Neuroscience Methods* **16** 483–8

[205] Jakubowski W, Bartosz G and Niedzielski P 2004 Nanocrystalline diamond surface is resistant to bacterial colonization *Diamond and Related Materials* **13** 1761–1763

[206] Mortet V, Williams O A and Haenen K 2008 Diamond: a material for acoustic devices *phys. stat. sol. (a)* **205** 1009–20

[207] Pedrosa V A, Miwa D, Machado S A S and Avaca L A 2006 On the Utilization of Boron Doped Diamond Electrode as a Sensor for Parathion and as an Anode for Electrochemical Combustion Of Parathion *Electroanalysis* **18** 1590–7

[208] Edgington R J, Thalhammer A, Welch J O, Bongrain A, Bergonzo P, Scorsone E, Jackman R B and Schoepfer R 2013 Patterned neuronal networks using nanodiamonds and the effect of varying nanodiamond properties on neuronal adhesion and outgrowth *J. Neural Eng.* **10** 056022

[209] Bonnauron M, Saada S, Rousseau L, Lissorgues G, Mer C and Bergonzo P 2008 High aspect ratio diamond microelectrode array for neuronal activity measurements *Diamond & Related Materials* **17** 1399–404

[210] Bergonzo P, Bongrain A, Scorsone E, Bendali A, Rousseau L, Lissorgues G, Mailley P, Li Y, Kauffmann T, Goy F, Yvert B, Sahel J A and Picaud S 2011 3D shaped mechanically flexible diamond microelectrode arrays for eye implant applications: The MEDINAS project *IRBM* **32** 91–4

[211] Cottance M, Nazeer S, Rousseau L, Lissorgues G, Bongrain A, Kiran R, Scorsone E, Bergonzo P, Bendali A, Picaud S, Joucla S and Yvert B 2013 Diamond micro-electrode arrays (MEAs): A new route for in-vitro applications *DTIP proceedings*

[212] Taniguchi J, Tokano Y, Miyamoto I, Komuro M and Hiroshima H 2002 Diamond nanoimprint lithography *Nanotechnology* **13** 592–6

[213] Ding G, Yao J, Yu A, Zhao X, Wang L and Shen T 2000 Micromachining and Microfabrication Process Technology VI Micromachining and Microfabrication *SPIE* **4174** 451–454

[214] Ramanathan M, Darling S B, Sumant A V and Auciello O 2010 Nanopatterning of ultrananocrystalline diamond thin films via block copolymer lithography *Journal of Vacuum Science & Technology A* **28** 979–83

[215] Ando Y, Kuwabara J, Suzuki K and Sawabe A 2004 Patterned growth of heteroepitaxial diamond *Journal of Neuroscience Methods* **13** 1975–9

[216] Maybeck V, Edgington R and Bongrain A 2014 Boron-Doped Nanocrystalline Diamond Microelectrode Arrays Monitor Cardiac Action Potentials *Advanced Healthcare Materials* **3** 283–289

[217] Domonkos M, Izak T, Stolcova L, Proska J and Kromka A 2014 Fabrication of periodically ordered diamond nanostructures by microsphere lithography *Phys. Status Solidi (b)* **251** 2587–92

[218] Wang X D, Hong G D, Zhang J, Lin B L, Gong H Q and Wang W Y 2002 Precise patterning of diamond films for MEMS application *Journal of Neuroscience Methods* **127** 230–3

[219] Narayan J and Chen X 1992 Laser patterning of diamond films *J. Appl. Phys.* **71** 3795

[220] Ral'Chenko V G, Korotushenko K G and Smolin A A 1995 Fine patterning of diamond films by laser-assisted chemical etching in oxygen *Diamond and Related Materials* **4** 893–896

[221] Shimoni O, Cervenka J, Karle T J, Fox K, Gibson B C, Tomljenovic-Hanic S, Greentree A D and Prawer S 2014 Development of a Templated

Approach to Fabricate Diamond Patterns on Various Substrates *ACS Appl. Mater. Interfaces* **6** 8894–902

[222] Chen Y-C, Tzeng Y, Cheng A-J, Dean R, Park M and Wilamowski B M 2009 Inkjet printing of nanodiamond suspensions in ethylene glycol for CVD growth of patterned diamond structures and practical applications *Diamond & Related Materials* **18** 146–50

[223] Fox N A, Youh M J, Steeds J W and Wang W N 2000 Patterned diamond particle films *J. Appl. Phys.* **87** 8187–91

[224] Zhuang H, Song B, Staedler T and Jiang X 2011 Microcontact Printing of Monodiamond Nanoparticles: An Effective Route to Patterned Diamond Structure Fabrication *J. Phys. Chem. C* **27** 11981–9

[225] Lee S-K, Kim J-H, Jeong M-G, Song M-J and Lim D-S 2010 Direct deposition of patterned nanocrystalline CVD diamond using an electrostatic self-assembly method with nanodiamond particles *Nanotechnology* **21** 505302

[226] Hebert C, Scorsone E, Bendali A, Kiran R, Cottance M, Girard H A, Degardin J, Dubus E, Lissorgues G, Rousseau L, Picaud S and Bergonzo P 2013 Boron doped Diamond Biotechnology: from sensors to neurointerfaces *Faraday Discuss* **00** 1–3

[227] Cheng N-S 2008 Formula for the Viscosity of a Glycerol−Water Mixture *Ind. Eng. Chem. Res.* **47** 3285–8

[228] Kulakova I I 2004 Surface chemistry of nanodiamonds *Phys. Solid State* **46** 636–43

[229] Ascarelli P and Fontana S 1993 Dissimilar grit-size dependence of the diamond nucleation density on substrate surface pretreatments *Applied Surface Science* **64** 307–11

[230] Avigal Y and Hoffman A 1999 A new method for nucleation enhancement of diamond *Diamond & Related Materials* **8** 127–131

[231] Osswald S, Mochalin V N, Havel M, Yushin G and Gogotsi Y 2009 Phonon confinement effects in the Raman spectrum of nanodiamond *Phys. Rev. B* **80** 075419

[232] Sun K W, Wang J Y and Ko T Y 2008 Raman spectroscopy of single nanodiamond: Phonon-confinement effects *Applied Physics Letters* **92** 153115

[233] Ferrari A and Robertson J 2000 Interpretation of Raman spectra of disordered and amorphous carbon *Phys. Rev. B* **61** 14095–107

[234] Ondič L, Dohnalová K, Ledinský M, Kromka A, Babchenko O and Rezek B 2011 Effective Extraction of Photoluminescence from a Diamond Layer with a Photonic Crystal *ACS Nano* **5** 346–50

[235] Nebel C E, Shin D, Rezek B, Tokuda N, Uetsuka H and Watanabe H 2007 Diamond and biology *J. R. Soc. Interface* **4** 439–461

[236] Hees J, Heidrich N, Pletschen W, Sah R E, Wolfer M, Williams O A, Lebedev V, Nebel C E and Ambacher O 2012 Piezoelectric actuated micro-resonators based on the growth of diamond on aluminum nitride thin films *Nanotechnology* **24** 025601

[237] Fontaine F, Saguy C U and Philosoph B 1996 Boron implantation/insitu annealing procedure for optimal p‐type properties of diamond *Applied Physics Letters* **68** 2264–2266

[238] Braunstein G and Kalish R 1983 Effective p-type doping of diamond by boron ion implantation *J. Appl. Phys.* **54** 2106

[239] Visser E P, Bauhuis G J, Janssen G, Vollenberg W, Enckevort J P V and Giling L J 1999 Electrical conduction in homoepitaxial, boron-doped diamond films *J. Phys.: Condens. Matter* **4** 7365–76

[240] Yokoya T, Nakamura T, Matsushita T, Muro T, Takano Y, Nagao M, Takenouchi T, Kawarada H and Oguchi T 2005 Origin of the metallic properties of heavily boron-doped superconducting diamond. *Nature* **438** 647–50

[241] Bustarret E, Achatz P, Sacepe B, Chapelier C, Marcenat C, Ortega L, Klein T 2008 Metal-insulator transition and superconductivity in boron-doped diamond *Phil. Trans. R. Soc. A* **366** 267–279

[242] Hupert M, Muck A, Wang J, Stotter K, Cvackova Z, Haymond S, Show Y, Swain G M 2003 Conductive diamond thin-films in electrochemistry *Diamond and Related Materials* **12** 1940–1949

[243] Chaplin B P, Hubler D K, Farrell J 2013 Understanding anodic wear at boron doped diamond film electrodes *Electrochimica Acta* **89** 122–131

[244] Vanhove E, De Sanoit J and Mailley P 2009 High reactivity and stability of diamond electrodes: The influence of the B-doping concentration *Phys status solidi (a)* **206** 2063–2069

[245] Wei J J, Li C M, Gao X H, Hei L F and Lvun F X 2012 The influence of boron doping level on quality and stability of diamond film on Ti substrate *Applied Surface Science* **18** 6909–6931

[246] Fujishima A 2005 *Diamond Electrochemistry* (Elsevier)

[247] Suzuki A, Ivandini T A, Yoshimi K, Fujishima A, Oyama G, Nakazato T, Hattori N, Kitazawa S and Einaga Y 2007 Fabrication, characterization, and application of boron-doped diamond microelectrodes for in vivo dopamine detection. *Anal. Chem.* **79** 8608–15

[248] Park J, Quaiserová-Mocko V, Patel B A, Novotný M, Liu A, Bian X, Galligan J J and Swain G M 2008 Diamond microelectrodes for in vitro electroanalytical measurements: current status and remaining challenges. *Analyst* **133** 17–24

[249] Panizza M and Cerisola G 2005 Application of diamond electrodes to electrochemical processes *Electrochimica Acta* **51** 191–199

[250] Wenmackers S, Vermeeren V, vandeVen M, Ameloot M, Bijnens N, Haenen K, Michiels L and Wagner P 2009 Diamond-based DNA sensors: surface functionalization and read-out strategies *phys. stat. sol. (a)* **206** 391–408

[251] Vermeeren V, Wenmackers S, Wagner P and Michiels L 2009 DNA sensors with diamond as a promising alternative transducer material. *Sensors* **9** 5600–36

[252] Lee J and Park S M 2005 Direct electrochemical assay of glucose using boron-doped diamond electrodes *Analytica chimica acta* **545** 27–32

[253] Popa E 1999 Selective Electrochemical Detection of Dopamine in the Presence of Ascorbic Acid at Anodized Diamond Thin Film Electrodes *Electrochem. Solid-State Lett.* **2** 49

[254] Popa E, Kubota Y, Tryk D A and Fujishima A 2000 Selective Voltammetric and Amperometric Detection of Uric Acid with Oxidized Diamond Film Electrodes *Anal. Chem.* **72** 1724–1727

[255] Bonnauron M, Saada A, Rousseau L, Lissorgues G, Mer P and Bergonzo P 2008 High aspect ratio diamond microelectrode array for neuronal activity measurements *Diamond & Related Materials* **17** 1399–1404

[256] Chen Y C, Lee D C, Hsiao C Y, Chung Y F, Chen H C, Thomas J P, Pong W F, Tai N H, Lin I N and Chiu I M 2009 The effect of ultra-nanocrystalline diamond films on the proliferation and differentiation of neural stem cells. *Biomaterials* **30** 3428–35

[257] Chen Y C, Lee D C, Tsai T Y, Hsiao C Y, Liu J W, Kao C Y, Lin H K, Chen H C, Palathinkal T J, Pong W F, Tai N H, Lin I N and Chiu I M 2010 Induction and regulation of differentiation in neural stem cells on ultra-nanocrystalline diamond films *Biomaterials* **31** 5575–87

[258] Ariano P, Budnyk O, Dalmazzo S, Lovisolo D, Manfredotti C, Rivolo P and Vittone E 2009 On diamond surface properties and interactions with neurons. *Eur Phys J E Soft Matter* **30** 149–56

[259] Garrett D J, Ganesan K, Stacey A, Fox K, Meffin H and Prawer S 2012 Ultra-nanocrystalline diamond electrodes: optimization towards neural stimulation applications. *J. Neural Eng.* **9** 016002

[260] Amaral M, Dias A G, Gomes P S, Lopes M A, Silva R F, Santos J D and Fernandes M H 2008 Nanocrystalline diamond: In vitro biocompatibility assessment by MG63 and human bone marrow cells cultures. *J Biomed Mater Res A* **87** 91–9

[261] Kalbacova M, Rezek B and Baresova V 2009 Nanoscale topography of nanocrystalline diamonds promotes differentiation of osteoblasts *Acta Biomaterialia*

[262] Kalbacova M, Broz A, Babchenko O and Kromka A 2009 Study on cellular adhesion of human osteoblasts on nano-structured diamond films *Phys. Status Solidi (b)* **246** 2774–7

[263] Yang L, Li Y, Sheldon B W and Webster T J 2011 Altering surface energy of

nanocrystalline diamond to control osteoblast responses *Lab Chip* **22** 205

[264] Amaral M, Gomes P S, Lopes M A, Santos J D, Silva R F and Fernandes M H 2009 Cytotoxicity evaluation of nanocrystalline diamond coatings by fibroblast cell cultures. *Acta Biomaterialia* **5** 755–63

[265] Clem W C, Chowdhury S, Catledge S A and Weimer J J Shaikh F M, Hennessy K M, Konovalov V V, Hill M R, Waterfeld A, Bellis S L, Vohra Y K 2008 Mesenchymal stem cell interaction with ultra-smooth nanostructured diamond for wear-resistant orthopaedic implants *Biomaterials* **29** 3461–3468

[266] Regan E, Taylor A, Uney J B, Dick A D and May P W 2011 Spatially Controlling Neuronal Adhesion and Inflammatory Reactions on Implantable Diamond *IEEE Emerging Topics in Circuits and Systems* **1** 577–565

[267] Girard H A, Perruchas S and Gesset C 2009 Electrostatic Grafting of Diamond Nanoparticles: A Versatile Route to Nanocrystalline Diamond Thin Films *ACS Applied Materials & Interfaces* **1** 2738–2746

[268] Lagneau A, Martin M, Martin F and Michel M F 1977 [Cytotoxic effect of peritoneal macrophages on an intestinal carcinoma in rats. Demonstration of a new cytotoxicity test]. *C. R. Seances Soc. Biol. Fil.* **171** 90–3

[269] Pacey L, Stead S, Gleave J, Tomczyk K and Doering L 2006 Neural Stem Cell Culture: Neurosphere generation, microscopical analysis and cryopreservation

[270] Santoro F, Schnitker J, Panaitov G and Offenhäusser A 2013 On Chip Guidance and Recording of Cardiomyocytes with 3D Mushroom-Shaped Electrodes *Nano Lett.* **13** 5379–84

[271] Nel A E, Mädler L, Velegol D, Xia T, Hoek E M V, Somasundaran P, Klaessig F, Castranova V and Thompson M 2009 Understanding biophysicochemical interactions at the nano|[ndash]|bio interface *Nature Publishing Group* **8** 543–557

[272] Yim E, Reano R, Pang S, Yee A, Chen C and Leong K 2005 Nanopattern-induced changes in morphology and motility of smooth muscle cells *Biomaterials* **26** 5405–5413

[273] Kulangara K, Yang J, Chellappan M, Yang Y and Leong K W 2014 Nanotopography Alters Nuclear Protein Expression, Proliferation and Differentiation of Human Mesenchymal Stem/Stromal Cells *PLoS ONE* **9** e114698

[274] Zamani F, Amani-Tehran M, Latifi M and Shokrgozar M A 2013 The influence of surface nanoroughness of electrospun PLGA nanofibrous scaffold on nerve cell adhesion and proliferation *J Mater Sci: Mater Med* **24** 1551–60

[275] Wei G and Ma P X 2008 Nanostructured biomaterials for regeneration *Adv. Funct. Mater.* **18** 3568–3582

[276] Brunetti V, Maiorano G, Rizzello L, Sorce B, Sabella S, Cingolani R and

Pompa P P 2010 Neurons sense nanoscale roughness with nanometer sensitivity. *Proceedings of the National Academy of Sciences* **107** 6264–6269

[277] Engler A J, Sen S, Sweeney H L and Discher D E 2006 Matrix Elasticity Directs Stem Cell Lineage Specification *Cell* **126** 677–89

[278] Discher D E, Janmey P and Wang Y 2005 Tissue cells feel and respond to the stiffness of their substrate *Science* **310** 1139–43

[279] Xu Y, Takai M and Ishihara K 2009 Protein adsorption and cell adhesion on cationic, neutral, and anionic 2-methacryloyloxyethyl phosphorylcholine copolymer surfaces. *Biomaterials* **30** 4930–8

[280] Ohgaki M, Kizuki T, Katsura M and Yamashita K 2001 Manipulation of selective cell adhesion and growth by surface charges of electrically polarized hydroxyapatite. *Journal of Biomedical Materials Research* **57** 366–73

[281] Spatz J P and Geiger B 2007 Molecular Engineering of Cellular Environments: Cell Adhesion to Nano‐Digital Surfaces *Cell Mechanics* Methods in Cell Biology vol 83 (Elsevier) pp 89–111

[282] Vogel V and Sheetz M 2006 Local force and geometry sensing regulate cell functions *Nat Rev Mol Cell Biol* **7** 265–75

[283] Velzenberger E, Kirat K E, Legeay G, Nagel M-D and Pezron I 2009 Characterization of biomaterials polar interactions in physiological conditions using liquid–liquid contact angle measurements *Colloids and Surfaces B: Biointerfaces* **68** 238–44

[284] Wei J, Igarashi T, Okumori N, Igarashi T, Maetani T, Liu B and Yoshinari M 2009 Influence of surface wettability on competitive protein adsorption and initial attachment of osteoblasts *Biomed. Mater.* **4** 045002

[285] Beckerle M C 2001 *Cell Adhesion* (Oxford University Press, USA)

[286] Arnold M, Cavalcanti-Adam E A, Glass R, Blümmel J, Eck W, Kantlehner M, Kessler H and Spatz J P 2004 Activation of integrin function by nanopatterned adhesive interfaces. *ChemPhysChem* **5** 383–8

[287] Scadden D T 2006 The stem-cell niche as an entity of action. *Nature* **441** 1075–9

[288] Gage F H 2000 Mammalian Neural Stem Cells *Science* **287** 1433–8

[289] Arenas E 2010 Towards stem cell replacement therapies for Parkinson's disease. *Biochem. Biophys. Res. Commun.* **396** 152–6

[290] Wu S, Sasaki A, Yoshimoto R, Kawahara Y, Manabe T, Kataoka K, Asashima M and Yuge L 2008 Neural Stem Cells Improve Learning and Memory in Rats with Alzheimer's Disease *Pathobiology* **75** 186–94

[291] Lindvall O and Kokaia Z 2006 Stem cells for the treatment of neurological disorders *Nature* **441** 1094–6

[292] Baharvand H 2015 *Stem Cell Nanoengineering* ed H Baharvand and N Aghdami (Hoboken, NJ: John Wiley & Sons)

[293] Park S Y, Park J, Sim S H, Sung M G, Kim K S, Hong B H and Hong S 2011 Enhanced Differentiation of Human Neural Stem Cells into Neurons on Graphene *Small* **23** 263–267

[294] Li N, Zhang Q, Gao S, Song Q, Huang R, Wang L, Liu L, Dai J, Tang M and Cheng G 2013 Three-dimensional graphene foam as a biocompatible and conductive scaffold for neural stem cells *Scientific Reports* **3** 1–6

[295] Jan E and Kotov N A 2007 Successful differentiation of mouse neural stem cells on layer-by-layer assembled single-walled carbon nanotube composite. *Nano Lett.* **7** 1123–8

[296] Chao T-I, Xiang S, Chen C-S, Chin W-C, Nelson A J, Wang C and Lu J 2009 Carbon nanotubes promote neuron differentiation from human embryonic stem cells *Biochem. Biophys. Res. Commun.* **384** 426–30

[297] Mahairaki V, Lim S H, Christopherson G T, Xu L, Nasonkin I, Yu C, Mao H-Q and Koliatsos V E 2011 Nanofiber Matrices Promote the Neuronal Differentiation of Human Embryonic Stem Cell-Derived Neural Precursors In Vitro *Tissue Engineering* **17** 855–863

[298] Jiang X, Cao H Q, Shi L Y, Ng S Y, Stanton L W and Chew S Y 2012 Nanofiber topography and sustained biochemical signaling enhance human mesenchymal stem cell neural commitment *Acta Biomaterialia* **8** 1290–302

[299] Christopherson G T, Song H and Mao H-Q 2009 The influence of fiber diameter of electrospun substrates on neural stem cell differentiation and proliferation *Biomaterials* **30** 556–64

[300] Taylor A C, Vagaska B, Edgington R, Hebert C, Ferretti P, Bergonzo P and Jackman R B 2015 Biocompatibility of nanostructured boron doped diamond for the attachment and proliferation of human neural stem cells *J. Neural Eng.* **12** 066016

[301] Hebert C, Mazellier J P, Scorsone E, Mermoux M and Bergonzo P 2014 Boosting the electrochemical properties of diamond electrodes using carbon nanotube scaffolds *CARBON* **71** 27–33

[302] Williams O A, Douhéret O, Daenen M, Haenen K, Osawa E and Takahashi M 2007 Enhanced diamond nucleation on monodispersed nanocrystalline diamond *Chemical Physics Letters* **445** 255–8

[303] Ojovan S M, McDonald M, Rabieh N, Shmuel N, Erez H, Nesládek M and Spira M E 2014 Nanocrystalline diamond surfaces for adhesion and growth of primary neurons, conflicting results and rational explanation. *Front. Neuroeng.* **7** 17

[304] Nistor P A, May P W, Tamagnini F, Randall A D and Caldwell M A 2015 Long-term culture of pluripotent stem-cell-derived human neurons on diamond – A substrate for neurodegeneration research and therapy *Biomaterials* **61** 139–49

[305] Osawa E 2008 Monodisperse single nanodiamond particulates *Pure Appl. Chem.* **80** 1365–79

[306] Cooper G M 2000 The Cell: A Molecular Approach (Sinauer Associates)

[307] Biazar E, Heidari M, Asefnejad A, Asefnezhad A and Montazeri N 2011 The relationship between cellular adhesion and surface roughness in polystyrene modified by microwave plasma radiation. *Int J Nanomedicine* **6** 631–9

[308] Hallab NJ, Bundy KJ, O'Connor K, Clark R and Moses RL 1994 Cell adhesion to biomaterials: correlations between surface charge, surface roughness, adsorbed protein, and cell morphology. *J Long Term Eff Med Implants* **5** 209–31

[309] Chen W, Villa-Diaz L G, Sun Y, Weng S, Kim J K, Lam R H W, Han L, Fan R, Krebsbach P H and Fu J 2012 Nanotopography influences adhesion, spreading, and self-renewal of human embryonic stem cells. *ACS Nano* **6** 4094–103

[310] Dalby M J, Gadegaard N and Oreffo R O C 2014 Harnessing nanotopography and integrin-matrix interactions to influence stem cell fate *Nature Publishing Group* **13** 558–69

[311] Reilly G C and Engler A J 2010 Intrinsic extracellular matrix properties regulate stem cell differentiation *Journal of Biomechanics* **43** 55–62

[312] Größner Schreiber B, Herzog M, Hedderich J, Dück A, Hannig M and Griepentrog M 2006 Focal adhesion contact formation by fibroblasts cultured on surface‐modified dental implants: an in vitro study *Clinical Oral Implants Research* **17** 736–45

[313] Lim J Y, Dreiss A D, Zhou Z, Hansen J C, Siedlecki C A, Hengstebeck R W, Cheng J, Winograd N and Donahue H J 2007 The regulation of integrin-mediated osteoblast focal adhesion and focal adhesion kinase expression by nanoscale topography *Biomaterials* **28** 1787–97

[314] Ikada Y 2011 Tissue Engineering: Fundamentals and Applications (Elsevier)

[315] Lampin M, Warocquier Clérout R, Legris C, Degrange M and Sigot Luizard M F 1997 Correlation between substratum roughness and wettability, cell adhesion, and cell migration *Journal of Biomedical Materials Research* **36** 99–108

[316] Aramesh M, Shimoni O, Ostrikov K, Prawer S and Cervenka J 2015 Surface charge effects in protein adsorption on nanodiamonds *Nanoscale* **7** 5726–36

[317] Mathiowitz E, Chickering D E III and Lehr C-M 1999 *Bioadhesive Drug Delivery Systems* (CRC Press)

[318] Macdonald P R, Lustig A, Steinmetz M O and Kammerer R A 2010 Laminin chain assembly is regulated by specific coiled-coil interactions *Journal of Structural Biology* **170** 398–405

[319] Hall P E, Lathia J D, Caldwell M A and ffrench-Constant C 2008 Laminin enhances the growth of human neural stem cells in defined culture media *BMC Neuroscience 2008 9:1* **9** 1

[320] Stéphanie Pasche, Janos Vörös, Hans J Griesser, Nicholas D Spencer A and Textor M 2005 *Effects of Ionic Strength and Surface Charge on Protein Adsorption at PEGylated Surfaces* (American Chemical Society)

[321] Powell S K and Kleinman H K 1997 Neuronal laminins and their cellular receptors *The International Journal of Biochemistry & Cell Biology* **29** 401–14

[322] Hohenester E, Tisi D, Talts J F and Timpl R 1999 The Crystal Structure of a Laminin G–like Module Reveals the Molecular Basis of α-Dystroglycan Binding to Laminins, Perlecan, and Agrin *Molecular Cell* **4** 783–92

[323] Mochalin V N, Shenderova O, Ho D and Gogotsi Y 2012 The properties and applications of nanodiamonds. *Nature Nanotechnology* **7** 11–23

[324] Casarosa S, Bozzi Y and Conti L 2014 Neural stem cells: ready for therapeutic applications? *Molecular and Cellular Therapies 2014 2:1* **2** 1

[325] Lindvall O, Barker R A, Brüstle O, Isacson O and Svendsen C N 2012 Clinical Translation of Stem Cells in Neurodegenerative Disorders *Cell Stem Cell* **10** 151–5

[326] Clelland C D, Barker R A and Watts C 2008 Cell therapy in Huntington disease *Neurosurgical Focus* **24** E9

[327] Temple S 1989 Division and differentiation of isolated CNS blast cells in microculture. *Nature* **340** 471–3

[328] Fuchs E, Tumbar T and Guasch G 2004 Socializing with the neighbors: stem cells and their niche. *Cell* **116** 769–78

[329] Watt F M and Driskell R R 2010 The therapeutic potential of stem cells *Philosophical Transactions of the Royal Society of London B: Biological Sciences* **365** 155–63

[330] Little L, Healy K E and Schaffer D 2008 Engineering biomaterials for synthetic neural stem cell microenvironments. *Chem. Rev.* **108** 1787–96

[331] Lutolf M P, Gilbert P M and Blau H M 2009 Designing materials to direct stem-cell fate. *Nature* **462** 433–41

[332] Robert J S 2004 Model systems in stem cell biology - Robert - 2004 - BioEssays - Wiley Online Library *BioEssays*

[333] Silva G A, Czeisler C, Niece K L, Beniash E, Harrington D A, Kessler J A and Stupp S I 2004 Selective differentiation of neural progenitor cells by high-epitope density nanofibers. *Science* **303** 1352–5

[334] Ananthanarayanan B, Little L, Schaffer D V, Healy K E and Tirrell M 2010 Neural stem cell adhesion and proliferation on phospholipid bilayers functionalized with RGD peptides *Biomaterials* **31** 8706–15

[335] Li Y J, Chung E H, Rodriguez R T, Firpo M T and Healy K E 2006 Hydrogels as artificial matrices for human embryonic stem cell self-renewal *J Biomed Mater Res A* **79A** 1–5

[336] Svendsen C N, Borg ter M G, Armstrong R J E, Rosser A E, Chandran S, Ostenfeld T and Caldwell M A 1998 A new method for the rapid and long term growth of human neural precursor cells *Journal of Neuroscience Methods* **85** 141–52

[337] Carpenter M K, Cui X, Hu Z-Y, Jackson J, Sherman S, Seiger Å and Wahlberg L U 1999 In Vitro Expansion of a Multipotent Population of Human Neural Progenitor Cells *Experimental Neurology* **158** 265–78

[338] Riaz S S, Jauniaux E, Stern G M and Bradford H F 2002 The controlled conversion of human neural progenitor cells derived from foetal ventral mesencephalon into dopaminergic neurons in vitro *Developmental Brain Research* **136** 27–34

[339] Rodrigues M, Griffith L G and Wells A 2010 Growth factor regulation of proliferation and survival of multipotential stromal cells *Stem Cell Res Ther* 1:32

[340] Reynolds B A and Rietze R L 2005 Neural stem cells and neurospheres–re-evaluating the relationship *Nat Meth* **2** 333–6

[341] Singec I, Knoth R, Meyer R P, Maciaczyk J, Volk B, Nikkhah G, Frotscher M and Snyder E Y 2006 Defining the actual sensitivity and specificity of the neurosphere assay in stem cell biology *Nat Meth* **3** 801–6

[342] Wang Y, Deng H, Zu Z-H, Shen X-C, Liang H, Cui F-Z, Xu Q-Y and Lee I-S 2010 Interactions between neural stem cells and biomaterials combined with biomolecules *Front. Mater. Sci. China* **4** 325–31

[343] Subramanian A, Krishnan U M and Sethuraman S 2009 Development of biomaterial scaffold for nerve tissue engineering: Biomaterial mediated neural regeneration. *Journal of biomedical science* **16** 108

[344] Chen Y-C, Lee D-C, Hsiao C-Y, Chung Y-F, Chen H-C, Thomas J P, Pong W-F, Tai N-H, Lin I-N and Chiu I-M 2009 The effect of ultra-nanocrystalline diamond films on the proliferation and differentiation of neural stem cells *Journal of Neuroscience Methods* **30** 3428–35

[345] Kim S-H, Turnbull J and Guimond S 2011 Extracellular matrix and cell signalling: the dynamic cooperation of integrin, proteoglycan and growth factor receptor. *J. Endocrinol.* **209** 139–51

[346] Wells R G 2008 The role of matrix stiffness in regulating cell behavior *Hepatology* **47** 1394–400

[347] Campos L S 2005 β1 integrins and neural stem cells: making sense of the extracellular environment *BioEssays* **27** 698–707

[348] Flaumenhaft R and Rifkin D B 1991 Extracellular matrix regulation of growth factor and protease activity *Current Opinion in Cell Biology* **3** 817–23

[349] Harrill J A, Freudenrich T M, Machacek D W, Stice S L and Mundy W R 2010 Quantitative assessment of neurite outgrowth in human embryonic stem cell-derived hN2™ cells using automated high-content image analysis *NeuroToxicology* **31** 277–90

[350] Sanes D H, Reh T A and Harris W A 2011 *Development of the Nervous System* (Academic Press)

[351] Patel M R and Shen K 2009 Neurite extension: starting at the finish line. *Cell* **137** 207–9

[352] Parsons X H, Teng Y D, Parsons J F, Snyder E Y, Smotrich D B and Moore D A 2011 Efficient derivation of human neuronal progenitors and neurons from pluripotent human embryonic stem cells with small molecule induction. *J Vis Exp* e3273–3

[353] Ganesan K, Garrett D J, Ahnood A, Shivdasani M N, Tong W, Turnley A M, Fox K, Meffin H and Prawer S 2014 An all-diamond, hermetic electrical feedthrough array for a retinal prosthesis *Biomaterials* **35** 908–15

[354] Haycock J W 2011 3D cell culture: a review of current approaches and techniques. *Methods Mol. Biol.* **695** 1–15

[355] Choi S H, Kim Y H, Hebisch M, Sliwinski C, Lee S, D'Avanzo C, Chen H, Hooli B, Asselin C, Muffat J, Klee J B, Zhang C, Wainger B J, Peitz M, Kovacs D M, Woolf C J, Wagner S L, Tanzi R E and Kim D Y 2014 A three-dimensional human neural cell culture model of Alzheimer/'s disease *Nature* **515** 274–8

[356] Moreno E L, Hachi S, Hemmer K, Trietsch S J, Baumuratov A S, Hankemeier T, Vulto P, Schwamborn J C and Fleming R M T 2015 Differentiation of neuroepithelial stem cells into functional dopaminergic neurons in 3D microfluidic cell culture *Lab Chip* **15** 2419–28

[357] Kilian K A, Bugarija B, Lahn B T and Mrksich M 2010 Geometric cues for directing the differentiation of mesenchymal stem cells *Proceedings of the National Academy of Sciences* **107** 4872–7

[358] Zuk P A, Zhu M, Ashjian P, De Ugarte D A, Huang J I, Mizuno H, Alfonso Z C, Fraser J K, Benhaim P and Hedrick M H 2002 Human Adipose Tissue Is a Source of Multipotent Stem Cells *Mol. Biol. Cell* **13** 4279–95

[359] Bunnell B, Flaat M, Gacliardi C, Patel B and Ripoll C 2008 Adipose-derived stem cells: Isolation, expansion and differentiation☆ *Methods* **45** 115–20